PONTIFICIA UNIVERSIDAD CATÓLICA DE CHILE

SCHOOL OF ENGINEERING

SEISMIC PERFORMANCE FACTORS FOR WOOD FRAME BUILDINGS IN CHILE

EDISSON XAVIER ESTRELLA ARCOS

Thesis submitted to the Pontificia Universidad Católica de Chile and University of Technology Sydney in partial fulfillment of the requirements to receive the degree of Doctor in Engineering Sciences and Doctor of Philosophy

Advisors:
JOSÉ LUIS ALMAZÁN
PABLO GUINDOS

Santiago de Chile, October 2020

PONTIFICIA UNIVERSIDAD CATOLICA DE CHILE
SCHOOL OF ENGINEERING

SEISMIC PERFORMANCE FACTORS FOR WOOD FRAME BUILDINGS IN CHILE

EDISSON XAVIER ESTRELLA ARCOS

Members of the Committee:

JOSÉ LUIS ALMAZÁN	DocuSigned by: E2A0767E989D419...
PABLO GUINDOS	DocuSigned by: PABLO GUINDOS DBA68430D7B3412...
SARDAR MALEK	DocuSigned by: Sardar Malek FDF38E615A1D491...
HERNÁN SANTA MARÍA	DocuSigned by: HERNAN SANTA MARIA OYANEDEL B706775C4B554CB...
GONZALO RODRÍGUEZ	DocuSigned by: 3A401157B6564BD...
PETER DECHENT	DocuSigned by: Peter Dechent Anglada C952ACCA7F094B1...
JUAN DE DIOS ORTÚZAR	DocuSigned by: Juan de Dios Ortúzar 376BE4D3F7A24BE...

Thesis submitted to the Pontificia Universidad Católica de Chile and University of Technology Sydney in partial fulfillment of the requirements to receive the degree of Doctor in Engineering Sciences and Doctor of Philosophy

Santiago de Chile, October 2020

If I have seen further it is by standing on the shoulders of giants.

Isaac Newton, 1675

ACKNOWLEDGMENTS

This research project would not have been possible without the help, assistance, and relentless support of several people and institutions that have been by my side throughout this journey. No text would be enough to express my gratitude to all those who have contributed to developing this work, overcoming the countless issues that came up, and forging my personal growth as a researcher and human being. Thank you all, I could not have done it without you.

I wish to express my deepest gratitude to my parents, Miguel and Gabriela, for being my principal support during the last four years. You always were there to back me up, cheer me up, and push me to keep going when things got tough. Thank you for teaching me the habit of hard work, the value of humility, and to never give up regardless of the circumstances. I owe it all to you.

To my siblings Stephany and Juan Carlos, thanks for never leaving me alone during the good and difficult times. Without the laughs, talks, fights, advice, and support, this journey would not have been the same.

To my beautiful family for their valuable support during all these years. Thanks for the talks, care, attention, and backing. You have been the best group of people to have by my side.

Infinite gratitude to the greatest group of friends a man could ask for. Thanks for the support, caring, fun moments, learnings, adventures, trips, and so on. I am thankful to fate for having met you, and as Ally Condie would say, *"growing apart doesn't change the fact that for a long time we grew side by side; our roots will always be tangled. I'm glad for that"*.

To my supervisor José Luis Almazán, for trusting my capabilities when no one else did and giving me the opportunity to get into timber engineering. Thanks for the wisdom and advice, for taking care of my personal growth besides my professional preparation, and for teaching me a creative-based way of thinking. Above all, you taught me that success does not deprive you of being a humble human being. This was a game-changing lesson for me.

To my co-supervisor Pablo Guindos, who undoubtedly has the essence of a genius. You guided and encouraged me to be professional and give my best even if the road was tough. Without your relentless support, the aim of this thesis would not have been completed.

To my co-supervisor Sardar Malek, who taught me how to hone my skills and conduct cutting-edge research. Thanks for the direction and support during my stay in Australia, for guiding me to think out of the box with breakthrough ideas, and for teaching me to recognize the value of effective communication in research. I do not have enough words to express my gratitude to you.

I am grateful to UC professor Hernán Santa María, principal investigator of the research project framed in this thesis, for providing guidance and feedback throughout this investigation, and for the thoughtful comments and recommendations on this manuscript.

I would like to express my gratitude and appreciation for Jairo Montaño, whose guidance and advice were essential for the development of this research. This project would not have gone ahead without your assistance throughout the experimental tests. I am extremely grateful for our friendly chats and your personal support in my academic endeavor.

To Sebastian Berwart, for his continued support, advice, and guidance in the development of the structural archetypes discussed in this manuscript. Thanks for always being willing to lend me a hand when I needed it.

To my irreplaceable, intriguing, encouraging, and always enthusiastic great friend David Solano. Thanks for the valuable support and company along these long years. The deep and endless talks we had on aleatory topics provided me a new perspective on thinking and living, and were greatly thought-provoking and helpful in tackling many of the problems of this project.

Very special gratitude goes out to Ana Fernanda Villacís for her relentless support at the beginning of this journey. Thanks for the talks, company, countless teachings, and insightful advice during tough times. I would not have done it without your backing.

To my wonderful Aussie family, for the priceless help to develop myself as a better human being. For teaching me kindness, empathy, humility, and faithful friendship. You did in six months what life did not in twenty-six years. Thank you all.

To my very good friend Yona Benzaken, whose craziness kept me sane during the tricky final stages of this journey. Thank you for the endless conversations, unexplainable fun, unconditional support, and constant care. I have no words to express my gratitude for the lessons you taught me. It would not have been the same without you.

To the Chilean National Agency for Research and Development (ANID Chile) for the financial support granted for this research.

To the Pontifical Catholic University of Chile and its Graduate School for the financial and administrative support throughout this project.

To the University of Technology Sydney and its Graduate Research School, whose financial and logistic support was crucial for the development of this research.

LIST OF CONTENTS

LIST OF TABLES

LIST OF FIGURES

SEISMIC PERFORMANCE FACTORS FOR WOOD FRAME BUILDINGS IN CHILE

ABSTRACT

Seismic performance factors are an engineering tool to estimate force and displacement demands on structures designed through linear methods of analysis. In Chile, the NCh433 standard provides the regulations, requirements, and factors for the seismic design of several structural typologies and systems. However, when it comes to wood frame structures, previous research has found that the NCh433 provisions are highly restrictive and result in over-conservative designs. Therefore, this project presents an experimental and numerical investigation aimed at proposing new, less restrictive seismic performance factors for wood frame buildings. Following the FEMA P-695 guidelines, this research embraced: (1) testing of materials, connections, and full-scale specimens, (2) developing of detailed and simplified nonlinear numerical models, (3) developing of a new FEMA P-695 ground motion set for subduction zones, and (4) analyzing the seismic performance of a comprehensive set of structural archetypes. 201 buildings were analyzed and results showed that changing the NCh433 performance factors from R = 5.5 & Δ_{max} = 0.002 to R = 6.5 & Δ_{max} = 0.004 decreases the average collapse ratio of wood frame structures by 13.3% but keeps the collapse probability below 20% for all the archetypes under study. Besides, it improves the cost-effectiveness of the buildings and enhances their competitiveness when compared to other materials, since savings of 40.4% in nailing, 15.9% in OSB panels, and 7.3% in timber studs were found for a 5-story building case study. Further analyses showed that the buildings designed with the new factors reached the “enhanced performance objective” as defined by the ASCE 41-17 standard, guaranteeing a neglectable structural and non-structural damage under highly recurring seismic events. Finally, dynamic results revealed that 87% of archetypes collapsed on the first and second floors, and that the minimum base shear requirement C_{min} of the NCh433 standard is somewhat restrictive for soil classes A, B, and C, leading to conservative results compared to archetypes where the C_{min} requirement did not control the structural design.

FACTORES DE DISEÑO SÍSMICO PARA EDIFICACIONES DE MADERA MARCO-PLATAFORMA EN CHILE

RESUMEN

Los factores de diseño sísmico son una herramienta ingenieril para estimar las demandas de fuerza y desplazamiento en estructuras diseñadas a través de métodos lineales de análisis. En Chile, la normativa NCh433 proporciona las regulaciones, requerimientos, y factores para el diseño sísmicos de varias tipologías y sistemas estructurales. Sin embargo, cuando se trata de estructuras de madera marco-plataforma, investigaciones anteriores han encontrado que las disposiciones de la normativa NCh433 son altamente restrictivas y resultan el diseños sobre-conservadores. Por lo tanto, este proyecto presenta una investigación numérica y experimental que apunta a proponer factores de diseño sísmico menos restrictivos para edificaciones marco-plataforma. Siguiendo la metodología FEMA P-695, esta investigación abarcó: (1) pruebas experimentales de materiales, conexiones, y especímenes a escala real, (2) desarrollo de modelos numéricos no-lineales detallados y simplificados, (3) creación de un nuevo set de registros sísmicos FEMA P-695 para zonas de subducción, y (4) análisis del desempeño sísmicos de un exhaustivo conjunto de arquetipos estructurales. Se analizaron 201 edificaciones y los resultados mostraron que cambiar los factores de diseño sísmicos NCh433 de $R = 5.5$ & $\Delta_{max} = 0.002$ hacia $R = 6.5$ & $\Delta_{max} = 0.004$ reduce el margen de colapso de estructuras marco-plataforma en 13.3% pero mantiene la probabilidad de colapso bajo 20% para todos los arquetipos analizados. Además, mejora la relación costo-beneficios de las edificaciones e incrementa su competitividad al compararlas con otros sistemas estructurales, ya que se encontraron ahorros del 40.4% en clavado, 15.9% en paneles de OSB, y 7.3% en pie-derechos para el caso de estudios de una edificación de cinco pisos. Análisis adicionales mostraron que las edificaciones diseñadas con los nuevos factores propuestos alcanzaron el "*enhanced performance objective*" definido por el estándar ASCE 41-17, garantizando un daño estructural y no estructural despreciable bajo demandas sísmicas de alta recurrencia. Finalmente, los resultados dinámicos revelaron que 87% de los arquetipos colapsaron en los pisos primero y segundo, y que el corte mínimo C_{min} requerido en el estándar NCh433 es algo restrictivo para tipos de suelo A, B, y C, llevando a resultados conservadores al compararlos con arquetipos donde el requerimiento de C_{min} no controló el diseño estructural.

PREFACE

TIMBER ENGINEERING: A NEW PARADIGM FOR MID-RISE CONSTRUCTION IN CHILE

The Chilean real estate market is mainly dominated by masonry for low-rise houses and reinforced concrete for mid- to high-rise buildings. Given the high seismic risk of the region, the local engineering community has developed a robust know-how regarding the seismic design of buildings employing these well-known materials. As a consequence, previous research has shown that the Chilean reinforced concrete buildings are capable of withstanding strong earthquakes with minor damage at the structural and non-structural level (Westenenk et al. 2012). Furthermore, during the last decades, the local industry has developed the mechanisms to provide good quality materials for the construction sector with an unbeatable benefit-cost ratio. In this context, an important question arises. Why moving towards timber construction? Three main points should be considered to answer this question: (1) local timber industry, (2) environmental footprint, and (3) engineering advantages.

The data provided by the Chilean Forestry Institute (INFOR 2016) shows that the local timber industry accounts for 2.6% of Chile's gross domestic product, and generates employment (direct and indirect) for more than 300,000 workers across the country (CORMA 2014), which is about 4% of the total number of people employed in Chile. However, recent research (INFOR 2017a) revealed that in 2016, only 30% of the wood sawn and produced in Chile was used inside the country, while the remainder was exported to countries such as China, the USA, Brazil, among others. The construction sector has a major role in this low level of timber domestic use. Recent data show that in Chile only 32% of the residential homes use timber, and at present, there is a ~0% of mid-rise timber buildings (Santa María et al. 2017), which is a relatively low figure when compared to rates in other countries such as New Zealand or the USA, where 90% of houses use timber as the main material (Ajay 1995; Buckett 2014). Therefore, pushing the growth of the timber construction industry will boost the internal use of wood across different sectors significantly contributing to the country’s economy.

In terms of environmental footprint, Chile has been struggling against pollution problems in several areas across the country in the past few years, as a consequence of highly populated cities and poor airflow through the high mountain ranges of the region. For instance, in 2016 the city of Coyhaique in the south of Chile was declared the most polluted city in Latin America (WHO 2016). Given the high demand for housing in the big cities, the timber construction sector may significantly contribute to mitigating this issue. For instance, studies have shown that the energy consumption of concrete houses is 60-80% higher compared to timber houses (Börjesson & Gustavsson 2000), and that the CO_2 production during the life span of a concrete building is 30-130 kg/m2 greater (Gustavsson, Pingoud & Sathre 2006). In countries with very marked seasons such as Chile, it has been calculated that a timber house consumes between 15% and 16% less energy for heating/cooling when compared to a concrete or steel house. Over a period of 100 years, it is estimated that a timber house could reduce the net emissions of greenhouse gases by between 20% and 50% when compared to traditional systems (Upton et al. 2008).

From an engineering performance perspective, it is universally acknowledged that timber structures have several engineering advantages that make them highly attractive when designing buildings in seismic prone areas (van de Lindt 2004). Their low seismic mass and high flexibility result in low design forces and economically efficient structures (Dechent et al. 2016; Follesa et al. 2018). Furthermore, their high capacity of inelastic deformation (ductility) allows them to achieve high performance levels when subjected to ground motions of low exceedance probability (Jayamon, Line & Charney 2017). This latter follows the current seismic design philosophy for earthquake-resistant buildings, which requires the structure to be able to withstand large inelastic deformations before collapse. Based on the information described above, although it would not be indisputable to affirm that timber buildings are the absolute solution for new constructions, it stands out that this structural system has several advantages over the others in terms of the local economy, environmental footprint, and engineering performance. Nevertheless, due to very conservative regulations, the growth of timber structures has slowed down over the last few years in Chile.

To tackle this issue, this thesis presents the results of a research project aimed at quantifying a new set of less conservative regulations for wood frame buildings in Chile. Following a rational methodology, the feasibility of employing a new R factor and elastic drift limit Δ_{max} is verified, aiming at improving the efficiency and cost of the wood frame buildings across the different zones of the country, and without compromising their safety during moderate and severe earthquakes.

HYPOTHESES AND OBJECTIVES

HYPOTHESES

GENERAL: It is possible to employ less conservative seismic performance factors when designing wood frame buildings in Chile in order to improve the cost-benefit ratio of such structures.

SPECIFIC 1: A new numerical model can be developed to efficiently compute the nonlinear response of 'strong' wood frame walls under lateral loads.

SPECIFIC 2: A continuous rod hold-down anchorage allows wood frame walls to withstand large lateral and overturning loads without showing a brittle or premature failure.

SPECIFIC 3: It is possible to develop a ground motion set for zones prone to subduction earthquakes keeping consistency with the guidelines provided by the FEMA P-695 methodology.

OBJECTIVES

GENERAL: To statistically prove the feasibility of employing less conservative seismic performance factors for wood frame structures in Chile.

SPECIFIC 1: To develop a new efficient numerical model to reproduce the nonlinear response of ‘strong’ wood frame walls under large lateral loads.

SPECIFIC 2: To validate the lateral response of wood frame walls with continuous rod hold-down anchorages through experimental tests.

SPECIFIC 3: To develop a new ground motion set consistent with the FEMA P-695 methodology and suitable to conduct dynamic analyses in areas prone to subduction earthquakes.

THESIS STRUCTURE AND ORGANIZATION

This thesis has been developed following an article-based format; therefore, each chapter of this document corresponds to published or publishable content. Besides, each chapter was designed to address one of the objectives proposed for this research project. Chapter 1 presents the overall project, methodology, and results, and Chapters 2, 3, and 4 present detailed support studies carried out to back up the main research in Chapter 1. This way, even though all the content of this thesis is strongly connected and interrelated, each chapter is self-contained and presents independent research that might be read and understood by itself. Aiming at achieving self-contained chapters, some concepts and explanations might be found more than once across this document for the sake of clarity. However, there is no research overlapped between chapters and sections. The content of this thesis has been organized as follows:

Chapter 1 addresses the General Objective proposed for this project. It presents the formulation of the project, background, methodology, and results of the new proposed seismic performance factors for wood frame buildings in Chile. Further analyses regarding the seismic response of wood frame structures are also presented in this chapter.

Chapter 2 addresses the Specific Objective 1. It presents a support investigation carried out to develop a new numerical model for wood frame walls. This new numerical model is employed in Chapter 1 to study the seismic response of mid-rise wood frame structures.

Chapter 3 addresses the Specific Objective 2. It presents a support experimental investigation that tested real-scale wood frame walls with continuous rod hold-downs. The results of this section fed the numerical models employed in Chapter 1 and provided a better understanding of the behavior of wood frame walls.

Chapter 4 addresses the Specific Objective 3. It presents the development of a new set of ground motions for subduction zones. This new set was employed as a dynamic input in the seismic performance analyses carried out in Chapter 1.

Chapter 5 presents the main findings and conclusions of this research project. In order to highlight the contributions to each field addressed in this thesis, conclusions were sorted out and grouped by chapters.

Finally, Appendixes A, B, C, and D present additional information about the structural archetypes analyzed in this thesis and their fragility functions for different performance levels.

CHAPTER ONE

VALIDATION OF SEISMIC PERFORMANCE FACTORS FOR WOOD FRAME BUILDINGS IN CHILE

CHAPTER DISCLAIMER

The content, methodology, results, and figures presented in this chapter are based on the following article:

- Estrella, X., Almazán, J., Guindos, P., Santa María, H., and Malek, S. Seismic performance factors for wood frame buildings in Chile. *In preparation for submission.*

1.1. INTRODUCTION

Seismic performance factors (SPFs) are a relevant tool when designing modern earthquake-resistant structures. They provide a first approach to estimate strength and displacement demands on structural systems designed with linear elastic methods, but that are expected to behave nonlinearly during moderate to severe earthquakes. Due to their simplicity and ease of use, SPFs represent an everyday tool for researchers and practitioners of structural engineering and are included in most seismic standards worldwide. The current state-of-the-art proposes several SPFs for different purposes during the design phase, such as the response modification factor R, the system overstrength factor Ω_0, the maximum allowable drift Δ_{max}, or the deflection amplification factor C_d (FEMA 2009; Baker et al. 2010; INN 2009). However, the most widely used factors in national and international building codes are the R factor and the maximum allowable drift Δ_{max}.

The design philosophy behind the SPFs relies on the nonlinear deformation capacity of code-compliant buildings. For a given fundamental period T_1, the R factor reduces the design base shear V_s calculated from an elastic design acceleration spectrum Sa_D, as pictured in Figure 1-1(a). This means $V_s(T_1) = W \times Sa_D/R$, where W is the effective seismic mass of the building. The ductility of the structural system determines how much the base shear is reduced; the higher the ductility, the higher the R factor, and the lower the base shear. For instance, the ASCE 7-16 standard (ASCE 2016) defines an R factor equal to 4 for ordinary reinforced concrete shear walls, while for ordinary plain concrete shear walls R is equal to 1.5. The rationale of an R factor which depends on the ductility is allowing the structure to suffer damage during strong earthquakes, but at the same time to assure that a life-threatening performance level is not reached. This way, the cost-effectiveness of the building improves by reducing the cost of the main structural system. Therefore, the R factor determines the relative acceleration that the structure is required to resist to guarantee the resilience of the building. On the other hand, the maximum allowable drift Δ_{max} provides a means to improve structural performance by controlling the stiffness of the building. As illustrated in Figure 1-1(b), it limits the maximum interstory drift for linear elastic designs (under a design spectrum reduced by the R factor), aiming at minimizing the non-structural damage during moderate earthquakes and the structural damage during severe earthquakes.

The quantification of the values adopted for the SPFs is usually based on detailing and expected performance. However, for novel or undefined structural systems they are typically determined using engineering criteria and qualitative comparisons to achieve an equivalent behavior to that of other code-defined systems. Although a good performance may be achieved for buildings designed using such factors, the lack of a robust methodology to quantify them may lead to over-conservative designs that are not economically competitive in the real estate market.

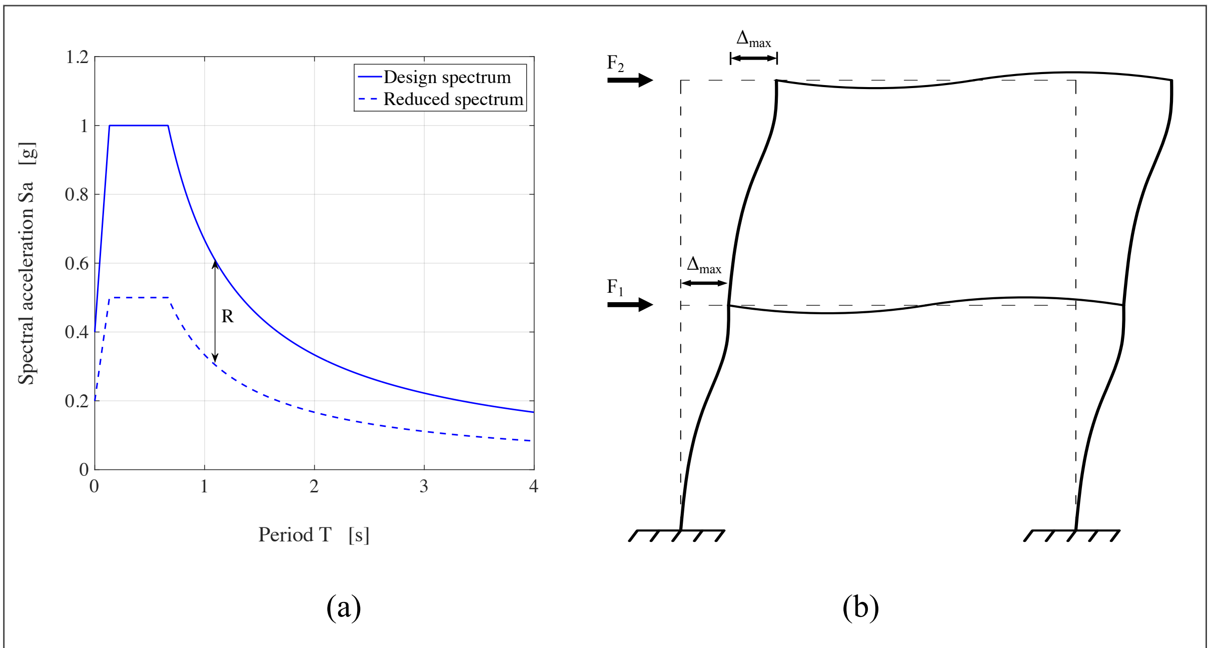

Figure 1-1. Seismic performance factors: (a) response modification factor R, and (b) maximum allowable drift Δ_{max}.

Nowadays, to design mid- to high-rise buildings in Chile, the current normative stipulates that the requirements of the national standard for seismic design of buildings NCh433 (INN 2009) must be met. For wood frame construction, the standard establishes an R factor equal to 5.5, and a maximum allowable drift Δ_{max} of 0.002H, where H is the interstory height. This maximum drift controls the relative displacement of the center of mass of two consecutive stories and was adopted to guarantee the performance of stiff systems such as reinforced concrete wall structures. However, this requirement may be difficult to achieve by flexible systems such as wood frame buildings, resulting in very rigid structures with short periods and low ductility demands, wasting the inherent advantages of timber construction.

The suitability of the Chilean SPFs regarding wood frame construction can be analyzed by comparing them to those defined in international standards. As discussed by Dolan et al. (Dolan, Dechent & Giuliano 2008), the American ASCE 7-16 standard (ASCE 2016) defines an R factor equal to 6.5 for light-frame shear walls with wood structural panels. If the differences in the seismic demand (i.e., seismic design spectrum) between both countries are not taken into account, the lower R factor in the NCh433 standard (INN 2009) results in wood frame buildings being designed for accelerations 18% higher than equivalent structures designed under the USA requirements. If the different design spectra are considered, the accelerations can be up to 2.75-3.0 times higher (Dolan, Dechent & Giuliano 2008). It is also of relevant interest to analyze how other materials are considered with respect to timber in both standards. For instance, the R factors for ordinary reinforced concrete and masonry walls in the ASCE 7-16 standard (ASCE 2016) are 4 and 2, while in the NCh433 (INN 2009) standard are 7 and 4, respectively. This gives timber construction a market advantage in the USA, while reinforced concrete has a market advantage in Chile. Furthermore, it can be noted that concrete and masonry are required to resist 30% and 225% higher accelerations than timber in the USA, while they are required to resist 21% lower and 25% higher accelerations than timber in Chile, respectively. As noted by Dolan et al. (Dolan, Dechent & Giuliano 2008), these differences illustrate a bias towards more familiar and better-known materials, highlighting the need for a rational quantification of the SPFs in seismic standards and codes.

Regarding the maximum allowable drift Δ_{max}, the ASCE 7-16 (ASCE 2016) requirement is 0.00625H for all structures 4 stories or less ($\Delta_{max} = \Delta_{adm} / C_d = 0.025H/4 = 0.00625H$), meaning that the Chilean code requires timber buildings to be over 3 times stiffer than similar buildings in the USA. Therefore, the lateral design is mainly controlled by drift restrictions that are difficult to meet in areas prone to high seismic accelerations. The small deflections expected for a Δ_{max} of 0.002H result in overdesigned wood frame walls; hence, the potential of wood frame constructions is not fully harnessed, as it has been reported by previous researchers. For instance, Santa María et al. (Santa María et al. 2016) reported large cross-sections and sturdy walls while designing a six-story wood frame building according to the current Chilean seismic regulations. Cárcamo et al. (Cárcamo, Caamaño & Cid 2017) highlighted the need to incorporate rigid structures, such as concrete or cross-laminated timber CLT walls, in wood frame buildings in order to meet the maximum drift requirement. Guíñez et al. (Guíñez, Santa María & Almazán 2019) reported that, at a 0.002H drift, wood frame walls only have reached about 16% to 23% of their maximum strength capacity, showing that these walls allow larger drifts than, for instance, concrete ones. Additionally, a maximum allowable drift Δ_{max} equal to 0.004H was recommended by Guíñez et al. (Guíñez, Santa María & Almazán 2019) for mid-rise timber buildings so that about 40% of the strength capacity of wood frame walls is harnessed.

A robust seismic design standard is crucial for the development and growth of timber construction in Chile. However, according to previous research (Dechent et al. 2017), the basis of the SPFs for timber structures in the current Chilean seismic standard is not quite clear. Therefore, this thesis presents the results of a comprehensive research project aimed at validating a new set of seismic performance factors for wood frame buildings through a rational approach. Following the guidelines of the FEMA P-695 methodology (FEMA 2009), this investigation included: (1) testing of full-scale wall assemblies, (2) nonlinear numerical modeling of wood frame walls under monotonic and cyclic loads, (3) ground motion selection, (4) performance evaluation of a comprehensive set of wood frame buildings through 3D nonlinear dynamic analyses, and (5) validation of a new set of SPFs.

1.2. MATERIALS AND METHODOLOGY

This section presents the work conducted on wood frame structures at the first stage of this project, which provided a sound background to support the validation of the new set of SPFs discussed in Section 1.3. In order to appropriately adapt the FEMA P-695 guidelines (FEMA 2009) to the local Chilean context, different research fields were covered throughout this investigation: experimental tests, computational models, seismological ground motions, architectural designs, structural designs, and tridimensional dynamic simulations. A brief description of the work carried out in each field is presented in the following subsections.

1.2.1. Testing program

Wood is a natural material whose mechanical properties are influenced by the environment in which it is grown. It is universally acknowledged that, even if the same timber grade is employed, wood frame walls may exhibit an important uncertainty in their behavior under lateral and vertical loads. For instance, previous research (Guíñez, Santa María & Almazán 2019) has reported variability of about 20% in strength and stiffness for wood frame walls analyzed under similar conditions. Therefore, this section aimed at experimentally analyzing the suitability of Chilean timber products for use in mid-rise buildings, testing the elements that make up a wood frame wall, and verifying the response of walls with different properties under large lateral displacements as those expected during severe earthquakes. Furthermore, it provided relevant data to calibrate and validate the numerical models presented in Section 1.2.2.

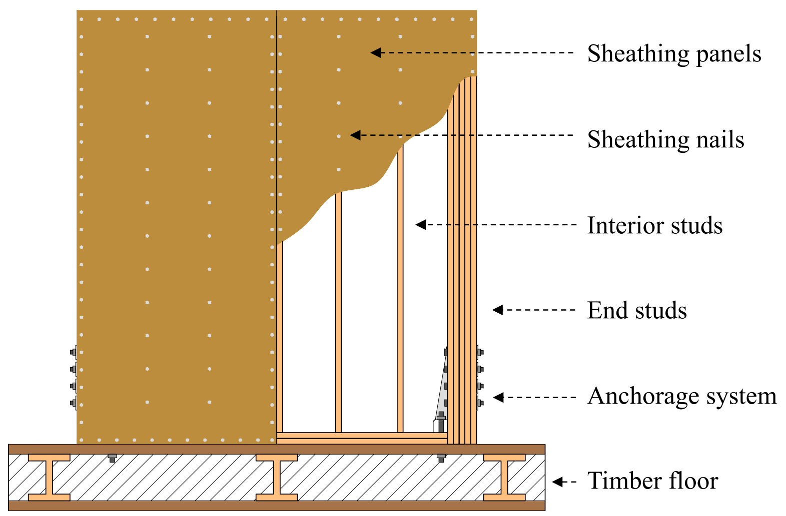

Figure 1-2. Schematic configuration of wood frame walls.

A combination of timber and steel elements make up a wood frame wall. For mid-rise buildings, a typical wall consists of a 1200 to 2400 mm long timber frame assembled with 38×135 mm studs. To resist the high vertical loads, end studs have several members, while interior studs are single members spaced at 400 mm on center. Top and bottom plates consist of double members, and the wall is fixed to the floor by means of a steel anchorage system (a discrete or continuous hold down). The lateral capacity of the wall is provided by 9.5 to 15.1 mm thick sheathing OSB panels on one or both sides of the wall, which are attached to the timber frame with steel nails spaced at 50 to 100 mm on center along the panel edges. At the interior studs, nails are spaced at 200 mm. A schematic configuration of a typical wood frame wall is shown in Figure 1-2.

In the first stage of the testing program, forty-five timber studs were mechanically tested under bending, tensile, and compression load at the facilities of the INFOR Structural Timber Laboratory, in Concepción, Chile, following the guidelines of the Chilean standard NCh3028/1 (INN 2006). Specimens consisted of mechanically graded Chilean MGP10 radiate pine with a cross-section of 38×135 mm and 2400 mm in length. Additionally, twenty 11.1 mm thick OSB panels (127×127 mm) were tested according to the ASTM D2719 standard (ASTM 2013) at the facilities of the Engineered American Wood Association in Tacoma, USA, to study their shear modulus in the longitudinal and transverse direction. Test results were consistent with those reported by previous investigations (Folz & Filiatrault 2001; Segura 2017; Cartes, González & Padilla 2017; INN 2014), showing that Chilean wood products meet the requirements for use in structural engineering. Further details of this testing program and its experimental results can be found in (INFOR 2017b) and Section 2.2.

Subsequently, thirty-six sheathing-to-framing (S2F) connections were tested by Jara and Benedetti (Jara & Benedetti 2017) at the facilities of the University of Bío-Bío, in Concepción, Chile. The specimens consisted of pneumatically-driven double shear OSB-stud joints, employing 70 mm long spiral nails with 3 mm in diameter. The studs were 38×135 mm, and the panel thickness ranged from 9.5 to 15.1 mm. Six tests were monotonic and thirty were cyclic, applying the CUREe-Caltech loading protocol proposed by Krawinkler et al. (Krawinkler et al. 2001). Results were consistent with previous investigations (Seim et al. 2016; Folz & Filiatrault 2001; Sartori & Tomasi 2013; Casagrande et al. 2020) in terms of strength capacity, stiffness, ductility, energy dissipation, and nonlinear response, showing a pinched hysteresis under large reversed displacements. Typical failure modes were observed during the tests: yielding and shear fatigue of nails, pulling out of nails, pulling through the OSB panels of nail heads, and crushing of the OSB panel. A comprehensive report of the results can be found in (Jara & Benedetti 2017). The test setup and results for a cyclic specimen are shown in Figures 1-3(a) and 1-3(b), respectively.

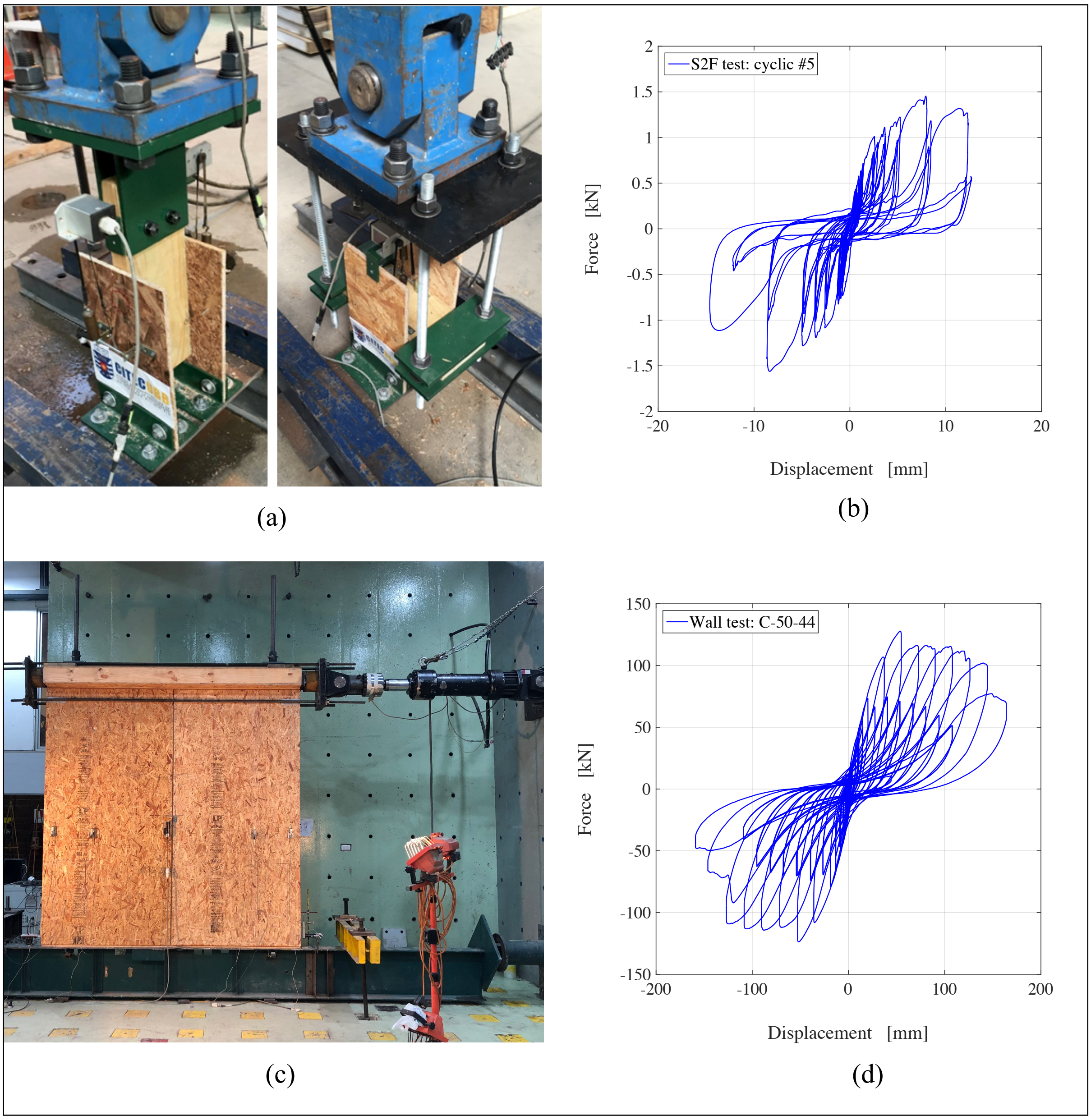

Figure 1-3. Experimental program: (a) setup for sheathing-to-framing S2F tests, (b) results of cyclic S2F test #5, (c) setup for full-scale wood frame wall tests, and (d) cyclic results for a 2400 mm long wall with continuous rod hold-downs.

Finally, twenty-three full-scale wood frame walls were tested at the facilities of the Structural Engineering Laboratory at the Pontifical Catholic University of Chile. Out of the twenty-three specimens, nineteen were tested by Guíñez et al. (Guíñez, Santa María & Almazán 2019) and four were tested as part of this thesis (presented in Chapter 3). In total, seven specimens were tested monotonically and sixteen were tested cyclically applying the CUREe-Caltech protocol (Krawinkler et al. 2001). The walls were 2400 mm high and the lengths ranged from 700 to 3600 mm. All specimens were sheathed with 11.1 mm thick OSB panel on both sides, employing 70 mm long spiral nails (3 mm in diameter) spaced at 50 and 100 mm. Two different anchorage systems were used: discrete and continuous hold-downs. Additionally, Ø1×10" shear bolts were installed through the bottom plate to prevent sliding of the wall. Results showed a good behavior of the walls under large lateral deformation, having a ductile failure mode after the force peak was reached. The damage was mainly concentrated in the S2F connections located at the central studs and wall corners, with little damage to the framing and anchorage system. Stiffness and capacity were found to depend on the wall length and nail spacing. Interestingly, it was found that the shear capacity estimated by the Special Design Provisions for Wind and Seismic SDPWS standard (American Wood Council 2015) underestimated the strength and overestimated the stiffness for most of the specimens. A detailed report and discussion of the tests and results can be found in (Guíñez, Santa María & Almazán 2019) regarding wood frame walls with discrete hold-downs, and in Chapter 3 for wall with continuous hold-downs. The test setup and results for a 2400 mm long wall are shown in Figures 1-3(c) and 1-3(d), respectively.

1.2.2. Nonlinear modeling

Numerical models are a convenient tool to expand the scope of the research beyond the testing laboratory. They provide a means to overcome the physical and economic limitations of the experimental programs, allowing a wider range of scenarios and conditions to be analyzed. Therefore, based on the experimental data discussed in the previous section and the work conducted by previous researchers (Folz & Filiatrault 2001; Pang & Hassanzadeh 2012), a new modeling approach was developed for the wood frame walls under study. This new model takes into account the special features of the walls for mid-rise buildings (Guíñez, Santa María & Almazán 2019; Sadeghi Marzaleh et al. 2018), allowing accurate nonlinear analyses for large displacements to be conducted.

In order to minimize the computational overheads and the input parameters, the proposed model followed a simplified strategy between mechanistic lumped approaches and complex FEM models. Consequently, the nonlinearity of the model was introduced by the sheathing-to-framing connections, while the other wall components were assumed to behave within the elastic regime. Figure 1-4(a) shows a comparison of the test results and model predictions for a 2400 mm long wall with discrete hold-downs, and Figure 1-4(b) pictures a schematic representation of the model and its components. A full description of the modeling approach and its validation with experimental tests can be found in Chapter 2.

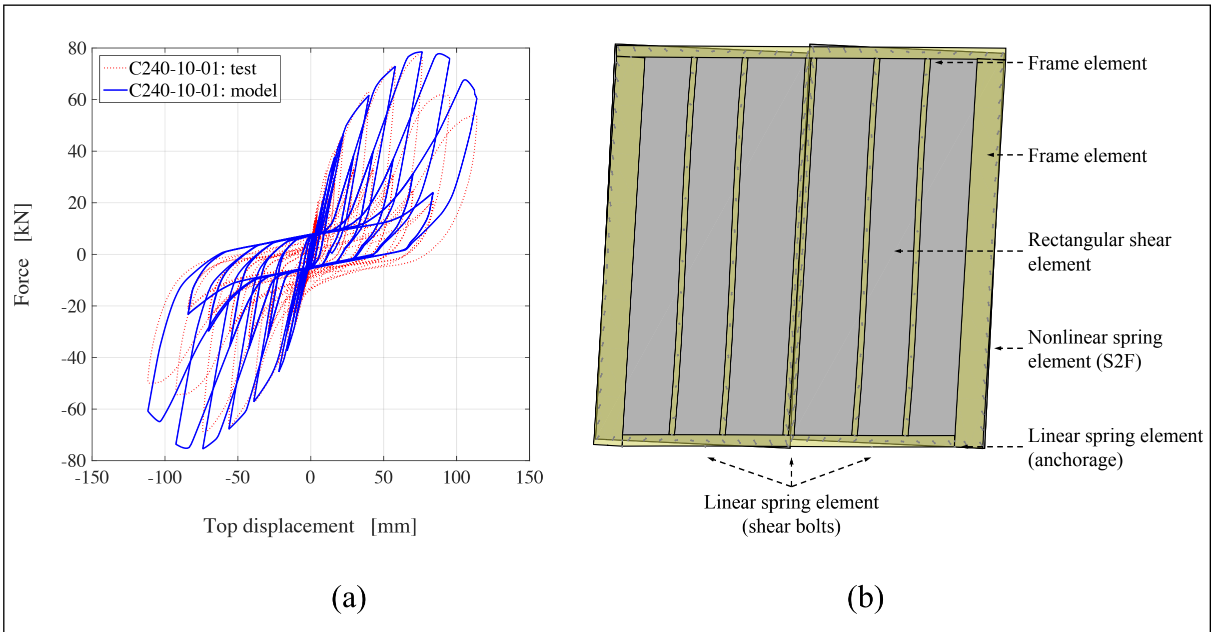

Figure 1-4. (a) Comparison between test results and model predictions for a 2400 mm long wall with discrete hold-downs, and (b) schematic representation of the proposed modeling approach.

When developing numerical models for wood frame buildings with several stories and structural elements, an efficient approach may be necessary to carry out static and dynamic nonlinear analyses without compromising the available computational resources. Such an approach should be able to capture the intrinsic properties of the nonlinear behavior of timber structures and, at the same time, be efficient enough to maximize the cost-effectiveness of the analyses. For wood frame buildings, Pei and van de Lindt (Pei & van de Lindt 2009) proposed a simple approach that employs springs and rigid diaphragms to model the 3D behavior of the structure under lateral loads, whose accuracy has been validated with full-scale tests of low- and mid-rise assemblies (van de Lindt, Pei, Liu, et al. 2010; Pei & van de Lindt 2011). As illustrated in Figure 1-5, such a model uses a nonlinear horizontal spring to represent the shear response of each wall, and bi-linear vertical springs to capture the wall uplifting due to the anchorage elongation. The horizontal spring employs the MSTEW nonlinear hysterical model proposed by Folz and Filiatrault (Folz & Filiatrault 2001), which is able to capture phenomena such as strength degradation, stiffness degradation, and pinching, commonly observed for wood frame walls under large lateral deformations. The horizontal floor diaphragm in each story is modeled as a rigid body (i.e., a rigid plate) with 6-DOF at its center of gravity, where the seismic mass of the floor is concentrated. A detailed formulation of the model can be found in (Pei & van de Lindt 2009). This modeling approach has been incorporated in the software SAPWOOD (Pei & van de Lindt 2010).

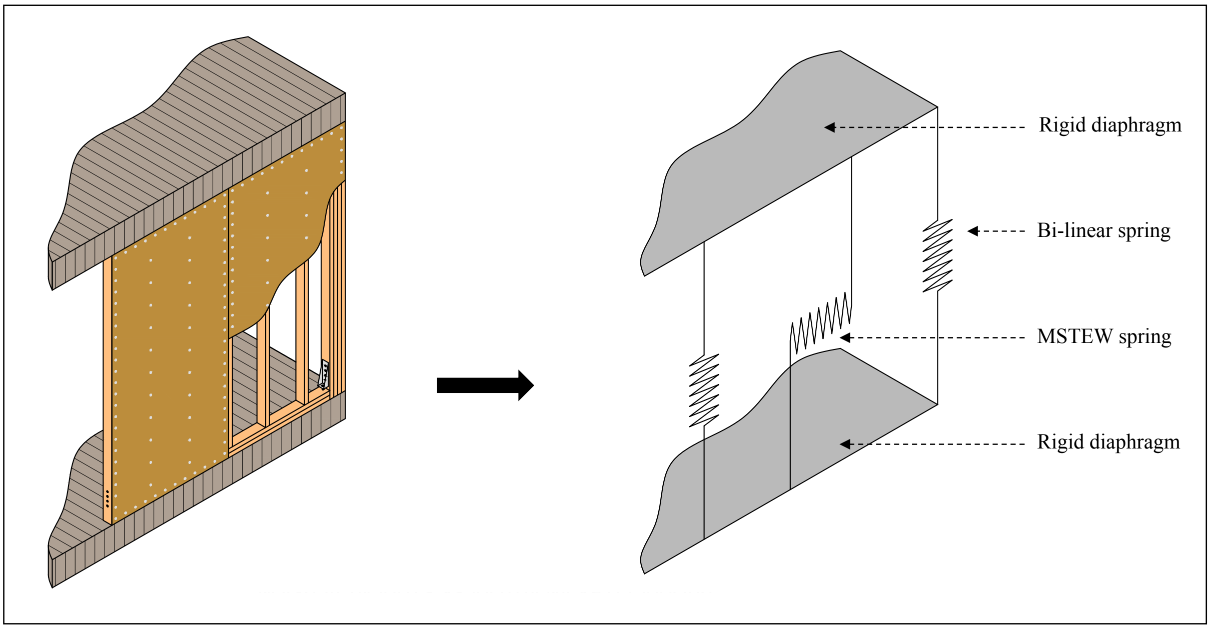

Figure 1-5. Simplified modeling approach proposed by Pei and van de Lindt (Pei & van de Lindt 2009) for wood frame walls and anchorage systems.

Employing the modeling approach shown in Figure 1-4(a) and the shear data from the experimental program, the parameters of the MSTEW model were calibrated for wood frame walls with different properties. This way, a database was generated with the aim of providing a robust framework to develop simplified nonlinear models for wood frame structures. These results can be found in Chapter 2 in detail.

By way of example, Figure 1-6 shows a comparison between the shear response of a 2400 mm long wall test and the predictions of the MSTEW model. As can be noted from the plots, with a very low computational effort the MSTEW model accurately predicts the test results even for large deformations, properly capturing the nonlinear behavior of the specimen in terms of strength, stiffness, and deformation capacity. This simplified modeling approach will be used in subsequent sections to study the seismic behavior of multistory wood frame buildings and validate the new set of SPFs.

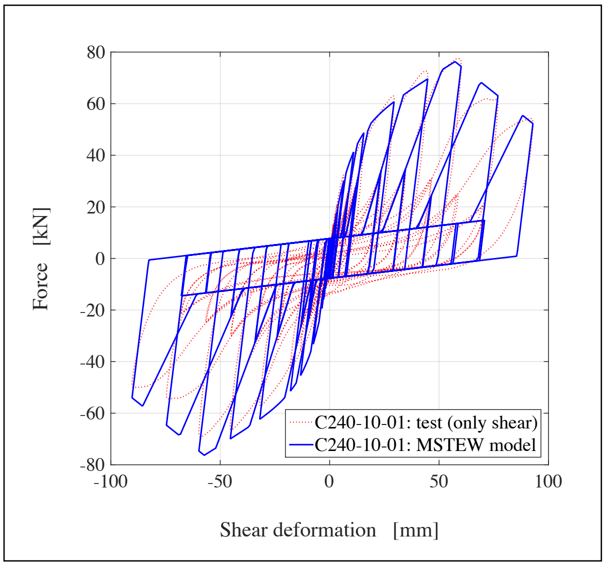

Figure 1-6. Comparison between test results and MSTEW model predictions for a 2400 mm long wall with discrete hold-downs. Test results correspond to the shear deformation of the specimen.

1.2.3. Architectural archetypes

The validation of a set of SPFs through the FEMA P-695 guidelines (FEMA 2009) requires analyzing the seismic behavior of a comprehensive group of buildings (structural archetypes) in order to determine if the new SPFs lead to structures that reach appropriate performance levels. Such a group of structural archetypes must cover a thorough spectrum of scenarios regarding architecture, structural configuration, seismic design load, and structure emplacement. In this section, the different architectural archetypes employed in this research are briefly presented and discussed.

After a comprehensive analysis of the most common floor-plan configurations in the Chilean real estate market of concrete and masonry mid-rise buildings, four architectures (so-called "Q", "C", "P", and "D") were developed for this investigation by Cárcamo (Cárcamo 2017). As Figures 1-7(a), 1-7(b), 1-7(c), and 1-7(d) show, the floor-plans take into account the inherent features of wood frame buildings regarding space distribution, placement of structural elements, and climatization needs, and embrace different architectural possibilities for both the private and social market. A detailed report on the floor-plans development can be found in (Cárcamo 2017).

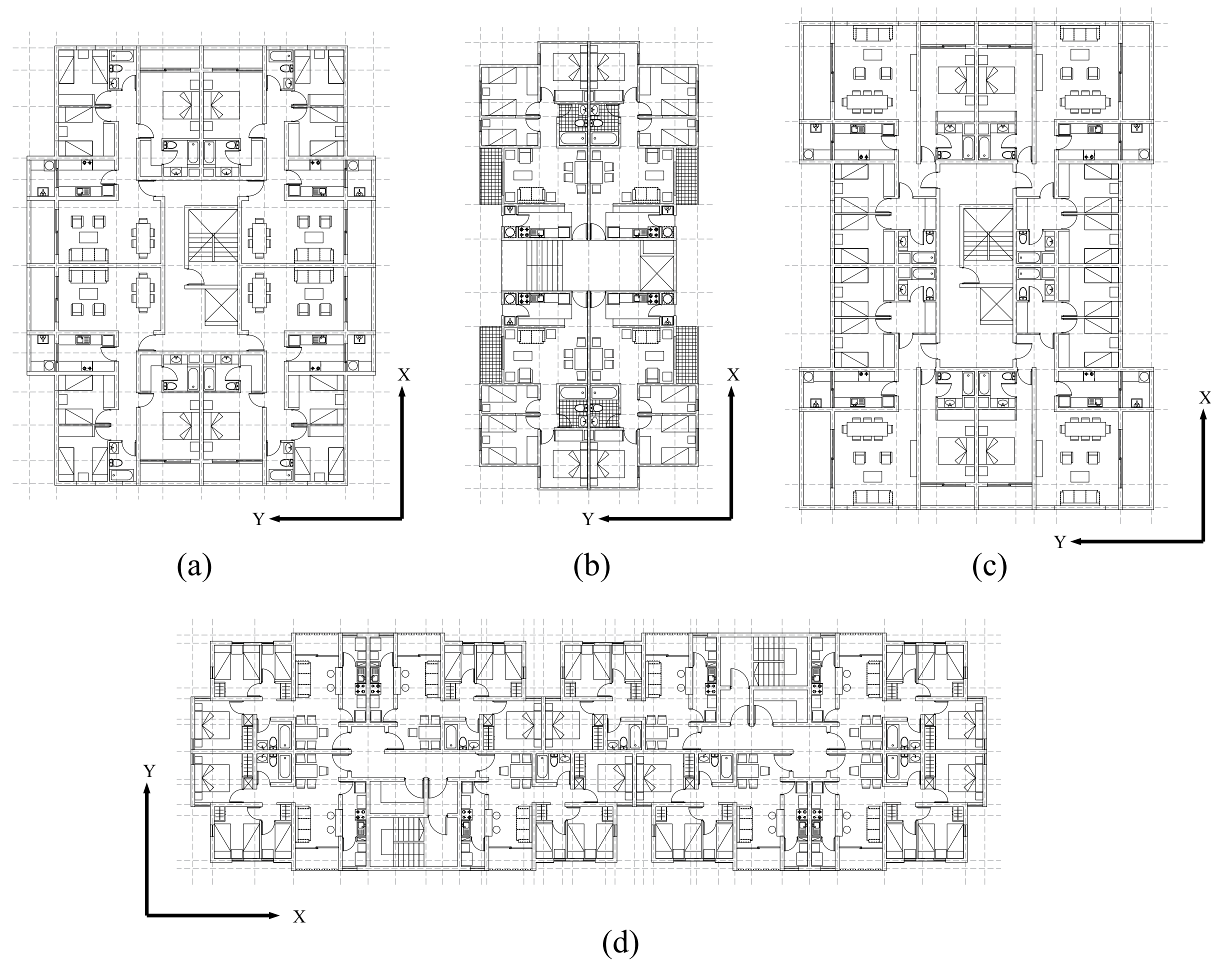

Figure 1-7. Floor-plan configurations developed for this investigation: (a) floor-plan “Q”, (b) floor-plan “C”, (c) floor-plan “P”, and (d) floor-plan “D”. Additional information is detailed in Table 1-1.

The floor area of the archetypes ranged from 252.66 to 530.28 m^2, with a space efficiency η_a above 93% in all cases. The floor-plans Q and P were mostly square-shaped with a plan aspect ratio equal to 1.50 and 1.38, while for the plans C and D, the plan aspect ratio was 2.05 and 3.6, respectively. Considering only structural walls (wall aspect ratio ≤ 2) in each floor-plan, the wall density for a given direction (X or Y) ranged from 3.05% to 5.96%, a value consistent with previous investigations (Cárcamo, Caamaño & Cid 2017), and somewhat higher than that of other materials. For instance, for Chilean concrete buildings, the typical wall density is about 2.8% (Chacón et al. 2017). The average ratio of wall linear meters (X or Y) to the floor perimeter was 1.11. Additional information on the architectural archetypes is listed in Table 1-1.

Table 1-1. Geometric parameters of the architectural archetypes: B_x and B_y = plan dimensions, B_x/B_y = plan aspect ratio, A = floor area, A_c = core area (elevators and staircases), η_a = space efficiency = $1-(A_c/A)$, ρ_x and ρ_y = wall density, P = perimeter, L_x and L_y = wall linear meters, L_x/P and L_y/P = ratio of wall linear meters to perimeter.

Archetype	B_x [m]	B_y [m]	B_x/B_y	A [m²]	A_c [m²]	η_a [%]	ρ_x	ρ_y	P [m]	L_x [m]	L_y [m]	L_x/P	L_y/P
Q	24.23	16.16	1.50	436.61	17.07	96.09	3.69	3.73	86.9	101.30	102.32	1.17	1.01
C	24.75	12.09	2.05	252.66	14.98	94.07	3.10	5.96	78.58	49.24	94.61	0.63	1.92
P	26.92	19.54	1.38	491.88	17.07	96.53	3.63	3.05	99.8	112.26	94.36	1.12	0.84
D	43.89	12.20	3.60	530.28	32.58	93.86	3.84	4.61	128.05	127.86	153.64	1.00	1.20

1.2.4. Structural archetypes

In addition to the architectural floor-plans discussed in the previous section, different design scenarios were taken into account when developing the structural archetypes for this investigation. Firstly, following the Chilean NCh433 standard (INN 2009), two seismic zones (Zone 1 and Zone 3) and four soil classes (from A to D) were considered when siting the archetypes. This resulted in different design base shear values since the design spectrum of the NCh433 standard (INN 2009) is a function of the seismic zone and soil class. Secondly, two SPF sets were included when designing the archetypes: (1) $R = 5.5$ & $\Delta_{max} = 0.002$, and (2) $R = 6.5$ & $\Delta_{max} = 0.004$. The first set aimed at validating the suitability of the current regulations in the NCh433 standard (INN 2009), while the second set proposes new less-restrictive SPFs for wood frame buildings. The values for the second set were selected after a preliminary parametric study on selected archetypes to find the SPFs that maximize the cost-benefit ratio of the structural design. Thirdly, the height of the buildings ranged from three to six stories, covering the most common applications for wood frame mid-rise structures in Chile and providing a wide range of fundamental periods T_1 in the archetype set. And fourthly, two solutions were implemented regarding the structural anchorage system: (1) discrete hold-downs, and (2) continuous rod hold-downs. This way, variations on the strength and stiffness of the walls due to the anchorages were considered when analyzing the archetypes. After permuting the variables listed above along with the architectural floor-plans described in Section 1.2.3, a set of 201 structural archetypes was obtained for this investigation. A detailed report of the set can be found in Appendix A. Table 1-2 summarizes the design scenarios and building features of the archetype set.

Table 1-2. Design scenarios and building features considered in the structural archetype set.

Variable	Variations
Floor-plan	Q, C, P, and D
Seismic zone	Zone 1 and Zone 3
Soil class	A, B, C, and D
SPF sets	5.5 & 0.002 and 6.5 & 0.004
Number of stories	3, 4, 5, and 6
Anchorage system	Discrete and continuous hold-down
Total archetypes	201

Structural designs were carried out for each archetype in the set according to the different design scenarios and building features listed in Table 1-2. Design loads were computed from the NCh433 guidelines (INN 2009). A live load L equal to 200 kg/m^2 for residential buildings was considered in all archetypes, and dead loads D were calculated for each case based on the self-weight of structural elements and timber slabs (dead loads ranged from 200 to 250 kg/m^2, approximately). Subsequently, the seismic mass of each floor was calculated as D+0.25L (INN 2009). As established by the NCh433 standard (INN 2009), for archetypes up to 5 stories the seismic design loads were obtained through static analyses on linear models of the archetypes, while the 6-story archetypes employed a modal analysis to compute the design loads. The design base shear was calculated from code-defined acceleration spectra as a function of the seismic zone, soil type, occupancy category, and R factor. An occupancy category II was considered for all archetypes. It should be noted that for all 6-story archetypes an R_o factor equal to 7.0 was considered, since the NCh433 standard (INN 2009) establishes this criterium when modal analyses are used. Therefore, for these archetypes the sets of SPFs were: (1) R_o = 7.0 & Δ_{max} = 0.002, and (2) R_o = 7.0 & Δ_{max} = 0.004. When calculating the base shears through static analyses, the fundamental period of the structure was computed using Equation 1-1 proposed by Nassani (Nassani 2014):

$$T_1 = 2\pi \sqrt{\frac{2\delta_n}{3g}} \qquad \text{Eq. 1-1}$$

where δ_n is the roof displacement of the structure when a lateral load equal to the seismic weight of the building is applied on a linear model. Additionally, accidental torsion effects were also considered when calculating the design base shear, incorporated as a geometric eccentricity in the structural design (INN 2009). In the static analyses, the vertical distribution of the shear loads for each floor followed the guidelines in Section 6.2.5 of the NCh433 standard (INN 2009). The shear load for each wall of the floor was distributed assuming a rigid diaphragm behavior of the timber slab. As previous researchers have reported, this is a suitable assumption when the floor-plan is regular, a properly detailing is used, and the floor/wall stiffness ratio does not exceed nominal values as defined by Wescott and Huang (Wescott 2005; Huang 2013). Thereby, the shear load for each wall was computed proportionally to its stiffness. Regarding the vertical loads on the wall, they were calculated based on the tributary areas determined from the floor-plan distribution for each wall. Finally, the design properties of walls (strength and stiffness) were estimated from the SDPWS guidelines (American Wood Council 2015), the mechanical characteristics of materials from the Chilean NCh1198 standard (INN 2014), and the capacities of the hold-down devices (discrete and continuous) from the design catalogs provided by the supplier (Simpson Strong-Tie 2015, 2018). A thorough report of the structural design process can be found in (Berwart, Montaño & Santa María 2020).

1.2.5. Ground motion selection

When evaluating the seismic behavior of structural archetypes with the aim of validating a new set of SPFs, the FEMA P-695 guidelines (FEMA 2009) require performing nonlinear static and dynamic analyses using a numerical model of each archetype. Regarding dynamic analyses, these are carried out in the form of an incremental dynamic analysis (IDA) for each archetype of the set. An IDA is a series of response-history nonlinear analyses employing a pre-defined group of ground motions, whose amplitude increases progressively until a given performance level is reached (Vamvatsikos & Cornell 2002). In this context, the FEMA P-695 standard (FEMA 2009) provides two ground motion sets to be used in the IDAs. The first set consists of 22 pairs of far-field accelerograms recorded at sites more than 10 km away from the fault rupture, and the second set of 28 pairs of near-field accelerograms recorded at sites less than 10 km away from the fault rupture. Both the far-field and near-field accelerograms were recorded from shallow crustal earthquakes (typical in the Western United States), and they do not include records from deep subduction earthquakes such as those expected in Japan, New Zealand, or in areas on the Pacific Coast in South America. This limits the application of the sets provided by the FEMA P-695 methodology in regions threatened by subduction earthquakes since the intrinsic features of subduction records (such as frequency content, record duration, or energy released) are neglected, leading to obtaining non-conservative results from the IDAs. Therefore, since Chile is located in a seismic subduction area, a new set of ground motions that is entirely consistent with the FEMA P-695 guidelines and properly includes subduction ground motions was developed for this research.

The new ground motion set consisted of 26 pairs of accelerograms (horizontal components) obtained from seismological reports of different countries around the globe. In order to avoid bias towards a particular region, records were chosen regardless of the zone or country of origin. The ground motions were selected such that 2/3 were subduction records and 1/3 crustal ones. Therefore, the set was comprised of 18 records from subduction earthquakes and 8 from shallow crustal earthquakes, of which 3 were from thrust faults and 5 from strike-slip faults. Earthquake magnitudes ranged from M = 6.5 to 9.0 Mw, covering seismic events in a time window of 30 years, approximately. Figure 1-8 shows the response spectra for the 26 pairs of records and the mean spectrum of the set plus one and two standard deviations. It can be observed that the average spectral acceleration for short periods is close to 0.8 g, and for a 1-second period, it is about 0.35 g. The transition from the constant acceleration zone to the constant velocity zone occurs at T = 0.5 s, a value consistent with the expected response of soft rock sites or rigid soils. A complete report of the ground motion set, selection criteria, normalization procedure, spectral shape factors, and further analyses can be found in Chapter 4.

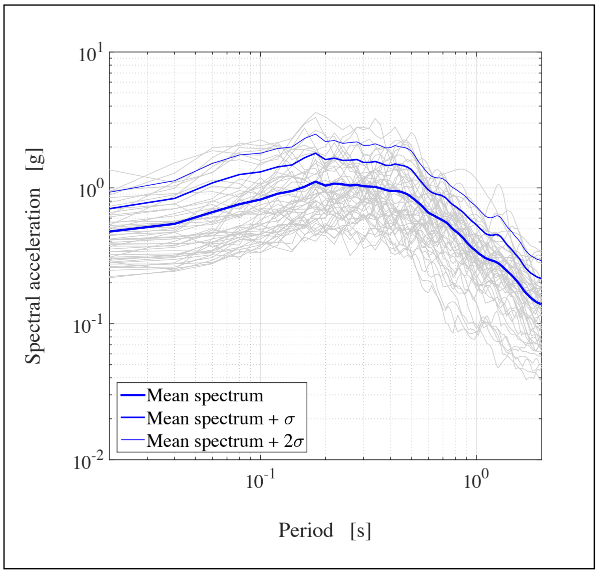

Figure 1-8. Response spectra of the 26 pairs of records and mean spectrum of the set plus one and two standard deviations.

1.2.6. Nonlinear static and dynamic analyses

This section briefly summarizes the nonlinear static and dynamic analyses conducted on each structural archetype of Section 1.2.4. As prescribed by the FEMA P-695 guidelines (FEMA 2009), these analyses provided a means for a rational and sound validation of the new set of SPFs as will be discussed later in this chapter. Firstly, employing the simplified modeling approach presented in Section 1.2.2, a nonlinear model was developed for each of the 201 structural archetypes of the set employing the SAPWOOD software (Pei & van de Lindt 2010). Static analyses were conducted on each model in the X and Y direction employing a modal adaptive lateral load distribution over the building height. This way, valuable information was obtained for each archetype, such as the system over-strength, overall stiffness, ductility, damage distribution, among others. By way of example, Figure 1-9(a) shows the base-shear versus roof-displacement plot for archetype 103, i.e., a 5-story building, floor-plan "P", seismic zone A, soil type A, SPFs 6.5 & 0.004, and discrete hold-downs. A full report of the static results for all archetypes can be found in Appendix A.

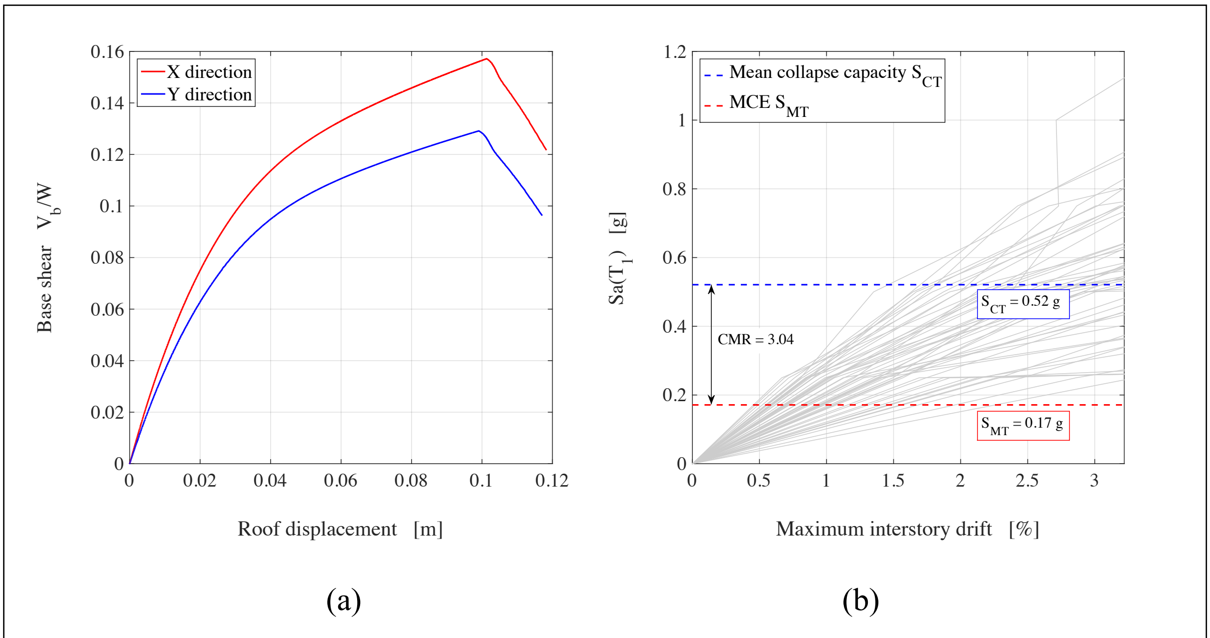

Figure 1-9. Nonlinear numerical results for archetype 103: (a) static lateral results for the X and Y directions, and (b) IDA results along with the mean collapse capacity S_{CT}, MCE spectral acceleration S_{MT}, and collapse margin ratio CMR.

Dynamic analyses consisted of a bidirectional IDA for each archetype employing the ground motion set presented in Section 1.2.5. Each record pair of the set was applied twice to each model, once with the components oriented along the principal directions, and then again with the components rotated 90 degrees. The records were systematically scaled based on the spectral acceleration $Sa(T_1)$ corresponding to the fundamental period of the building, increasing the record intensity until structural collapse took place defined as the occurrence of a 3% inter-story drift at any floor. Subsequently, the collapse margin ratio was computed as CMR = S_{CT}/S_{MT}, where S_{CT} is the mean collapse capacity defined as the mean spectral acceleration from the IDA curves for a 3% drift, and S_{MT} is the code-defined spectral acceleration corresponding to the maximum considered earthquake MCE for the building under analyses (INN 2009, 2013). Figure 1-9(b) shows the IDA results for archetype 103 along with the S_{CT}, S_{MT}, and CMR values.

According to the FEMA P-695 guidelines (FEMA 2009), the validation of a new set of SPFs is carried out by means of the adjusted collapse margin ratios ACMR of the structural archetypes. ACMRs are computed as ACMR = CMR×SSF×1.2, where SSF is the spectral shape factor to take into account the spectral shape of the ground motions employed in the dynamic analyses (FEMA 2009), and 1.2 is a factor to account for the 3D dynamic analysis effects induced by the numerical models (FEMA 2009). The SSF value is a function of the ductility and fundamental period of the archetype under study and is specific for the ground motion set used in the analysis. A detailed report of the SSFs employed in this research and their calculation procedure can be found in Chapter 4. For the example shown in Figure 1-9(b), ACMR = 3.04×1.26×1.2 = 4.59.

1.3. RESULTS AND DISCUSSION

1.3.1. Validation of seismic performance factors through ACMRs

The suitability of a new set of SPFs is assessed through evaluating the acceptability of the adjusted collapse margin ratios ACMR calculated from the incremental dynamic analyses, as detailed in Section 1.2.6. Such acceptability is determined by comparing the calculated ACMRs to minimum acceptable values $ACMR_{min}$ that guarantee to meet a given collapse probability for the structural archetype under study. The benchmark $ACMR_{min}$ values depend on two factors: (1) the quality of the information employed in the process, and (2) the limits established for the structural collapse probability.

The quality of the information and data employed over the course of the investigation has a direct influence on the total uncertainty of the results. Therefore, the higher the total uncertainty of the process, the higher the ACMR values must be in order to meet the acceptable collapse probabilities set for the structural archetypes. Four uncertainty sources (FEMA 2009) have been considered in this research: (1) record-to-record variability β_{RTR}, due to uncertainty in the response of the structural archetypes to different ground motions, (2) design requirements variability β_{DR}, related to the completeness and robustness of the design guidelines employed when developing the structural archetypes, (3) test data variability β_{TD}, related to the robustness of the experimental information used to define the system and develop the numerical models, and (4) modeling variability β_{MDL}, related to how well the numerical models reproduce the full range of structural responses and capture collapse behavior by means of direct simulated or non-simulated element checks. Following the guidelines of the FEMA P-695 methodology (FEMA 2009), the variability values for this research were defined as $\beta_{RTR} = 0.4$, $\beta_{DR} = 0.1$, $\beta_{TD} = 0.1$, and $\beta_{MDL} = 0.2$. The total variability β_{TOT}, computed as the squared root of the summation of the squares of the individual variabilities, was equal to $\beta_{TOT} = 0.469$. A full description of this process can be found in (FEMA 2009).

The fundamental aspect when evaluating the suitability of a set of SPFs is that an acceptably low, yet reasonable, probability of collapse can be reached by the structural archetypes designed with such SPFs. In this context, the guidelines of the FEMA P-695 methodology (FEMA 2009) recommend assessing the collapse probabilities at two different levels: individual and group. At the individual level, each structural archetype is recommended to meet a collapse probability equal to 20% for MCE ground motions. For the group level evaluation, firstly, the archetypes are binned into performance groups that reflect their primary differences in configuration and structural design, providing a basis for statistical assessment of the SPFs sets under investigation. In this research, five aspects were considered when identifying the performance groups: (1) the SPFs used for design, (2) anchorage system, (3) seismic zone, (4) soil type, and (5) fundamental period of the archetype. Fundamental periods were classified into two categories: short and long ones, defined by the boundary between the constant acceleration and constant velocity regions of the design spectrum. Since the design spectra of the NCh433 standard (INN 2009) are defined as continuous functions and not as piecewise-linear functions (for instance, as Newmark-Hall spectra), the boundary between the constant acceleration and constant velocity regions was defined following the recommendations by the ASCE 7-16 standard (ASCE 2016) to define a transition period. Taking into account the five binning aspects described above, 33 performance groups were identified for this research out of the 201 structural archetypes presented in Section 1.2.4. Further details about the development of the performance groups can be found in Appendix B. Finally, as suggested by the FEMA P-695 guidelines (FEMA 2009), to validate the suitability of the SPFs set used for structural design, each performance group should meet an average collapse probability equal to 10% for MCE ground motions. It can be noted that the collapse probability for performance groups is limited to one-half of that for individual archetypes. This judgment aims at recognizing the variability in the seismic response of the structural systems, providing a criterion to assess the acceptability of potential outliers within each performance group.

In order to evaluate the suitability of the SPF sets, the benchmark $ACMR_{min}$ values are defined based on the total variability β_{TOT} and the collapse probability limits established for both individual archetypes and performance groups. $ACMR_{min}$ values are computed assuming that the distribution of the spectral intensities at collapse level is lognormal with a median value S_{CT} and a lognormal standard deviation equal to the total variability β_{TOT}. Considering β_{TOT} = 0.469, the $ACMR_{min}$ values for a 20% and 10% collapse probability are $ACMR_{20\%}$ = 1.49 and $ACMR_{10\%}$ = 1.84, respectively (FEMA 2009). Figure 1-10(a) shows the ACMR values for the 201 structural archetypes analyzed in this research along with the $ACMR_{20\%}$ limit, and Figure 1-10(b) shows the average ACMR values for the 33 performance groups along with the $ACMR_{10\%}$ limit. The results were classified by the SPFs set used for structural design: R = 5.5 & Δ_{max} = 0.002, and R = 6.5 & Δ_{max} = 0.004.

Results in Figure 1-10(a) show that the 201 structural archetypes analyzed in this research meet the minimum ACMR requirement to reach a 20% collapse probability limit. The average ACMR for each set of SPFs is 3.64 and 3.16, respectively, with standard deviations equal to 1.12 and 1.17. When the SPFs changed from R = 5.5 & Δ_{max} = 0.002 to R = 6.5 & Δ_{max} = 0.004, the average ACMR reduced by 13.3%, however, no archetype went below the $ACMR_{20\%}$ requirement. This means that, even though the new set of SPFs results in less conservative structural systems, they still have an acceptable low probability of collapse that does not compromise the structural performance or lead to life-threatening scenarios. On the other hand, results in Figure 1-10(b) show that all performance groups are above the $AMCR_{10\%}$ limit, with average values of 3.60 and 3.05 for each SPF set, and standard deviations equal to 0.92 and 0.99, respectively. The average ACMR value reduced by 15.3% when the new SPF set was employed; however, no performance group showed an average ACMR lower than the 10%

collapse probability limit. This way, the 201 archetypes analyzed in this research prove to meet the FEMA P-695 requirements (FEMA 2009) at the individual and group check level, showing that the new proposed set of SPFs results in code-compliant structures with an improved cost-effectiveness ratio. For instance, a quick analysis of a 5-story building showed that changing the SPFs from R = 5.5 & Δ_{max} = 0.002 to R = 6.5 & Δ_{max} = 0.004 during the design phase resulted in a 40.4% saving in nailing, 15.9% in OSB panels, and 7.3% in timber studs.

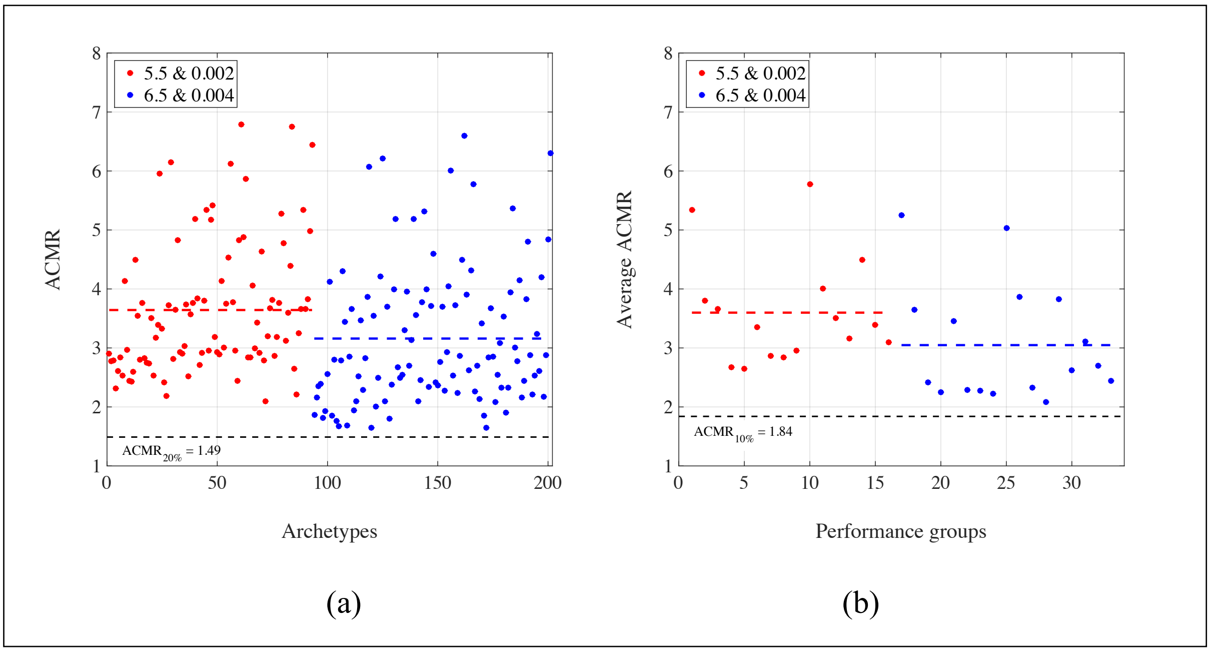

Figure 1-10. ACMR results and $ACMR_{min}$ values for: (a) individual structural archetypes, and (b) performance groups.

It is interesting to note that according to Figure 1-10 several archetypes have a considerable high ACMR value compared to the minimum required to guarantee structural safety. As Figure 1-10(a) shows, out of the 201 archetypes, 35 have an ACMR over three times the $ACMR_{20\%}$ limit (i.e., 3×1.49 = 4.47). This means that about 17% of the archetypes resulted in over-conservative structural systems regardless of the SPF set employed during design. Seeking to understand this phenomenon, Figures 1-11(a) and 1-11(b) sort out the ACMR results by SPF sets and number of stories, respectively. It can be observed that the building height does not have a significant influence on the lateral behavior of the structure since similar average ACMR values are observed for the different number of stories analyzed. Interestingly, the six-story archetypes for both SPF sets show relatively low ACMRs compared to other building heights. A detailed analysis showed that this phenomenon was not due to the number of stories itself, but to the design procedure employed for these archetypes. As explained in Section 1.2.4, all 6-story archetypes used an R_o factor equal to 7.0 and their seismic design loads were computed by means of modal analysis, as the NCh433 standard requires (INN 2009). Therefore, it is noted that these two guidelines lead to more efficient structural systems in terms of seismic behavior, since the archetypes designed under such requirements show ACMR values that satisfy the 20% collapse probability requirement and do not exhibit an over-conservative response. Thereby, even though modal analyses might be more time consuming to carry out when compared to static analyses (i.e., because it is necessary to develop a numerical model of the structure), they proved to be an efficient approach to optimize the cost-effectiveness when designing structural systems under seismic loads.

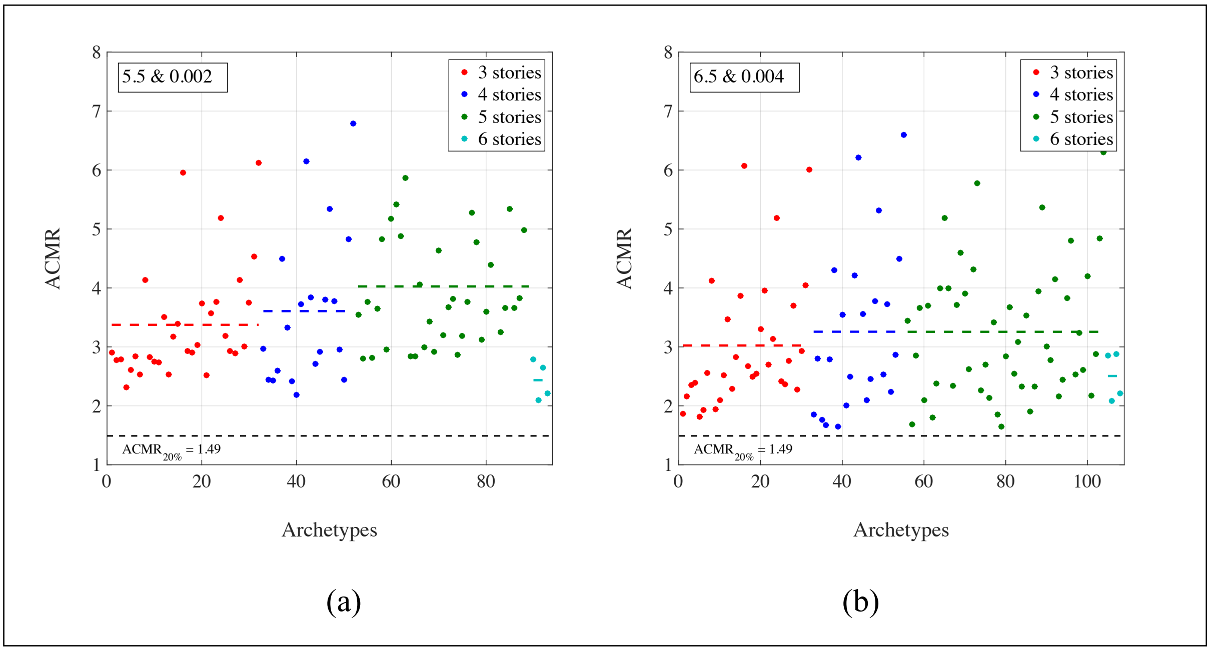

Figure 1-11. ACMR results classified by number of stories: (a) archetypes designed with R = 5.5 & Δ_{max} = 0.002, and (b) archetypes designed with R = 6.5 & Δ_{max} = 0.004.

On the other hand, it is of relevant interest to analyze the influence of the design soil class on the ACMR of the archetypes. Figures 1-12(a) and 1-12(b) show the ACMR results classified by SPF sets and soil classes, respectively. Unlike the results shown in Figure 1-11, Figure 1-12 shows a clear correlation between the soil class and ACMR values: the "better" the soil class, the higher the ACMR. The design soil class has a direct influence on the performance of the structural archetypes since it determines (along with the seismic zone and occupancy category) the design base shear computed from code-defined spectra. Soil quality ranges from A to D, being A a "good" soil and D a "poor" soil, therefore, archetypes on soil A were designed with a lower base shear compared to those on soil D. However, when calculating ACMRs (i.e., CMR = S_{CT}/S_{MT}, and ACMR = CMR×SSF×1.2), S_{MT} values are also a function of the soil class, thereby, the differences in design base shear should not be reflected in the ACMR results, opposite of what Figure 1-12 shows. A careful analysis of the archetypes showed that the trend observed in Figure 1-12 is not due to the soil class itself, but to the minimum base shear requirement of the NCh433 standard (INN 2009).

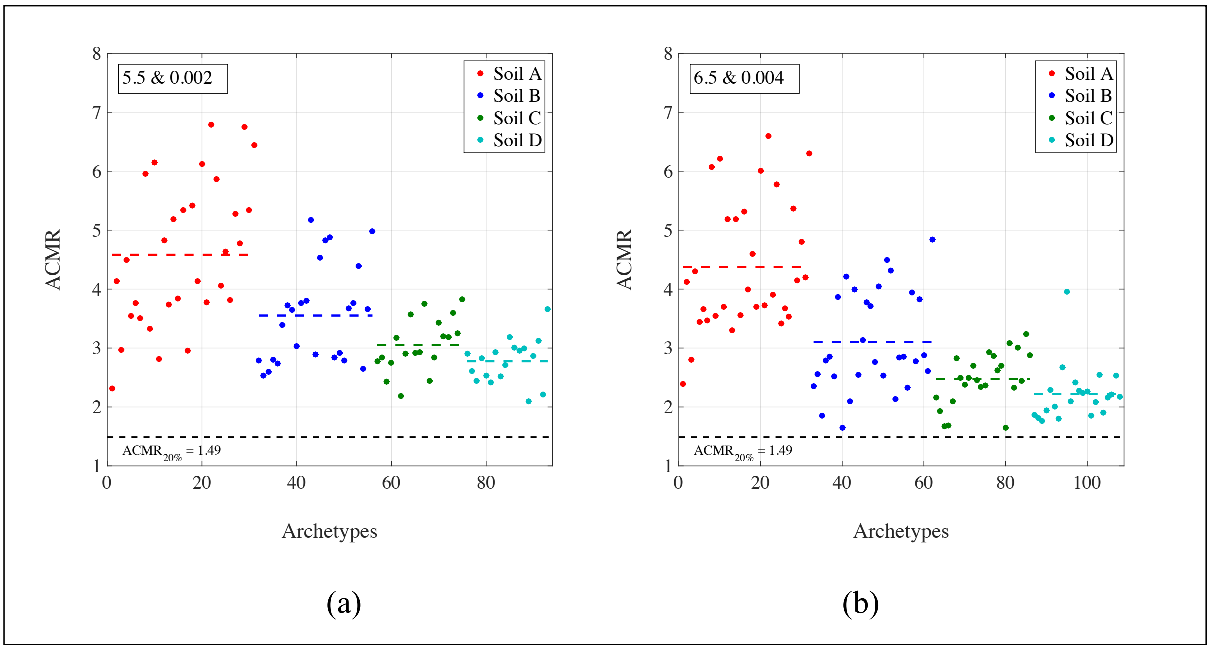

Figure 1-12. ACMR results classified by soil class: (a) archetypes designed with R = 5.5 & Δ_{max} = 0.002, and (b) archetypes designed with R = 6.5 & Δ_{max} = 0.004.

When designing any structure under the NCh433 standard (INN 2009), the spectrum-computed base shear is required not to be less than a minimum value given by $C_{min} = A_0S/6g$, where A_0 depends on the seismic zone, and S depends on the soil type. A_0 is equal to 0.2g, 0.3g, and 0.4g for seismic zones 1, 2, and 3, and S is equal to 0.9, 1.0, 1.05, and 1.2 for soil classes A, B, C, and D, respectively. After analyzing the ACMR results of the 201 archetypes, it was found that the minimum base shear C_{min} requirement of the NCh433 standard might be somewhat restrictive for soils A, B, and C, leading to conservative results compared to archetypes where the minimum base shear C_{min} did not control the structural design. By way of example, Figure 1-13 shows a comparative analysis of the design base shear versus the ACMR parameter for a 5-story building, archetype "C", seismic zone 1, R = 5.5, and Δ_{max} = 0.002. Soil classes A, B, C, and D were analyzed, and the minimum base shear requirement C_{min} for each soil class is shown by vertical dashed lines. For the soil class D, it can be observed that the C_{min} value is just right to meet the 20% collapse probability limit. However, for the other soil classes, the C_{min} requirement is much higher than the necessary to meet the 20% limit. This explains the high average ACMR values for soils A, B, and C observed in Figure 1-12, since several archetypes were designed under the C_{min} requisite.

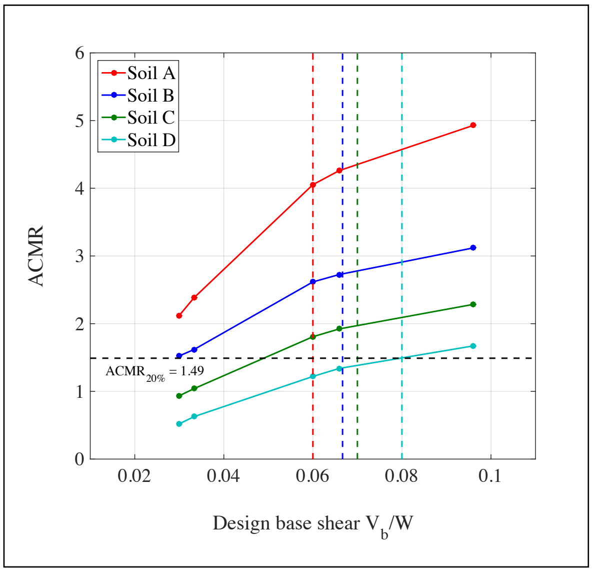

Figure 1-13. Comparative analysis of design base shear versus the ACMR parameter for a 5-story building, archetype "C", seismic zone 1, R = 5.5, and Δ_{max} = 0.002. The minimum base shear requirement C_{min} for each soil class is shown by the vertical dashed lines.

To better understand the effect of C_{min} on the ACMRs, Figure 1-14 shows the results for the entire set of archetypes analyzed in this study after removing the data for the cases where the structural design was controlled by the C_{min} requirement. For these results, the average ACMRs are 3.14 and 2.45 for each SPF set, with standard deviations equal to 0.64 and 0.55, respectively. By comparing Figure 1-14 and Figure 1-10(a), it can be noted that when the C_{min}-controlled archetypes are not considered, the average ACMRs decreased by 13.9% and 22.4%, and the standard deviations decreased by 43.1% and 52.9% for each SPF set, respectively. These findings remark that the C_{min} requirement of the NCh433 standard (INN 2009) leads to inflated results regarding collapse ratios, biasing the average data for the entire set. However, it should be highlighted that the conservatism of the C_{min} requirement for "good" soils is due to the inherent uncertainty of the seismic hazard, aiming at providing a design base shear high enough to guarantee the resilience of the structures under moderate and severe earthquakes. Therefore, further research is needed to evaluate the suitability of the C_{min} requirement of the NCh433 guidelines (INN 2009).

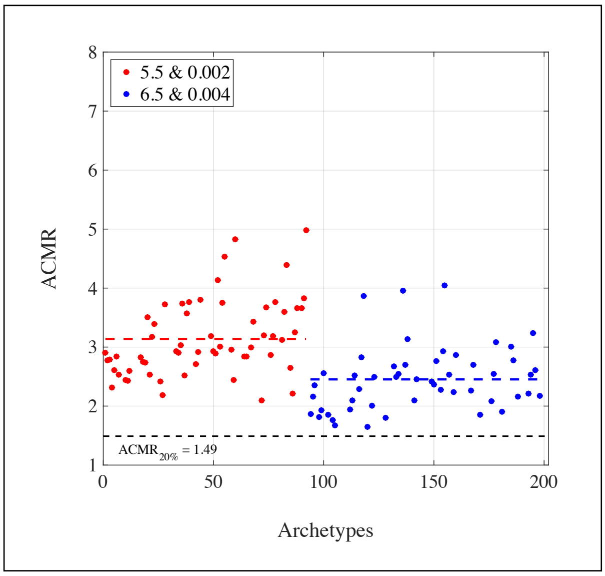

Figure 1-14. ACMR results for the archetype set after removing the data for the cases where the structural design was controlled by the C_{min} requirement.

1.3.2. Performance levels other than collapse

As presented in the previous section, the evaluation of the suitability of a given set of SPFs through the FEMA P-695 guidelines is carried out by analyzing collapse probabilities under spectral accelerations equal to the code-defined MCE seismic hazard. This way, an acceptably low probability of life-threatening scenarios can be guaranteed for the structures under study. However, it is also of relevant interest to examine the behavior of the archetypes under seismic demands with a lower return period and higher exceedance probability, and how performance levels other than collapse may threaten the resilience of the structure under such seismic demands. This concept is consistent with the current philosophy of perform-based seismic design PBSD, which seeks that modern structures, besides not collapsing under severe earthquakes, show limited or negligible structural and non-structural damage after frequent events, minimizing repair costs and maximizing the resilience of societies. Therefore, this section presents a brief analysis of the response of the 201 archetypes to different seismic demands and performance levels, aiming at providing a robust and sound framework for the validation of the new SPF set analyzed in this research.

The ASCE 41-17 standard (ASCE 2017) provides a set of guidelines for the perform-based evaluation and retrofit of existing and new buildings, defining three potential performance objectives for the structure under analysis: limited, basic, and enhanced. The selection of a performance objective is directly related to the extent of damage that would be sustained by the structure and its components in a seismic event, and is controlled by the acceptable damage level set by local regulations or private stakeholders. Thereby, each performance objective is quantitatively defined based on a certain combination of seismic hazard levels and building performance levels.

Seismic hazard levels aim at representing different seismic demand intensities for a particular area and are defined as spectral accelerations for a given structural period. The ASCE 41-17 standard (ASCE 2017) defines seismic hazard levels ranging from 50%/50 years (50% probability of exceedance in 50 years) to 2%/50 years, with discrete intervals as a function of the performance objective under evaluation. On the other hand, building performance levels are determined based on a combination of the performance of structural and non-structural elements, and are defined as discrete damage states from the infinite spectrum of possible scenarios that a structure might sustain during a seismic event. The ASCE 41-17 standard (ASCE 2017) lists four performance levels: operational (very light overall damage), immediate occupancy (light), life safety (moderate), and collapse prevention (severe). For a given structural system, performance levels are usually associated with an engineering demand parameter (such as interstory drift, settlement, plastic rotation, residual strength, among others) to enable a straightforward evaluation of the fulfillment of the performance level. Regarding wood frame structures, the FEMA 356 standard (FEMA 2000) defines interstory drift limits for three performance levels: 1% for immediate occupancy, 2% for life safety, and 3% for collapse prevention. For the operational level, previous experimental research showed that a 0.6% drift (van de Lindt & Gupta 2006; Langlois, Gupta & Miller 2004) satisfies its performance requirements as outlined by the ASCE 41-17 standard (ASCE 2017).

For the evaluation of the archetypes presented in this research, the enhanced performance objective was selected since it seeks to guarantee the proper behavior of a structure across a wide range of seismic scenarios, evaluating low-damage states for service-level earthquakes and near-collapse scenarios for rare earthquakes. According to the ASCE 41-17 standard (ASCE 2017), one of the ways for a building to reach the enhanced operational objective is meeting the following: (1) fulfill either the operational or immediate occupancy performance level for a 50%/50 years seismic demand, (2) fulfill the life safety performance level for a 20%/50 years seismic demand, and (3) fulfill the collapse prevention performance level for a 5%/50 years seismic demand. These three scenarios were analyzed for the 201 archetypes of this research, and results are presented in Figure 1-15.

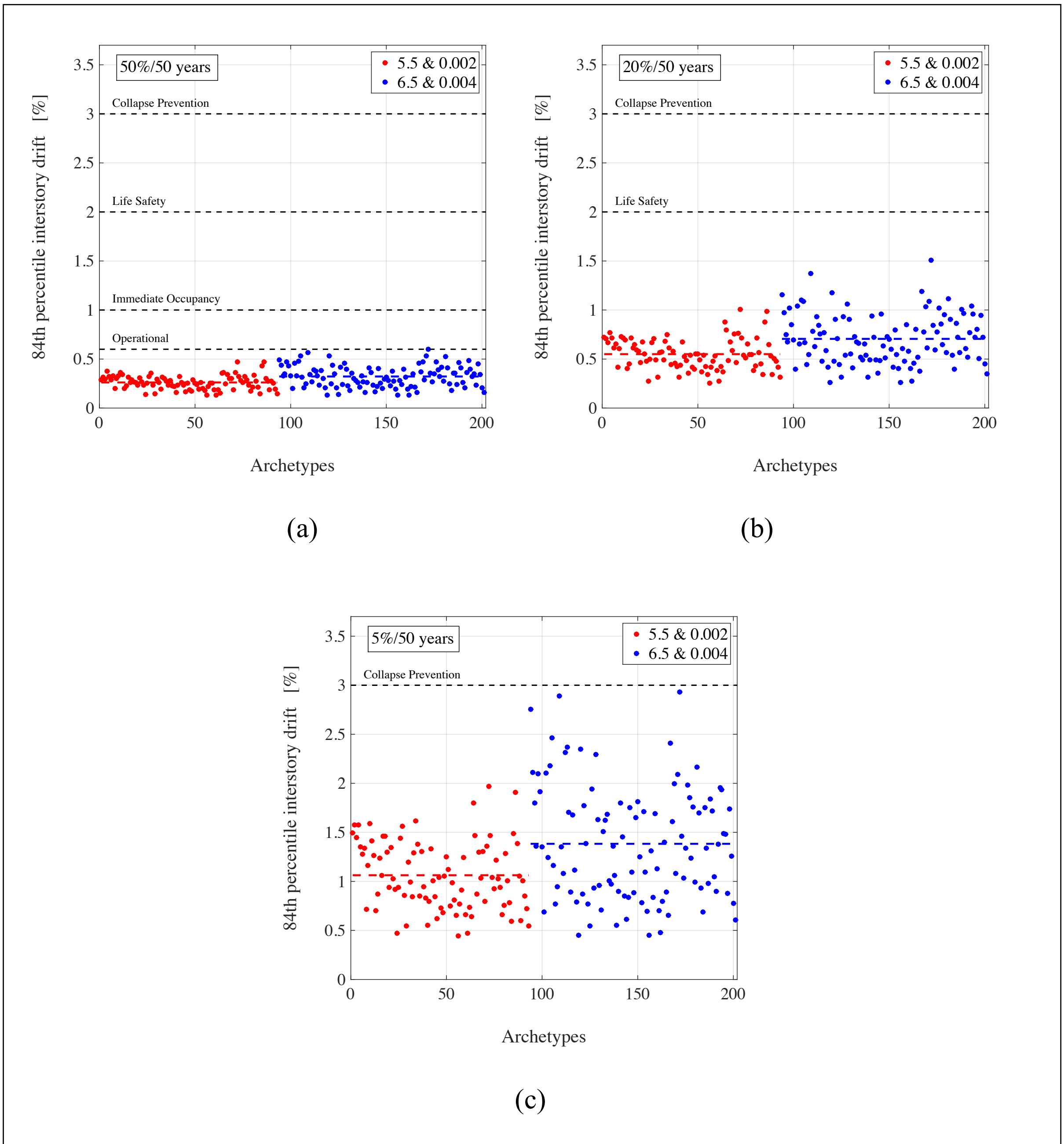

Figure **1-15.** 84th percentile interstory drift of the 201 archetypes under analysis for different seismic hazards: (a) 50%/50 years, (b) 20%/50 years, and (c) 5%/50 years. The black dashed lines mark the drift limits for different performance levels. The red and blue dashed lines mark the mean interstory drift value of the set.

Figure 1-15(a) shows the interstory drifts expected for a 50%/50 years seismic hazard, computed as the 84th percentile values from the IDA analyses presented in Section 1.2.6. Figures 1-15(b) and 1-15(c) shows the expected drifts for a 20%/50 years and 5%/50 years seismic hazard, respectively. The spectral accelerations for each seismic hazard level were extrapolated from the NCh433 design spectra (INN 2009) based on the recommendations provided by Guendelman and Aguiar (Guendelman 2002; Aguiar 2003). Results show that both SPF sets accomplish the requirements for the enhanced performance objective under the three specified seismic hazards, meeting the drift limits for each archetype in the set. Just one archetype slightly fails the operational limit for the 50%/50 hazards; however, this does not affect the overall statistical suitability of the SPFs under analysis. These results highlight that a change towards less conservative SPFs for wood frame buildings does not have a harmful effect on the seismic response of the structures, proving a resilient behavior under different levels of seismic hazard. Results in Figure 1-15(a) are significant to show that, even if the overall stiffness of the structure is reduced due to a change in the maximum allowable drift Δ_{max} from 0.002 to 0.004, an operational performance level can be expected for low seismic demands. This is important in the Chilean context since several minor earthquakes are expected throughout the lifespan of buildings, and SPFs should guarantee not to result in structural and non-structural issues under highly recurring seismic events.

1.3.3. Analysis of collapse floors

Previous research has reported that wood frame buildings are prone to sustain soft-story failure modes (ATC 2008; van de Lindt et al. 2012) under moderate to severe earthquakes. This is mainly due to the presence of garage lines or wide entrance doors that weaken the capacity of first stories and concentrate the lateral deformations on the ground floor walls, even if a proper procedure was followed for structural design. However, this phenomenon is not only due to the architectural configuration of the building, but also to the inherent dynamic response of the structure under lateral accelerations. For multi-story buildings, ground-level floors have a higher seismic mass on top of them compared to upper floors, resulting in high lateral displacements due to the inertial forces caused by lateral accelerations. This basic concept of structural dynamics is applicable even if the architectural configuration is the same across all floors in the building. In order to analyze the extent of this phenomenon, the response-history results of the 201 archetypes of this research were analyzed to find out which stories collapsed first, and overall results are presented in Figure 1-16. It is important to highlight that all architectural configurations showed in Figure 1-7 had the same wall distribution across all levels.

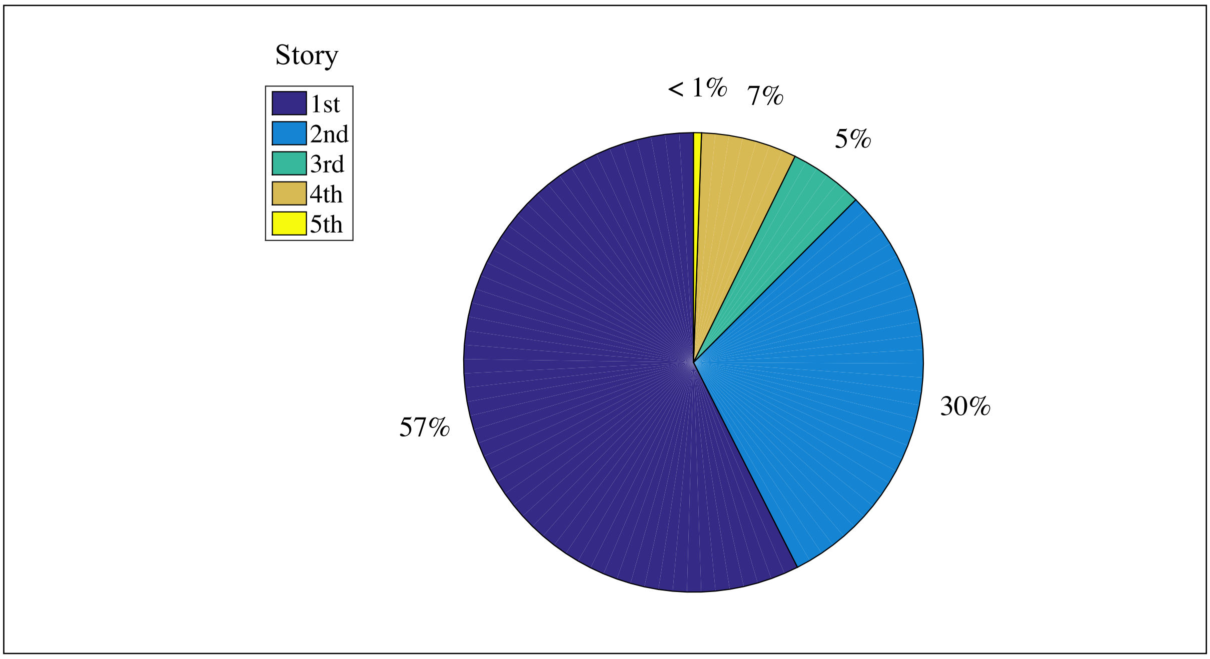

Figure 1-16. Collapse story percentages for the 201 archetypes analyzed in this research.

Figure 1-16 shows that in 57% of cases the first story collapsed first, in 30% the second story, and in the remaining cases the upper levels (in 5%, 7%, and <1% of cases, the third, fourth, and fifth story, respectively). No case showed a collapse on the sixth floor. Interestingly, it can be noted that 87% of the analyses collapsed on the ground floors due to the increased seismic forces at the ground levels regardless of their architectural configuration. Figure 1-17 shows the collapse levels classified by the number of stories of the archetype. Results show the same trend discussed above for all archetype heights, with most collapses occurring on the first and second stories. However, it is interesting to note that for the five- and six-story buildings, a significant amount of cases (12% and 28%) collapsed on the fourth floor. This may be explained due to the fact that as the height of the structure increases, its modal shapes change and higher modes of vibrations become significant, affecting the overall response of the structure. However, the collapse percentages on the lower stories for those archetypes are still high, with 79% and 51% of the cases collapsing on the first two levels for the five- and six-story archetypes, respectively. Several mechanisms could be implemented into wood frame structures to mitigate this phenomenon and enhance the response of the building, such as stiffening of the first floors with higher capacity materials (such as steel frames), incorporating seismic dampers at critical levels, or installing base isolators at the ground floor to reduce the seismic energy input to the structure. Further research should investigate the suitability and cost-effectiveness of these approaches.

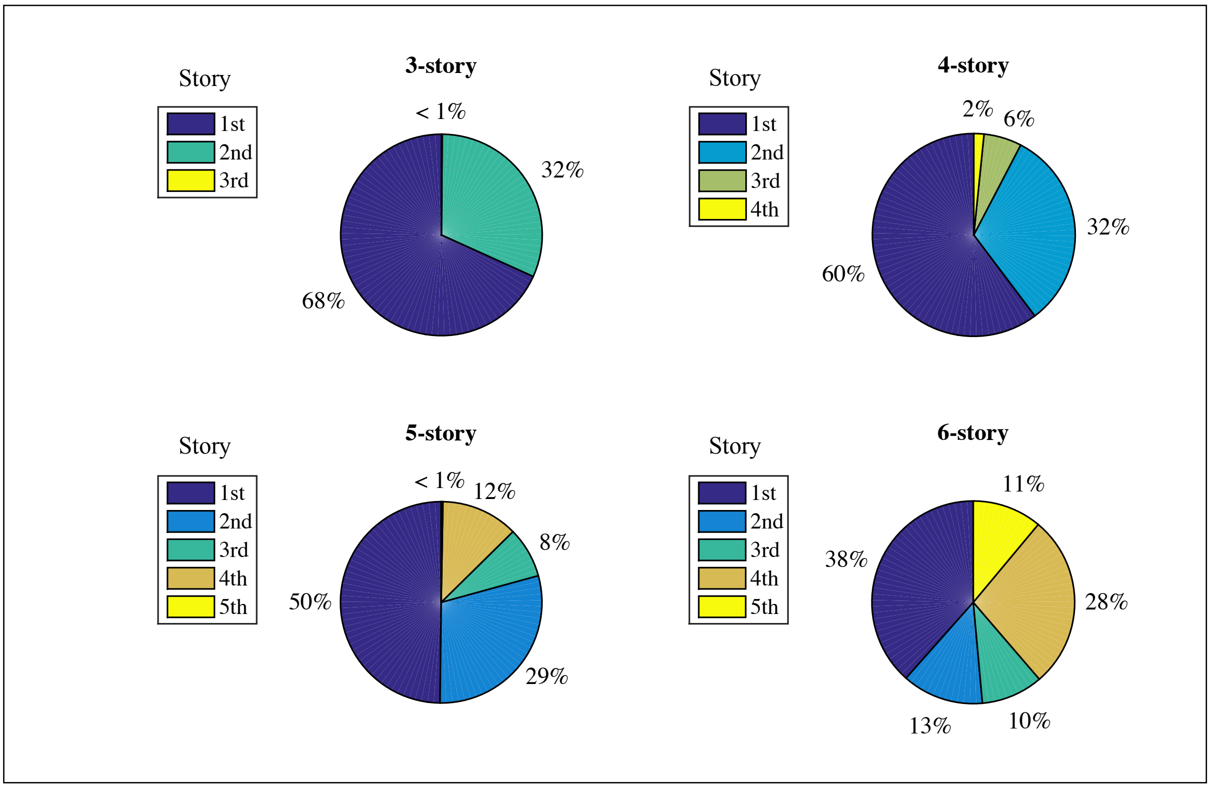

Figure 1-17. Collapse story percentages classified by building height.

CHAPTER TWO

NONLINEAR MODELING OF STRONG WOOD FRAME SHEAR WALLS FOR MID-RISE BUILDINGS

CHAPTER DISCLAIMER

The content, methodology, results, and figures presented in this chapter are based on the following article:

- Estrella X, Guindos P, Almazán J, Sardar M. Efficient nonlinear modeling of strong wood frame shear walls for mid-rise buildings. Engineering Structures 2020; 215: 1–15.

2.1. INTRODUCTION

Over the past few decades, wood frame structures have gained a significant presence in low-rise construction throughout North America, Europe, and Oceania. Recent data (Follesa et al. 2018) show a promising future for multi-story timber buildings worldwide for the years to come. When wood frame structures are subjected to earthquake loading, shear walls are commonly employed as the primary component of the lateral load resisting system. Typically, a wood frame shear wall consists of a 1.2 to 2.4 m long wood frame with 38×89 mm (2×4”) interior studs spaced at 400 mm on center, double end studs, single members for the top and sole plate, and conventional corner hold-downs to prevent overturning of the wall.

In a low-rise wood frame structure, the lateral resistance is usually provided by 9 to 11 mm thick oriented strand board (OSB) panels on one side of the wall, with nails spaced at 150 mm on center along all panel edges and 300 mm for interior studs, as shown in Figure 2-1(a). However, for mid-rise structures, a wall configuration of higher capacity is often required to resist the larger vertical and horizontal forces due to the increased gravitational and seismic loads. This higher capacity configuration is referred to as “strong” throughout this chapter. A strong wood shear wall usually consists of 38×135 mm (2×6”) framing members, sturdy end studs, stronger hold-down devices, OSB panels on both sides of the wall, and a smaller nail spacing both along the panel edges and interior studs, as shown in Figure 2-1(b). Previous research has shown that these practices also increase the damping in wood frame shear walls (Jayamon, Line & Charney 2018).

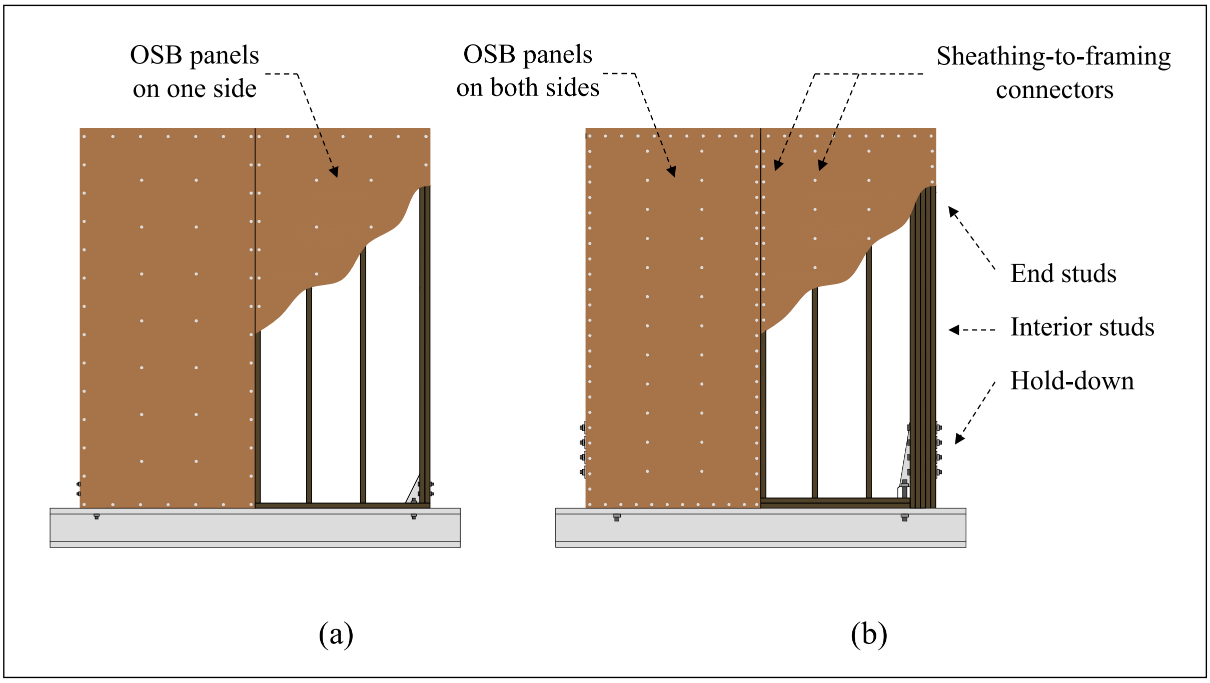

Figure 2-1. Schematic configuration of (a) conventional and (b) strong wood frame shear walls.

2.1.1. State of the art: experimental programs

Understanding the structural behavior of strong wood frame shear walls is a key step for the development of mid-rise timber buildings in seismic countries, since the current building codes and design procedures have been developed based on previous works conducted on conventional walls. However, investigations on strong wood frame walls are scarce. van de Lindt et al. (van de Lindt, Pei, Pryor, et al. 2010) studied the experimental seismic response of a full-scale, six-story, wood frame apartment building at the world's largest shake table in Miki, Japan. The results showed a good behavior of the building even under high seismic demands, with a maximum averaged interstory drift of 2% and only minor nonstructural damage. Seim et al. (Seim et al. 2016) carried out a comparative study of the lateral behavior of wood frame walls with OSB and gypsum fiber board (GFB) panels. Eight 2.5×2.5 m strong walls were tested at the testing facilities of the University of Kassel under vertical and horizontal (monotonic and cyclic) load. The specimens were sheathed with two 1.25×2.5 m panels on both sides, which were attached to the framing with 2.8×65 mm nails spaced at 75 mm. Results showed that there is no significant difference in the performance of walls with thick GFB panels (18 mm thick) and standard OSB ones (10 or 18 mm thick) under lateral loads. However, walls constructed with thin GFB panels (10 mm thick) had a slightly lower performance in terms of maximum load-bearing capacity, ultimate deformation, ductility, and equivalent damping. Marzaleh et al. (Sadeghi Marzaleh et al. 2018) investigated the monotonic response of wood frame shear walls with strong anchorage and sturdy end studs subjected to vertical load and bending moment, reproducing the expected load conditions in multi-story buildings. Three racking tests were conducted under different load conditions, and a substantial increase in shear resistance and stiffness was found for strong walls.

Recently, Guíñez et al. (Guíñez, Santa María & Almazán 2019) studied the monotonic and cyclic lateral response of strong wood frame walls with different lengths and nail spacings. It was found that strong walls have increased capacity and delayed stiffness degradation. Furthermore, the results showed that the current design guidelines underestimate the shear strength and overestimate the stiffness of strong wood frame walls.

2.1.2. State of the art: numerical modeling

Since real-scale tests are usually complex, expensive, and time-consuming, a more viable approach to study the behavior of wood frame walls is through virtual testing using numerical models. Much research efforts have been devoted to the development of models capable of predicting the monotonic and cyclic response of wood frame walls in the past decades. In the early 1980s, Easley et al. (Easley, Foomani & Dodds 1982) developed a set of analytical expressions based on test results to predict the stiffness and force-displacement relationship of wood frame walls. Results showed that the model is mainly accurate in the linear range of the force-displacement response. Itani and Cheung (Itani & Cheung 1984) employed a detailed FEM model to study the nonlinear response of wood frame diaphragms. In their model, the studs and the sheathing panels were represented by beam and plane-stress elements, and nonlinear springs were used to represent the sheathing-to-framing connections. Over time, more detailed FEM models have also been developed by various researchers (Gutkowski & Castillo 1988; Dolan 1989; Dolan & Foschi 1991; White & Dolan 1995; Xu & Dolan 2009).

As the wall response is mainly governed by the nonlinear behavior of the sheathing-to-framing connections (Filiatrault 1990), the global force-displacement relationship can be well-predicted employing simpler models, as the one proposed by Gupta and Kuo (Gupta & Kuo 1987). They studied the effect of uplifting in vertical studs through a five degree-of-freedom model for single-story shear walls (with two extra degrees of freedom for each additional story). This allowed them to gain knowledge about the effect of vertical load on the cyclic response of walls.

Due to the great damage observed in wood frame structures after the Northridge earthquake, the Consortium of Universities for Research in Earthquake Engineering (CUREE)–Caltech Woodframe Research Project was initiated for improving the wood construction engineering in 1998 (Seible, Filiatrault & Uang 1999). As part of this project, Folz and Filiatrault (Folz & Filiatrault 2001) proposed a simplified mechanistic model to predict the in-plane behavior of wood frame walls under quasi-static loading. The model's numerical formulation was based on three structural components: pin-jointed rigid framing members, linear elastic sheathing panels, and nonlinear sheathing-to-framing connectors. The latter employed a hysteretic model which considers strength and stiffness degradation and pinching under cyclic loading. The model predicted accurately the force-displacement response and the energy dissipation of wood frame walls under general cyclic loads when compared to test results. The proposal was incorporated into a computer program called Cyclic Analysis of Shear Walls (CASHEW). A modified version of this model was later proposed by Pang and Hassanzadeh (Pang & Hassanzadeh 2012), who employed a corotational formulation and large-displacement theory to predict the collapse load and failure mechanism of both engineered and nonengineered wood frame shear walls. This new model was coded into a computer program called M-CASHEW. The model was verified by comparing its predictions with the data obtained for shear walls and diaphragms tested by previous researchers, showing good agreement even at large displacements.

Casagrande et al. (Casagrande, Rossi, Sartori, et al. 2016; Casagrande, Rossi, Tomasi, et al. 2016) developed an analytical tool to predict the elastic and elasto-plastic behavior of conventional wood frame walls under lateral and vertical load. Based on the results of a comprehensive parametric study, the authors proposed a rheological model as function of the mechanical properties of the sheathing-to-framing connectors. Results showed good agreement between test data and model predictions for walls with different configurations. Seim et al. (Seim et al. 2016) developed a numerical model to study the nonlinear response of the strong walls tested in their experimental program (described in the previous section). The framing was represented by pin-jointed elastic beam-column elements, while the sheathing panels were modeled as an equivalent truss system with stiff boundary elements and elastic diagonals. For the sheathing-to-framing connections, zero-length springs with the MSTEW model were employed. The walls were fully anchored to the ground by restraining the vertical and lateral displacements of the bottom rail. Results showed good agreement between the model predictions and the test measurements, highlighting that the wall response can be assessed with relatively large accuracy only on the basis of the calibrated data of sheathing-to-framing connections.

Despite the exhaustive efforts that have been devoted to the nonlinear model of conventional wood frame walls, investigations on modeling approaches for strong walls are limited. Even though the different configuration of the strong wood frame walls does not change the overall force-displacement behavior when compared to conventional walls, the force and displacement demands are distributed differently among elements that make them up. Whilst in conventional walls the top displacement is mainly due to the deformation in the sheathing-to-framing connectors, in strong walls the anchoring system has a significant contribution to the lateral top displacement. This is because the deformation mechanism in wood frame walls has three major components: (1) the sheathing-to-framing connectors, (2) the flexural flexibility of the studs, and (3) the anchoring devices (American Wood Council 2015). These components can be represented by three elements connected in series. In strong walls, the shear stiffness associated to the sheathing-to-framing connectors is high enough to induce significant deformations in the anchorage system when the wall is subjected to lateral forces. The contribution of such deformations to the global lateral displacement depends on the wall aspect ratio. As will be discussed later in this chapter, wood frame walls with four different aspect ratios were investigated in this research (3.43, 2.0, 1.0, and 0.67). It was found that the percentage of lateral deformation due to wall uplift was, on average, 50.7%, 50.3%, 25.0%, and 7.1 % for each aspect ratio, respectively. Interestingly, it can be noted that for slender walls, about half of the lateral deformation is due to uplift. This is due to the small distance between the pivot points at the ends of the wall, which increases the lever arm from the top, and provokes small uplifts to induce large lateral displacements. Therefore, traditional modeling approaches that consider a fixed base and ignore the anchoring system deformation, as in the CASHEW model, may not be applicable to reproduce the lateral behavior of strong walls.

Since accurate numerical models are crucial to promote the development of mid-rise timber buildings, the investigation in this chapter proposes an efficient approach for modeling strong wood frame walls. The proposed model was developed based on the efforts of the previously discussed investigations (Folz & Filiatrault 2001; Judd & Fonseca 2005; Pang & Hassanzadeh 2012; Seim et al. 2016; Casagrande, Rossi, Sartori, et al. 2016; Casagrande, Rossi, Tomasi, et al. 2016), and aims at developing a more comprehensive approach that embraces walls with different aspect ratios, takes into account the effects of sturdy end studs, and incorporates the deformation demands in the anchoring system. The model was validated by statistically comparing its predictions with twelve real scale tests of strong wood frame walls with different characteristics. Additionally, in-depth analyses were conducted to better understand the nonlinear behavior of wood frame walls and to gain knowledge about strategies to improve their response under earthquake cyclic loads. The model follows a simplified approach, which lies between mechanistic lumped models and complex FEM models. This reduces both the computational costs and the necessary input parameters, which can be obtained easily from previously published research or through simple standard tests.

2.2. EXPERIMENTAL PROGRAM

An exhaustive experimental program was conducted to characterize the behavior and mechanical properties of framing studs, structural OSB panels, sheathing-to-framing connections, and strong wood frame walls of different configurations and aspect ratios. These tests were carried out by colleagues external to this thesis, and are briefly presented in this section for clarity purposes.

Framing tests consisted of mechanically graded Chilean MGP10 (Australian structural grade) radiate pine. In total, forty five studs were mechanically tested under bending, tensile, and compression tests (15 specimens each) in the facilities of the INFOR Structural Wood Laboratory, Concepción, Chile, according to the Chilean standard NCh3028/1 (INN 2006). Additionally, twenty OSB specimens (11.1 mm thick and made of radiate pine strands) were tested according to the ASTM D2719 standard (ASTM 2013) in the facilities of the Engineered American Wood Association (APA) in Tacoma, WA, USA, to determine their shear modulus in both the longitudinal and transverse directions. The mean results of framing and structural panels testing are listed in Table 2-1. The results are consistent with those reported in the literature (Segura 2017; Cartes, González & Padilla 2017; Folz & Filiatrault 2001). Documentation of the testing program and further details of experimental results can be found in (INFOR 2017b).

Table 2-1. Mechanical properties for radiate pine framing and 11.1-mm-thick OSB panels obtained from testing.

Test	**Framing members**			**OSB**	
	Bending E (MPa)	**Tensile σ_u (MPa)**	**Compression σ_u (MPa)**	**Along G_{LT} (MPa)**	**Across G_{LR} (MPa)**
Number of tests	15	15	15	20	20
Mean	11400	26.54	34.78	1307.49	1255.66
Standard deviation	1810	13.30	8.23	88.31	187.22

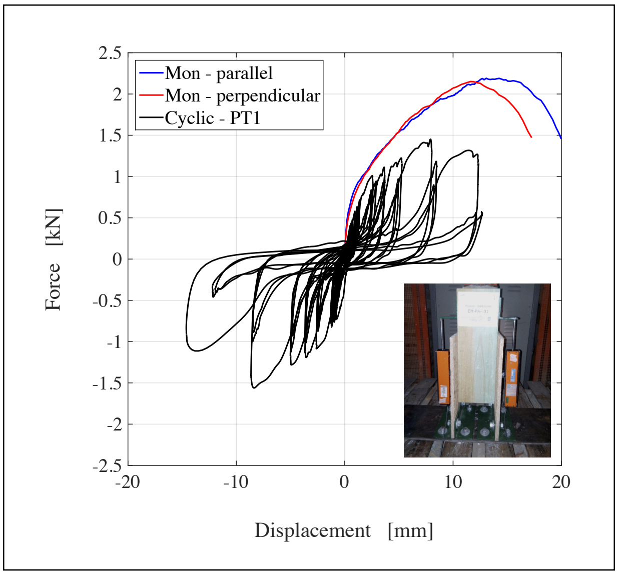

Figure 2-2. Sheathing-to-framing connection test setup and results.

The monotonic and cyclic behavior of the sheathing-to-framing connections was examined at the University of the Bío-Bío in Concepción, Chile. Double shear OSB-radiate pine framing joint specimens were pneumatically driven with 70-mm-long spiral nails with a shank diameter of 3.0 mm. Both directions (parallel and perpendicular to framing grain) were analyzed in each monotonic test, whilst all cyclic ones were conducted parallel to fiber direction. The yielding displacement obtained in the monotonic tests was used to compute the CUREe-Caltech cyclic testing protocol (Krawinkler et al. 2001). Figure 2-2 shows an illustration of the testing set up and the monotonic and cyclic results of one specimen. Results are consistent with those reported in previous research (Folz & Filiatrault 2001; Sartori & Tomasi 2013; Casagrande et al. 2020; Seim et al. 2016) in terms of capacity, stiffness, ductility, and energy dissipation, exhibiting a pinched response under reversed load for large displacements. Typical failure mechanisms were observed such as nail fatigue, pulling out of nails, or crushing of the OSB panel. A detailed report of the results can be found in (Jara & Benedetti 2017).

To evaluate the overall behavior of strong wood frame walls, nineteen real-scale specimens were tested under monotonic and cyclic in-plane shear load. The walls were 2470 mm high with four different lengths: 700, 1200, 2400, 3600 mm. All framing materials were 38×135 mm (2×6”) dimensional lumber, and studs were spaced at 407 mm on center. The top and bottom plate consisted of double members, whereas the end studs had three members (for 700 mm long walls) and five members (for the 1200, 2400 and 3600 mm walls), respectively. Double 11.1 mm thick OSB panels were installed on both sides of the walls, employing 70 mm long spiral nails (3.0 mm shank diameter) spaced at 50 or 100 mm along all panel edges and at 200 mm for interior studs. SIMPSON Strong-Tie HD12 hold-down anchorages were bolted with four φ1×10” horizontal bolts to the end studs and with one φ1-1/8×10” bolt to the foundation. Additionally, φ1×10” shear bolts were installed to prevent sliding of the wall. Four 1200 mm and three 2400 mm long walls were tested monotonically, and two 700 mm, four 1200 mm, four 2400 mm and two 3600 mm long walls were tested cyclically. The results of the monotonic tests and the guidelines provided by the ASTM E2126 standard (ASTM 2018) were used to calibrate the CUREe-Caltech protocol (Krawinkler et al. 2001) for the cyclic tests. The test setup is shown in Figure 2-3. A detailed report of the experimental program can be found in Guíñez et al. (Guíñez, Santa María & Almazán 2019).

Figure 2-3. Test setup (front and right view) for a 1200 mm long strong wall, labelled as C120-10-01 by Guiñez et al. (Guíñez, Santa María & Almazán 2019).

2.3. NONLINEAR MODELING APPROACH

To better understand the nonlinear behavior of walls under large displacements, a new nonlinear model which takes into account the different deformation mechanisms in a wood frame wall was developed. Similar to Pang and Hassanzadeh (Pang & Hassanzadeh 2012), three types of elements were used to represent the wall assemblies: (1) 6-DOF planar-frame (beam) elements for the framing members, (2) 5-DOF shear-panel elements for the sheathing panels, and (3) 3-DOF link elements for sheathing-to-framing connections and hold-down devices. Since the nonlinear behavior of wood frame walls is dominated by the force-displacement characteristics of the sheathing-to-framing connections, the nails were modeled using nonlinear hysteretic springs, whereas the framing, sheathing members and hold-down devices were assumed to be linear and elastic. The model was developed in the MATLAB M-CASHEW (Pang & Hassanzadeh 2012) environment.

2.3.1. Model description

Wood frame shear walls generally consist of six basic structural components: (1) framing members (i.e., interior and end studs), and top and bottom plates, (2) framing-to-framing connectors, which join studs with top and bottom plates, (3) sheathing-to-framing connectors, (4) sheathing OSB panels, (5) hold-down anchorage devices, and (6) shear bolts. Frame members were modeled using two-node Euler-Bernoulli frame elements with corotational formulation and 3 DOFs per node: two translational and one rotational. In the experiments, the framing elements for the end studs and top and bottom plates were bonded using high-quality structural glue so that they behaved as a single member under large deformations. Hence, in the nonlinear model, these elements were represented by a single frame element considering the total width of all the studs, as shown in Figure 2-4. Based on the results from the previous bending tests, a mean value of E = 11.4 MPa was considered for the studs.

Following the general practice in wood frame construction, only nominal nailing to hold the frame together was used in the tested walls, i.e., three 3×100 mm nails per joint. As the contribution of this connection type to the overall stiffness of the wall is small, its effect can be neglected (Folz & Filiatrault 2001; Seim et al. 2016). Therefore, framing-to-framing connections (framing nails) were modeled as pin-ended connections using two-node 3-DOF link elements with two infinitely rigid springs for translation and one with zero stiffness for rotation. Sheathing-to-framing connectors (edge and field nails) were also modeled using two-node 3-DOF link elements, as discussed in detail in the following section. Sheathing OSB panels were modeled using rectangular shear-panel elements with 5 DOFs; one rigid-body rotation, two rigid-body translations, and two in-plane shear angles. Shear panels and frame elements are fastened together by sheathing-to-framing connectors. From the OSB shear tests, an average value of G = 1.3 GPa was selected as the input shear modulus for the model.

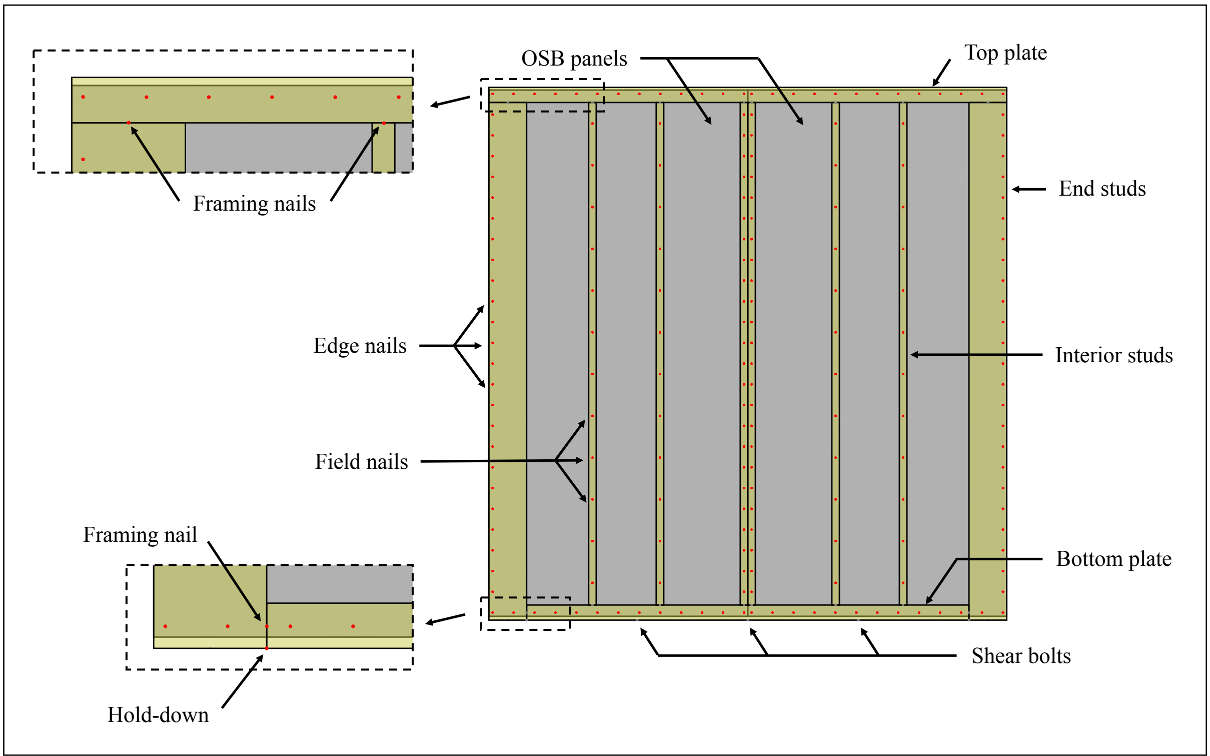

Figure 2-4. Nonlinear model of a 2400 mm long wall.

The response of the hold-down system is the result of a complex combination of the behavior of the wooden members, the steel bolts and the anchorage bar. Therefore, it is a common practice that the force-displacement response of hold-downs is represented by a nonlinear hysteretic model which captures its overall behavior (Li et al. 2012; Pang & Hassanzadeh 2012). However, if high capacity hold-down models are used (e.g., SIMPSON Strong-Tie HBD models with low-deflection performance), it is reasonable to assume that their response falls into the linear range. As it will be shown later in this chapter, the demands on the hold-downs remain well under their maximum tensile capacity. Therefore, a linear 3-DOF link element that fixes the bottom plate to the base was used to represent the hold-down response. The vertical translational spring had a tensile stiffness of k_t = 11.85 kN/mm, which was determined based on the allowable tensile and deflection data provided in design the catalog (Simpson Strong-Tie 2015), and a high compression stiffness to simulate the contact between the bottom plate and the foundation. The horizontal translational spring is also infinitely rigid to prevent sliding of the wall, whilst the rotational spring has zero stiffness. Finally, additional 3-DOF link elements were included to simulate the action of the shear bolts, preventing the sliding of the wall by assigning them an infinity horizontal stiffness. A detailed description of the model formulation, connectivity, deformed geometry, and equilibrium equations of the elements can be found in Pang and Hassanzadeh (Pang & Hassanzadeh 2012).

2.3.2. Model calibration for sheathing-to-framing connections

The force-displacement behavior of nail connections is highly nonlinear under monotonic loading and exhibits pinched hysteretic behavior with strength and stiffness degradation under cyclic loading (Dolan & Madsen 1992). Despite the existence of fairly sophisticated finite-element models which represent individual connectors as an elastoplastic pile embedded in a layered nonlinear foundation (Chui, Ni & Jaing 1998; Foschi 2000; Li et al. 2012), each connection was modeled with three orthogonal uncoupled springs to achieve reasonable computational overheads in this research. Hence, the force-displacement response of each connection was represented by a hysteretic model based on a minimum number of path-following rules. The modified Stewart hysteretic model (MSTEW) proposed by Folz and Filiatrault (Folz & Filiatrault 2001) was adopted in this investigation. Previous research has demonstrated the accuracy of the MSTEW model in representing the nonlinear response of sheathing-to-framing connections and wood frame walls (Folz & Filiatrault 2001; Judd & Fonseca 2005; Pang et al. 2010; Pei & van de Lindt 2011).

The MSTEW model consists of 10 modeling parameters which phenomenologically capture the crushing of the wood (framing and sheathing) along with yielding of the nails. As depicted in Figure 2-5(a), the nonlinear backbone envelope curve of the model is represented by the following set of equations:

$$
\begin{aligned}
F(\delta) &= \operatorname{sgn}(\delta) \times (F_0 + r_1 K_0|\delta|) \times [1 - \exp(-K_0|\delta| / F_0)] && |\delta| \le |\delta_u| \\
F(\delta) &= \operatorname{sgn}(\delta) \times F_u + r_2 K_0[\delta - \operatorname{sgn}(\delta)\times\delta_u] && |\delta_u| \le |\delta| \le |\delta_F| \qquad \text{Eq. 2-1} \\
F(\delta) &= 0 && |\delta| > |\delta_F|
\end{aligned}
$$

Under cyclic loading, unloading off the envelope curve follows a path with a stiffness r_3K_0. At this point, both the connector and wood are assumed to unload elastically. Under continued unloading, the response adopts a reduced stiffness r_4K_0. Detailed information on the MSTEW model can be found in (Folz & Filiatrault 2001).

Through nonlinear functional minimization procedures and based on the average data from the sheathing-to-framing connection tests published by Jara and Benedetti (Jara & Benedetti 2017), the 10 modeling parameters of the MSTEW model were identified for this research, and the results of the adjusted SDOF model are shown in Figure 2-5(b). The values of the 10 parameters are shown in Table 2-2. Results from Folz and Filiatrault (Folz & Filiatrault 2001) for the connection tests carried out by Durham et al. (Durham, Lam & Prion 2001) are also listed in Table 2-2 for comparison.

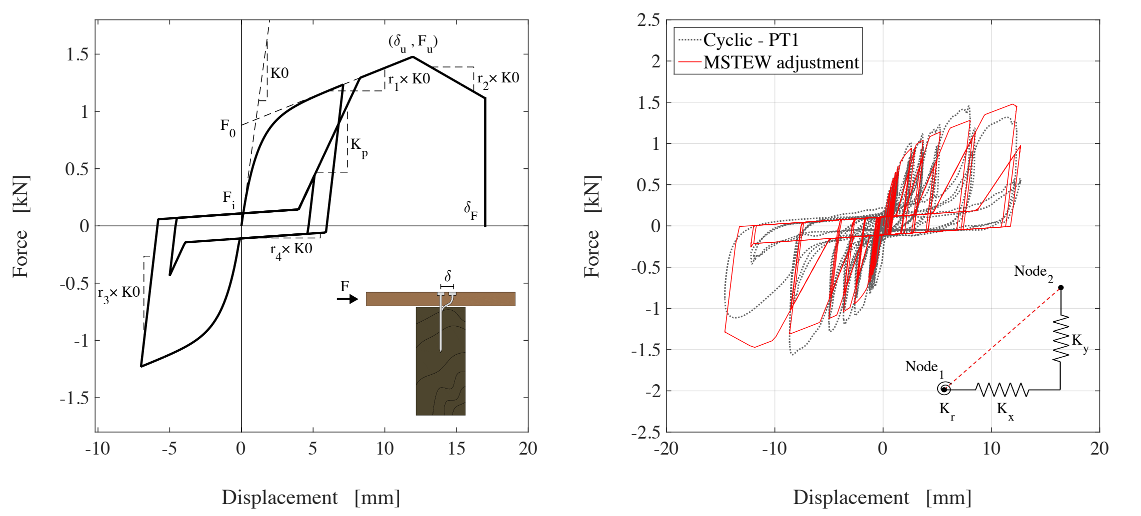

Figure 2-5. MSTEW (a) model description and (b) prediction for sheathing-to-framing test #1.

Good agreement is observed between the test and the MSTEW model, with an error in the cumulative energy dissipation (calculated as the area enclosed by the hysteresis cycles) of 4.2%. In the wood frame walls models, 3-DOF link elements were used to model sheathing-to-framing connections by employing three uncoupled springs: two translational and one rotational, as shown in Figure 2-5(b). Each translational spring was assigned the MSTEW hysteretic model previously described. Since the rotational stiffness has a negligible effect on the response and behavior of the connection, the rotational spring was assigned a linear model with zero stiffness. On the other hand, previous research has shown that employing a pair of non-oriented springs (which keep a constant orientation) to represent sheathing connections overestimates the initial stiffness and the ultimate capacity of the shear walls (Folz & Filiatrault 2001; Judd & Fonseca 2005). To avoid this issue, the true oriented (corotation) connection model proposed by Pang and Hassanzadeh (Pang & Hassanzadeh 2012) was employed in this work.

Table 2-2. MSTEW modeling parameters for sheathing-to-framing connections computed for this research and those obtained by (Folz & Filiatrault 2001).

Case	MSTEW parameters									
	K_0 (kN/mm)	r_1	r_2	r_3	r_4	F_0 (kN)	F_I (kN)	δ_u (mm)	α	β
Current research	0.911	0.055	-0.079	1.177	0.010	0.879	0.109	11.951	0.569	1.165
Folz and Filiatrault	0.561	0.061	-0.078	1.400	0.143	0.751	0.141	12.500	0.800	1.100

2.3.3. Model validation

This section validates the accuracy of the proposed model when predicting the overall force-displacement response of strong wood frame walls with varying aspect ratios under different loading scenarios. Out of the total nineteen walls tested in the experimental program carried out by Guíñez et al. (Guíñez, Santa María & Almazán 2019), twelve walls with four different aspect ratios and distinct responses were selected to explore the validity of the model. Four monotonic and eight cyclic tests were selected to demonstrate the accuracy of the model under different conditions for walls ranging from 700 mm to 3600 mm in length. For clarity purposes, the same specimen labeling of Guiñez et al. (Guíñez, Santa María & Almazán 2019) has been adopted in this chapter. For instance, the label M120-10-01 denotes the monotonic test of a 1200 mm long wall, with a nail spacing of 100 mm for the specimen number one. Monotonic results (test data and model predictions) for 1200 mm and 2400 mm walls are shown in Figure 2-6. Monotonic analyses (pushover) were conducted by applying displacement in 0.5 mm increments. A norm displacement increment test (Pang & Hassanzadeh 2012) was used as the convergence criteria, with a residual tolerance of 1e-6 kN and 20 maximum iterations per increment. Analyses were stopped when the maximum force fell by 40% or when the algorithm was no longer able to reach convergence.

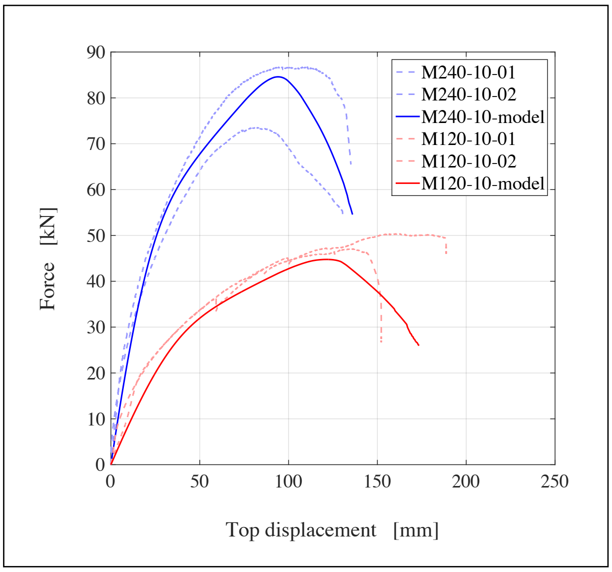

Figure 2-6. Comparison between monotonic test results and model predictions for 1200 mm and 2400 mm long walls.

Figure 2-6 shows good agreement between the tests results and model predictions for 1200 mm and 2400 mm long walls. Monotonic tests were only conducted on these two walls. The M240-10-02 specimen showed a low maximum capacity, probably due to construction issues or poor nailing procedure. However, the model showed good accuracy when compared with the M240-10-01 test regarding wall capacity, stiffness, and ductility. The same was found for both 1200 mm walls.

In addition to the four monotonic tests, eight cyclic analyses were conducted to prove the accuracy of the model under a reversed load path. The top displacement data obtained from the test measurements were used as input in the control displacement analyses, and the results for four specimens are shown in Figure 2-7. In general, good agreements between the test results and model predictions were observed for cyclic tests. The characteristic properties of nonlinear behavior, such as force and stiffness degradation and pinching, were fully captured by the model. It should be highlighted that the model is capable of estimating the wall response reasonably well for a wide range of aspect ratios (i.e. for 700 mm, 1200 mm, 2400 mm, and 3600 mm long), reaching good accuracy when predicting the reversed force-displacement response.

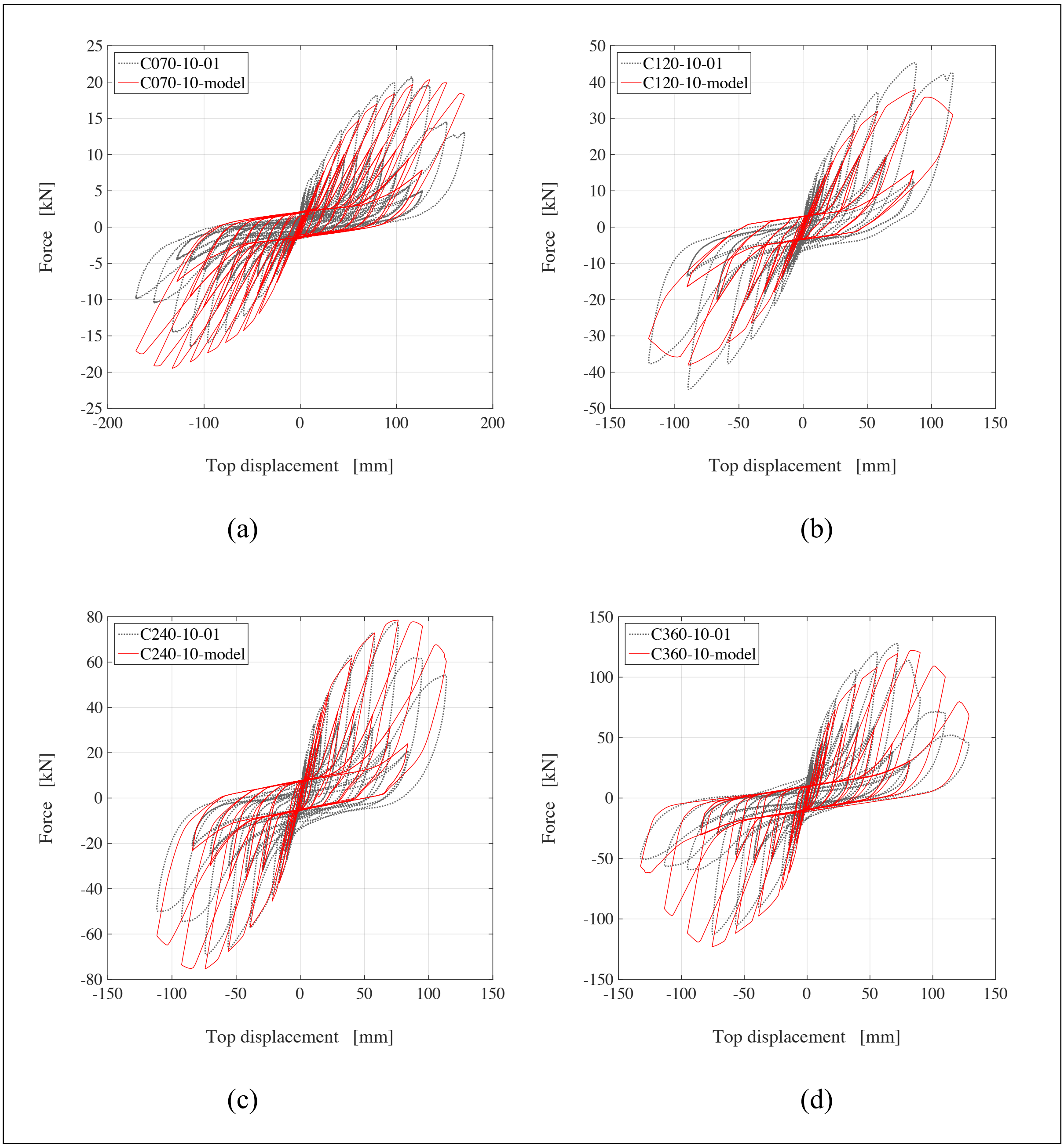

Figure 2-7. Cyclic behavior of strong wood frame walls. Comparison between experiments and model predictions for the specimens: (a) C070-10-01, (b) C120-10-01, (c) C240-10-01 and (d) C360-10-01.

For a detailed assessment of the proposed model, a quantitative comparison between test results and model predictions was also carried out for the selected twelve walls. Six engineering parameters were established as benchmarks for the evaluation: (1) maximum force F_{max}, (2) maximum displacement D_{max}, (3) initial stiffness K_0, (4) ultimate displacement D_u, (5) ductility μ, and (6) energy absorbed E_{abs}. The D_u value was estimated as the corresponding displacement to a force degradation of 20% (i.e., $0.8F_{max}$). When estimating the ductility, the yield force and displacement were calculated based on the equivalent energy elastic-plastic (EEEP) approach, according to the ASTM E2126 standard (ASTM 2018). The EEEP approach is defined as an elastic-plastic plot with the same area enclosed by the force-displacement curve, with the elastic stiffness defined at $0.4F_{max}$. For the monotonic analyses, the benchmark parameters can be obtained directly from the test and model force-displacement results. For cyclic analyses, a positive and a negative envelope was calculated for each force-displacement relationship, and the mean envelope was obtained as the average of both, up to the D_u displacement. Then, the aforementioned parameters were obtained from the mean envelope, and the absorbed energy was calculated as the area enclosed by the hysteretic cycles. This process is shown in Figure 2-8 for the specimen C240-10-01.

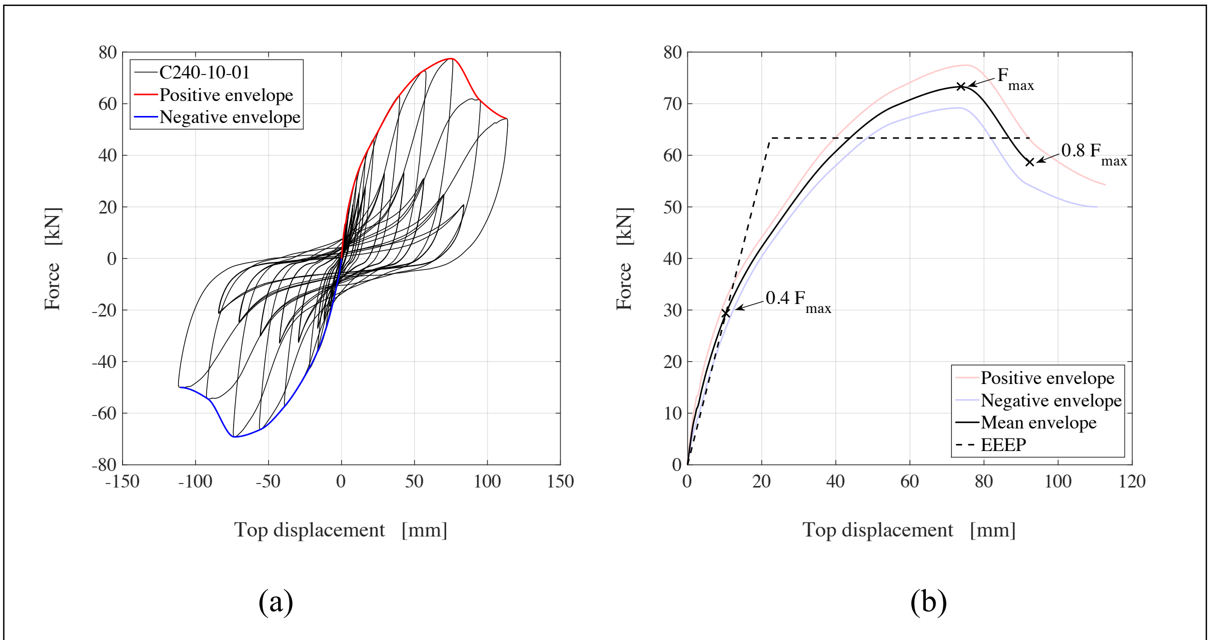

Figure 2-8. Calculation of (a) cyclic envelopes and (b) EEEP curve for 2400 mm long wall results.

The quantitative evaluation of the proposed model was done by normalizing the parameters obtained from the numerical models by those from the experimental tests. Consequently, values greater than one indicate that the model overestimates the parameter, while values less than one show that the model underestimates it. In Figure 2-9, the six normalized parameters for each wall specimen are summarized in boxplots. The top and bottom of each box are the 25th and 75th percentiles, respectively. The distances between the tops and bottoms are the interquartile ranges. The red line in the middle of each box is the median, and when it is not centered in the box, it shows data skewness. Whiskers are plotted from the ends of the interquartile ranges to the furthest values, and data beyond the whisker length are marked as outliers (red cross). A data point was identified as an outlier if it is more than 1.5 times the interquartile range away from the top or bottom of the box.

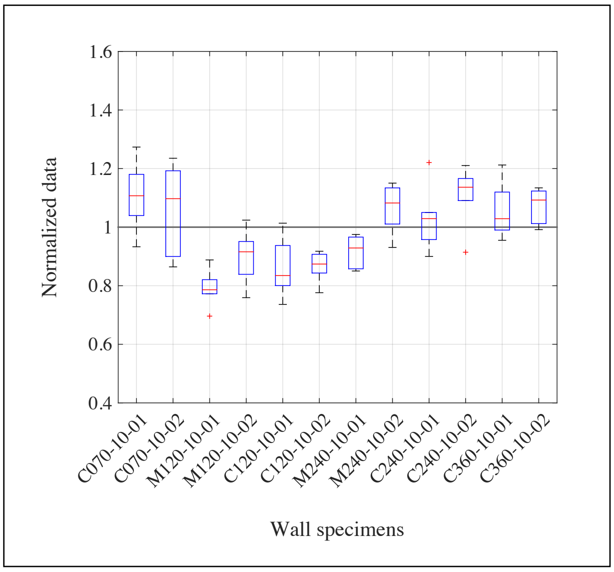

Figure 2-9. Median values of the analyzed six parameters for each specimen.

Figure 2-9 shows reasonable agreements between tests results and model predictions, with errors within the allowable range considering the inherent wood material properties' variation, as listed in Table 2-1. The highest median value of 1.14 is for the specimen C240-10-02 due to an overestimation of about 20% of D_{max} and D_u, while the lowest median value of 0.79 is for M120-10-01. However, the mean value of the medians is 0.99 with a standard deviation of 0.12, which seems reasonable for nonlinear modeling under large displacements. The interquartile ranges (IQR) are useful when evaluating the data scattering. The largest IQR is 0.29 for the C070-10-02, with 25th and 75th percentiles of 0.90 and 1.19, respectively. The lowest IQR value is 0.05 for M120-10-01, and the mean IQR for all specimens is 0.12.

For engineering purposes, it is interesting to analyze the capability of the proposed model when predicting the response of 1:1 walls (2400 mm long). This latter is relevant since it is a common practice to ignore walls with an aspect ratio greater than 2 (i.e., with length less than 1200 mm) in the lateral resistant system of wood frame buildings (interestingly, recent research has shown that high-aspect-ratio shear walls could have a positive influence on the building overstrength (Jayamon, Line & Charney 2019)). The medians for each 2400 mm wall analyzed in this work are 0.93, 1.08, 1.03 and 1.14 respectively, with a mean of 1.04. The average IQR is 0.10. Despite these median values being close to 1 (i.e., a zero-error performance), results show some inaccuracy when predicting the D_u value for 1:1 walls. This is due to the complex phenomena that occur once the maximum capacity has been reached and the stiffness degradation begins; the crushing of the wood, failure of the OSB panels, nonlinear behavior of the anchorage system, tearing of sheathing-to-framing and framing-to-framing nails, could be associated with the discrepancy between the predictions and experimental data. Figure 2-10 summarizes the accuracy of the model for each benchmark parameter analyzed, employing the data from all twelve specimens previously discussed and summarizing them in boxplots.

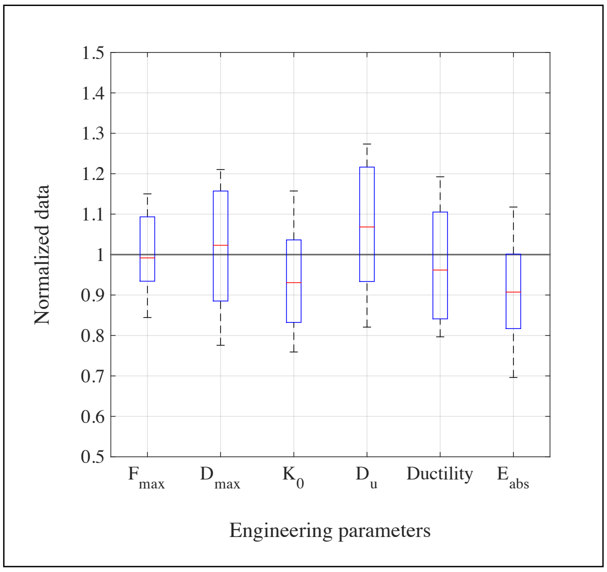

Figure 2-10. Normalized data for each engineering parameter computed from the12 specimens under analysis.

According to Figure 2-10, the maximum force and displacement are well predicted by the model, with median values of 0.99 and 1.03. Furthermore, the remaining parameters also have close-to-one median values. The average of the medians is 0.98, and the average of the IQRs is 0.23. As a general trend, the energy absorbed tends to be underestimated by the model, with a median of 0.91 and 25th and 75th percentiles of 0.82 and 1.0, respectively.

Even though the modeling strategy proposed in this investigation has been developed to capture the intrinsic properties of strong wood frame walls, its generic approach allows it to be employed for predicting the lateral behavior of conventional walls as well. To prove the latter, one of the specimens tested by Durham et al. (Durham, Lam & Prion 2001) at The University of British Columbia has been modeled employing the methodology presented in this chapter. The specimen corresponds to a shear wall commonly used in two-story wood frame houses. The test dimensions were 2400×2400 mm, i.e., a 1:1 wall. The framing material was 38×89 mm lumber, with studs spaced at 400 mm on center. The top plate and end studs were double members, whereas the bottom plate and the interior studs consisted of single members. To prevent overturning of the wall, conventional two-bolt discrete hold-downs were installed, which also ensured a racking mode of deformation. The OSB sheathing panels were 9.5-mm-thick with an elastic shear modulus of 1.5 GPa and sheathed just on one side of the wall. Three panels were used: a 1200×2400 mm panel for the bottom half of the wall and two 1200×1200 mm panels covered the top half of the wall. The sheathing-to-framing connections were pneumatically driven 50-mm-long nails with a shank diameter of 2.67 mm. Nails spacing was 150 mm on center along all panel edges and 300 mm for all interior studs.

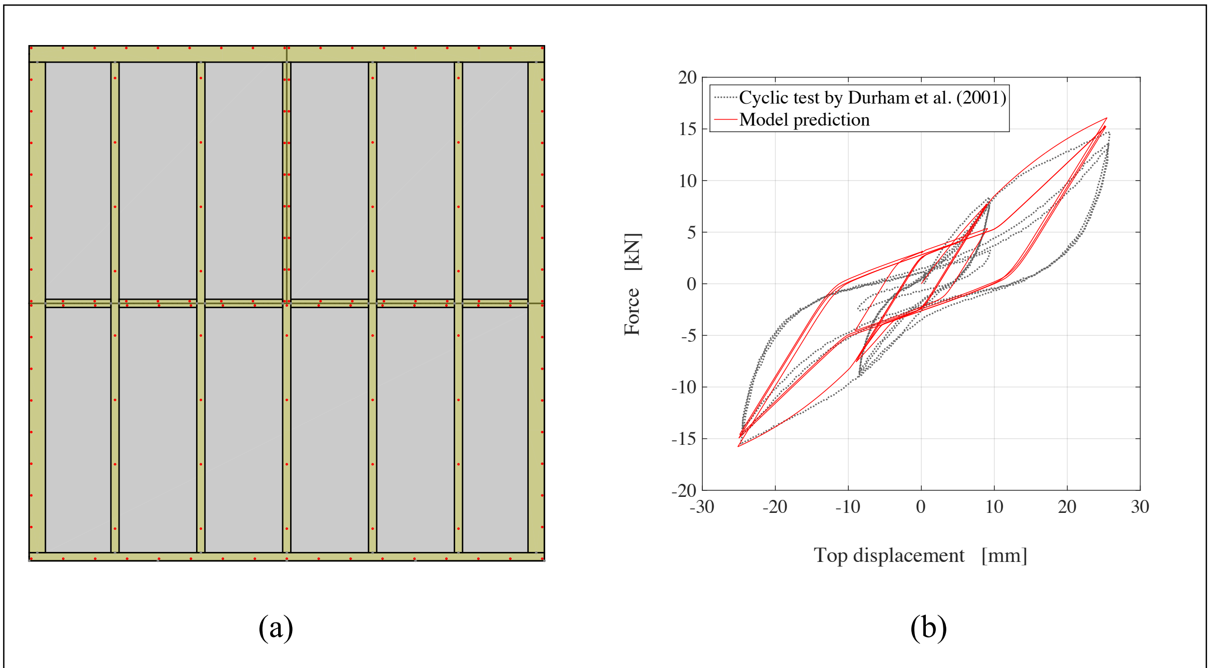

Figure 2-11. Schematic of the wood frame wall tested by Durham et al. (Durham, Lam & Prion 2001): (a) modeling approach, (b) comparison between test results and model prediction.

Figure 2-11(a) shows the schematic of the nonlinear model developed for the test of Durham et al. (Durham, Lam & Prion 2001), where the MSTEW modeling parameters originally proposed by Folz and Filiatrault (Folz & Filiatrault 2001) for sheathing-to-framing connections were employed (see Table 2-2). Figure 2-11(b) depicts a comparison between the test result and model prediction under a cyclic loading path. As shown, the model predicts accurately the lateral force-displacement response of the wall for both small and large amplitude cycles in terms of stiffness and force, with an average error of 4.41% and 5.56%, respectively. It should be noted that the model does not capture properly the unloading stiffness. This results in an underestimation of the energy dissipated by the wall (16.05% error). This issue can be addressed by a better calibration of the r_3 parameter in the MSTEW model for the sheathing-to-framing connections. For instance, if $r_3 = 1.65$, the error reduces to 8.66% when predicting the dissipated energy.

It should be highlighted that the shear stiffness of conventional wood frame walls is lower compared to that of strong walls ($k_{strong}/k_{conventional} = 3.24$, calculated for $0.1F_{max}$) since they are built up with less OSB panels and sheathing-to-framing nails. Therefore, the deformation of the anchoring system is expected to reduce. This is due to the fact that the shear stiffness is not high enough to induce important demands in the hold-downs when the wall is subjected to lateral forces.

Employing the model developed for the work of Durham et al. (Durham, Lam & Prion 2001), the percentage of top lateral deformation due to wall uplift was estimated to be 10.02% for 1:1 conventional walls. This value is lower than the one for 1:1 strong walls (25.0%). Previous research has shown that for the vertical loads expected in the first floor of a typical two to four-story wood frame house (~25 kN/m) such small uplifts can be neglected, and that hold-down devices have minimal effect on the lateral behavior of walls (Dean & Shenton 2005; Johnston, Dean & Shenton 2006).

2.4. LOCAL RESPONSE ASSESSMENT

The proposed model was employed to conduct in-depth analyses of the nonlinear behavior of wood frame shear walls, and the results are discussed in this section. Even though FEM models (such as the one presented here) have computational overheads higher than simplified-mechanistic models, a relevant advantage is that they explicitly provide information about the response of each structural element (i.e., studs, nails, hold-downs, and panels). Such information is quite valuable for performance-based seismic design procedures, where nonlinear models that explicitly evaluate the local damage at the component level are highly desirable.

2.4.1. Anchorage system

When evaluating the performance of wood frame walls, it is widely acknowledged that the damage level is related to the lateral drift or interstory drift. For instance, the FEMA 356 guidelines (FEMA 2000) establish three performance levels: immediate occupancy (IO), life safety (LS), and collapse prevention (CP), which are related to drifts of 1%, 2%, and 3%, respectively. However, these performance levels assume that all the damage is due only to shear deformation and that the wall is fully anchored. If the anchorage system (hold-down devices) fails, the wall loses its load-carrying capacity. Hence, analyzing the anchorage behavior in addition to the overall response of the wall could be relevant for large displacement demands. Figure 2-12(a) shows the vertical force-displacement plot of a hold-down device of a 2400 mm long wall obtained from the proposed numerical model. The tensile force was normalized by the allowable tensile capacity $T_{allowable}$ provided in the design catalog.

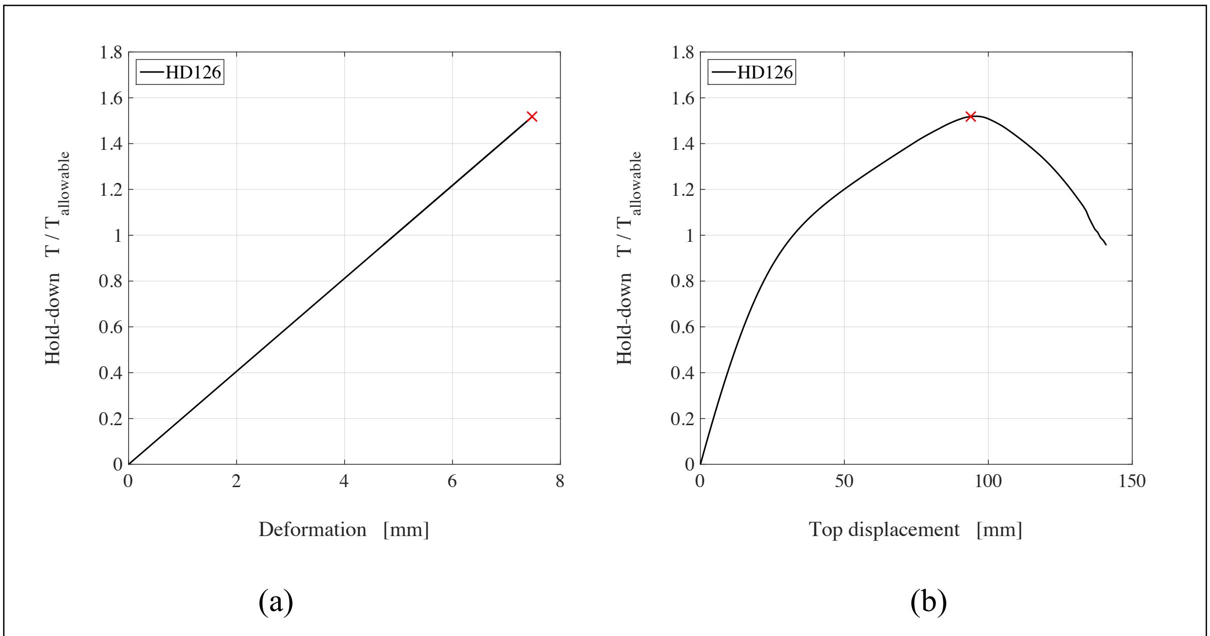

Figure 2-12. Hold-down HD126 response in the strong shear walls system: (a) load versus hold-down deformation, and (b) load versus wall top displacement. The point where the wall reached its maximum capacity is highlighted with a red cross.

Figure 2-12(a) shows the linear force-displacement response of the two-node link element employed to model the hold-down device in the lower-left corner of the wall. The maximum tensile force and displacement demand were $1.52T_{allowable}$ and 7.49 mm, respectively. In the design catalog, the allowable tension $T_{allowable}$ was determined as one-third of the maximum tension T_{ult}. Hence, the maximum tensile demand in the hold-down could be calculated as $1.52T_{allowable} = 0.51T_{ult}$. This means that the anchorage system remains below its failure capacity, and justifies the assumption of assigning a linear elastic behavior to the hold-down. Furthermore, it is interesting to note that the force-displacement relationship did not increase monotonically, but it unloaded after the wall reached its maximum capacity. This phenomenon can be observed in Figure 2-12(b), where the wall top displacement was plotted versus force demand in the hold-down. The cross highlights the point where the wall reached its maximum capacity, which falls very close to maximum tensile force in the hold-down. At this point, the sheathing-to-framing connectors have reached their maximum capacity, and the stiffness degradation begins. Since the wall works as a series system, when there is a loss of stiffness in the sheathing-to-framing connectors, they will experience greater deformations while the demand in the anchoring system will be reduced. This failure mechanism works as a safety switch that ensures a shear failure of the wall and prevents the hold-downs from pulling out. Similar results were found for walls of different aspect ratios, as Figure 2-13 shows. As noted by Schick and Seim (Schick & Seim 2019), this highlights the importance of over-designing non-ductile elements (such as hold-downs) to ensure the ductile behavior of wood frame walls.

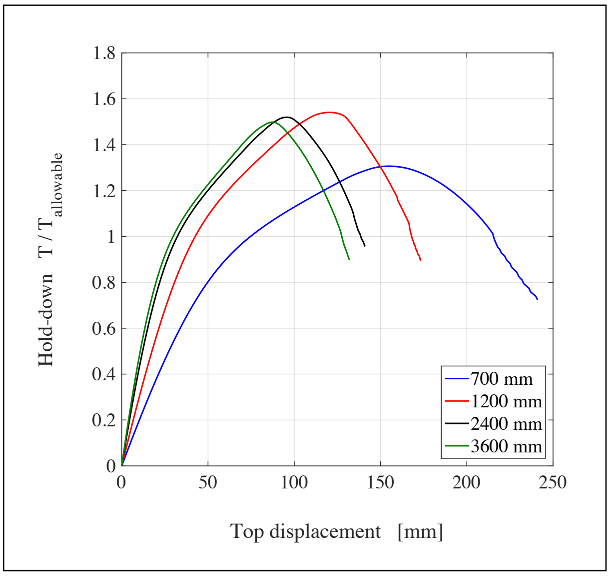

Figure 2-13. Hold-down force demands for walls with different aspect ratios.

Interestingly, the tensile demands in the hold-downs remained low even for high aspect ratio walls. Therefore, the high contribution of that the uplift has to the lateral top deformation in these walls is not due to higher tensile demands, but due to the slender geometry of the wall (i.e., small uplifts at the lower corners lead to large displacements at the top of the wall). On the other hand, the properties of the sheathing-to-framing connectors do have a relevant effect on the anchorage system demands. Figure 2-14 shows the hold-down responses for a 2400 mm long wall which was modeled employing connections with different ductilities and capacities.

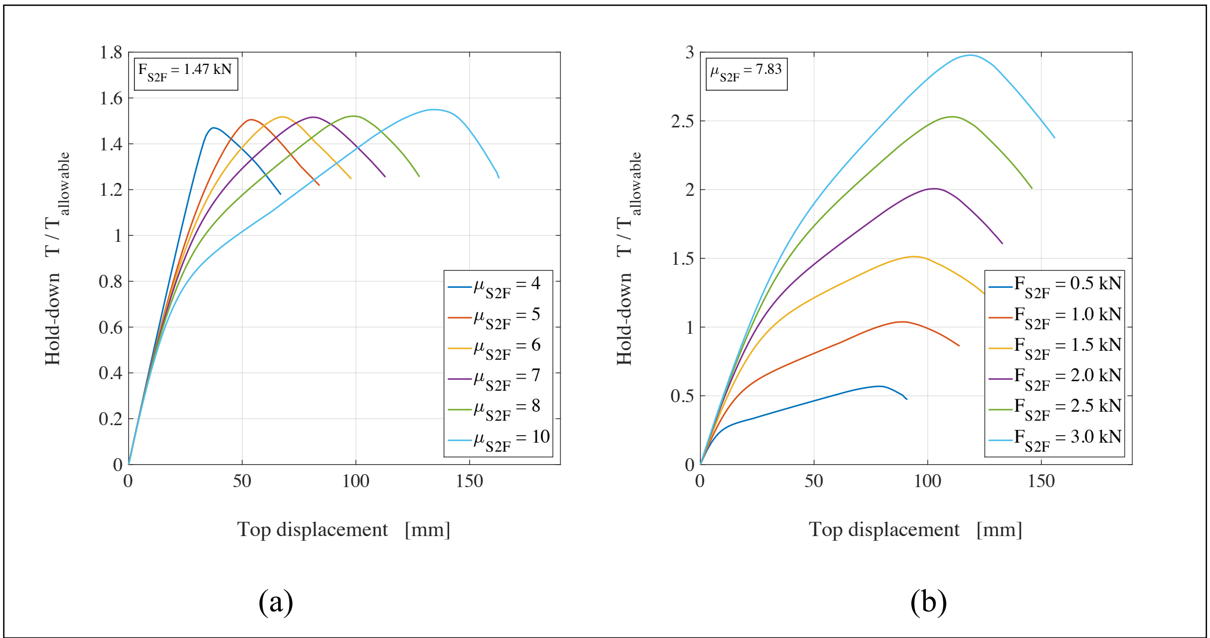

Figure 2-14. Hold-down force demands for walls with different S2F (a) ductilities and (b) maximum capacities.

For the results shown in Figure 2-14(a), the hysteretic model of the sheathing-to-framing connectors was modified so that it had the same maximum capacity but different values of ductility. For Figure 2-14(b), the maximum capacity was modified, and the ductility was kept constant. As can be seen, an increment in ductility capacity did not increase the demand in the anchorage system, but only *delayed* the point at which the maximum demand was reached. However, an increment in the maximum capacity of the sheathing-to-framing connectors raised the tensile force demands and may cause the failure of the hold-downs, as seen when F_{S2F} = 3.0 kN. Assuming that further failure mechanisms such as shear buckling do not take place, special care must be taken when designing the anchoring system if high-strength connectors, such as screws, are used in the wall design.

2.4.2. Sheathing-to-framing connectors

The deformation of sheathing-to-framing connectors is due to the relative displacement between the OSB panels (sheathing) and the wood frame. Because of the rectangular geometry of the panels and the deformed configuration (racking mode) of the framing, the maximum deformation of a sheathing-to-framing (S2F) connector depends on its position within the wall. Figure 2-15(a) shows the maximum deformation field for a 2400 mm long wall calculated based on the results of a monotonic analysis. The data show that the S2F connectors located in the upper and lower corners and in the central studs are prone to the greatest deformations. In other words, they contribute mostly to the resistance of the wall. Figure 2-15(b) shows the percentage of energy absorbed by an S2F connector during a cyclic analysis as a function of its position within the wall. Similarly, the most demanded connectors are those in the upper and lower corners and in the central studs. The S2F connectors placed on the interior studs have little contribution to the overall response of the wall, and their main function is to prevent the out-of-plane buckling of OSB panels. Based on the results described above, it is feasible to redesign the distribution of the S2F connectors within the wall, with the aim of optimizing their location in the areas of greatest demand and increasing the capacity of the wall. An alternative design is proposed in Figure 2-16(a) to demonstrate this.

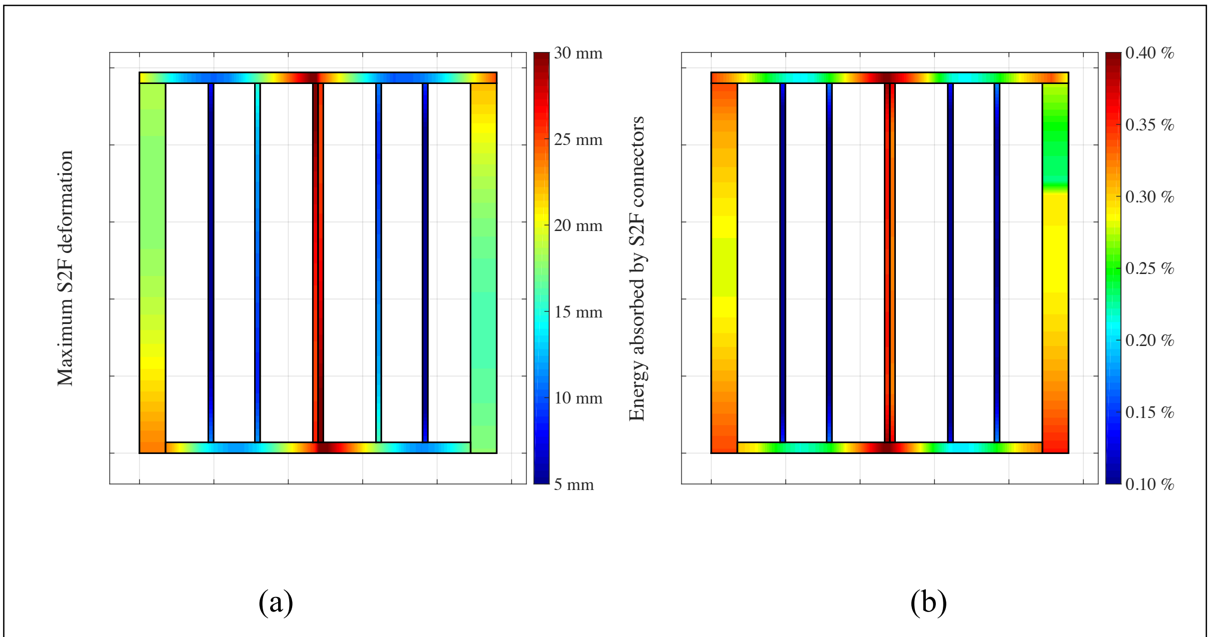

Figure 2-15. Demands on sheathing-to-framing connectors: (a) deformation and (b) energy dissipation.

For the optimization of the nailing pattern, the S2F connectors were concentrated in the upper and lower corners with a nail spacing of 50 mm, while in the intermediate zones the spacing was 150 mm. In the interior studs, a 300 mm spacing was used. This meets the minimum requirement to the avoid out-of-plane buckling of OSB panels. In addition, the total number of connectors was kept constant before and after the optimization, i.e., 392. According to Figure 2-16(b), the optimized wall has a 10% higher capacity than the original one, whilst the maximum displacement D_{max} remained almost the same (92.50 and 94.00 mm, respectively). However, a lower ductility was also observed, due to a reduction in the ultimate displacement of the wall from 125.21 mm to 120.62 mm. When the S2F connectors are concentrated in the zones of greater demand, they reach the failure capacity simultaneously, reducing the post-peak residual capacity of the wall. It should be highlighted that although a non-uniform nailing pattern (such as the one presented above) may not be efficient for on-site constructions, it can be used in automated prefabrication processes to improve the cost-effectiveness of wood frame walls.

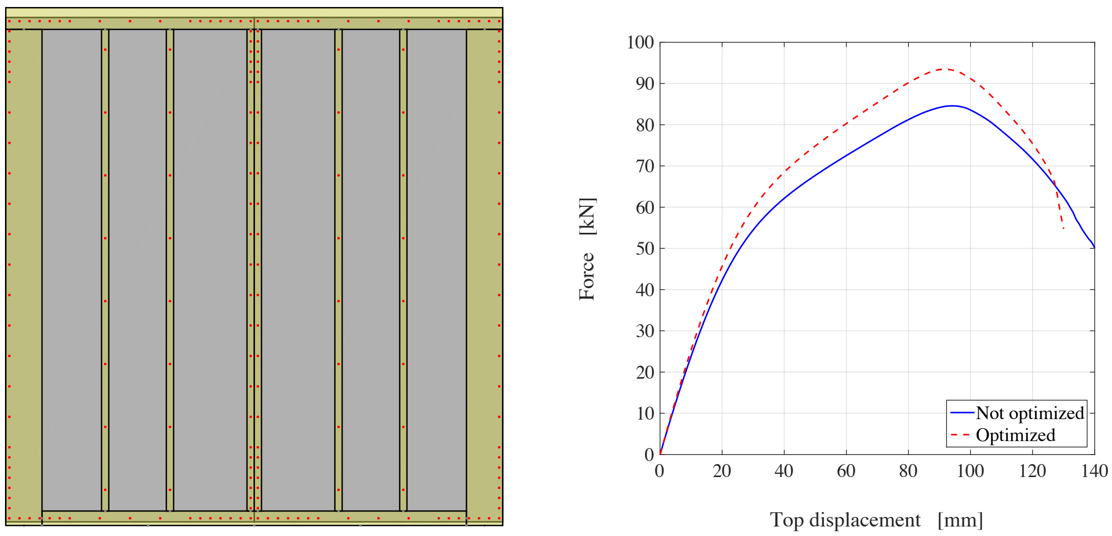

(a) (b)

Figure 2-16. Optimization of wood frame walls: (a) nailing pattern of the S2F connectors and (b) monotonic results before and after the optimization.

2.5. SIMPLIFIED MODELING FOR STRONG WALLS IN MULTI-STORY BUILDINGS

Due to the structural complexity and the large number of elements that wood frame walls have, it is not feasible to develop detailed FEM models (as the one presented in this chapter) for buildings with several stories. The computational and modeling effort involved in developing and analyzing such models would be quite intensive and thus limits their practical application.

In contrast, simplified numerical models with reasonable accuracy levels are more attractive for practice engineers. Simplified lumped mass models which consider both the pure shear deformation (Folz & Filiatrault 2004a) and the *bending* deformation of the building (Pei & van de Lindt 2009) have been developed in the last few years, and they have been proven to work well when compared with test data (Folz & Filiatrault 2004b; Pei & van de Lindt 2011). In order to balance accuracy and computational overheads, these models represent the shear response of wood frame walls through nonlinear springs by employing hysteretic models which are capable of capturing the phenomena associated with the nonlinear behavior under large displacements, such as the MSTEW model (Folz & Filiatrault 2001) or the EPHM model (Pang et al. 2007). Therefore, it is of relevant interest to determine the suitability of such models for strong wood frame walls as a necessary step towards studying the seismic behavior of mid-rise timber buildings using simplified approaches.

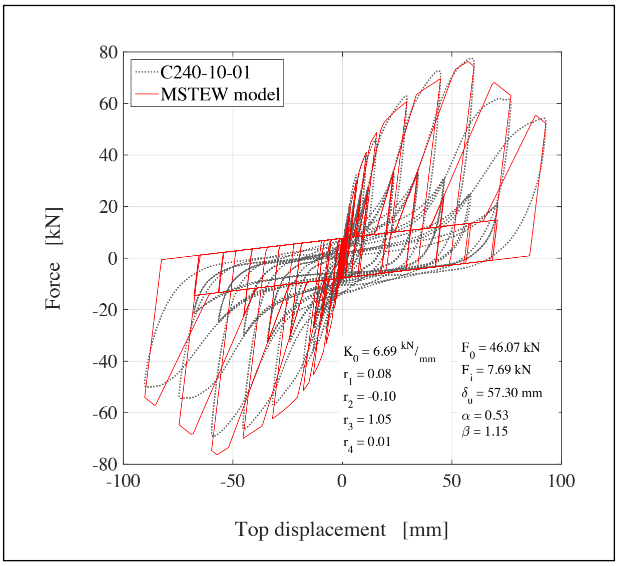

Figure 2-17. Comparison between the test data and model predictions using the MSTEW model with adjusted parameters for the shear response of a 2400 mm long wall.

Employing the pure shear data from diagonal measurements of a 2400 mm long wall (C240-10-01 specimen) during the test, a nonlinear spring was calibrated for the MSTEW model using a functional minimization procedure to estimate the model parameters, and the results are shown in Figure 2-17. According to this figure, a single degree of freedom (SDOF) spring is able to reasonably capture the nonlinear behavior of the wall even for large displacements. As noted by Pei and van de Lindt (Pei & van de Lindt 2011), the model parameters K_0, F_0, and F_i that control force and stiffness can be scaled proportionally to the wall length. Consequently, the same set of MSTEW parameters can be used to predict the cyclic response of walls with the same nailing properties but of different lengths. Using the nonlinear model described in the previous section, the MSTEW parameters per unit length were calculated to predict the cyclic shear behavior of walls with different nailing patterns, and the results are listed in Table 2-3.

Table 2-3. MSTEW parameters per unit length for modelling the shear response of strong wood frame walls.

Wall properties		**MSTEW parameters**									
OSB	**Nail spacing [mm]**	**K_0 [kN/mm/m]**	**r_1**	**r_2**	**r_3**	**r_4**	**F_0 [kN/m]**	**F_i [kN/m]**	**δ_u [mm]**	**α**	**β**
Single	50	2.374	0.072	-0.046	1.000	0.017	10.275	2.048	45.450	0.532	1.139
	100	1.393	0.079	-0.101	1.047	0.015	9.600	1.603	57.300	0.531	1.146
	150	1.080	0.079	-0.090	1.075	0.014	7.104	1.202	55.820	0.522	1.150
Double	50	2.487	0.097	-0.080	1.002	0.021	26.685	2.935	42.887	0.800	1.150
	100	2.786	0.079	-0.101	1.047	0.015	19.196	3.205	57.300	0.531	1.146
	150	2.159	0.079	-0.090	1.075	0.014	14.208	2.403	55.820	0.522	1.150

The data in Table 2-3 were calculated considering a field nail spacing of 200 mm, and assuming that the materials used for the walls have mechanical properties similar to those described in Section 2.2. Figure 2-18 shows the accuracy of the MSTEW model to predict the shear response of walls with different lengths, using the data in Table 2-3 for double-OSB walls with an edge nail spacing of 100 mm. As can be seen, the MSTEW model works well when predicting the cyclic behavior of shear walls, achieving an acceptable degree of accuracy to be used in the nonlinear evaluation of wood frame buildings. In addition, considering that it is an SDOF model with a very low computational overhead, the cost-accuracy balance is adequate for the purpose pursued. It should be highlighted that, employing the data provided in Table 2-3, practicing engineers could also create simpler linear models for wood frame buildings in any commercial software (such as SAP2000, ETABS, RISA-3D, SAPWood, among others) and use them in force-based design methods, such as modal analysis or demand-capacity. Figure 2-18 also shows a quantitative evaluation of the SDOF model using the previous six engineering parameters for each wall specimen, and the normalized data were summarized in boxplots. The close-to-one results show a good performance of the model, with average values of the medians and IQRs of 0.97 and 0.15, respectively.

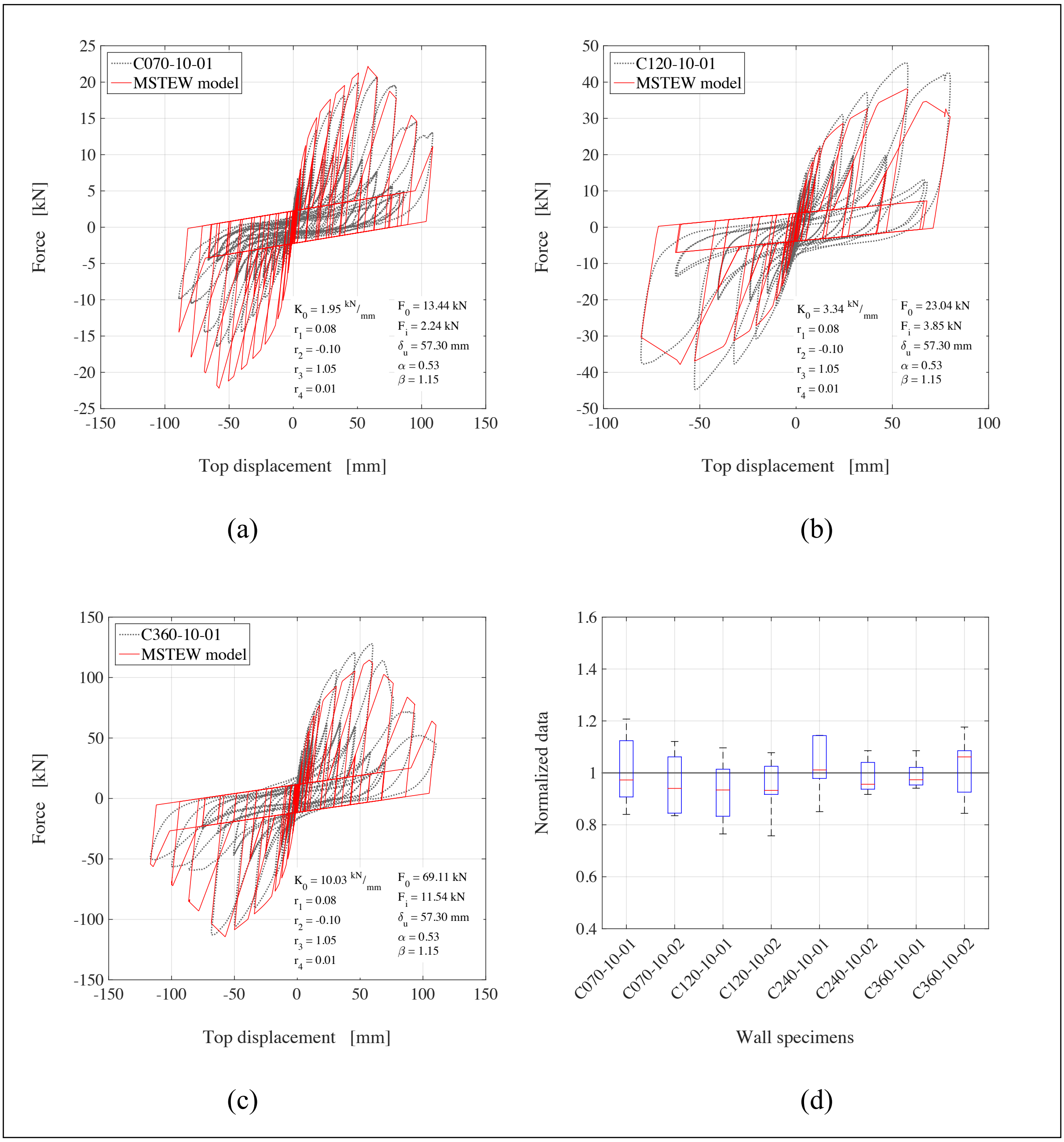

Figure 2-18. MSTEW predictions for the shear response of (a) 700 mm, (b) 1200 mm, and (c) 3600 mm walls, and (d) quantitative validation of the SDOF model.

CHAPTER THREE

EXPERIMENTAL INVESTIGATION ON THE CYCLIC RESPONSE OF WOOD FRAME SHEAR WALLS WITH CONTINUOUS ROD HOLD-DOWN ANCHORAGES

CHAPTER DISCLAIMER

The content, methodology, results, and figures presented in this chapter are based on the following article:

- Estrella X, Malek S, Almazán J, Guindos P, Santa María H. Effects of continuous rod hold-down anchorages on the cyclic response of wood frame walls. Engineering Structures 2020; *Submitted: May 13, 2020.*

3.1. INTRODUCTION

Wood frame buildings have gained ground within the engineering community during the past years mainly due to their low-cost and ease of construction. Furthermore, some of their inherent mechanical properties (such as low weight and high ductility) make them appealing for mid-rise structures in high seismicity zones, where the lateral capacity of the structure is provided by shear walls. Typically, conventional wood frame shear walls are composed of a timber frame (2400 mm high and 1200 to 2400 mm length) made up of 38×89 mm (2”×4”) inner studs spread out at 400 mm on center, with single members for the bottom and top plate, and double members for the end-studs. In order to avoid overturning of the wood frame wall, discrete hold-downs are installed at the lower corners. The shear stiffness and strength are often provided by wood-based structural panels (plywood or oriented strand board OSB panels 9 to 15 mm in thickness) installed on one side of the wall, employing 50 to 70 mm long steel nails spaced at 300 mm on center for inner studs and 150 mm along panel edges.

Recent research has introduced the concept of 'strong' wood frame shear walls (Guíñez, Santa María & Almazán 2019; Sadeghi Marzaleh et al. 2018), defined as higher capacity assemblies intended to withstand the increased vertical and lateral loads in multistory buildings. A 'strong' wood frame wall comprises 38×135 mm (2”×6”) frame members with several elements for the end-studs, stronger discrete hold-downs, OSB panels installed on both sides of the specimen, and a smaller nail spacing for inner studs and along panel edges. However, when designing mid-rise timber structures in high seismic risk areas, rigid body rotation governs flexibility as overturning moments induce large tensile forces in the anchoring system that cannot be resisted by either conventional or sturdy discrete hold-downs. To address this issue, continuous rod hold-down anchorages are employed instead, allowing to transfer high tensile forces across several stories to the foundation. A continuous rod hold-down anchorage consists of a 12.7 to 44.5 mm (1/2 to 1-3/4 in) diameter threaded steel rod, a coupler nut to connect one rod to another, bearing plates to transfer loads from the bottom and top plates to the rods, and shrinkage compensation devices, as shown in Figure 3-1(a). Shrinkage compensation devices consist of an arrangement of prestressed helicoidal springs fitted inside a steel shell that expands filling the gap formed between the bearing plate and the steel nut, this way mitigating the effects of wood shrinkage and building settlement.

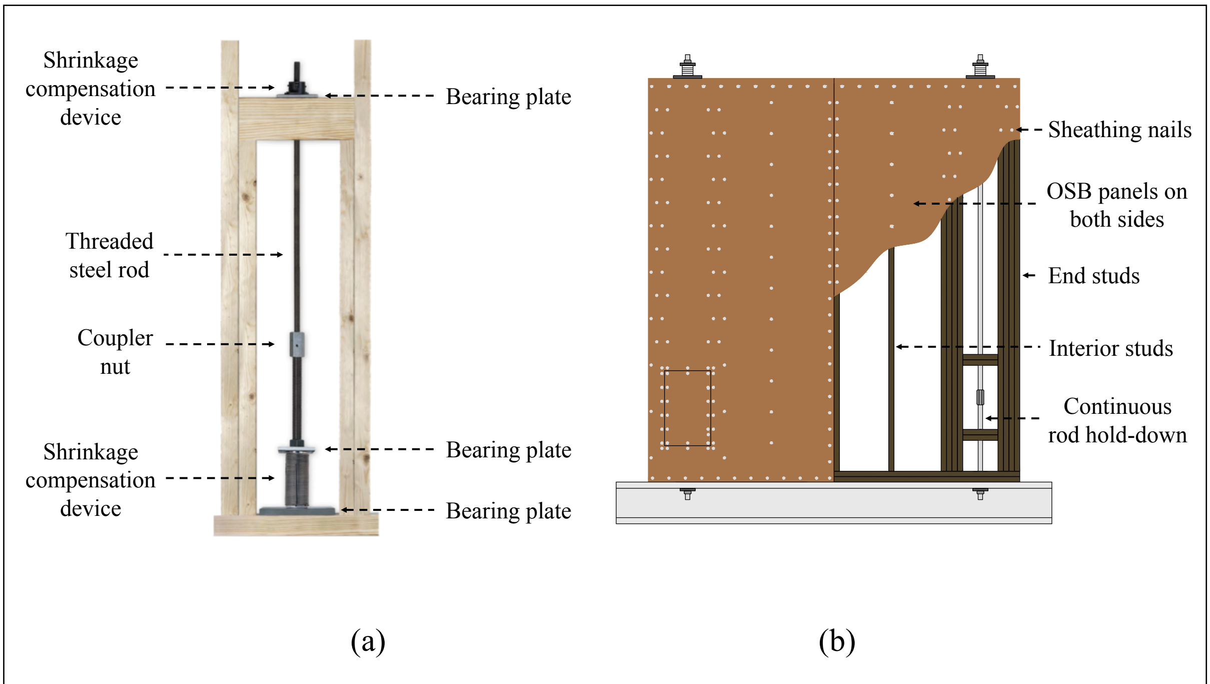

Figure 3-1. Configuration of: (a) a continuous rod hold-down anchorage (Simpson Strong-Tie 2018), and (b) a wood frame wall.

A thorough understanding of the lateral behavior of wood frame shear walls with continuous rod hold-downs is crucial for the growth of mid-rise timber structures, since the anchorage system is responsible for providing a continuous vertical load path to guarantee structural integrity and has a relevant impact on the overall cost of the structure (as much as 20%).

However, research on this topic is scarce. The NEES-Wood Project was a five-university multi-industry effort carried out from 2005 to 2009 aimed at increasing the engineering knowledge about the seismic resilience of multistory timber buildings in the USA. It included the development of a performance-based seismic design (PBSD) philosophy for wood frame structures (van de Lindt et al. 2013), a shake table testing program of a full-scale six-story apartment building (van de Lindt, Pei, Pryor, et al. 2010; Pei et al. 2010), and the development of nonlinear numerical models (Pei & van de Lindt 2009, 2011). Regarding the anchorage system, the main contributions of the project to the state-of-the-art were: (1) continuous rod hold-downs provide a suitable solution for the tensile demands when designing mid-rise timber buildings, (2) if a proper design procedure is followed for the anchorages, the structure can remain standing following a major earthquake (i.e., 2,500-year event), (3) uplift force demands for continuous rod hold-downs in mid-rise buildings are significant and need to be considered in PBSD approaches, and (4) rocking of the walls due to uplift and cumulative rod elongation contribute significantly to the overall lateral deformation in multi-story buildings.

Subsequently, van de Lindt et al. (van de Lindt et al. 2016) tested a full-scale four-story wood frame building as a part of the NEES-Soft project, an initiative aimed at validating different retrofit methodologies for wood frame structures. A total of eight continuous rod hold-downs were installed in the building to transfer the uplift forces at the end of shear walls down to the foundation (i.e., the shake table). Results showed that continuous rod hold-downs are able to properly resist the tensile forces caused by both translational and torsional responses (caused by an irregular walls layout), thereby allowing the building to resist major earthquakes with a low probability of collapse. However, a detailed discussion of the anchorages' behavior was not included in the results. Bagheri (Bagheri 2018) tested two conventional (not 'strong') wood frame walls with continuous rod hold-downs under monotonic load and compared the results with those of walls with discrete hold-downs. Data showed that employing continuous hold-downs increased the strength (13.8%), stiffness (17.1%), and ductility (21.5%) of the walls. However, the overall impact on the response of the specimens was not very significant, since the lateral behavior of the wall was mainly governed by the sheathing-to-framing connectors.

Despite the comprehensive work that has been conducted on wood frame walls, there is no research on the cyclic response of walls with continuous rod hold-downs in the published literature, nor on the effects of this anchorage system on the reversed force-displacement response of the wall. Although this issue has been somewhat globally studied through the full-scale shake table tests discussed above, an in-depth analysis of such cyclic response (in terms of the wall mechanical properties, failure mode, and nonlinear behavior) has not been reported so far. This information is of relevant value to properly assess the seismic performance of wood frame walls under earthquake loads, gain knowledge about engineering approaches to reduce structural and non-structural damages, and evaluate the design expressions proposed in the current seismic standards. On the other hand, cyclic loading paths with large displacements allow gaining insight into the wall nonlinear response and the effects of pinching on the energy dissipation properties of the structure. Furthermore, continuous reversed deformation of the sheathing-to-framing connections leads to steel nails fatigue, and have a significant effect on the force and stiffness degradation of the wall during large-amplitude cycles. This phenomenon is key to PBSD procedures, and can only be evaluated through cyclic (experimental or numerical) analyses.

Given the relevance of this topic for mid-rise timber engineering, this chapter presents the results of an experimental, numerical, and analytical investigation aimed at studying the cyclic behavior of wood frame walls with continuous rod hold-downs. Four standard ‘strong’ walls with different properties and configurations were tested under a reversed loading protocol, and the effects of employing continuous anchorages instead of discrete ones were evaluated by comparing the results with those obtained by previous researchers (Guíñez, Santa María & Almazán 2019). In order to evaluate the suitability of the Special Design Provisions for Wind and Seismic (SDPWS) standard (American Wood Council 2015) for wood frame walls with continuous rod anchorages, a comparison between the measured wall mechanical properties and the estimations from the standard was also carried out. Finally, a nonlinear numerical model of the tested specimens was developed to provide more insights into the test results under large lateral displacements. Test specimens, setup, and methodology are described in Section 3.2. Section 3.3 presents the test results and discusses the effects of continuous rod hold-downs, and the numerical model and further analyses are presented in Section 3.4.

3.2. MATERIALS AND METHODOLOGY

3.2.1. Test specimens

Four test specimens were assembled following typical practices and based on the structural designs for ground-floor walls of a six-story building. As shown in Figure 3-2, the wall configuration consisted of seven studs spaced at 400 mm on center. Since vertical loads and overturning moments are high in multistory buildings, end-studs consisted of four members each. Both bottom and top plates consisted of double members. All framing members were 35×138 mm (2”×6”) dimensional lumber, employing MGP10 Chilean radiata pine (INN 2014) with a measured modulus of elasticity E = 11400 MPa (see Table 2-1). The studs were end-nailed to the bottom and top plates with steel nails, 3 mm in diameter and 100 mm in length. The walls were sheathed on both sides with 11.1 mm thick APA rated OSB panels (1220 mm in width and 2400 mm in height) with a measured modulus of shear G_{LT} = 1307.49 MPa (see Table 2-1). The panels were oriented in the vertical direction and attached to the frame employing spiral nails 3 mm in diameter and 70 mm in length. The edge nailing was spaced at 50 or 100 mm on center and the field nailing at 200 mm on center. In order to avoid stress concentrations and crushing of the wood at the end-studs, the edge nailing was uniformly distributed among the four framing members. A pneumatic nail gun was employed for all nailing.

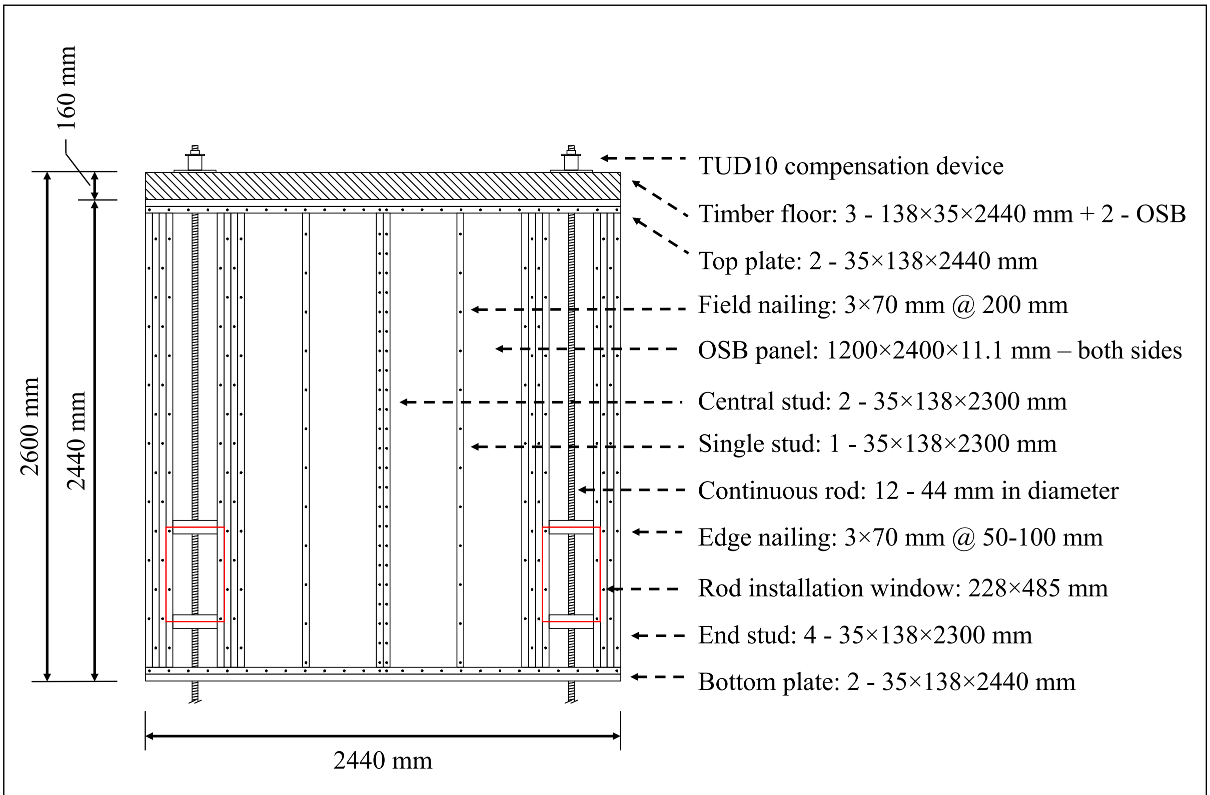

Figure 3-2. Configuration, components, and dimensions of the wood frame wall specimens with continuous rod hold downs. The red rectangles show the location of the rod installation windows.

Simpson Strong-Tie continuous rod hold-downs (fabricated in Pleasanton, CA, USA,) were employed to anchor the wall to the foundation, i.e., a reaction steel beam. The rods were 12.7, 31.8, and 44.5 mm (1/2”, 1-1/4”, and 1-3/4”) diameter threaded bars grade 105 (yield strength equal to 724 MPa), and no coupler nuts were used in the specimens since only one rod diameter was employed for each wall. Additionally, a Simpson Strong-Tie TUD10 shrinkage compensation device was installed at the top end of each rod along with a 38 mm thick bearing plate to properly distribute the load on the top plate.

Following typical practices, a 228×485 mm section was removed from the front OSB panels (and re-installed afterward using screws) at the lower corners. This is aimed at allowing a proper installation of coupler nuts (if used) when the walls are pre-assembled in factory and stacked together on site. Additionally, in order to replicate the real conditions when installing continuous rod hold-downs, a 160 mm height timber floor was added on top of the wall. Therefore, the dimensions of the specimen were 2440×2600 mm (2440×2440 mm without the timber floor).

Finally, four 25.4 mm diameter shear bolts were installed at the bottom plate to avoid lateral sliding of the wall. A detailed description of the configuration of each specimen is listed in Table 3-1. The labels shown is Table 3-1 describe the characteristics of the tested specimens; for instance, C-100-12 stands for a cyclic test, edge nails spaced at 100 mm, and a rod diameter equal to 12.7 mm.

Table 3-1. Labeling and description of the test specimens.

Wall label	Nail spacing (mm)		Rod diameter
	Edge	Field	(mm) [in]
C-100-12	100	200	12.7 [1/2]
C-100-44	100	200	44.5 [1-3/4]
C-50-32	50	200	31.7 [1-1/4]
C-50-44	50	200	44.5 [1-3/4]

3.2.2. Test setup

A post-tensioned L-shape reaction wall and a strong floor were employed to carry out the tests. As shown in Figure 3-3 and 3-4, the continuous rod hold-downs were anchored to the foundation beam employing steel nuts, and the foundation beam was fixed to the strong floor using two small self-reacting frames. The lateral load was applied by means of a hydraulic Aries actuator of 600 kN (~ 60 tonf) capacity and evenly distributed to the wall through the top timber floor. In order to prevent out-of-plane displacements and deformations, the specimens were laterally braced by two steel bars attached to the timber floor and fixed to the reaction wall.

All specimens were instrumented with sixteen displacement transducers (LVDTs) to measure the lateral displacement at the top of the wall, slip of the bottom plate, diagonal (shear) deformation, uplift at the lower corners, stud deformation, and relative displacement between OSB panels. Additionally, strain gauges were installed in the rod hold-downs to measure the tensile demands in the anchorage system. A PC-based system was used to control the test and to acquire the data.

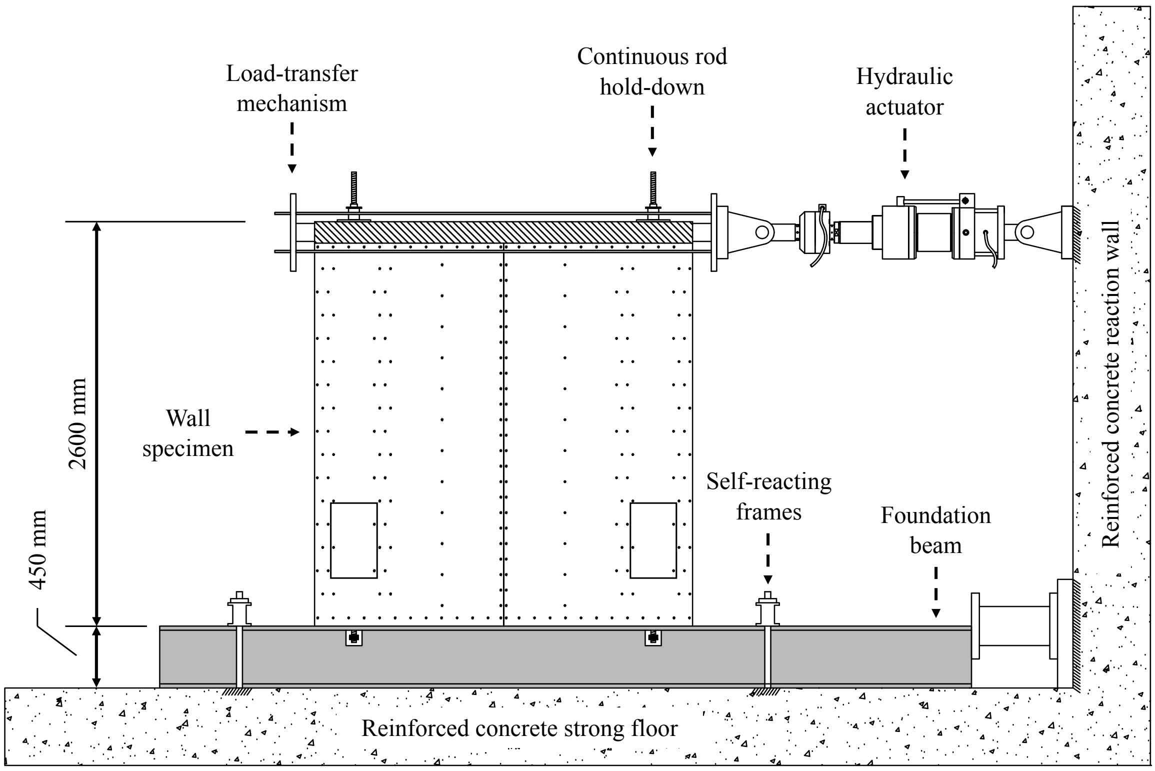

Figure 3-3. Schematic plan of the test setup in the lab: wall specimen, reaction structure (steel beam, strong floor, and reaction wall), loading mechanism, and anchorage system. Taking into account the top timber floor, the final dimensions of the specimens are 2440×2600 mm.

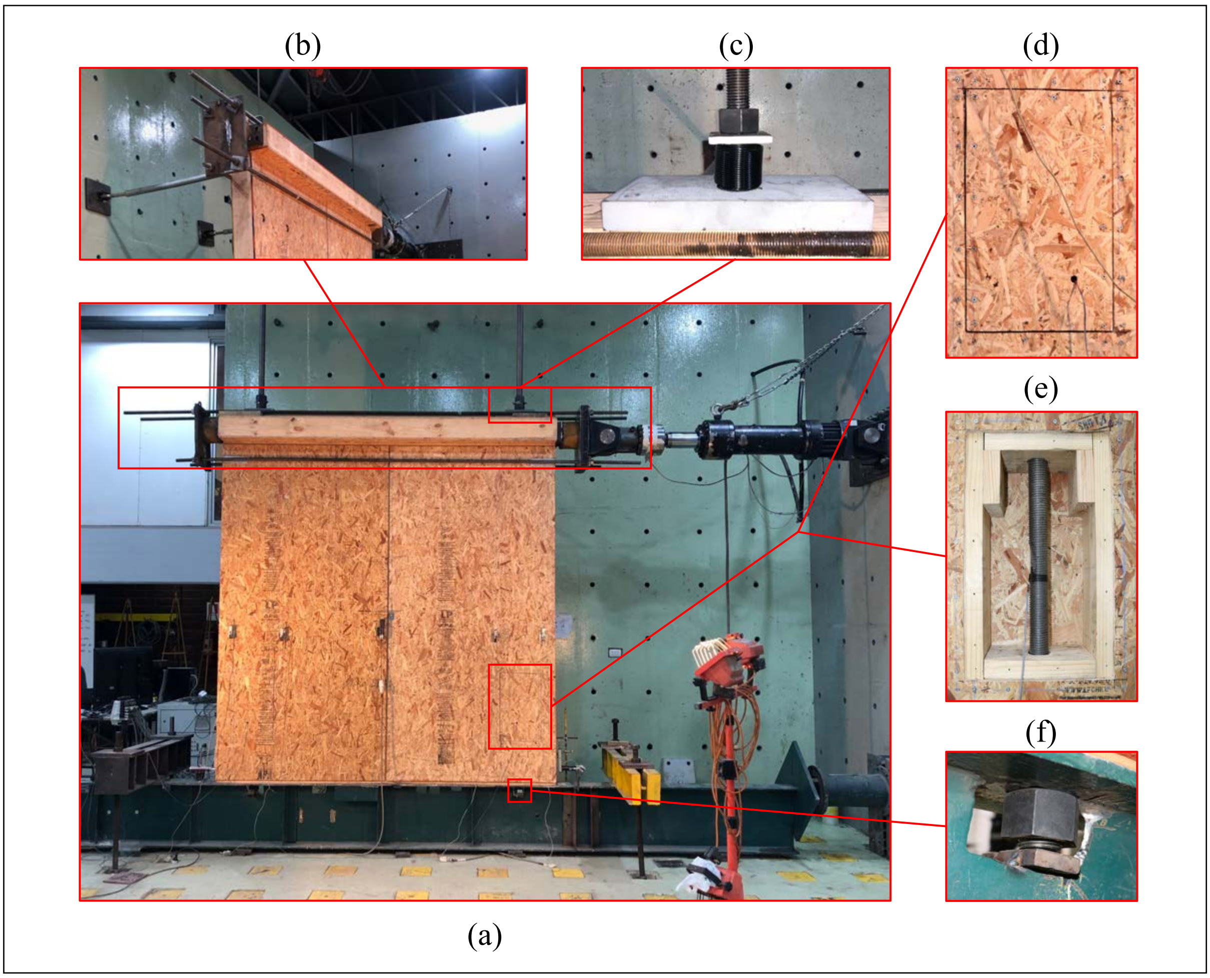

Figure 3-4. Test set up: (a) overall view, (b) timber floor, (c) TUD10 compensation device, (d) rod installation window, (e) open rod installation window, and (f) anchoring nut.

3.2.3. Test procedure

The specimens were loaded cyclically following the CUREE test protocol proposed by Krawinkler et al. (Krawinkler et al. 2001). This protocol was selected as it allows evaluating the seismic performance of structural elements under conditions similar to those expected during earthquake loads with a probability of exceedance of 10% in 50 years. As shown in Figure 3-5, the loading history was composed of different deformation amplitudes which were computed based on a predefined reference deformation Δ. In order to be consistent with previous investigations (Guíñez, Santa María & Almazán 2019; Orellana 2020), a value of $\Delta = 61$ mm was adopted in this research calculated as $\Delta = 0.6\Delta_m$ (Krawinkler et al. 2001), where Δ_m is the top lateral deformation at which the applied load drops below 80% of the maximum load during a monotonic test. From the monotonic tests conducted by Guíñez et al. (Guíñez, Santa María & Almazán 2019), a value of $\Delta_m = 102$ mm was reported. As shown in Figure 3-

5, the cyclic protocol consisted of three cycle types: initiation, primary, and trailing. Six initiation cycles (amplitude equal to 0.05Δ) were performed at the beginning of the protocol to check the loading equipment, instrumentation, and the load-slip behavior at small displacements. Subsequently, twelve cycle groups were performed. Each group consisted of a primary cycle followed by trailing cycles. The amplitude of the primary cycles ranged from 0.075Δ up to 2.5Δ, while the amplitude of the trailing cycles was equal to 75% of that of the preceding primary cycle. All cycles were symmetric, i.e., positive and negative amplitudes were identical. All tests were displacement controlled when applying the loading protocol.

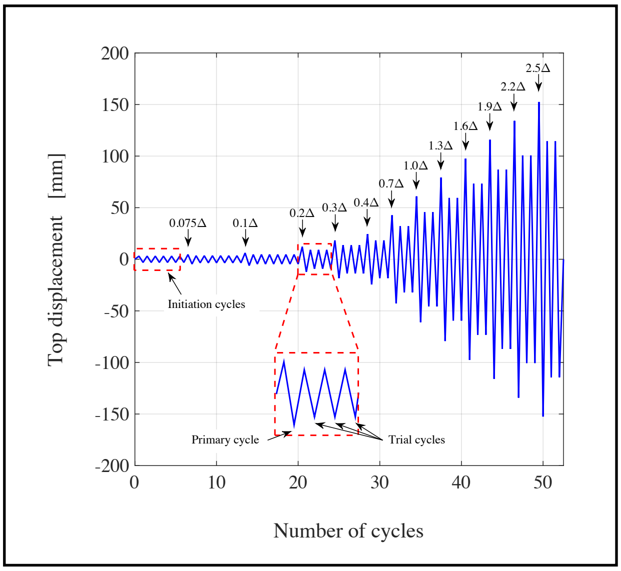

Figure 3-5. Reversed loading protocol used in cyclic tests.

3.3. RESULTS AND DISCUSSION

This section presents the test results and provides a discussion regarding the measured mechanical properties of the specimens. Failure mode, hysteresis shape, strength, stiffness, deformation, ductility, energy dissipation, and equivalent viscous damping were analyzed for each test. Furthermore, the effects of continuous rod hold-downs on the lateral behavior of wood frame walls were analyzed by comparing the test results with those provided by previous researchers (Guíñez, Santa María & Almazán 2019) for discrete hold-down walls. Finally, the accuracy of the design guidelines provided by the Special Design Provisions for Wind and Seismic (SDPWS) standard (American Wood Council 2015) was studied to validate their suitability for wood frame walls with continuous rod anchorages. Table 3-2 summarizes the test results for each specimen and the following sections provide a throughout analysis of them.

Table 3-2. Summary of the test results for each specimen.

Wall label	Failure mode	Strength F_{max} [kN]	Initial secant stiffness [kN/mm]	Displacement at F_{max} [mm]	Displacement at $0.8F_{max}$ [mm]	Ductility	Energy dissipation [kN-mm]	Damping ratio ξ_{eq}
W-100-12	Anchorage failure	57.55	4.17	53.40	60.83	2.99	11490.14	0.12
W-100-44	Nails ductile failure	89.67	6.19	56.60	81.91	4.14	38888.27	0.11
W-50-32	Nails ductile failure	142.81	7.18	78.50	104.27	3.75	59885.37	0.09
W-50-44	Timber frame failure	125.63	7.53	52.80	137.71	6.32	114670.09	0.12

3.3.1. Failure mode

Detailed inspections of all wall components were carried out after each test. In all four specimens, three failure modes were identified for the sheathing-to-framing connections: (1) pulling out of the nail shank from the panels and framing members, (2) pulling of the nail head through the OSB panels, and (3) shear fracture of the nail, as shown in Figures 3-6(a), 3-6(b), and 3-6(c), respectively. These failure modes are consistent with those identified by previous researchers (Guíñez, Santa María & Almazán 2019; Lebeda et al. 2005; Johnston, Dean & Shenton 2006; Shenton, Dinehart & Elliott 1998) for typical wood frame walls. However, the nail damage location followed a different pattern for the walls tested in this research. Typically, due to the racking deformation of the sheathing panels, the nail damage is concentrated at the lower and upper corners of the wall for large lateral displacements, as reported in Chapter 2. Nevertheless, for the walls under investigation, the additional nails employed for the sturdy end-studs stiffened the lower and upper corners of the walls, moving the damage towards the center studs, as can be noted in Figure 3-6(d) marked in red. Interestingly, this phenomenon also minimized the crushing damage of the sheathing panels due to the contact between the panel corners and the top or bottom floor, as it has been reported by previous researchers for traditional walls (Guíñez, Santa María & Almazán 2019).

The redistribution of the nail damage also affected the failure mode of the timber frame. The central studs and their connections with the top and bottom plates experienced moderate damage under large displacements, with crushing of the wood and pulling out of the stud-to-plate nails. As shown in Figures 3-6(d) and 3-6(f), the specimen C-50-44 showed severe damage at the central zone, with a full detachment of the central stud from the top plate. This was mainly due to the high loading capacity and ductility of the wall provided by the 50 mm nailing space and 44.5 mm diameter rod anchorage, allowing the specimen to withstand a large shear deformation. On the other hand, as expected due to the nail damage pattern, Figure 3-6(g) shows that the end-studs showed little or no damage at both upper and lower corners (compared to the damage in the center studs shown in Figure 3-6(f)), guaranteeing the integrity of the anchorages and the ductile failure of the wall.

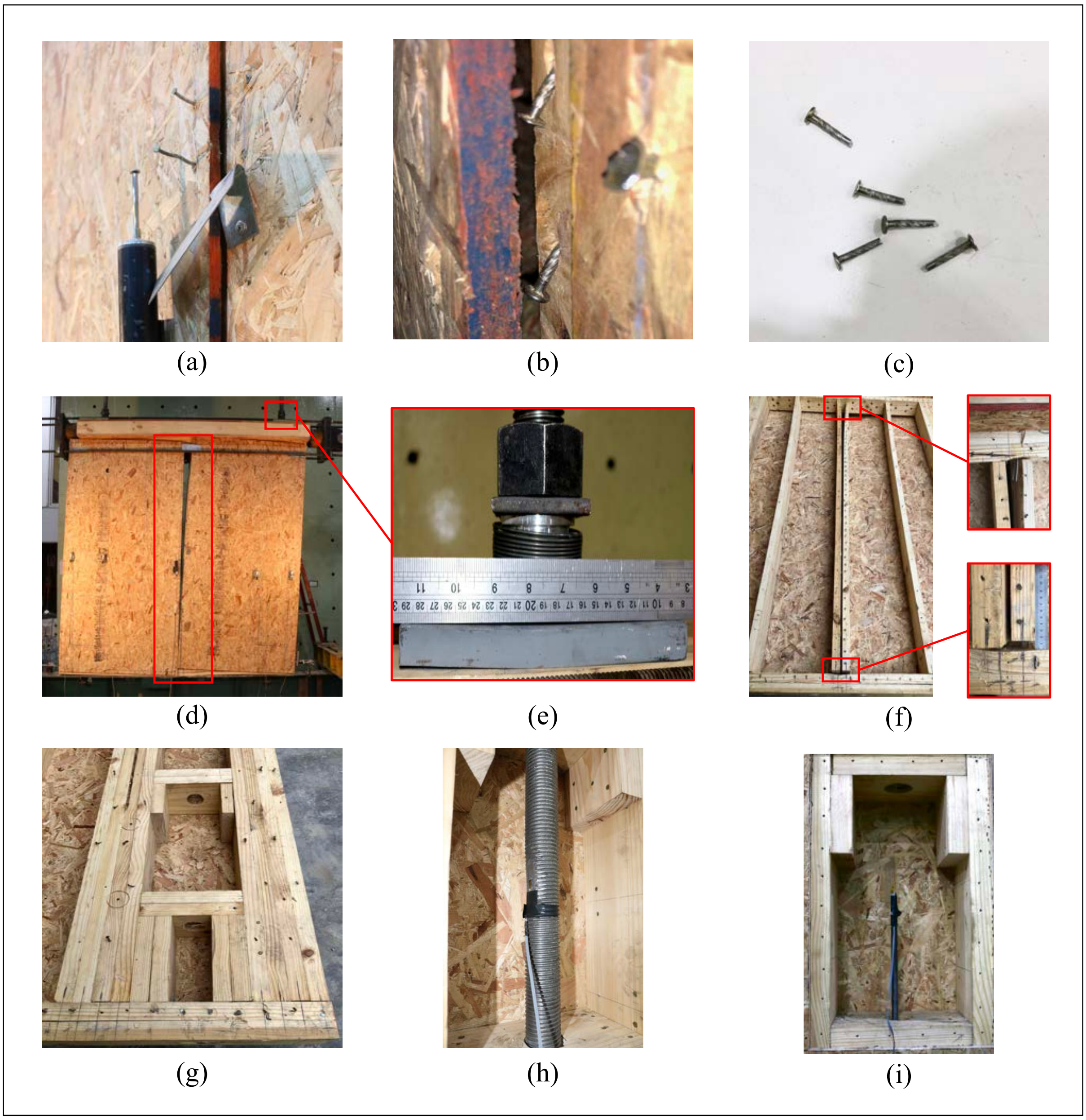

Figure 3-6. Damage observed in the tests: (a) pull out of nails, (b) pull through of nail heads, (c) shear fracture of nails, (d) damage to timber frame, (e) bent top bearing steel plate (f) detachment of central studs from top and bottom plates, (g) undamaged end-studs, (h) undamaged steel rod, and (i) tensile fatigue of steel rod.

The anchorage system showed almost no damage in most of the tests, with the steel rods behaving elastically along all their length, as shown in Figure 3-6(h). However, for drifts larger than about 3% (calculated as the ratio between the top lateral displacement and the wall length L = 2440 mm), the top bearing steel plate crushed into the timber floor and showed a small permanent curvature, as depicted in Figure 3-6(e). This deformation did not affect the performance of the anchorage system since the gap between the plate and the timber floor was taken over by the shrinkage compensation device.

The only test whose anchorage system failed was the specimen C-100-12. At a 1.4% lateral drift (33.6 mm), the overturning forces exceeded the capacity of the anchorage and the steel rod (12.7 mm in diameter) failed, as Figure 3-6(i) shows. This was then followed by the wall losing all its load-carrying capacity. As noted by previous investigations (Schick & Seim 2019; Schwendner, Hummel & Seim 2018), from a practical design perspective this failure mode is avoided by designing the anchorage rods as elastic elements and assuring that the overturning capacity of the wall has a larger over-resistance factor than the shear lateral capacity. This way, dominating failure mode in the system is guaranteed to be ductile nail yielding.

3.3.2. Global force-displacement response

Figure 3-7 shows the global force-displacement hysteresis for the four specimens tested in this research, showing the total top lateral displacement of the wall and the lateral load applied through the timber floor. Displacements due to sliding were removed from the total top lateral displacement of the specimens. The overall shape of the hysteresis is consistent with the results reported by previous researchers for conventional and strong wood frame walls (Guíñez, Santa María & Almazán 2019; Lebeda et al. 2005; Johnston, Dean & Shenton 2006; Shenton, Dinehart & Elliott 1998).

The initial response of the walls was elastic up to drifts of about 0.8%, after which it became nonlinear mainly due to the deformation of the sheathing-to-framing connections. The force and stiffness degradation observed after the peak strength was caused by the progressive failure of the nails under any of the three modes previously described in Section 3.3.1. However, such degradation is gradual and smooth because of the high redundancy of the nailed connections; for instance, there were about 750 sheathing-to-framing nails in the C-50-32 specimen. Only the C-100-12 wall showed an abrupt drop in the loading capacity as shown in Figure 3-7(a) with a red circle; this was due to the failure of the anchorage rod as explained in Section 3.3.1 and shown in Figure 3-6(i). Under reversed lateral load, the specimens showed a highly pinched hysteresis (illustrated in Figure 3-7(b)) as a result of the gap formed by the crushed wood at the nailed connections. Figure 3-8(b) depicts this phenomenon by comparing a damaged connection with an undamaged one.

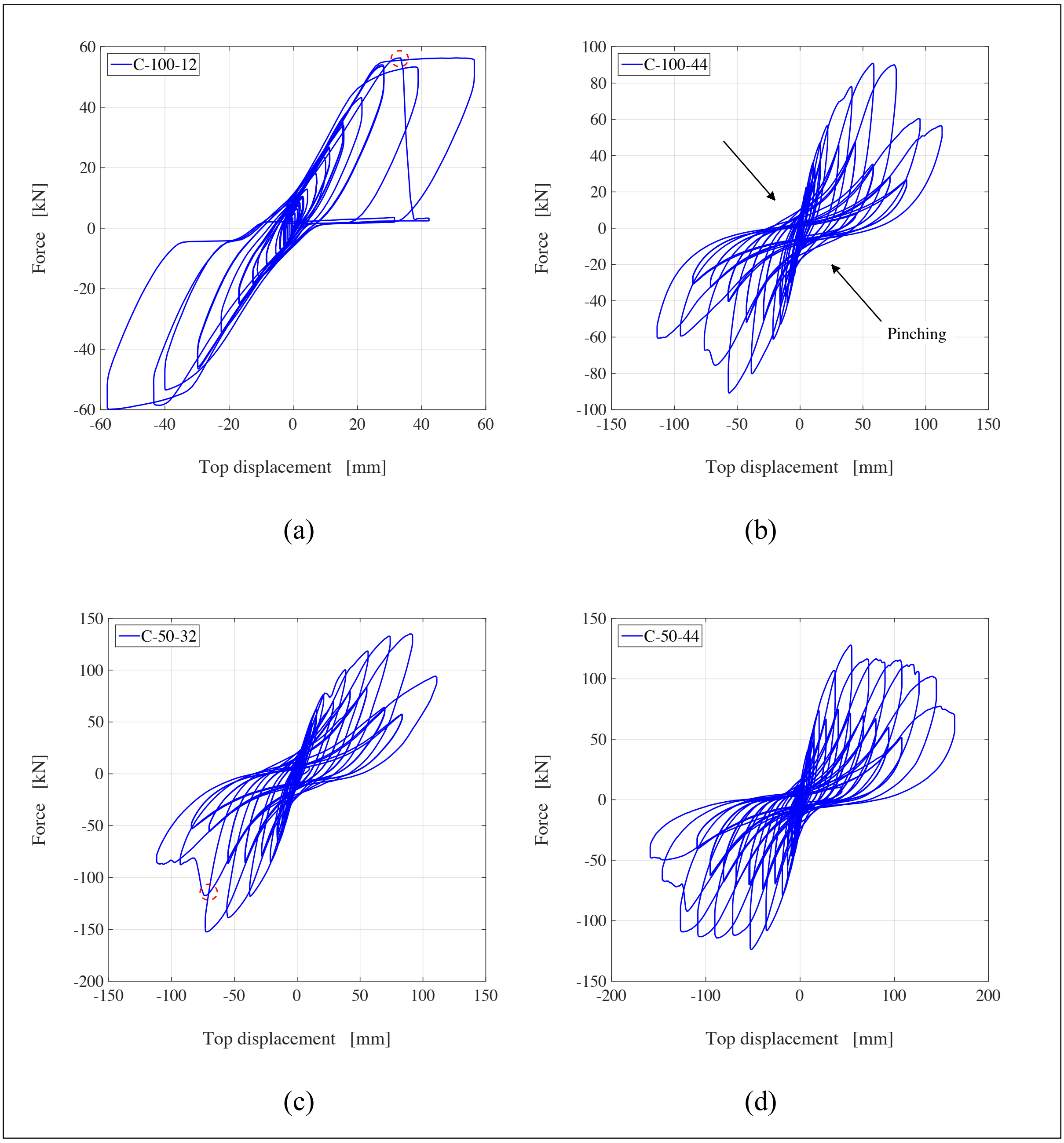

Figure 3-7. Global force-displacement response for specimens: (a) C-100-12, (b) C-100-44, (c) C-50-32, and (d) C-50-44. Sudden force drops were denoted by red circles for the specimens C-100-12 and C-50-32.

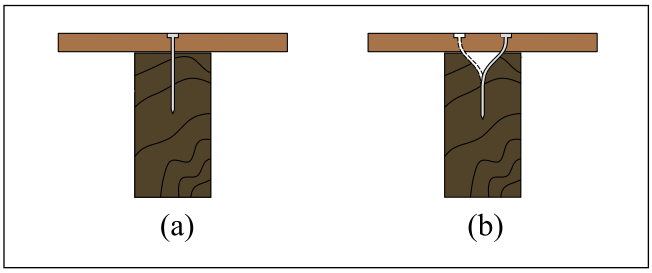

Figure 3-8. Sheathing-to-framing connection: (a) undamaged connection, and (b) damaged connection and gap caused by crushing of the wood under reversed loading.

3.3.3. Anchorage response

Figure 3-9 shows the anchorage response for the specimens C-100-44 and C-50-32. The data were calculated based on the strain gauges installed on the rods and the LVDTs placed at the wall lower corners. Even though a linear trend is observed for both specimens, results show a hysteretic behavior of the anchorages and some energy dissipation under reversed loading. This is mainly due to the crushing of the wood at the anchorage zone and bending of the bearing plates at the top of the wall, as Figure 3-6(e) shows. However, the damage to the anchorage was minimum and did not affect the performance of the wall (except for specimen C-100-12, as explained above). Additionally, the steel rods remained in the elastic regime since their yield strength (724 MPa) was not reached in any test. Interestingly, a displacement gap of ~1.5 mm is noted at the onset of the hysteretic plots due to tolerance dimensions and anchorage details.

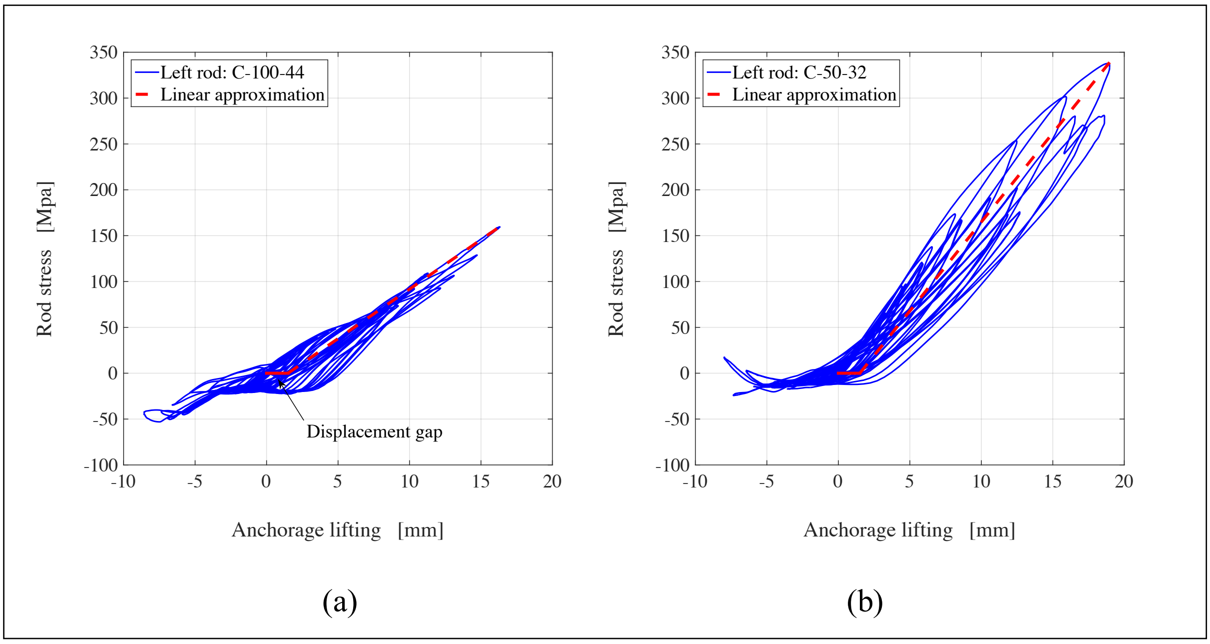

Figure 3-9. Anchorage response: (a) C-100-44 specimen, and (b) C-50-32 specimen.

3.3.4. Strength

The wood frame walls' strength is governed by the nailing and sheathing properties since their shear strength is mainly provided by the sheathing-to-framing connections. However, the response of other components (such as the anchorage system or the framing) may have a significant influence on the wall response. Therefore, it is of interest to study the effect of different variables on the wall strength for the specimens tested in this research. For a quantitative evaluation of the measured strengths, a force-displacement envelop was calculated for each specimen. As illustrated in Figure 3-10(a), positive and negative envelopes were computed for the hysterical responses employing the data from two opposite quadrants, and subsequently, an average envelope was obtained from the results. The average envelopes for each specimen are shown in Figure 3-10(b).

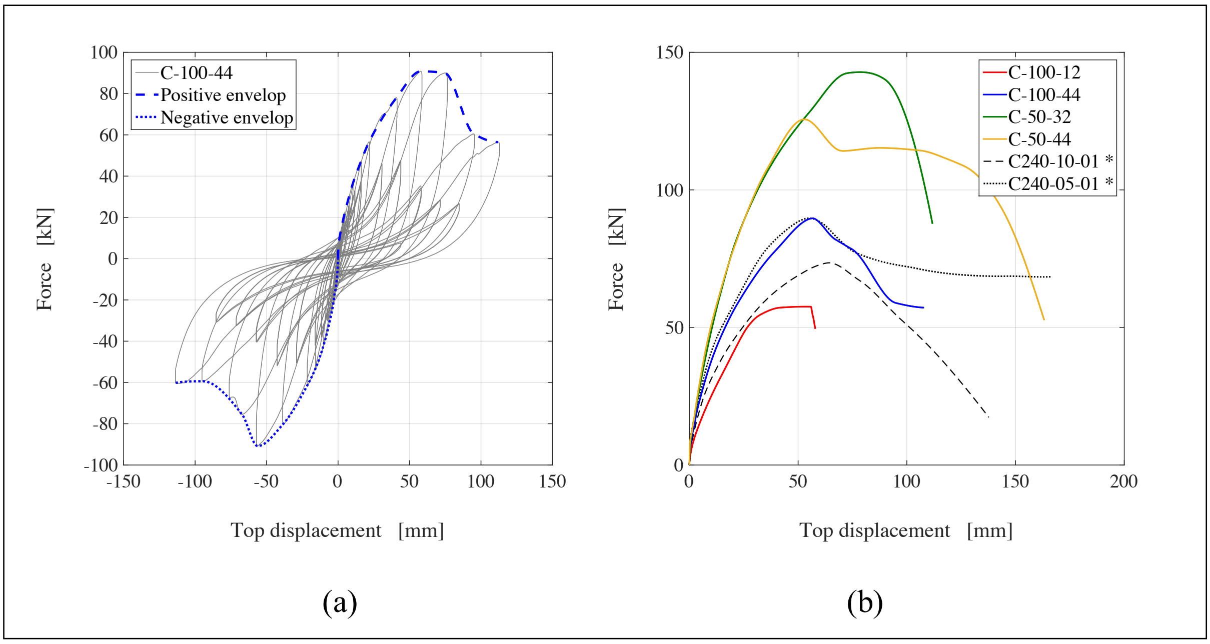

Figure 3-10. (a) Positive and negative envelope for the C-100-44 specimen, and (b) envelop comparison for the walls with continuous rod hold-downs tested in this research and walls with discrete hold-downs tested by Guíñez et al. (Guíñez, Santa María & Almazán 2019). These latter are marked with an asterisk.

Specimen C-100-12 had a relatively low strength (57.6 kN) due to the tensile failure of its anchorage system. However, if a stronger anchorage is used instead, the wall strength increases by 55.7% (up to 89.7 kN), as observed in the specimen C-100-44. Reducing the nail spacing from 100 to 50 mm increased the wall strength by 40%, as measured in the specimen C-50-44 that showed a peak value of 126.6 kN. Interestingly, the C-50-32 specimen, that employed a smaller diameter rod (31.7 mm), showed a 13.7% higher strength (142.8 kN) when compared to the C-50-44 one. It was due to an early failure of the timber frame of the C-50-44 specimen, as depicted in Figure 3-6(d). Besides, the higher strength and stiffness of the anchorage system provided by the 44.5 mm rod induces higher shear deformations on the sheathing-to-framing connectors, as discussed in Chapter 2.

Figure 3-11. Fragile failure mode of a timber frame (bottom plate) caused by a discrete bolted hold-down (Guíñez, Santa María & Almazán 2019).

To evaluate the effects of continuous rod hold-downs on the lateral behavior of wood frame walls, the results of this research were compared with those reported by Guíñez et al. (Guíñez, Santa María & Almazán 2019), who tested a comprehensive set of walls with discrete hold-downs. Such walls were structurally equivalent to those studied in this investigation, since the same timber grade, stud dimensions, OSB thickness, and nail type were employed. The specimens labeled as C240-10-01 and C240-05-01 by Guíñez et al. (Guíñez, Santa María & Almazán 2019) were selected for this analysis since their wall dimensions (2440×2440 mm) and nail spacing (100 and 50 mm, respectively) were the same as in this research. The average envelopes of both specimens are also shown in Figure 3-10(b). For a 100 mm nail spacing, results show that employing continuous rod hold-downs increases the strength by 22%, while for a 50 mm nail spacing it increases by 49.6%, on average. Two main reasons could explain such higher strength values. First, the configuration of the continuous rod system does not compromise the structural integrity of the end-studs as the discrete hold-downs do, since the latter are installed on the frame and may crush the wood under large tensile demands, as shown in Figure 3-11. In contrast, when continuous hold-downs are used, end-studs only face compression loads. Second, the sturdy end-studs of the specimens under investigation add up additional sheathing-to-framing connections to the wall, increasing its lateral shear strength and moving the failure mode towards the center of the wall, as discussed previously.

The suitability of the design guidelines provided by the SDPWS standard (American Wood Council 2015) for wood frame walls is also evaluated in this section. The nominal unit shear capacity v_s for walls with different configurations can be obtained from Table 4.3A (American Wood Council 2015). For the walls of this research, 7/16 in (11.11 mm) OSB panels and 8d nails were considered on both faces of the wall. For a nail spacing of 100 mm, the unit design capacity was 20.4 kN/m (1400 plf), and for a 50 mm nail spacing it was 34.2 kN/m (2340 plf). For 2440 mm length walls, it is equal to 49.9 kN and 83.3 kN, respectively. As shown in Figure 3-12, the wall strength values were underestimated by the SDPWS provisions for all cases (even for the C-100-12 specimen). The underestimations ratios were 13.4%, 44.4%, 41.7%, and 33.7% for each specimen, respectively. Without considering the C-100-12 specimen, the average underestimation ratio was 39.9%. These results are consistent with those reported by previous studies on wood-frame walls (Guíñez, Santa María & Almazán 2019). A full discussion of these results is presented in Section 3.3.9.

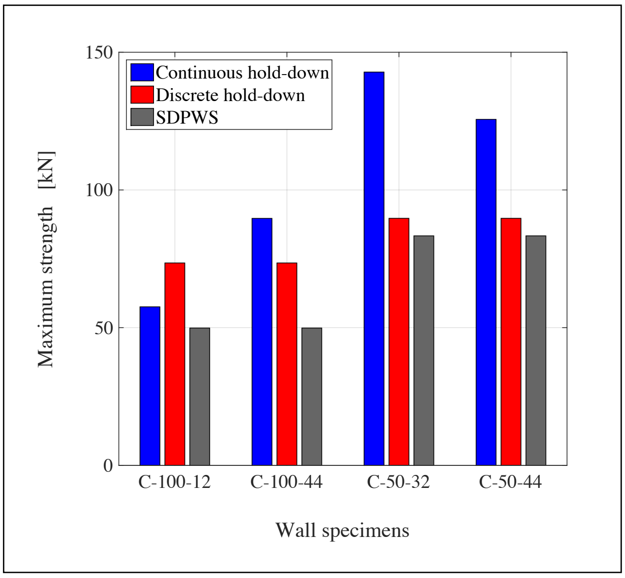

Figure 3-12. Comparison of shear strengths of the walls with continuous rod hold-downs (current research), the walls with discrete hold-downs tested by Guíñez et al. (Guíñez, Santa María & Almazán 2019), and the SDPWS guidelines (American Wood Council 2015).

3.3.5. Stiffness

The anchorage system has a direct influence on the stiffness of wood frame elements since it prevents rocking of the wall under lateral forces (Casagrande et al. 2012). Therefore, this section compares the stiffness of the walls tested in this research, the walls tested by Guíñez et al. (Guíñez, Santa María & Almazán 2019), and the design values provided by the SDPWS standard (American Wood Council 2015). The SDPWS estimations were obtained through Equation 3-1 below which takes into account the shear, bending, and rocking components of displacement. This equation was derived by Guíñez et al. (Guíñez, Santa María & Almazán 2019) based on Equation 4.3-1 provided in the SDPWS standard to compute the lateral wall deflection for elastic analysis.

$$K_{SDPWS} = \left(\frac{2h^3}{3EAb^2}+\frac{h}{bnG_a}+\frac{h^2}{K_{hd}bb'}\right)^{-1} \quad \text{Eq. 3-1}$$

where:

h = wall height = 2440 mm

E = elasticity modulus of studs (value for radiata pine according to (INN 2014)) = 10000 MPa

A = area of end-studs = 35×138×$N_{EndStuds}$

$N_{EndStuds}$ = Number of end-studs = 8

b = wall width = 2440 mm

n = sheathed wall faces = 2

G_a = apparent wall shear stiffness (Table 4.3A (American Wood Council 2015))

K_{hd} = stiffness of the hold-down system

b' = distance between the rod in tension and end-studs in compression = 2116 mm

Equation 3-1 has been properly adapted from the SDPWS standard to be used with any consistent set of units. For the walls under analysis, the apparent wall shear stiffnesses G_a were 3.85 kN/mm and 7.36 kN/mm (22 kips/in and 42 kips/in) for nail spacings of 100 and 50 mm, respectively, obtained from Table 4.3A provided in the SPDWS standard (American Wood Council 2015). For continuous rod hold-downs, the stiffness K_{hd} can be computed as:

$$K_{hd} = \frac{E_{steel}A_{net}}{L_{rod}} \quad \text{Eq. 3-2}$$

where:

E_{steel} = modulus of elasticity of steel = 200000 MPa

A_{net} = net tensile area of the rod

L_{rod} = length of the rod = h + h_{floor} = 2440 + 160 = 2600 mm

The net tensile area of the rod can be calculated employing Equation 3-3 provided in Table 7-17 of the AISC standard (AISC 2011):

$$A_{net} = 0.7854\times\left(d - \frac{0.9743}{n}\right)^2 \quad \text{Eq. 3-3}$$

where:

d = rod diameter in inches

n = threads per inch (see Table 7-17 (AISC 2011))

Figure 3-13(a) shows the secant stiffness measured for a 0.1% drift (2.4 mm) for the walls under analysis. Results show that reducing the nail spacing from 100 to 50 mm increases the initial stiffness of the wall by 21.7% (from 6.19 to 7.53 kN/mm), since more sheathing-to-framing connections contribute to the lateral shear deformation of the wall. The stiffness also augments by 48.4% and 5.0% (from 4.17 to 6.19 and from 7.17 to 7.53 kN/mm) when the rod diameter increases from 12.7 to 44.5 mm and from 31.7 to 44.5 mm, respectively; an increment somewhat proportional to the rod area. Employing continuous rod hold-downs shows not to have a significant impact on the initial stiffness when compared to using discrete hold-downs, as it can be noted for most of the tests. However, it does have an important effect at drifts levels larger than 0.1%. For instance, average increases of 23.5%, 31.9%, and 35.3% on the secant stiffness were found for drifts of 0.5%, 1%, and 2%, respectively.

Regarding the design values, results show that Equation 3-1 from the SDPWS guidelines overestimates the stiffness by 10.5%, 44.9%, and 57.2% for specimens C-100-44, C-50-32, and C-50-44, respectively. For the specimen C-100-12, the stiffness was underestimated by 19.5%. These results are consistent and coherent with those reported by previous investigations (Guíñez, Santa María & Almazán 2019) for wood frame specimens employing discrete hold-downs.

Figure 3-13(b) shows the secant stiffness of each test as a function of the lateral drift, calculated for each hysteresis cycle in the loading protocol. Very large initial stiffnesses are observed at the beginning of the tests, which are mainly due to the friction and contact forces between the different elements that make up the wall. All plots show that, as the cycles progress and the deformation increases, the wall stiffness degrades significantly. For large drifts, the walls reached a residual stiffness of about 1 to 2 kN/mm. This is equivalent to 15-20% of the initial stiffness. The degradation rate is similar for all wall specimens, with a steep drop up to drifts of about 0.5%, followed by a steady decay until the end of the test. Interestingly, both specimens with 50 mm nail spacing showed a pretty similar stiffness throughout the test despite employing different rod diameters. This highlights that, when strong anchorage systems are employed (C-50-32 and C-50-44 specimens), the lateral deformation of the wall is mostly due to shear.

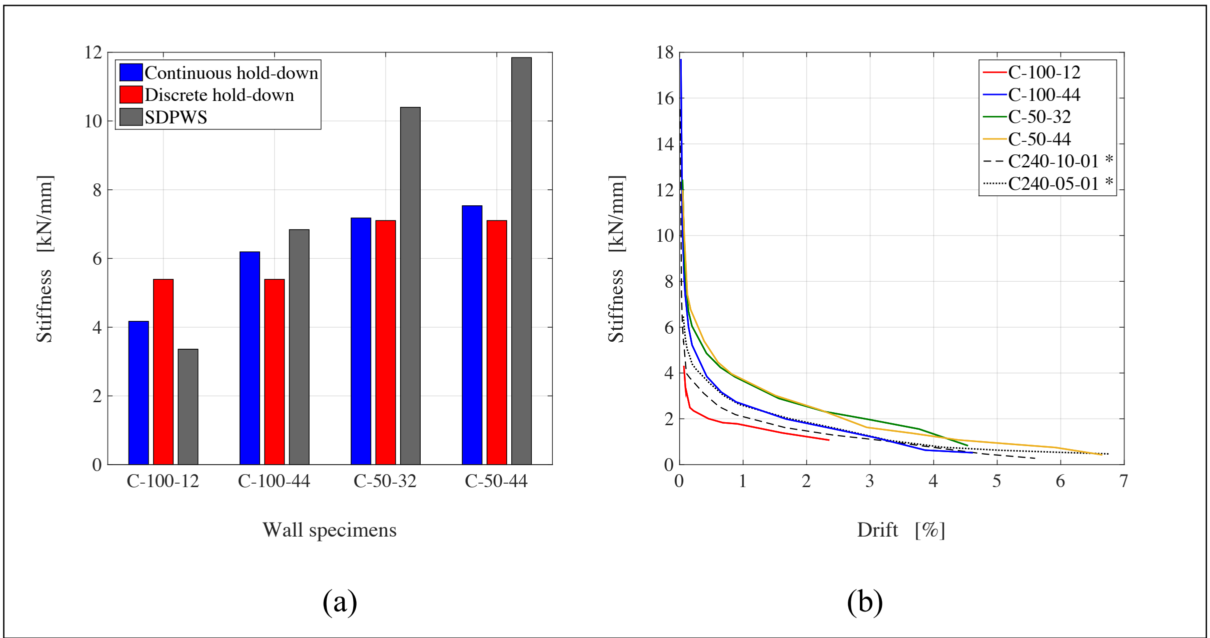

Figure 3-13. Comparison of measured stiffnesses: (a) initial stiffness for a lateral drift of 0.1%, and (b) stiffness degradation as a function of the lateral drift. In Figure 3-13(b), the walls with discrete hold-downs are marked with an asterisk.

3.3.6. Deformation and ductility

In wood frame walls, deformation capacity and ductility are governed mainly by the mechanical properties of the sheathing-to-framing connections. However, the anchorage system may have a significant effect on the wall response, since a poor behavior of it could lead to low performance of the specimen under large demands. To study this effect, the ultimate displacement D_u and ductility μ were calculated for each wall and analyzed in this section. The D_u parameter was computed as the displacement related to a force drop of 20% or 0.8 F_{max}. For the ductility value μ, the yield force F_y and displacement D_y were estimated employing the equivalent energy elastic-plastic EEEP method, following the guidelines of the ASTM E2126 standard (ASTM 2018). The EEEP method defines an elastic-plastic curve that encloses the same area as the test response (average envelope) employing an initial linear stiffness computed for 0.4 F_{max}, as Figure 3-14(a) illustrates. Then, the ductility was calculated as $\mu = D_u/D_y$.

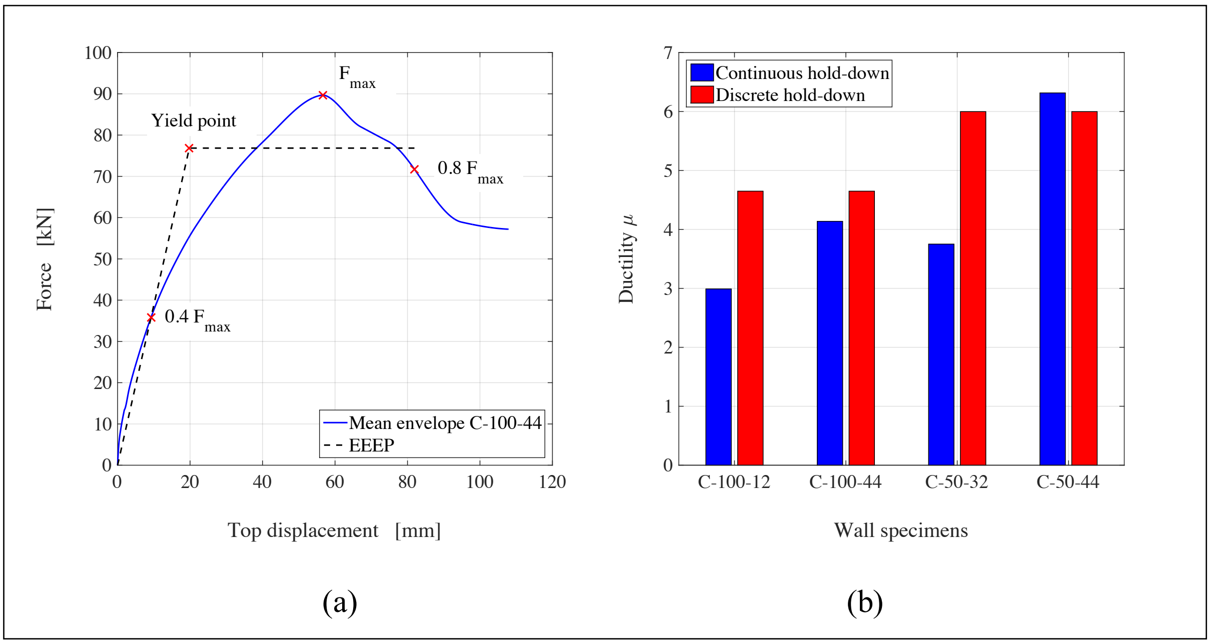

Figure 3-14. Ductility analysis: (a) EEEP approach for the C-100-44 specimen, and (b) ductility values for the walls in this research and those tested by Guíñez et al. (Guíñez, Santa María & Almazán 2019).

Figure 3-14(b) shows the ductility results for the different walls under study. Specimen C-100-12 had a low ductility (2.99) due to the failure of the anchorage system, as discussed before.

However, when the rod diameter increased from 12.7 to 44.5 mm, the ductility increased by 38.3% (up to 4.14) as noted for the C-100-44 wall. Specimen C-50-32 also showed a relatively low μ value (3.75) due to the failure of a full line of nails at the central studs just after reaching the peak force. This phenomenon is illustrated in Figure 3-6(b). As shown by a red circle in Figure 3-7(c), the force suddenly dropped because of this failure. However, the specimen C-50-44, which employed a larger rod diameter, showed a greater ductility (6.32) with a large nonlinear displacement capacity and a high residual force. On the other hand, results from the specimens C-100-44 and C-50-44 showed that there is not a remarkable difference in the ductility between using discrete or continuous hold-downs, while for the specimens C-100-12 and C-50-32 ductility dropped by about 35% for continuous hold-downs. It should be noted that this decrease was due to the specific problems aforementioned for each test and is not representative of the nonlinear response of wood frame shear walls.

3.3.7. Energy dissipated

The energy dissipated by a structural element during reversed loading is a good indicator of its seismic performance and capacity to dissipate the kinetic energy induced by earthquakes. For wood frame walls, an optimal behavior is reached when the energy is mostly dissipated by the sheathing-to-framing connectors under shear deformation, while the framing and the anchorage system remain in the elastic regime. Figure 3-15 shows the energy dissipated (cumulative) by each wall in this research, computed as the area enclosed by the cycles of hysteresis along the loading protocol. As expected, the specimens C-50-32 and C-50-44 were capable of dissipating more energy throughout the test because more nails were undergoing shear deformation in each wall. The C-50-44 specimen dissipated slightly more energy than the C-50-32 one (11.3% more, calculated at a 4% drift), which may indicate an influence of the rod diameter on the energy dissipation of the wall.

The C-100-12 specimen exhibited the lowest energy dissipation of all tests. This is explained because, due to the small rod diameter, a great fraction of its top displacement was due to rocking of the wall and not to shear deformation of the sheathing-to-framing connections. Interestingly, the walls tested by Guíñez et al. (Guíñez, Santa María & Almazán 2019) also showed a low energy dissipation compared to the walls of this research. This highlights the influence of the anchorage system and the extra connections added by the sturdy end-studs on the performance of the wall under large nonlinear deformations.

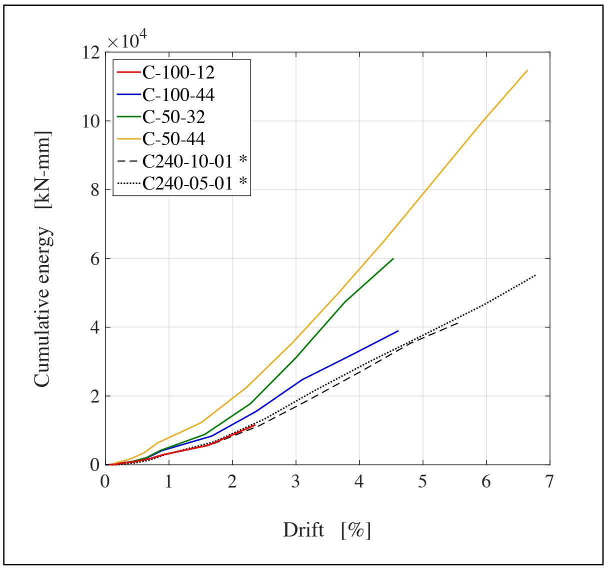

Figure 3-15. Energy absorbed by specimens with continuous and discrete hold-downs as a function of the lateral drift. The walls with discrete hold-downs are marked with an asterisk.

3.3.8. Equivalent viscous damping

The equivalent viscous damping ξ_{eq} (EVD) is a factor commonly used to quantify the capacity of structural elements to dissipate energy under cyclic or reversed loading. It may also be employed to calculate the damping ratio of the element when it is considered as an external damper. The EDV is computed as the ratio of the hysteretical energy dissipated by the test in one reversed cycle to the energy dissipated by a viscous damper during a sinusoidal loop of equivalent amplitude. For a given cycle *i*, the EVD is calculated employing the following expression (Guíñez, Santa María & Almazán 2019):

$$\xi_{eq,i} = \frac{E_{H,i}}{2\pi\left(0.5\ d_i^+ F_i^+ + 0.5\ d_i^- F_i^-\right)} \qquad \text{Eq. 3-4}$$

where $E_{H,i}$ represents the energy dissipated during the cycle *i*, computed as the area enclosed by the hysteresis loop, d_i^+ is the displacement corresponding to the maximum force F_i^+, and d_i^- is the displacement corresponding to the maximum force F_i^-. Figure 3-16(a) illustrates these variables.

Figure 3-16(b) shows the EVDs for the walls tested in this research as a function of the lateral drift. It can be observed that all specimens exhibited high damping ratios (almost up to 0.45) at the beginning of the test, then dropping to a steady value of 0.12 to 0.17 for lateral drifts larger than about 0.5%. The same behavior is observed for the walls with discrete hold-downs. The characteristic EVD values, defined as the 10th percentile EVD of all cycles for a given specimen, ranged from 0.09 to 0.12, with an average of 0.11. These values are usual for wood frame walls as reported by previous investigations (Guíñez, Santa María & Almazán 2019; Jayamon, Line & Charney 2018).

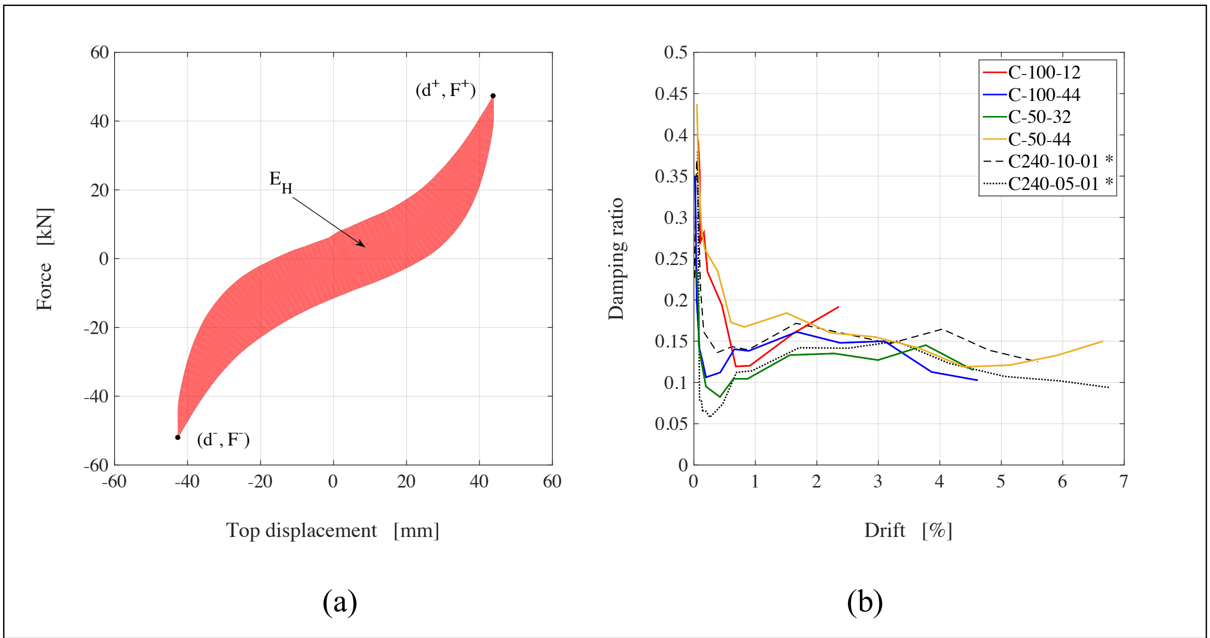

Figure 3-16. (a) Hysteresis loop for a loading cycle, and (b) equivalent viscous damping EVD ratios for different walls as a function of the lateral drift. The walls with discrete hold-downs are marked with an asterisk.

3.3.9. Design implications

Results discussed in previous sections show that the provisions of the SDPWS standard (American Wood Council 2015) may have some inaccuracy levels when estimating the mechanical properties of wood frame walls with continuous rod hold-downs. This has important implications for everyday practitioners of timber engineering since linear methods commonly used for structural design are developed based on the values computed from this standard. Two main aspects are worth analyzing in this section: underestimation of strength and overestimation of stiffness.

Wall strengths were underestimated by 39.9% (on average), indicating that the unit shear capacities v_s provided in the standard are below the real behavior of wood frame elements. Additionally, such estimations still need to be modified by the ASD or LRFD factors to accomplish with standard design methodologies, increasing, even more, the conservatism of the final structure. This places timber buildings in a complex situation since structural designs will need additional walls, sheathing panels, and nail connections to achieve the required seismic demands at a given zone. Therefore, architectural flexibility and cost-effectiveness are significantly affected, impacting the competitiveness of timber structures against traditional building systems. However, the rationale behind this strength underestimation may be explained by two reasons.

First, since the uncertainty of the mechanical properties of wood is high compared to that of other materials (Jayamon, Line & Charney 2015; Yin & Li 2010), codes and standards apply considerable safety factors to guarantee that timber structures meet the minimum requirements for a good performance. Second, the uncertainty of the seismic demand is high too (Lee & Rosowsky 2006; Ellingwood et al. 2004), forcing design standards to take conservative approaches when designing for earthquake loads. For better-known demands with low variability, the design values are less conservative. For instance, when designing wood frame structures for wind loads, the SDPWS standard (American Wood Council 2015) defines unit shear capacities v_s that are 40% higher compared to those for seismic loads. This way the standard assures the resilience of new timber structures in a wide spectrum of possible scenarios.

On the other hand, initial wall stiffnesses were overestimated by the SDPWS provisions. For a 0.1% drift, the values provided by the standard were 37.5% higher (on average) than the values measured from the tests. If larger drifts are analyzed, the overestimation is even higher. This indicates that the apparent wall shear stiffnesses G_a provided by the standard may be inaccurate. Therefore, the actual deformation of the structure under the lateral design forces will be larger than expected, compromising the performance and resilience of the building. This could result in structural and nonstructural damage even during moderate earthquakes if the inter-story drifts exceed certain critical values. For instance, for the performance levels of immediate operation IO, life safety LS, and collapse prevention CP, the FEMA 356 provisions (FEMA 2000) recommend limiting lateral drifts to 1%, 2%, and 3%, respectively. Moreover, overestimating the stiffness of the walls will also overestimate the actual stiffness of the full structure, resulting in a shorter fundamental period. This may lead to a miscalculation of the design base shear if spectrum-based methods are employed to estimate the lateral forces on the structural system. Additional research is necessary in the future to support the scope of these findings.

3.4. NONLINEAR MODELING OF WOOD FRAME WALLS WITH CONTINUOUS ROD HOLD-DOWNS

Numerical models that precisely reproduce the nonlinear behavior of structural systems are a powerful tool to extend the scope of the research beyond the lab, since they allow overcoming the limitations (physical and economic) of experimental testing. Therefore, numerical models help researchers and practitioners to manage some of the uncertainties associated with testing full-scale structures, and provide insight into test procedures, results, and findings. However, numerical models usually need to be validated against real specimens to prove the accuracy levels expected for structural engineering, especially when new or novel systems are under analysis.

Aiming at further development of wood frame walls with continuous rod hold-downs, this section presents a numerical model for the specimens in this chapter, validates its predictions against the experimental data of three tests (C-100-44, C-05-32, and C-05-44), and conducts further analyses to gain knowledge on the nonlinear response of wood frame walls. It is worth noting that the model was not validated against the C-100-12 specimen because, as explained in previous sections, its failure mode was due to tensile fatigue of the anchorage rod leading to a premature and non-ductile collapse of the wall.

The aforementioned model was developed in the MATLAB M-CASHEW software (Pang & Hassanzadeh 2012) following the guidelines described in Chapter 2. Inner and end-studs were modeled employing Euler-Bernoulli elastic frame elements with 3 degrees-of-freedom DOFs per node and considering a modulus of elasticity E equal to 11.4 kN/mm^2. A corotational approach was employed in the numerical formulation of the frame elements.

Sheathing-to-framing connections were incorporated in the model by means of link elements with 3 DOFs per node. For the X- and Y-direction, the MSTEW nonlinear hysterical model developed by Folz and Filiatrault (Folz & Filiatrault 2001) was employed, while a zero stiffness spring was used for the rotational component. The X and Y springs incorporated the true-oriented connection model proposed by Pang and Hassanzadeh (Pang & Hassanzadeh 2012) in order to avoid an overestimation in capacity and stiffness as reported by previous researchers (Folz & Filiatrault 2001; Judd & Fonseca 2005). The parameters of the MSTEW model were obtained by nonlinear functional minimization methods from the experimental data on sheathing-to-framing connectors reported by Jara and Benedetti (Jara & Benedetti 2017) and Section 2.3.2.

For the OSB sheathing panels, 5-DOF shear rectangular elements were employed: two DOFs for rigid-body translations, one DOF for rigid-body rotation, and two DOFs for in-plane shear deformation angles. A shear modulus G equal to 1.3 kN/mm^2 (as discussed in Chapter 2, Section 2.2) was considered in the numerical formulation of the panels. The continuous rod hold-downs were modeled with link elements (3-DOF) that fastened the bottom timber plate to the foundation. The positive Y-direction was calibrated based on the linear approximations of the anchorage response shown in Figure 3-9 (red dashed lines). The negative Y-direction had infinite stiffness to replicate the compression contact of the bottom plate of the wall and the reaction steel beam. The X-direction and the rotational component had a zero stiffness spring.

The analyses conducted with the model were displacement-controlled employing a norm displacement increment test as convergence criteria (Pang & Hassanzadeh 2012), with 20 iterations per step and a residual tolerance equal to 1e-6 kN. Monotonic analyses were carried out by applying 0.5 mm displacement increments at the top of the wall, while cyclic analyses employed the data measured from the tests as top displacement input. A thorough description of the modeling approach can be found in Chapter 2. Figure 3-17(a) shows a schematic representation of the model described above.

Figures 3-17(b), 3-17(c) and 3-17(d) show the cyclic results of the test and model for the specimens C-100-44, C-50-32, and C-50-44, respectively. The model properly captured the nonlinear behavior of the wall, showing good accuracy levels when predicting strength, stiffness, and post-peak deformation. Besides, phenomena associated with the non-linear response of wood frame shear walls such as pinching, stiffness degradation, and force degradation, were also well reproduced by the model.

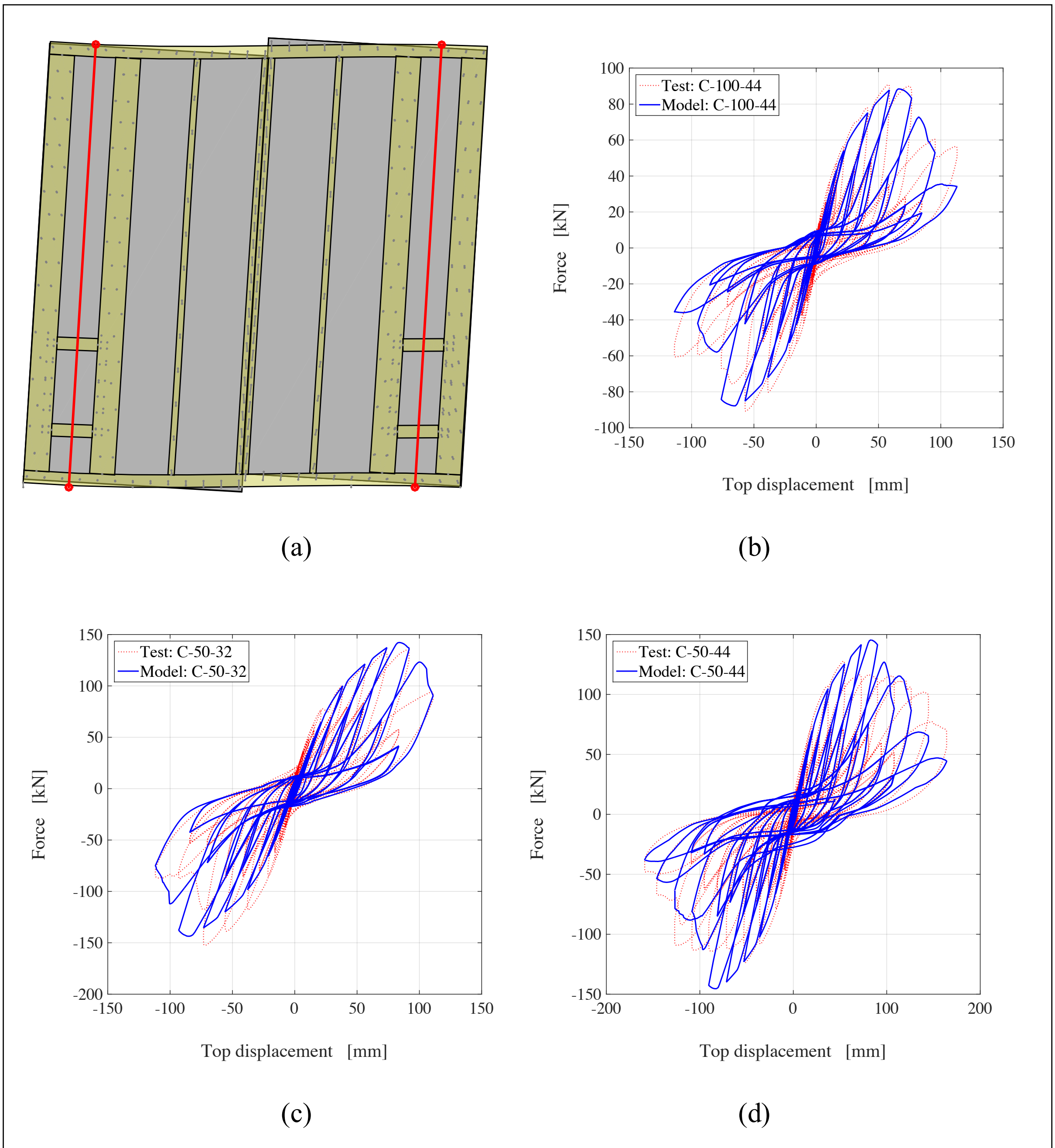

Figure 3-17. (a) Schematic representation of the numerical model developed for the walls under investigation, (b) comparison between model predictions and test results for the specimen C-100-44, (c) for the specimen C-50-32, and (d) for the specimen C-50-44.

Employing the cyclic results from the nonlinear springs employed for the sheathing-to-framing connectors, an analysis of the maximum deformation of nails as a function of their location in the wall was conducted. Results are presented in Figure 3-18(a) for the specimen C-100-44 and Figure 3-18(b) for the specimen C240-10-01 tested by Guíñez et al. (Guíñez, Santa María & Almazán 2019). Figure 3-18(a) shows that for walls with continuous rods, the damage is mostly condensed in the nails at the central studs, while the nails at the end-studs remain almost undamaged and elastic. This result is consistent with the damage observed during the test and reported in Figures 3-6(d), 3-6(f), and 3-6(g). Such behavior is explained because of the large number of sheathing-to-framing connections at the end-studs, providing a great redundancy of nails and increasing the shear stiffness at this zone. An important deformation demand is also noted at the joints between the central studs and the top and bottom plates, which explains the detachment of these elements observed during the tests. This overall response is somewhat desirable since it guarantees the integrity of the specimen at the anchorage zone, avoiding damage of the rods due to excessive distortion of the wall. On the other hand, Figure 3-18(b) shows that the damage is more evenly distributed throughout the wall for the specimens with discrete hold-downs. For these walls, deformation demands are in the same range for central and end-studs, providing a more ductile response towards the end of the test and avoiding a full failure of the elements due to a damage concentration.

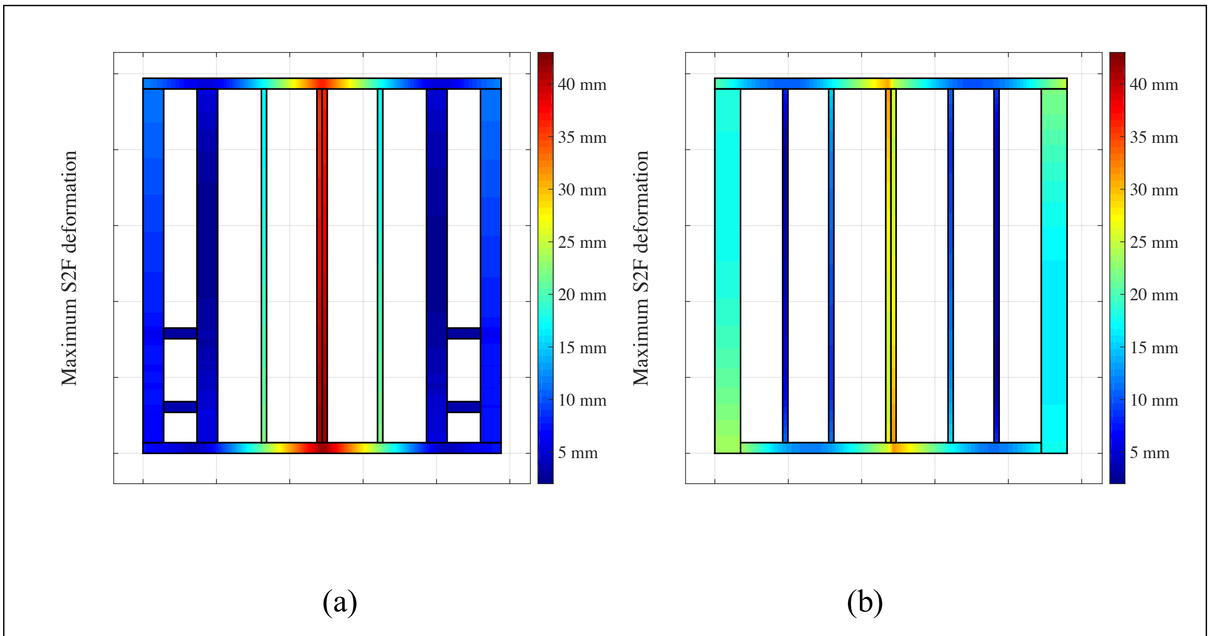

Figure 3-18. Deformation demand contour plots: (a) C-100-44 wall with continuous rod hold-downs, and (b) C240-10-01 wall with discrete hold-downs (Guíñez, Santa María & Almazán 2019).

Figure 3-19(a) shows three monotonic force-displacement plots for the specimen C-100-44: the average envelope calculated from the cyclic test, a pushover analysis from the numerical model presented above, and a monotonic analysis from a numerical model without the rod installation window. The latter was included because it is of relevant interest to study the influence of the installation window on the lateral behavior of the wall, since its sheathing-to-framing connectors (about 35 per window) may have an impact on the stiffness and strength of the specimen. First, results demonstrate that the numerical model was also able to reproduce the envelope response of the test, accurately predicting the maximum strength, force degradation, and ultimate displacement. Second, it is interesting to note that the rod installation window does not have a significant impact on the lateral behavior of the wall. When the window was removed, the strength of the wall decreased by 4.5%, and the stiffness only decreased slightly for drifts larger than 20 mm. Figure 3-19(b) shows the distribution of the connection damage on the wall when the rod installation window is removed. When compared with the results in Figure 3-18(a), it is noted that damage distribution did not change significantly, showing only a mild increase (~22%) in the deformation demand at the end-studs. Such results demonstrate that the rod installation window is not responsible for the new damage pattern found in this study for walls with continuous rod hold-downs.

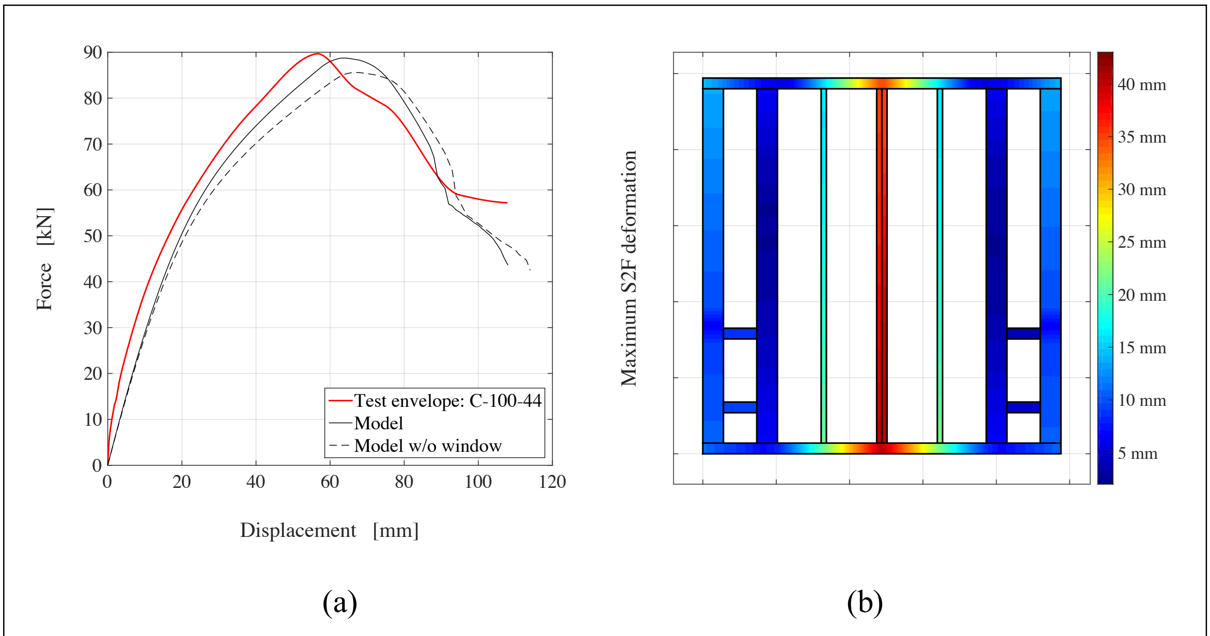

Figure 3-19. (a) Monotonic results for the test envelope, numerical model, and numerical model without the rod installation window, and (b) deformation demand contour plot for the specimen without rod installation windows.

CHAPTER FOUR

GROUND MOTIONS FOR APPLICATION OF THE FEMA P-695 METHODOLOGY IN SUBDUCTION ZONES

CHAPTER DISCLAIMER

The content, methodology, results, and figures presented in this chapter are based on the following article:

- Estrella X, Guindos P, Almazán J. Ground motions for FEMA P-695 application in subduction zones. Latin American Journal of Solids and Structures 2019; 16:1–19.

4.1. INTRODUCTION

Ground motion selection plays a fundamental role when evaluating the seismic performance of structural systems through dynamic analyses, because at the same time that the records have to reflect both the seismic hazard and the shallow geology of the area under study, they also have to consider the randomness and uncertainty inherent in the seismic demand (Iervolino, Maddaloni & Cosenza 2008). Generally speaking, there are three different ways to obtain seismic records: (1) artificially generated waveforms (spectrum-compatible accelerograms); (2) simulated accelerograms from seismological models; and (3) natural records. Although these three approaches have been widely used in seismic engineering, previous research has shown that natural accelerograms are more suitable than spectrum-compatible ones and more readily available than synthetic records derived from seismological fault models (Bommer & Acevedo 2004).

The methodology employed in Chapter 1 for the rational quantification of seismic performance factors and proposed by the Federal Emergency Management Agency (FEMA) employs incremental dynamic analyses (IDA) as a tool to evaluate the performance and collapse capacity of structural systems. An IDA analysis (Vamvatsikos & Cornell 2002) consists of multiple response-history analyses for a ground motion with increasing intensity until the structure reaches the collapse or a given limit state. Due to the variability in the seismic demand, this process has to be repeated for a set with a statistically significant number of ground motions such that it allows determining the average intensity that causes collapse as well as evaluating the variability of the set employed. Given this context, the FEMA P-695 (FEMA 2009) methodology provides two sets of ground motions to be used in the analyses, the first with 22 pairs of far-field accelerograms recorded at sites located more than 10 km from the fault rupture, and the second with 28 pairs of near-field ground motions recorded at sites located less than 10 km from the fault rupture, which is subdivided into 14 impulsive and 14 non-impulsive records. The accelerograms were extracted from the PEER NGA database (PEER 2002), and a detailed description of their selection can be found in the report published by FEMA (FEMA 2009).

Both the far-field and near-field sets consist of records from shallow crustal earthquakes, which are representative of areas in the Western United States. Therefore, they do not include strong motion records from Central and Eastern United States earthquakes, or from deep subduction earthquakes such as those expected in Japan, New Zealand, or in areas on the Pacific Coast in South America. Subduction earthquakes are known to have longer durations than shallow crustal ones, to release more energy, and to induce more damage even to buildings designed with modern codes. Duration of seismic records is a key factor when evaluating the collapse capacity of structural systems prone to degradation (Chandramohan 2016; Foschaar, Baker & Deierlein 2012; Raghunandan & Liel 2013). Furthermore, ground motions related to deep subduction earthquakes are also known to have, on average, stronger accelerations of greater length. For instance, a study conducted by Chandramohan et al. (Chandramohan, Baker & Deierlein 2016) showed that the estimated median collapse capacity is 29% lower when using a long-duration ground motion set compared to a short-duration set. Raghunandan et al. (Raghunandan, Liel & Luco 2015) also found that the median collapse capacity of ductile buildings designed with modern codes is 40% lower when subjected to subduction ground motions compared to crustal earthquakes. Interestingly, the researchers found that although the duration of the records has no impact on the peak structural response, long-duration ground motions impose higher energy demands and are more damaging for structural systems.

A careful selection of the set to employ allows for achieving the same reduction of bias and variation in the structural response that would be obtained by using more complex indicators of the record intensity, while still allowing the use of simple tools for processing the ground motions, such as elastic response spectra (Baker & Cornell 2005; Shome & Cornell 1999). For this reason, several methodologies have been proposed in the literature to select accelerograms for non-linear analyses, which are based on different selection criteria such as magnitude, distance to fault, soil profile, strong motion duration, seismotectonic environment, acceleration-to-velocity ratio, among others (Katsanos, Sextos & Manolis 2010). More complex methodologies have also been developed, such as record selection based on spectral matching (Bommer, Acevedo & Douglas 2003), ground motion intensity measures (Cornell 2005), the spectral shape (Baker & Cornell 2006), or the conditional mean spectrum (Baker 2010). The objective behind all these approaches is to choose ground motions that represent as accurately as possible the seismic demand that buildings will be subjected to during an earthquake at a given zone. Regarding the application of the FEMA P-695 methodology, there are previous investigations in the current literature that have extended its scope to areas prone to earthquakes other than shallow crustal ones. For instance, AlHamaydeh et al. (AlHamaydeh et al. 2011), Bezabeh et al. (Bezabeh, Tesfamariam & Popovski 2016), Vielma and Cando (Vielma & Cando 2017), and Ccanchi and Taboada (Ccanchi & Taboada 2018) developed sets of ground motions to apply the FEMA P-695 methodology in zones prone to subduction earthquakes. However, such sets are not suitable to be used in research projects other than the ones for which the ground motion sets were developed for, because either they are not consistent with guidelines of the methodology, are site-specific, or do not take into account the effects of the spectral shapes.

The lack of a well-established set of subduction ground motions restricts an extended and proper application of the methodology. Therefore, the investigation in this chapter proposes a set of ground motions for the application of the FEMA P-695 methodology in subduction zones, as well as the normalization factors for each accelerogram and the spectral shape factors (SSF) to adjust the collapse margin ratios obtained from incremental dynamic analyses.

4.2. GROUND MOTION SELECTION

A set of criteria was established before the selection of the ground motions, which is consistent with that proposed in the FEMA methodology (FEMA 2009) and intends to provide an objective selection of the records. Each criterion is listed below followed by a brief description.

- **Earthquake magnitude.** A minimum magnitude of $M \geq 6.5$ was established as a requirement. This is because large-magnitude earthquakes have strong ground motions of greater duration which release more energy. As a result, higher risks of structural collapse are expected. Earthquakes of lesser magnitude ($M < 6.5$) can cause significant damage to structural and non-structural elements. However, they are unlikely to cause the collapse of structural systems designed with modern requirements (FEMA 2009).

- **Fault type.** Due to the complex characteristics of the shallow Earth's crust, most subduction areas are also threatened by potentially dangerous shallow crustal earthquakes. For instance, the city of Santiago (Chile) is exposed to both the ongoing subduction of the Nazca Plate under the South American Plate and the San Ramón fault (a thrust fault across the city). Therefore, to adequately embrace the different seismic scenarios, ground motions from shallow crustal earthquakes (strike-slip and thrust) and deep subduction earthquakes have been selected for this set, noting that there are few available records of the latter for engineering use.

- **Distance to the fault.** A minimum distance of 10 km has been considered, which is consistent with the concept of far-field zone proposed in the design maps for the maximum considered earthquake by the ASCE 7-16 standard (ASCE 2016).

- **Components.** Records with two horizontal orthogonal components were selected. The existence of a vertical component was not considered as a selection criterion.

- **Intensity measures.** Limits of peak ground acceleration (PGA) > 0.2 g and peak ground velocity (PGV) > 15 cm/s were set for each of the orthogonal components. Although these values are arbitrary, it is considered that they represent the structural damage limit for buildings designed using modern seismic codes (FEMA 2009).

- **Number of records per earthquake.** To avoid bias towards more recent events that have been better and more widely recorded, a limit of two records per earthquake was set in case there were several ones matching with the selection criteria.

- **Accelerogram correction.** Only ground motions with instrumental and baseline correction were included in the set.

- **Soil conditions.** Ground motions recorded on soft rock (Site Class C) or stiff soil (Site Class D) sites were included.

Based on the aforementioned criteria, a set of 26 pairs of ground motions (horizontal components) was developed, which were obtained from reports published by seismological agencies of different countries. The robustness of this number of ground motions is validated later in this chapter. To avoid bias towards a particular seismic region, records were chosen regardless of the country of origin. Table 4-1 shows a summary of the proposed set as well as additional information of the ground motions. The normalization and scaling process of the records for use in incremental dynamic analyses are standardized for the application of the FEMA P-695 methodology. The details of these processes are described subsequently. Table 4-2 shows information about PGA, PGV, 1-second spectral acceleration, significant duration $Ds_{5\text{-}75}$, lowest usable frequency, and fault type of the selected ground motions.

Table 4-1. General information about the ground motions selected for the set.

#	Earthquake				Recording station	
	Name	**Magnitude**	**Year**	**Country**	**Name**	**Source**
1	Arequipa	8.4	2001	Peru	Arica Costanera	Renadic
2	Arequipa	8.4	2001	Peru	Poconchile	Renadic
3	Cape Mendocino	7.0	1992	USA	Rio Dell Overpass	CDMG
4	Coquimbo	8.4	2015	Chile	C11O	CSN
5	Coquimbo	8.4	2015	Chile	C260	CSN
6	Chi-Chi	7.6	1999	Taiwan	TCU045	CWB
7	Duzce	7.1	1999	Turkey	Bolu	ERD
8	Iquique	8.2	2014	Chile	T03A	CSN
9	Iquique	8.2	2014	Chile	T10A	CSN
10	Kaikoura	7.8	2016	New Zealand	CULC20	EQC
11	Kobe	6.9	1995	Japan	Nishi-Akashi	CUE
12	Landers	7.3	1992	USA	Coolwater	SCE
13	Las Colinas	7.7	2001	El Salvador	EX01001U	UCA
14	Loma Prieta	6.9	1989	USA	Capitola	CDMG
15	Maule	8.8	2010	Chile	Angol	Renadic
16	Maule	8.8	2010	Chile	StgoCentro	Renadic
17	Mejillones	6.7	2007	Chile	Mejillones Puerto	Renadic
18	Northridge	6.7	1994	USA	Canyon Country	USC
19	Pedernales	7.8	2016	Ecuador	AMNT	RENAC
20	Pedernales	7.8	2016	Ecuador	APO1	RENAC
21	Superstition Hills	6.5	1987	USA	El Centro Imp. Co.	CDMG
22	Tarapaca	7.9	2005	Chile	Cuya	Renadic
23	Tocopilla	7.7	2007	Chile	Papudo	Renadic
24	Tocopilla	7.7	2007	Chile	Tocopilla	Renadic
25	Tohoku	9.0	2011	Japan	IBR011	NIED
26	Tohoku	9.0	2011	Japan	IBR012	NIED

The ground motions were selected such that 2/3 were subduction records and 1/3 crustal ones. Hence, the proposed set includes eighteen records from subduction earthquakes and eight from shallow crustal earthquakes, of which three are from thrust faults and five from strike-slip faults. A period of approximately 30 years has been covered, with information recorded from 1987 until the recent earthquake in Kaikoura (New Zealand) in 2016. Earthquake magnitudes range from M = 6.5 for the Superstition Hills (USA) strike-slip earthquake, to M = 9.0 for the Japanese earthquake of Tohoku in 2011. The average magnitude of the set is M = 7.8.

Table 4-2. Information about PGA, PGV, 1-second spectral acceleration (ξ = 5%), significant duration $Ds_{5\text{-}75}$, lowest usable frequency, and fault type.

#	PGA [g]		PGV [cm/s]		Sa_{1s} [g]		$Ds_{5\text{-}75}$ [s]		Lowest freq [Hz]	Fault type
	C1	C2	C1	C2	C1	C2	C1	C2		
1	0.34	0.27	25.22	24.65	0.38	0.33	9.20	10.42	0.15	Subduction
2	0.25	0.26	29.57	29.10	0.33	0.27	9.77	9.62	0.15	Subduction
3	0.39	0.55	43.81	41.88	0.54	0.39	4.25	1.92	0.07	Thrust
4	0.83	0.71	36.60	42.83	0.29	0.17	17.02	20.79	0.01	Subduction
5	0.36	0.23	34.21	24.62	0.56	0.23	21.90	28.50	0.01	Subduction
6	0.51	0.47	39.07	36.70	0.43	0.30	8.74	7.43	0.05	Thrust
7	0.73	0.82	56.44	62.10	0.72	1.16	2.62	1.47	0.06	Strike-slip
8	0.58	0.61	35.10	18.82	0.27	0.14	25.11	27.76	0.01	Subduction
9	0.66	0.78	37.55	47.99	0.52	0.45	22.50	21.11	0.01	Subduction
10	0.22	0.25	22.95	33.06	0.22	0.30	21.89	20.80	0.20	Subduction
11	0.51	0.50	37.29	36.62	0.31	0.29	3.97	4.48	0.13	Strike-slip
12	0.28	0.42	25.65	42.35	0.20	0.36	5.93	3.80	0.13	Strike-slip
13	0.30	0.28	25.81	17.88	0.45	0.40	9.59	11.07	0.20	Subduction
14	0.53	0.44	35.01	29.22	0.46	0.28	5.74	5.55	0.13	Strike-slip
15	0.70	0.93	37.65	34.31	0.46	0.21	30.23	23.03	0.15	Subduction
16	0.21	0.31	21.92	25.65	0.27	0.22	23.05	20.31	0.15	Subduction
17	0.39	0.47	32.33	17.97	0.19	0.09	5.41	4.47	0.15	Subduction
18	0.41	0.48	42.97	44.91	0.38	0.63	3.15	2.94	0.13	Thrust
19	0.52	0.40	43.10	55.27	0.44	0.39	5.79	7.38	0.20	Subduction
20	0.38	0.32	47.57	42.55	0.30	0.30	5.73	5.62	0.20	Subduction
21	0.36	0.26	46.36	40.87	0.31	0.25	7.01	7.59	0.13	Strike-slip
22	0.44	0.45	18.51	18.42	0.08	0.10	12.46	15.67	0.15	Subduction
23	0.30	0.42	16.15	24.63	0.08	0.09	20.16	19.00	0.15	Subduction
24	0.50	0.59	20.89	21.53	0.14	0.18	12.45	11.62	0.15	Subduction
25	0.34	0.35	25.31	41.76	0.29	0.58	41.66	36.10	0.20	Subduction
26	0.29	0.30	40.59	30.94	0.71	0.37	48.30	45.17	0.20	Subduction

Ground motion duration was characterized by means of the significant duration parameter $Ds_{5\text{-}75}$, since it has been widely used in the literature and previous research has shown that it is a suitable metric when analyzing the effect of ground motion duration on the response of structural systems (Foschaar, Baker & Deierlein 2012). The $Ds_{5\text{-}75}$ parameter is defined as the time interval over which a particular percentage of the following integral is accumulated

$$\int_0^{t_{max}} a(t)^2\, dt \qquad \text{Eq. 4-1}$$

where a(t) represents the ground acceleration, and t_{max} represents the length of the record. The average $Ds_{5\text{-}75}$ for the ground motions set proposed in this research is 14.56 s, while for the FEMA P-695 far-field set is 6.54 s. As can be noted, due to the intrinsic properties of the fault mechanism, the inclusion of subduction records increases the average significant duration of the set more than twice. As previous research has shown, this latter is expected to exert a statistically significant influence on structural collapse capacity (Chandramohan, Baker & Deierlein 2016).

Figure 4-1(a) shows the response spectra for the 26 pairs of ground motions, as well as the average spectrum of the set plus one and two standard deviations. The average spectral acceleration for short periods is about 0.8 g, and for $T_n = 1$ s it approaches 0.35 g. The transition from the constant acceleration domain to the constant velocity domain occurs approximately at $T_n = 0.5$ s. This result is consistent with the expected response for soft rock sites or rigid soils.

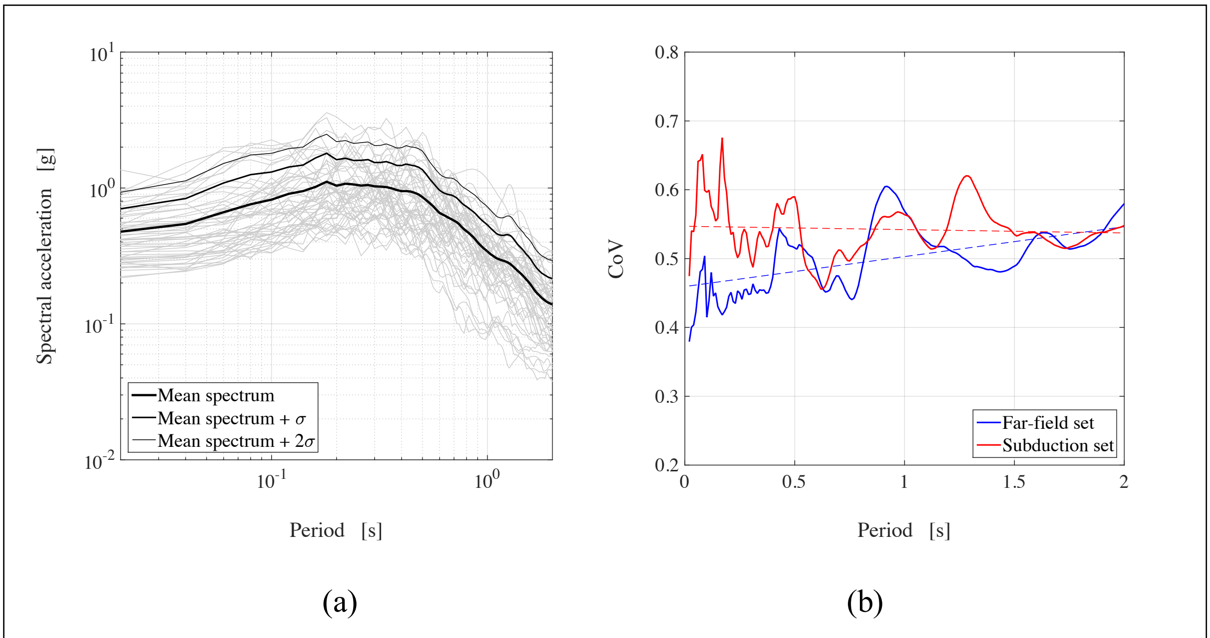

Figure 4-1. (a) Response spectra for the 26 pairs of ground motions and average spectrum of the set plus one and two standard deviations, and (b) coefficient of variation as a function of T for both subduction and far-field set.

The variability in the spectral acceleration of the proposed ground motion set was analyzed as a function of T and compared with that of the FEMA P-695 far-field set. The proxy to measure the variability was the coefficient of variation CoV, defined as the ratio between the standard deviation and the mean spectral acceleration for a given period T. Figure 4-1(b) shows that the CoV values are similar for both ground motion sets. For the new subduction set, it is about 0.55 for both short and long periods, whereas for the far-field set, it ranges from 0.45 for short periods to 0.55 for long ones. These variability levels are consistent with the dispersion values of typical ground motion prediction equations GMPE (Campbell & Borzorgnia 2003), and are due to the differences in site conditions, source, epicentral distance, and event magnitude.

4.3. NORMALIZATION AND SCALING

In order to determine the collapse capacity of structural archetypes through IDA analyses, it is necessary to follow a scaling protocol of the seismic records such that they increase their intensity progressively until a given limit state is reached. This is because there are almost no natural accelerograms that are capable of causing the collapse of modern structures (FEMA 2009). Before scaling the records, it is required to apply a normalization process, which is standard for the FEMA methodology P-695 and is detailed in the following paragraphs.

Normalization is a simple approach to eliminate the variability due to differences in the magnitude of the earthquake, type of fault, soil, and hypocentral distance, while still maintaining the intrinsic randomness of the records for an adequate probabilistic evaluation. Normalization is performed based on the geometric mean of the PGV of the two components, a parameter commonly used for the characterization of ground motions. In accordance with the FEMA P-695 methodology, the normalization factors are calculated as

$$NF_i = median(PGV_{set}) / PGV_i \qquad \text{Eq. 4-2}$$

where NF_i is the factor to be applied to each component of the *i* record, PGV_i is the geometric mean of the PGV values of the two components, and $median(PGV_{set})$ is the median of all the PGV_i values in the set. For the set in this investigation, $median(PGV_{set})$ = 32.73 cm/s. Depending on the PGV_i values, the record can be amplified if $NF_i > 1$ or reduced if $NF_i < 1$. Table 4-3 shows the NF_i factors as well as other properties of interest of the accelerograms after the normalization process.

Figure 4-2(a) shows the elastic response spectra of the 26 pairs of normalized ground motions, as well as the mean spectrum with one and two standard deviations. As observed, the average spectral acceleration for short periods is about 1.0 g, and for T_n = 1 s, it is about 0.30 g. The transition from the constant acceleration domain to the constant velocity domain occurs about T_n = 0.35 s. Interestingly, it has been found that a normalization process based on the geometric mean of the PGV is not very effective in reducing the variability of the ground motions set. Figure 4-2(b) shows the CoV for the subduction set before and after normalization. On average, there is a variability reduction of 13%; however, for periods shorter than 0.3 s the normalization procedure slightly increased the variability in the set. Similar results were found for the FEMA P-695 far-field set. Nevertheless, the calculation of collapse capacities is not affected by this issue, since each ground motion is scaled separately until collapse when performing incremental dynamic analyses.

Table 4-3. Normalization factors NF_i for each ground motion, as well as PGA, PGV and 1-second spectral acceleration (ξ = 5%) of both horizontal components after normalization.

#	Normalization factors	PGA [g]		PGV [cm/s]		Sa_{1s} [g]	
		C1	C2	C1	C2	C1	C2
1	1.31	0.44	0.36	33.11	32.36	0.50	0.43
2	1.12	0.27	0.29	32.99	32.48	0.36	0.30
3	0.76	0.29	0.42	33.48	32.00	0.41	0.30
4	0.89	0.74	0.64	36.16	29.64	0.26	0.15
5	1.09	0.40	0.25	37.76	28.38	0.60	0.25
6	0.86	0.44	0.41	33.78	31.72	0.37	0.26
7	0.55	0.40	0.45	31.21	34.34	0.40	0.64
8	1.30	0.75	0.79	41.14	26.04	0.36	0.18
9	0.76	0.50	0.59	31.10	34.45	0.39	0.34
10	1.19	0.26	0.30	27.27	39.29	0.26	0.36
11	0.89	0.45	0.45	33.03	32.44	0.27	0.25
12	0.99	0.28	0.41	25.47	42.06	0.20	0.36
13	1.52	0.46	0.42	39.33	27.25	0.68	0.61
14	1.02	0.54	0.45	35.83	29.90	0.47	0.28
15	0.91	0.63	0.85	34.29	31.25	0.42	0.19
16	1.38	0.30	0.43	30.26	35.41	0.37	0.30
17	1.36	0.53	0.63	43.91	24.40	0.26	0.12
18	0.75	0.31	0.36	32.02	33.46	0.28	0.47
19	0.75	0.39	0.30	28.83	37.17	0.33	0.29
20	0.77	0.29	0.25	35.48	30.20	0.22	0.23
21	0.75	0.27	0.19	34.86	30.73	0.23	0.19
22	1.77	0.77	0.80	32.81	32.66	0.15	0.17
23	1.64	0.49	0.68	26.51	40.42	0.13	0.15
24	1.54	0.77	0.91	32.24	33.23	0.22	0.28
25	1.01	0.34	0.36	25.48	42.05	0.30	0.59
26	0.92	0.27	0.28	37.49	28.58	0.66	0.34

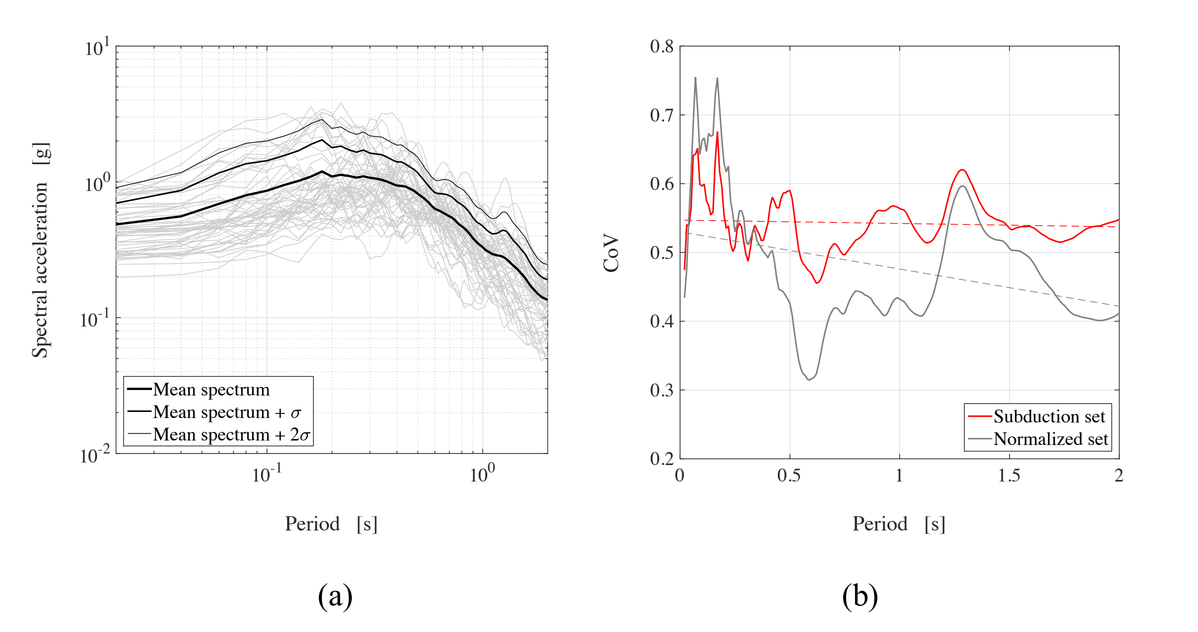

Figure 4-2. (a) Response spectra for the 26 pairs of normalized ground motions and average spectrum of the set plus one and two standard deviations, and (b) CoV as a function of T for the subduction set before and after normalization.

According to the FEMA P-695 methodology, the scaling process has to be done based on the spectral acceleration Sa_{T1} corresponding to the fundamental period of the structure up to an intensity such that 50% of the records have caused collapse. To keep consistency with the methodology, the period for scaling Sa_{T1} is the code-defined fundamental period $T_1 = C_uT_a$ and not the fundamental period obtained from eigenvalue analysis. This procedure is similar to that presented in the ASCE standard 7-16 (ASCE 2016), with the exception that in the FEMA P-695 methodology the value of Sa_{T1} has to be adjusted to a given intensity for T_1, and not for a range of periods.

4.4. SPECTRAL SHAPE FACTORS

Recent research has found that the calculation of the collapse capacity of structural systems through IDA analyses is influenced by the spectral shape of the ground motions, and several approaches have been proposed in order to measure both the spectral shape itself and its influence on the seismic response of structures. As noted by Eads et al. (Eads, Miranda & Lignos 2016), some relevant approaches to measure the spectral shape are: (1) the epsilon parameter ε, defined as the number of standard deviations by which the spectral acceleration of a record is above or below the mean spectral acceleration calculated by a GMPE, (2) the parameter η, which is a linear combination of the epsilon parameter and of the number of standard deviations that the peak ground velocity of the record is above or below the one predicted by a GMPE, (3) the Np parameter, defined as the ratio of the geometric mean of the pseudo-acceleration spectral values over a period range from T_1 to $2T_1$, to $Sa(T_1)$, and (4) the SaRatio parameter, which is the ratio of Sa_{T1} to the geometric mean of the pseudo-acceleration spectral values over a period range. In order to be consistent with the FEMA P-695 methodology, in this investigation the parameter epsilon ε will be used as a measure of the spectral shape.

For seismic demands with a low probability of exceedance, such as the maximum considered earthquake (MCE), the spectral shape is considerably different from that observed in design spectra or in uniform hazard spectra (Baker 2005; Baker & Cornell 2006). These response spectra show peaked Sa values around a given period when their intensity (at such period) is close to the MCE level. This is because it is unlikely that a ground motion with a spectral acceleration much larger than the expected mean at one period also has large spectral accelerations at all other periods (FEMA 2009). Intuitively, this peaked spectral shape is expected to result in positive ε values. For instance, Baker (Baker 2005) showed that on the Coast of California the typical values of ε range from 1.0 to 2.0 for ground motions at the MCE level (2% in 50 years). These positive values of ε are explained because the return period of the ground motion (i.e., 2475 years for a 2% exceedance probability in 50 years) is much larger than the return period of the earthquake that causes the ground motion (i.e., 150-500 years for typical events on the Coast of California).

On the other hand, it has been shown that collapse capacities calculated through dynamic analyses are higher for ground motions with a peaked spectral shape compared to records whose spectral shape does not peak. This is especially true when the peak is close to the fundamental period of the building and the seismic records are scaled based on Sa_{T1}, i.e., the first-mode spectral acceleration (Baker 2005; Goulet et al. 2006; Haselton & Baker 2006; Zareian 2006). However, spectral accelerations for periods other than T_1 are also important. When the structure responds in the nonlinear range, there is an elongation of the fundamental period which makes spectral accelerations beyond T_1 to have a significant effect. Moreover, the influence of higher modes makes accelerations for periods shorter than T_1 also important. Ground motions whose response spectrum has positive ε values usually have lower spectral demands for periods away from T_1.

It has also been shown that if ground motions with $\varepsilon(T_1) = 0$ are used for collapse assessment when it is rather appropriate to use ground motions with $\varepsilon(T_1) = 1.5 - 2.0$, collapse capacities can be underestimated by a factor of 1.3 to 1.8 times for relatively ductile structures (FEMA 2009). The most appropriate approach to consider the spectral shape in collapse analyses is to select ground motions that have an appropriate value of epsilon at the fundamental period, depending on the site and hazard level of interest (Baker & Cornell 2006). This approach is complex when evaluating different buildings with different fundamental periods, since a specific set of accelerograms should be considered for each of them. To deal with this problem, FEMA (FEMA 2009) presented a simplified methodology to correct collapse capacities when a single set of accelerograms is used, which implicitly considers the effects associated with the spectral shape. Therefore, this section focuses on replicating such correction methodology for the set of ground motions proposed for subduction zones. The results can be replicated for any site under study after selecting an adequate target ε_0, as detailed in the following paragraphs.

Haselton and Deierlein (Haselton & Deierlein 2007) investigated the relationship between the collapse capacity (expressed as the spectral acceleration of the fundamental period that causes collapse, SC_{T1}) and the epsilon parameter $\varepsilon(T_1)$, for which they analyzed a set of 65 modern reinforced concrete special moment frame buildings employing a set with 80 ground motions. It was found that SC_{T1} and $\varepsilon(T_1)$ can be related through the following logarithmic function

$$\ln(S_{CT1}) = \beta_0 + \beta_1\, \varepsilon(T_1) \qquad \text{Eq. 4-3}$$

where β_0 indicates the average collapse capacity when $\varepsilon(T_1) = 0$, and β_1 represents the sensitiveness of the collapse capacity to variations of $\varepsilon(T_1)$. Both parameters were obtained using linear regression procedures based on results from nonlinear dynamic analyses. It was found an average value of $\beta_1 = 0.29$ to be consistent for modern reinforced concrete special moment frame buildings with various heights.

For buildings with a large inelastic deformation capacity (i.e., ductility), the fundamental period tends to increase considerably near collapse. Thus, spectral values higher than T_1 become important and affect the structural response, the spectral shape has a larger impact, and the value of β_1 increases. To study this phenomenon, Haselton and Deierlein (Haselton & Deierlein 2007) also investigated the response of 26 old reinforced concrete buildings which do not have modern ductility requirements, and found an average value of $\beta_1 = 0.18$, which is

35% lower than the average for buildings with special moment frames. In addition, 20 buildings with ordinary frames were also analyzed finding that $\beta_1 = 0.19$, confirming the existence of a relationship between the inelastic deformation capacity and the β_1 parameter.

FEMA (FEMA 2009) developed a methodology to correct collapse capacities such that there is no need to calculate the value of $\varepsilon(T_1)$ for each building nor to obtain the value of β_1 by linear regression procedures. However, values of β_1 were necessary for several structural models with different inelastic deformation capacities. This was accomplished by analyzing the nonlinear dynamic results of a 118-buildings set. The set was comprised of: (1) 60 reinforced concrete special moment frame buildings (Haselton & Deierlein 2007), (2) 16 reinforced concrete ordinary frame buildings (FEMA 2009), (3) 26 non-ductile reinforced concrete buildings (Liel 2008), and (4) 16 wood frame wooden buildings (FEMA 2009). To consider the possible range of applications, the aforementioned set had buildings with different structural typologies, design criteria, and heights. For large inelastic deformation conditions, the elongation of the fundamental period T_1 can be related to the ductility μ_T, which is defined as the ratio between the ultimate roof displacement (defined as the roof displacement associated with a 20% loss of base shear strength) obtained from static analyses, and the effective yield roof displacement. Therefore, μ_T was used as a proxy to define a relationship between β_1 and the inelastic deformation capacity through the following equation (FEMA 2009)

$$\beta_1 = (0.14)(\mu_T - 1)^{0.42} \qquad \text{Eq. 4-4}$$

where $\mu_T \leq 8.0$. Finally, an expression to calculate the spectral shape correction factors of the collapse capacity depending on the fundamental period of the structure was also developed by FEMA (FEMA 2009)

$$SSF = \exp\left[\, \beta_1(\, \varepsilon_0 - \varepsilon(T_1)\,)\, \right] \qquad \text{Eq. 4-5}$$

where β_1 depends on the inelastic deformation capacity μ_T (Equation 4-4), ε_0 is the target ε value which depends on both the site and the hazard level of interest, and $\varepsilon(T_1)$ is the ε value calculated for the fundamental period, based on the mean response spectrum of the set and an appropriate GMPE for the site under study. These last two parameters are in the following paragraphs.

Employing data from the United States Geological Survey (USGS), Harmsen (Harmsen 2001) and Harmsen et al. (Harmsen, Frankel & Petersen 2003) determined the target ε_0 values for the different seismic design categories in the ASCE 7-16 standard (ASCE 2016) through probabilistic seismic hazard analyses and disaggregation. It was found that the values corresponding to T = 1 s at a hazard level of 0.5% of exceedance probability in 50 years were adequate. For seismic design categories B and C, ε_0 was set to 1.0, while for category D, ε_0 was set to 1.5.

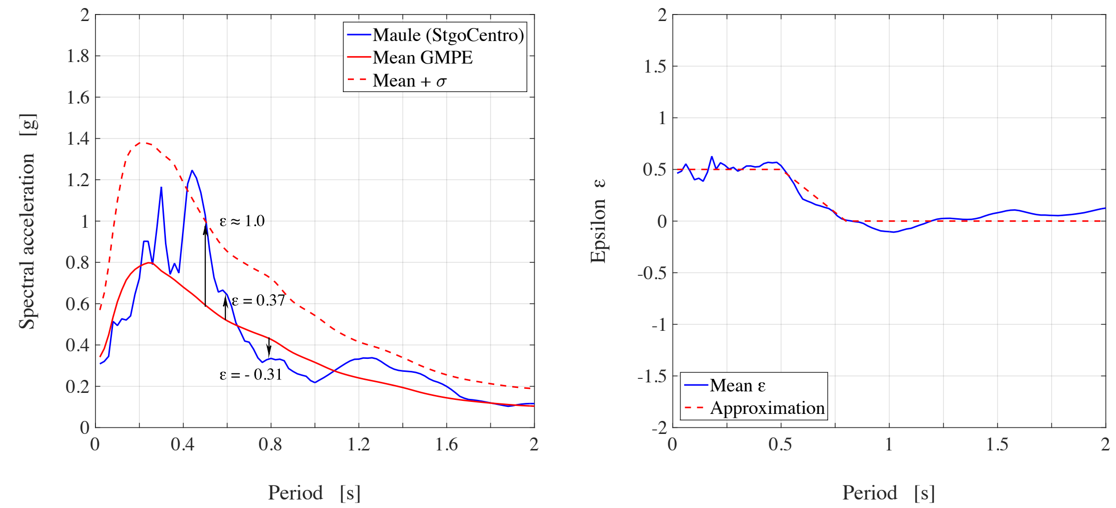

(a) (b)

Figure 4-3. (a) Parameter ε calculated for the Maule earthquake (Santiago Centro station) according to the GMPE proposed by Contreras and Boroschek (Contreras & Boroschek 2012), and (b) parameter ε for periods up to T = 2 s, calculated based on the average spectrum of the set and the GMPE proposed by Contreras and Boroschek (Contreras & Boroschek 2012).

Parameter ε depends both on the period and on the hazard level of the site under study, which is represented through a GMPE. In this research, the GMPE proposed by Contreras and Boroschek (Contreras & Boroschek 2012) was employed, since it was developed based on a large set of subduction earthquakes and has proved to be accurate when predicting expected spectral intensities. As previously mentioned, the parameter ε is defined as the number of standard deviations between a GMPE and the elastic response spectrum of a given ground motion. For instance, Figure 4-3(a) shows the response spectrum of the Maule earthquake recorded by the Santiago Centro station, the mean prediction of the GMPE, and the standard deviation. It can be seen that for T = 0.6 s, ε is equal to 0.37, while for T = 0.8 s it changes to ε = - 0.31. When T = 0.5 s, ε is close to 1.0.

When calculating correction factors to adjust collapse capacities through Equation 4-5, it is necessary to have the $\varepsilon(T_1)$ parameter for different periods, calculated based on the average response spectrum of the ground motion set. For the set in this investigation, the results are shown in Figure 4-3(b) for periods up to T = 2 s. The average values of ε are small and close to zero for periods greater than 0.8 s. Hence, the proposed set is classified as "ε -neutral" (FEMA 2009). Furthermore, for short periods the values of ε range from 0.4 to 0.6, which is due to the high limit of PGA (> 0.2 g) that was set in the selection of the records. For calculation purposes, it is useful to simplify the results shown in Figure 4-3(b) by a piecewise linear function given by

$$\varepsilon(T) = \frac{4 - 5\,T}{3} \qquad \text{Eq. 4-6}$$

where $0 \le \varepsilon(T) \le 0.5$. Hence, using Equations 4-4, 4-5, and 4-6, and an adequate value of ε_0, it is possible to calculate collapse capacity correction factors (also called spectral shape factors SSF) for different buildings. Tables 4-4 and 4-5 present the correction factors for $\varepsilon_0 = 1.0$ and $\varepsilon_0 = 1.5$, respectively, which have been calculated for discrete values of fundamental period T_1 and ductility capacity μ_T. Note that using the expressions aforementioned, it is possible to calculate the factors for any value that the variables take, which is recommended for the application of the FEMA P-695 methodology.

Table 4-4. Spectral shape factors for $\varepsilon_0 = 1.0$.

Period [s]	**Ductility μ_T**										
	1.0	**1.1**	**1.3**	**1.5**	**2.0**	**3.0**	**4.0**	**5.0**	**6.0**	**7.0**	**≥ 8.0**
≤ 0.50	1.00	1.03	1.04	1.05	1.07	1.10	1.12	1.13	1.15	1.16	1.17
0.55	1.00	1.03	1.05	1.06	1.09	1.12	1.14	1.16	1.17	1.19	1.20
0.60	1.00	1.04	1.06	1.07	1.10	1.13	1.16	1.18	1.20	1.22	1.24
0.65	1.00	1.04	1.07	1.08	1.11	1.15	1.18	1.21	1.23	1.25	1.27
0.70	1.00	1.05	1.07	1.09	1.12	1.17	1.20	1.23	1.26	1.28	1.30
0.75	1.00	1.05	1.08	1.10	1.14	1.19	1.23	1.26	1.29	1.31	1.34
≥ 0.80	1.00	1.05	1.09	1.11	1.15	1.21	1.25	1.28	1.32	1.35	1.37

Table 4-5. Spectral shape factors for ε_0 = 1.5.

Period [s]	**Ductility μ_T**										
	1.0	**1.1**	**1.3**	**1.5**	**2.0**	**3.0**	**4.0**	**5.0**	**6.0**	**7.0**	**≥ 8.0**
≤ 0.50	1.00	1.05	1.09	1.11	1.15	1.21	1.25	1.28	1.32	1.35	1.37
0.55	1.00	1.06	1.10	1.12	1.16	1.22	1.27	1.31	1.35	1.38	1.41
0.60	1.00	1.06	1.10	1.13	1.18	1.24	1.30	1.34	1.38	1.41	1.45
0.65	1.00	1.07	1.11	1.14	1.19	1.26	1.32	1.37	1.41	1.45	1.49
0.70	1.00	1.07	1.12	1.15	1.21	1.28	1.34	1.40	1.44	1.49	1.53
0.75	1.00	1.08	1.13	1.16	1.22	1.30	1.37	1.43	1.48	1.52	1.57
≥ 0.80	1.00	1.08	1.14	1.17	1.23	1.32	1.40	1.46	1.51	1.56	1.61

When ε_0 = 1.0, the spectral shape factors range from SSF = 1.00 - 1.37, and SSF = 1.00 - 1.61 for ε_0 = 1.5, being these results consistent with previous research (FEMA 2009). Note that Equation 4-4 saturates for values of ductility capacity μ_T greater than 8, thus if a structural archetype has a $\mu_T > 8$, it must be assumed as $\mu_T = 8$. In addition, to maintain consistency with the FEMA P-695 methodology, the ductility capacity μ_T must be calculated with the expressions provided by the ASCE 41-17 standard (ASCE 2017), which depends on both the period and the modal shape of the structure.

Figure 4-4(a) shows the spectral shape factors for the far-field set of the FEMA P-695 methodology and for the proposed subduction set, calculated for a fundamental period of T_1 = 0.7 s. As can be seen, both for ε_0 = 1.0 and ε_0 = 1.5, the spectral shape factors of the proposed subduction set are higher by, on average, 7.3%. This is because, due to the higher amplitudes of the subduction records, the mean response spectrum of the set is "closer" to the spectral prediction from the GMPE, which results in lower epsilon values compared to those from the far-field set. As the values of ε_0 which define the seismic hazard are kept the same in both cases, it is easy to note that Equation 4-5 will result in higher SSFs to avoid over-conservative collapse capacities. This highlights that a proper quantification of the seismic hazard through the ε_0 parameter is crucial before applying the aforementioned procedure. Higher SSF values can play a fundamental role when evaluating the collapse capacity of buildings, or when validating a new set of seismic performance factors through the FEMA P-695 methodology since they modify directly the collapse margin ratios calculated from IDA analyses. These results also stand out the importance of a proper calculation of the SSF if new or different ground motion sets are used. The same trend of higher SSF is also observed for fundamental periods other than 0.7 s. Additionally, it can also be noted from Figure 4-4(a) that the higher the ductility is, the higher the SSFs are, which is consistent with the results of Haselton and Deierlein (Haselton & Deierlein 2007). For structural systems with larger inelastic deformation capacity, the effective period elongates considerably before the collapse, causing the spectral values at periods greater than T_1 to have a greater influence on collapse response. Hence, the spectral shape of the ground motions becomes more important.

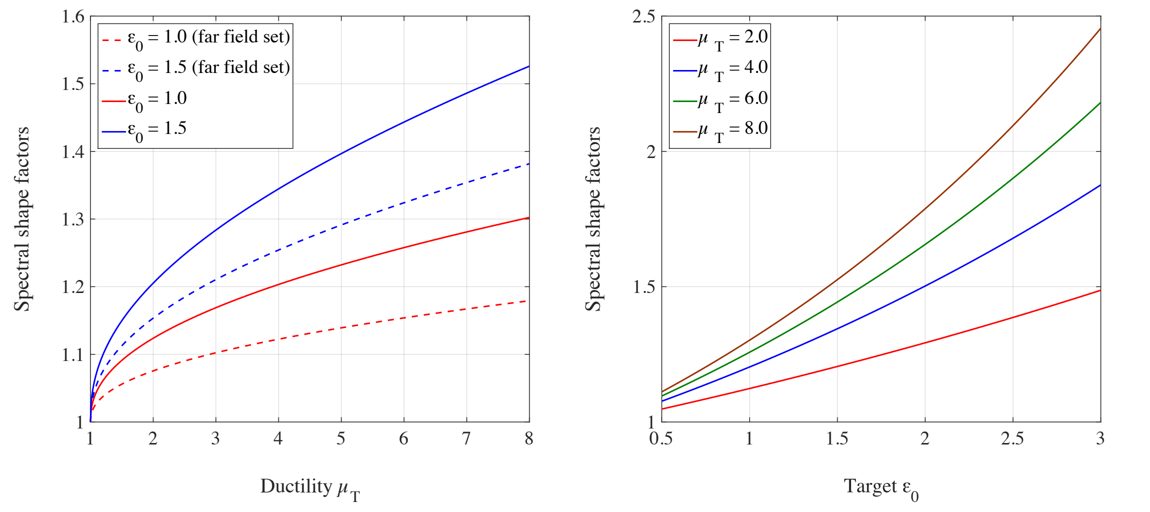

Figure 4-4. (a) Spectral shape factors for T_1 = 0.7 s, for both sets, and (b) relationship between the target ε_0 parameter and the SSFs, for a fundamental period T_1 = 0.7 s and different values of ductility.

Figure 4-4(b) shows the relationship between the target ε_0 parameter and the SSFs, for a fundamental period T_1 = 0.7 s and different values of ductility. It is interesting to note that the higher the ductility capacity, the higher the influence of the ε_0 on the calculation of the SSFs. For instance, whereas the ratio between the SSFs for ε_0 = 3 and ε_0 = 0.5 is 1.42 when μ_T = 2.0, it is 2.21 when μ_T = 8.0, an increment of 56% in the influence of ε_0. Hence, it highlights that an appropriate estimation of the ε_0 values is fundamental when adjusting collapse capacities based on the spectral shape parameter ε. For T_1 = 1 s, values of ε_0 = 0.50 to 1.25 are typical in zones other than the seismic regions of California. The values tend to be higher in most of California, since the earthquakes have shorter return periods, with typical values of ε_0 = 1.25 to 1.75, and some values ranging upward to 3.0. On the other hand, ε_0 falls below 0.75 for the New Madrid Fault Zone, regions of the eastern coast, most of Florida, southern Texas, and areas in the north-west zone of the U.S. (FEMA 2009; Harmsen 2001; Harmsen, Frankel & Petersen 2003).

4.5. SEISMIC PERFORMANCE EVALUATION

In this section, the impact of employing the proposed subduction set in nonlinear dynamic analyses is evaluated. Four 5-story wood frame wood buildings from Chapter 1 were included in the analyses, and the results were compared to those obtained by employing the FEMA P-695 far-field set. The buildings (named Q, C, P, D respectively) were designed in accordance with the requirements of the Chilean seismic code NCh433 (INN 2009) and the SDPWS standard (American Wood Council 2015) for a Seismic Zone 1 and a Soil Class B, as classified by the Chilean regulations. Figure 4-5 shows the floor plan of each building.

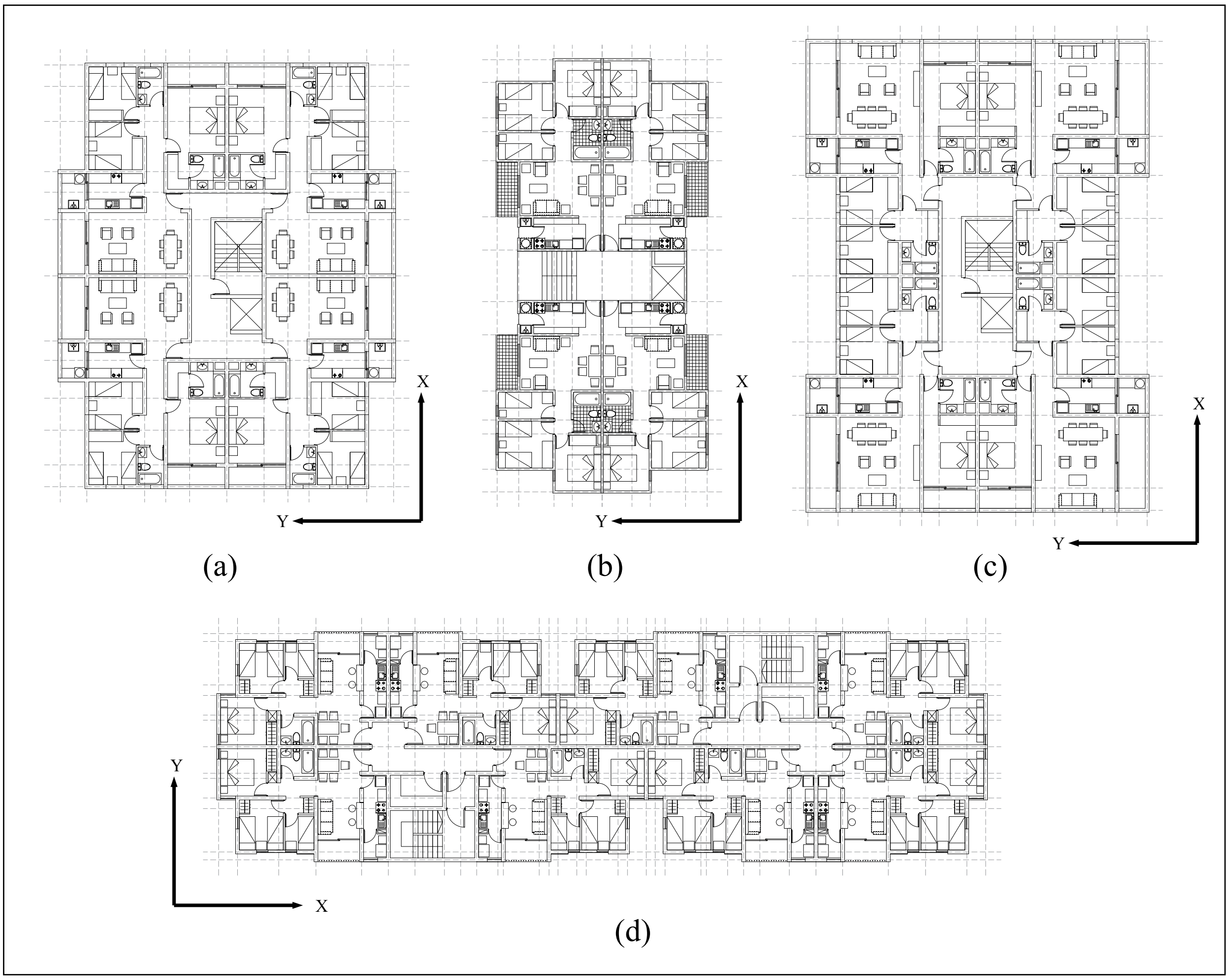

Figure 4-5. Floor-plan configurations developed for this investigation: (a) floor-plan "Q", (b) floor-plan "C", (c) floor-plan "P", and (d) floor-plan "D".

A 3D nonlinear model was developed for each building. As explained in Chapter 1 and Section 1.2.2., wood frame walls were modeled using nonlinear spring elements which connect two consecutive floors. The hysteretic behavior of each wood frame wall was modeled using the Modified-Stewart (MSTEW) model proposed by Folz and Filiatrault (Folz & Filiatrault 2001), which is able to properly capture phenomena associated to great damage states, such as force degradation, stiffness degradation, and pinching. Table 4-6 contains the MSTEW modeling parameters for wood frame walls of different configurations computed in Chapter 2. The vertical flexibility of the buildings was modeled using a simplified bi-linear model which represents the combined stiffness of hold-downs, shear wall studs, continuous steel rods, and any special fastener devices in the wall. Figure 4-6 depicts the approach employed to model each wall.

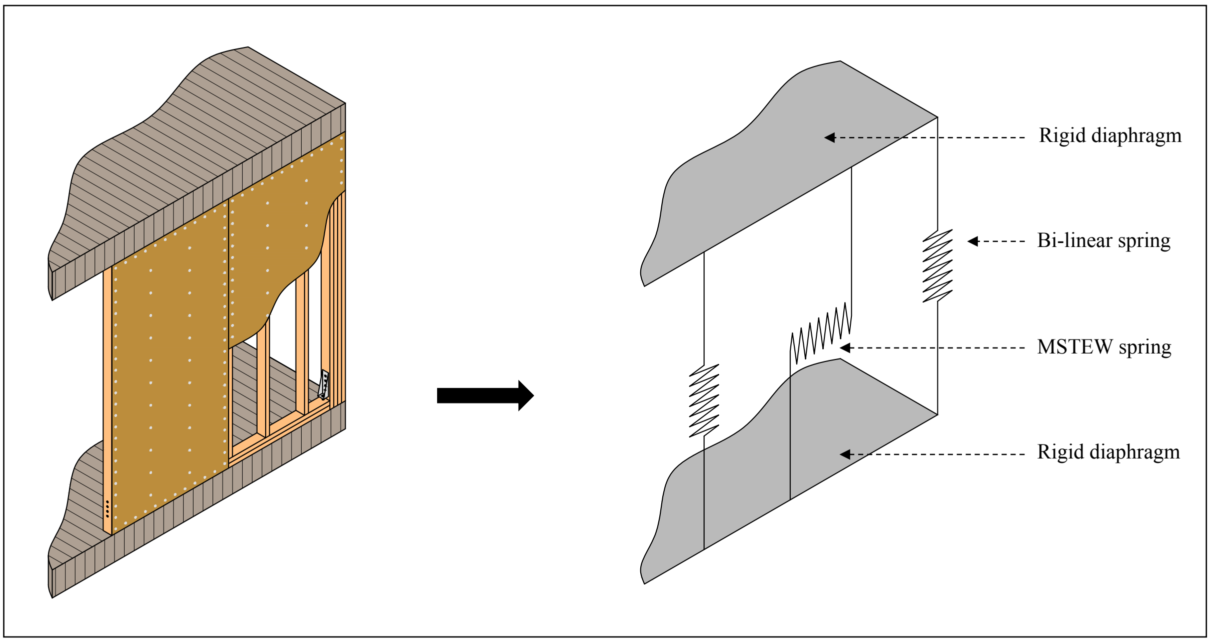

Figure 4-6. Modeling approach for wood frame walls.

In order to compute the collapse capacity of each building, bidirectional IDA analyses were conducted employing the software SAPWood V2.0 (Pei & van de Lindt 2010) for both the subduction set and the far-field set, by scaling the ground motions until one-half of the records in the set caused collapse, which was defined as the occurrence of a 3% inter-story drift at any floor. The record pairs of both sets were applied twice to each model, once with the ground motion records oriented along the principal direction, and then again with the records rotated 90 degrees.

Table 4-6. MSTEW modeling parameters for wood frame walls.

Wall properties		MSTEW parameters									
OSB	Nail spacing [mm]	K_0 [kN/mm/m]	r_1	r_2	r_3	r_4	F_0 [kN/m]	F_i [kN/m]	δ_u [mm]	α	β
Single	50	2.374	0.072	-0.046	1.000	0.017	10.275	2.048	45.450	0.532	1.139
	100	1.393	0.079	-0.101	1.047	0.015	9.600	1.603	57.300	0.531	1.146
	150	1.080	0.079	-0.090	1.075	0.014	7.104	1.202	55.820	0.522	1.150
Double	50	2.487	0.097	-0.080	1.002	0.021	26.685	2.935	42.887	0.800	1.150
	100	2.786	0.079	-0.101	1.047	0.015	19.196	3.205	57.300	0.531	1.146
	150	2.159	0.079	-0.090	1.075	0.014	14.208	2.403	55.820	0.522	1.150

Figure 4-7(a) shows the mean collapse capacities of each building computed for both the FEMA P-695 far-field set and for the subduction set. The results show a reduction in the collapse capacities of 14.7%, 12.0%, 10.1%, and 12.7% for each building, respectively, when the subduction set is used in IDA analyses. The average reduction is 12.4%. Lower collapse capacities are due to the longer duration of the set and to the greater energy that subduction earthquakes release. However, these results are different from those of previous research which found that the collapse capacity reduction can be as high as 40% when employing large-duration records (Raghunandan, Liel & Luco 2015). This difference is explained because the ground motion set proposed in this chapter also includes short-duration records from shallow crustal earthquakes. This strategy was adopted to extend the applicability of the proposed set to zones with different hazard functions, site, and source conditions, as required by the FEMA P-695 methodology (FEMA 2009).

Figure 4-7(a) also shows the variability when calculating the collapse capacities expressed as the coefficient of variation CoV. For the far-field set, the CoV ranges from 0.27 to 0.33, and for the subduction set, it ranges from 0.30 to 0.38. This uncertainty is due to variability in the response of the buildings to the different ground motion records in the sets and allows a proper evaluation of the structural seismic response when numerical models are employed. Previous research found that variability ranging from 0.35 to 0.45 is fairly consistent among various building types (Haselton 2006; Ibarra & Krawinkler 2005b, 2005a; Zareian 2006). Hence, the variability provided by the proposed ground motion set is robust enough for a probabilistic evaluation of collapse capacities.

The adjusted collapse margin ratio (ACMR) is employed as a proxy to evaluate structural performance in the FEMA P-695 methodology. Firstly, the collapse margin ratio (CMR) is computed as the ratio between the mean collapse capacity obtained from IDA analyses and the spectral intensity related to the maximum considered earthquake provided by design codes. Subsequently, the CMR is adjusted to account for the effects of spectral shape by means of the spectral shape factors SSF, as described previously. Hence, ACMR = CMR x SSF. If three-dimensional models are used, a factor of 1.2 is applied to the ACMR to reduce the conservative bias which occurs when ground motion records are applied in pairs in three-dimensional nonlinear dynamic analyses (FEMA 2009).

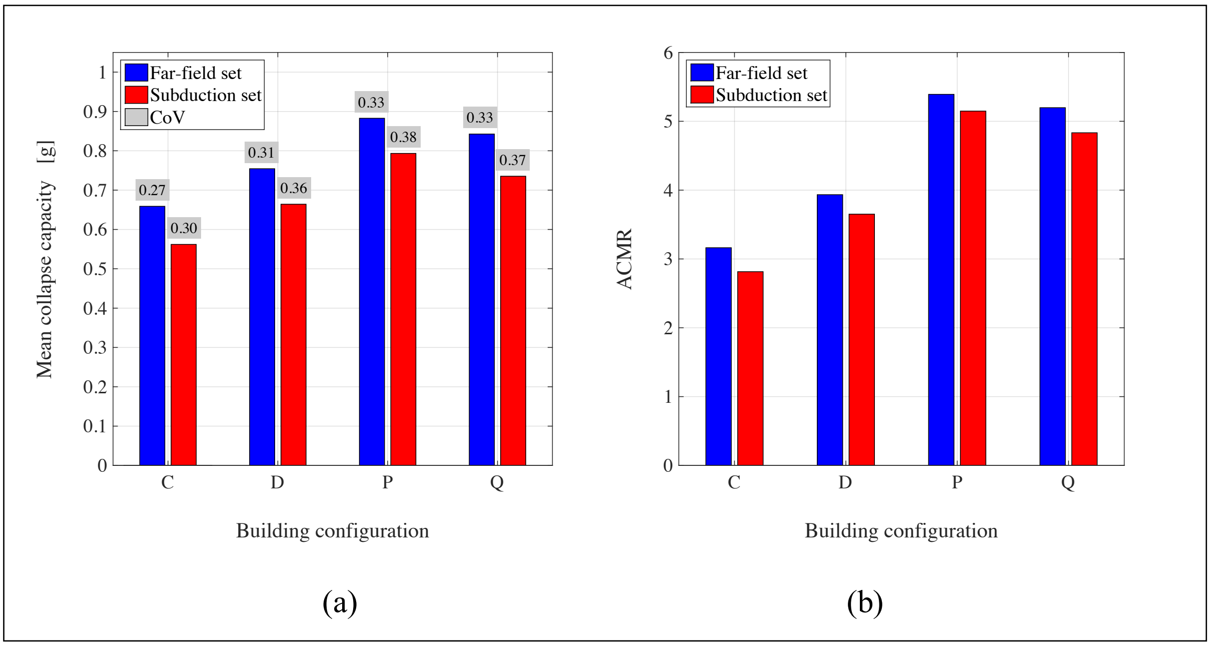

Figure 4-7. (a) Mean collapse capacities and CoV calculated for both the FEMA P-695 far-field set and the subduction set, and (b) adjusted collapse margin ratios ACMR for both the FEMA P-695 far-field set and the subduction set.

Figure 4-7(b) shows the ACMRs calculated employing both ground motion sets. It can be noted that ACMRs decreases when the subduction set is employed, by 11.0%, 7.2%, 4.5%, and 7.0%, respectively. The average reduction is 7.4%. Interestingly, the decrease percentages of the ACMRs are lower than those of the mean collapse capacities, a phenomenon which is mainly due to two reasons. First, the SSFs for the subduction set are, on average, higher than those for the far-field set. Hence, the CMRs are amplified by a higher factor. Second, wood frame buildings have a large inelastic deformation capacity, with ductilities which range from 4.0 to

5.0, and as observed in Figure 4-4(a), the larger the ductility, the higher the influence of the SSFs on the collapse capacities.

Intuitively, strong ground motions affect not only structural collapse capacities but also the behavior of non-structural components in buildings, which is relevant for performance-based seismic engineering that takes into account economic losses and building functionality. In this context, horizontal floor accelerations are considered critical, since they impose forces that can lead to failures of non-structural components and their connections to the primary structural system. Figure 4-8(a) shows a comparison between the mean peak floor accelerations obtained from both the far-field set and the proposed subduction set. For this purpose, the ground motions of both sets were scaled to match a spectral acceleration of Sa_{T1} = 0.25 g, which is close to the MCE level for all buildings. It can be noted that there is an increase of 29.9%, 34.1%, 31.9%, and 30.7% in the mean peak floor accelerations for each building when the subduction set is used. The average increase is 31.7%. These higher floor acceleration values are due to the stronger ground motion of greater length that subduction earthquakes are known to have, and which transmits higher levels of kinetic energy to buildings.

The total dissipated hysteretic energy is known to be a good indicator of structural damage, since the deformation demands imposed on structural systems by earthquakes are cyclic in nature and the associated effects of cumulative damage considerably can modify the seismic response of the structures (Kunnath & Chai 2004). Hence, it is of relevant interest to analyze the impact of using the proposed subduction set to compute the cumulative energy dissipated by structural systems. Employing the records of both sets matched to a spectral acceleration of Sa_{T1} = 0.25 g, the total mean hysteretic energy dissipated by all the wood frame walls of each building was calculated, and the results are shown in Figure 4-8(b). When the subduction set is used to perform nonlinear dynamic analyses, the mean hysteretic energy increases by 38.0%, 18.1%, 1.1%, and 5.8% for each building configuration, respectively. The mean increase is 15.7%. It is interesting to note that the increment for the buildings P and Q is low compared to that of the buildings C and D. This is because, as observed in Figures 4-7(a) and 4-7(b), these buildings have higher collapse capacities; hence, ground motions scaled to a spectral acceleration of Sa_{T1} = 0.25 g may not be strong enough to induce great damage to the structures regardless the ground motion set used in the analyses. As observed, higher amounts of dissipated hysteretic energy are due to the longer duration of the ground motions as well as to greater amplitude accelerations in the records. A proper quantification of the hysteretic energy is of relevant interest for performance-based seismic design approaches, since damage evaluation based on peak responses has found not to be an adequate measure of the potential damage of a ground motion, and therefore not a suitable indicator of structural performance because the strength, deformation, and energy-dissipation capacity of the building depend on the number of inelastic load cycles (Malhotra 2002).

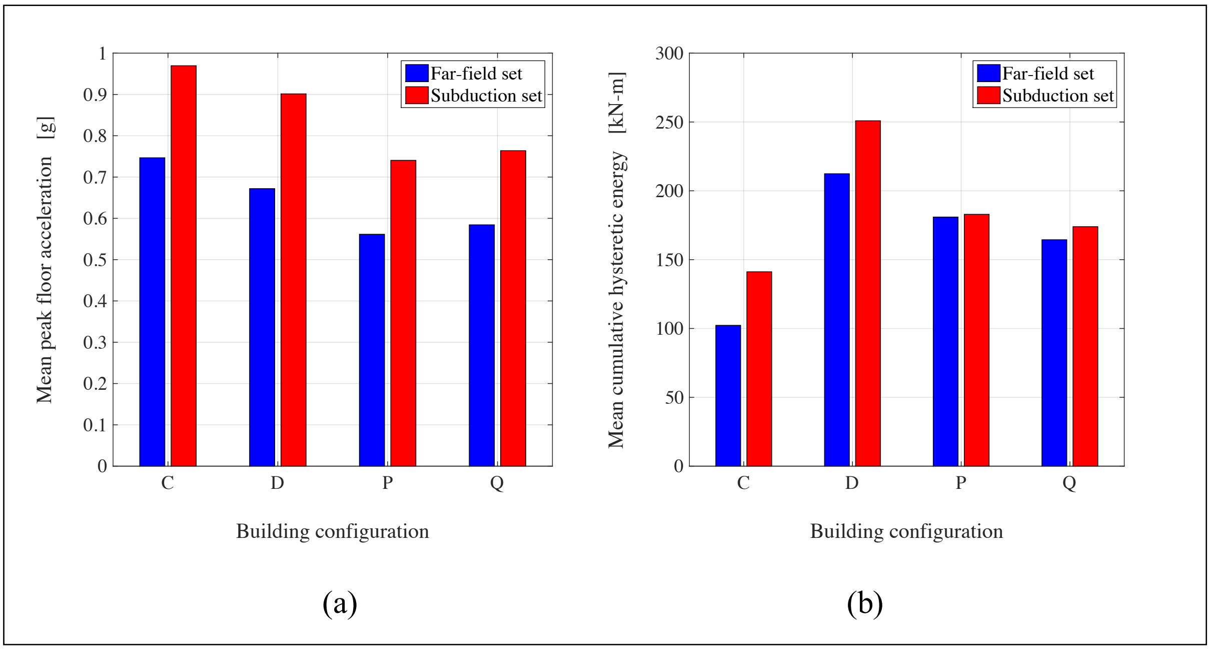

Figure 4-8. (a) Mean peak floor accelerations for both the FEMA P-695 far-field set and the subduction set, and (b) mean cumulative hysteretic energy for both the FEMA P-695 far-field set and the subduction set.

4.6. ROBUSTNESS ANALYSIS

This section is aimed at evaluating the robustness of the proposed subduction set and of the criteria applied to select the ground motions, in order to demonstrate that collapse capacity predictions are not highly sensitive to small variations in the selection criteria and to validate the suitability of the number of records included. This latter is of relevant interest when performing IDA analyses, since although ground motion sets are required to have a sufficiently large number of records to compute mean collapse capacities properly, it is also essential to find a balance between the number of records necessary to suitably consider the variability of the seismic demand and the computational overheads related to performing nonlinear IDA.

The robustness of the proposed subduction set was validated by comparing the previously computed collapse capacities to those obtained with a different set of ground motions proposed by Guerrero (Guerrero 2018). Such set consists of 209 pairs of ground motions recorded from interplate and intraplate earthquakes that occurred between 1985 and 2016 of magnitudes from 5.0 to 8.8. The PGA values in the set range from 0.04 g to 0.93 g, with an average PGA of 0.23 g. PGVs range from 0.59 cm/s to 69.28 cm/s, with an average of 14.5 cm/s. The mean significant duration $Ds_{5\text{-}75}$ of the set is 14.51 s. Figure 4-9 shows the mean collapse capacities for the four previously discussed wood frame buildings computed through IDA analyses for both the proposed subduction set and the Guerrero set (Guerrero 2018).

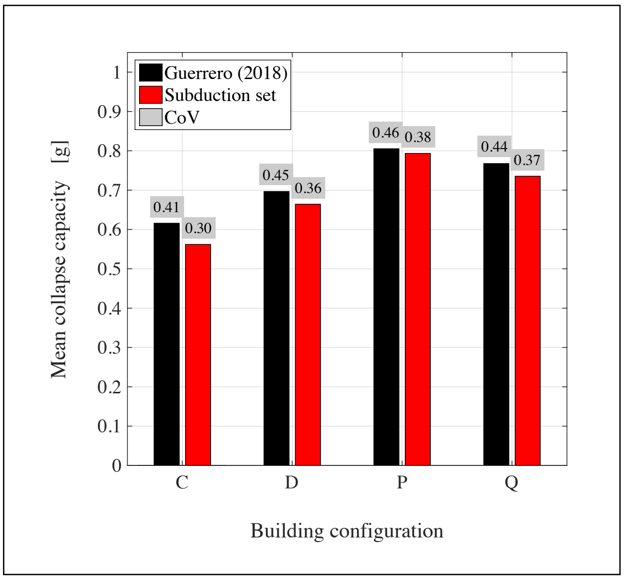

Figure 4-9. Mean collapse capacities and CoV calculated for both the set developed by Guerrero (Guerrero 2018) and the proposed subduction set.

The results show that the collapse capacities calculated with the larger ground motion set are slightly higher than those calculated using the proposed subduction set, with increases of 8.7%, 4.6%, 1.5%, and 4.2% for each building, respectively. The mean increase is 4.8%. The variability, measured as the CoV, also increases and ranges from 0.41 to 0.46, which is due to the wider interval of record intensities in the set proposed by Guerrero (Guerrero 2018). Interestingly, the data from Figure 4-9 indicates that the proposed subduction set is robust enough (in terms of the number of records and intensity levels) to provide the same reliability that can be obtained when employing a much larger ground motion set. Similarly, the results also show that collapse capacities are not highly sensitive to the PGA and PGV limits established when selecting ground motions, since records are scaled upwards in IDA analyses.

This latter is of relevant interest, since there are few earthquake records with high PGA and PGV values available in the current literature for engineering purposes. Hence, including records with low-intensity levels can also be a suitable strategy when performing IDA analyses.

CHAPTER FIVE

CONCLUSIONS

This thesis presents the results of an experimental and numerical investigation on the seismic performance factors (SPF) for wood frame buildings in Chile. Since previous research has shown that the current provisions of the Chilean NCh433 standard (INN 2009) result in over-conservative structures, the main goal of this research is to propose a new set of SPFs in order to improve the cost-effectiveness of new buildings without compromising their seismic response. Following the guidelines of the FEMA P-695 methodology (FEMA 2009), 201 structural archetypes were analyzed through nonlinear numerical models to study their dynamic behavior under different seismic hazards. The archetypes assessed two different sets of SPFs: (1) the current provision of the NCh433 standard, $R = 5.5$ & $\Delta_{max} = 0.002$, and (2) a new set of less conservative SPFs, $R = 6.5$ & $\Delta_{max} = 0.004$. Results showed that the new proposed set results in code-compliant structures with an acceptably low probability of collapse under maximum considered earthquake MCE accelerations. Besides, the structural efficiency improves, more flexible architectural designs are allowed, and the resilience of the buildings is guaranteed even for highly recurring seismic events. The main findings of this thesis are as follows:

- At the individual level, when the SPFs were changed from $R = 5.5$ & $\Delta_{max} = 0.002$ to $R = 6.5$ & $\Delta_{max} = 0.004$ the average collapse margin ratio of the archetypes reduced by 13.3%. However, no archetype showed a collapse probability higher than 20% for MCE accelerations.

- At the group level, when the SPFs were changed from $R = 5.5$ & $\Delta_{max} = 0.002$ to $R = 6.5$ & $\Delta_{max} = 0.004$, the average collapse margin ratio of the performance groups reduced by 15.3%. However, no group showed a collapse probability higher than 10% for MCE accelerations.

- Employing less conservative SPFs improves the cost-effectiveness ratio of wood frame structures and might enhance its competitiveness when compared to other materials. For instance, the new set of SPFs resulted in a 40.4% saving in nailing, 15.9% in OSB panels, and 7.3% in timber studs for a 5-story building case study.

- For wood frame structures, the building height proved not to have a relevant influence on the seismic behavior of the structure, since similar collapse ratios were found for archetypes with a different number of stories.

- The minimum base shear requirement C_{min} of the NCh433 standard is somewhat restrictive for soil classes A, B, and C, leading to conservative results compared to archetypes where the minimum base shear C_{min} does not control the structural design. However, the conservatism of the C_{min} value is due to the inherent uncertainty of the seismic hazard, and aims at providing a design base shear high enough to guarantee the resilience of the structures under moderate and severe earthquakes.

- Wood frame structures designed with the current SPFs of the NCh433 standard or the new SPFs proposed in this research proved to meet the enhanced performance objective defined by the ASCE 41-17 standard. This highlights that a change towards less conservative SPFs for wood frame buildings does not have a harmful effect on the seismic response of the buildings.

- A reduction in the overall stiffness of wood frame structures due to a change in the maximum allowable drift Δ_{max} from 0.002 to 0.004 does not prevent the buildings from reaching an operational performance level for low seismic demands. This is important in the Chilean context since several minor earthquakes are expected throughout the lifespan of buildings, and SPFs should guarantee not to result in structural and non-structural issues under highly recurring seismic events.

- Due to the higher seismic mass on top of ground-level floors, they sustain higher lateral displacements and are more likely to collapse under lateral accelerations compared to the upper floors. This is valid even if no garage lines or wide entrance doors are part of the architectural design of the first floor. In this research, it was found that 87% of the archetypes under analysis collapsed on the first and second floor regardless of the SPF set used during design.

Additionally, the following subsections present the main findings and conclusions withdrawn from the supporting studies (Chapters 2, 3 and 4) of this thesis. This way, the contributions to each field addressed along this thesis are remarked and highlighted.

5.1. CONCLUSIONS FROM CHAPTER TWO: NONLINEAR MODELING OF STRONG WOOD FRAME SHEAR WALLS FOR MID-RISE BUILDINGS

An efficient and accurate approach for monotonic and cyclic nonlinear modelling of strong wood frame shear walls was presented in this chapter. Compared to models developed in previous investigations, this new approach aims at developing a more comprehensive approach that embraces walls with different aspect ratios, while taking into account the effects of sturdy end-studs, and incorporating the deformation demands in the anchoring system. The good agreements between the model predictions and the results from twelve real-scale experimental tests demonstrated that the proposed methodology is able to accurately reproduce the nonlinear response of a wide range of walls. Results also showed that complex phenomena such as force and stiffness degradation and pinching in strong walls could be captured reasonably well using the model. Furthermore, the model was used to conduct in-depth analyses of the nonlinear behavior of wood frame walls, which led to the following findings:

- The demands on the hold-downs in strong walls are relatively low (~ 0.51 T_{ult}). Hence, they are expected to behave in the linear range. Such demands do not increase monotonically, but they decrease after the wall reaches its maximum capacity. This phenomenon guarantees a shear failure and prevents the hold-downs from pulling out. Thus, the main failure mechanism of strong shear walls with code compliant aspect ratios is expected to be nail ductile shearing. Additionally, the design procedure of the hold-downs could be optimized to reduce the cost of the anchorage system.

- The mechanical properties of the sheathing-to-framing connectors have a significant effect on the anchoring system demands. Special care must be taken when designing wood frame walls if high-strength connectors (such as screws) are employed, since the load transfer to hold-downs could lead to their failure under large displacement demands.

- In strong wood frame walls with high aspect ratios, the percentage of global lateral deformation due to the uplift of the anchoring system is about 50%. This high contribution level is not due to great tensile demands, but due to the slender geometry of the wall (i.e., small uplifts at the lower corners produce large displacements at the top of the wall). Based on such high rocking contributions to the wall deformation, yielding and ultimate drifts of strong shear walls may significantly increase.

- Due to the geometry of the OSB panels, the deformation demands are concentrated on the upper and lower corners of the wall and in the central studs. The contribution of the nails in the interior studs to the lateral capacity of the wall was found to be small.

- The nailing pattern can be optimized in wood frame walls to improve the performance of the wall without increasing the number of connections. It was shown that changing the nailing pattern can improve the maximum capacity of strong walls up to 10% at the price of slightly reducing ductility.

- The results of the presented numerical model can be used to calibrate a SDOF model. This simpler and easy-to-use model can then be employed to reproduce the nonlinear shear behavior of wood frame walls at a very low computational effort for further assessments. The SDOF model parameters can be normalized per unit length to predict the pure shear response of walls with similar nailing patterns but of different wall lengths. This simpler model is intended to make the nonlinear modeling of mid-rise timber structures efficient, guide earthquake engineers in practice, and provide valuable information for both force-based (Rossi et al. 2016; Seim, Hummel & Vogt 2014; Hummel, Seim & Otto 2016) and performance-based (van de Lindt et al. 2013; Mergos & Beyer 2015) seismic design procedures for multi-story wood frame buildings.

5.2. CONCLUSIONS FROM CHAPTER THREE: EXPERIMENTAL INVESTIGATION ON THE CYCLIC RESPONSE OF WOOD FRAME SHEAR WALLS WITH CONTINUOUS ROD HOLD-DOWN ANCHORAGES

This chapter presents the results of an experimental investigation on the lateral behavior of wood frame walls with continuous rod hold-downs. Compared to traditional walls with discrete hold-downs at the lower corners, these walls employ continuous anchorages to transfer high tensile forces across several stories to the foundation, providing an uninterrupted vertical load path that guarantees the structural integrity of the building. Four 2400 mm long specimens were tested under reversed cyclic load, employing different configurations regarding nail spacing and rod diameter. Results showed that, if the anchorage system was properly dimensioned, walls exhibit good lateral performance with enough strength and ductility to guarantee resilience in buildings designed with modern seismic codes. Besides, the continuous rod system proved to be capable of fully fixing the wall to the foundation, avoiding the overturning of the specimen and minimizing the uplift of the bottom plate. The main findings of this chapter are as follows:

- The overall cyclic force-displacement response of walls with continuous rod hold-downs is similar to that of conventional walls, with a pinched hysteresis and degradation of force and stiffness. Up to lateral drifts of about 0.8%, the responses of the walls of this investigation were mainly linear-elastic.

- If designed properly, the continuous anchorage system does not suffer damage even under large wall deformations, with the steel rod behaving within the elastic regime (less than $0.5F_y$). In only one of the four tests the anchorage system failed (specimen C-100-12), a purposefully designed incident in this investigation to study the behavior of the wall in the event of a rod failure.

- The nail spacing has the greatest influence on the strength and stiffness of the wall. As the spacing reduced from 100 to 50 mm, the strength increased by 40% and the stiffness by 21.7%. Moreover, the rod diameter showed not to have a significant impact on these parameters (except for the specimen C-100-12).

- The specimens experienced a remarkable stiffness degradation as the lateral deformation of the wall increased. After a 0.5% drift, the degradation followed a steady decay and kept a residual stiffness of about 15-20% of the initial.

- The ductility values computed for the walls in this research were consistent with those of typical wood frame walls, i.e., ~4. However, employing a small nail spacing (50 mm) and a large rod diameter (44.5 mm) increased the ductility up to 6.32 for one of the specimens.

- The characteristic damping ratios were consistent with the results reported by previous researchers for wood frame walls. The values ranged from 0.09 to 0.12, with an average of 0.11.

- Employing continuous hold-downs has a significant impact on the strength of the specimens when compared to walls with discrete hold-downs, increasing the maximum strength by 35.8%, on average. However, an important percentage of this increment is not due to the anchorage itself, but to the additional nails provided by the sturdy end-studs.

- The guidelines provided by the Special Design Provisions for Wind and Seismic (SDPWS) standard (American Wood Council 2015) have some levels of inaccuracy when estimating the mechanical properties of wood frame walls with continuous rod hold-downs. The strength of the walls was underestimated by 39.9% while the stiffness was overestimated by 37.5%, on average. However, the strength underestimation may be a mechanism for implicitly taking into account the variability of the mechanical properties of the wood and uncertainty of the seismic demand.

- The walls tested in this research showed a different damage pattern when compared to traditional walls. When the continuous anchorage system is used, the wall deformation demands are transferred from the corners to the center of the wall. Therefore, the damage mainly concentrates on the nails located at the central studs. This load transfer mechanism guarantees the integrity of the anchorage system.

5.3. CONCLUSIONS FROM CHAPTER FOUR: GROUND MOTIONS FOR APPLICATION OF THE FEMA P-695 METHODOLOGY IN SUBDUCTION ZONES

This chapter proposes a set of 26 pairs of ground motions aimed at extending the scope of the FEMA P-695 methodology to zones prone to subduction earthquakes, since the current FEMA P-695 record sets are representative only of shallow crustal earthquakes. The criteria to select the ground motions were designed to be consistent with those proposed in the FEMA methodology, to provide an objective selection of the records, and to embrace different ground motion hazard functions, sites, and source conditions. The proposed set contains 18 ground motions from subduction earthquakes and 8 from shallow crustal ones, recorded between 1987 and 2016 with magnitudes from 6.5 to 9.0. The average significant duration $Ds_{5\text{-}75}$ of the set is 14.56 s, more than twice that of the FEMA P-695 far-field set. To properly consider the effects of the spectral shape when computing collapse capacities, the spectral shape correction factors were calculated using the ground motion prediction equation proposed by Contreras and

Boroschek (Contreras & Boroschek 2012) for different fundamental periods and ductility capacities, which were found to be 7.3% higher (on average) than those of the FEMA P-695 far-field set.

Nonlinear incremental dynamic analyses of four five-story wood frame buildings revealed that, when the proposed ground motion set is used, collapse capacities and adjusted collapse margin ratios decreased by 12.4% and 7.4%, and peak floor accelerations and dissipated hysteretic energies increased by 31.7% and 15.7%, respectively. Additionally, the robustness of the proposed set was verified by comparing the collapse capacity results with those obtained using a set with 209 pairs of ground motions collected employing different selection criteria. The results showed that the proposed subduction set is robust enough in terms of the number of records and intensity levels to provide the same reliability that can be obtained when employing a much larger ground motion set. Although these results were computed only from wood frame buildings, they highlight that subduction ground motions can induce greater damage than shallow crustal ones to structures with high deformation capacities and rapid rates of cyclic deterioration. Besides, as previous research has shown, similar trends can be expected for other structural systems (FEMA 2009).

Additionally, the following general conclusions can also be drawn from the results of this chapter:

- Normalization procedures for ground motion sets based on the median peak ground velocity are not very effective in reducing the variability of the set, especially for short periods.

- Both ductility capacity u_T and target epsilon ε_0 have a significant impact when computing spectral shape factors. The higher the ductility or the target epsilon, the higher the spectral shape factors.

- Collapse capacities are not highly sensitive to the PGA and PGV limits established when selecting ground motions. Since there are few earthquake records with high PGA and PGV values available for engineering purposes, including records with low-intensity levels is also a suitable strategy when performing IDA analyses.

The subduction set proposed in this chapter was developed with the purpose of being a tool for engineers and researchers when applying the guidelines of the FEMA P-695 methodology to quantify seismic performance factors of structural systems. Although the set pretends to be suitable for a wide range of seismic threats and engineering applications, special care must be taken when evaluating sites with special conditions (such as those near active faults), structures with very long periods, or buildings with significant irregularities.

REFERENCES

Aguiar, R. 2003, *Análisis sísmico por desempeño*, ESPE, Sangolquí, Ecuador.

AISC 2011, *Steel construction manual*, American Institute of Steel Construction, Chicago, Illinois.

Ajay, M. 1995, *Estimating building stocks for earthquake mitigation and recovery planning*, American National Standards Institute and American Wood Council, Washington, D.C.

AlHamaydeh, M., Abdullah, S., Hamid, A. & Mustapha, A. 2011, 'Seismic design factors for RC special moment resisting frames in Dubai, UAE', *Earthquake Engineering and Engineering Vibration*, vol. 10, pp. 495–506.

American Wood Council 2015, *Special design provisions for wind and seismic*, ANSI/AWC SDPWS-2015, Leesburg, VA.

ASCE 2016, *Minimum design loads and associated criteria for buildings and other structures*, ASCE Standard ASCE/SEI 7-16, American Society of Civil Engineers, Reston, Virginia.

ASCE 2017, *Seismic evaluation and retrofit of existing buildings*, ASCE Standard ASCE/SEI 41-17, American Society of Civil Engineers, Reston, Virginia.

ASTM 2013, *ASTM D2719-13: Standard test methods for structural panels in shear through-the-thickness*, ASTM International, West Conshohocken, PA.

ASTM 2018, *ASTM E2126-11: Standard test methods for cyclic (reversed) load test for shear resistance of vertical elements of the lateral force resisting systems for buildings*, ASTM International, West Conshohocken, PA.

ATC 2008, *Here today—Here tomorrow, earthquake safety for soft-story buildings*, Applied Technology Council, San Francisco Department of Building Inspection, San Francisco, USA.

Bagheri, M. 2018, *Study of deflection of single and multi-storey light frame wood shear walls*, Ph.D. Dissertation, Department of Civil Engineering, University of Ottawa, Ontario, Canada.

Baker, J. 2010, ‘Conditional mean spectrum: tool for ground-motion selection’, *Journal of Structural Engineering*, vol. 137, no. 3, pp. 322–31.

Baker, J. 2015, ‘Efficient analytical fragility function fitting using dynamic structural analysis’, *Earthquake Spectra*, vol. 31, no. 1, pp. 579–99.

Baker, J. 2005, *Vector-valued ground motion intensity measures for probabilistic seismic demand analysis*, Ph.D. Dissertation, Department of Civil and Environmental Engineering, Stanford University, Stanford, CA.

Baker, J. & Cornell, C. 2006, ‘Spectral shape, epsilon and record selection’, *Earthquake Engineering and Structural Dynamics*, vol. 35, no. 9, pp. 1077–95.

Baker, J. & Cornell, C. 2005, *Vector-valued ground motion intensity measures for probabilistic seismic demand analysis*, Report #150, John A. Blume Earthquake Engineering Center, Stanford, CA.

Baker, W., Besjak, C., Sarkisian, M., Lee, P. & Doo, C. 2010, *Proposed methodology to determine seismic performance factors for steel diagrid framed systems*, Council on Tall Buildings and Urban Habitat, Chicago, Illinois.

Berwart, S., Montaño, J. & Santa María, H. 2020, *Manual de diseño de estructuras de madera*, Centro de Innovación en Madera CIM-UC, Santiago, Chile.

Bezabeh, M., Tesfamariam, S. & Popovski, M. 2016, ‘Seismic base shear modification factors for timber- steel hybrid structure: steel moment resisting frames with CLT infill walls’, *Proceedings of the 2016 World Conference on Timber Engineering*, Vienna, Austria.

Bommer, J. & Acevedo, A. 2004, ‘The use of real earthquake accelerograms as input to dynamic analysis’, *Journal of Earthquake Engineering*, vol. 8, no. 1, pp. 43–91.

Bommer, J., Acevedo, A. & Douglas, J. 2003, ‘The selection and scaling of real earthquake accelerograms for use in seismic design and assessment’, *Proceedings of the international conference on seismic bridge design and retrofit*, American Concrete Institute, La Jolla, California.

Börjesson, P. & Gustavsson, L. 2000, ‘Greenhouse gas balances in building construction: wood versus concrete from life-cycle and forest land-use perspectives', *Energy Policy*, vol. 28, pp. 575–88.

Buckett, N. 2014, *Advanced residential construction techniques – opportunities and implications for New Zealand*, Study Report SR311, BRANZ Ltd., Judgeford, New Zealand.

Campbell, K. & Borzorgnia, Y. 2003, 'Updated near-source ground-motion (attenuation) relations for the horizontal and vertical components of peak ground acceleration and acceleration response spectra', *Bulletin of the Seismological Society of America*, vol. 93, no. 1, pp. 314–31.

Cárcamo, S. 2017, *Report Nº 7 – Proposed architectural configurations*, Timber Innovation Center, Santiago, Chile.

Cárcamo, S., Caamaño, J. & Cid, A. 2017, 'Diseño interdisciplinario para el sistema constructivo marco y plataforma, recomendaciones para una buena estructuración', *CLEM-CIMAD*, Buenos Aires, Argentina.

Cartes, S., González, M. & Padilla, J. 2017, 'Actualizar tensiones basicas admisibles de madera aserrada de pino radiata para uso de elementos laminados', *Simposio de Habilitación Profesional*, Concepción, Chile.

Casagrande, D., Bezzi, S., D'Arenzo, G., Schwendner, S., Polastri, A., Seim, W. & Piazza, M. 2020, 'A methodology to determine the seismic low-cycle fatigue strength of timber connections', *Construction and Building Materials*, vol. 231, p. 117026.

Casagrande, D., Rossi, S., Sartori, T. & Tomasi, R. 2012, 'Analytical and numerical analysis of timber framed shear walls', *World Conference on Timber Engineering*, Auckland, New Zealand.

Casagrande, D., Rossi, S., Sartori, T. & Tomasi, R. 2016, 'Proposal of an analytical procedure and a simplified numerical model for elastic response of single-storey timber shear-walls', *Construction and Building Materials*, vol. 102, pp. 1101–12.

Casagrande, D., Rossi, S., Tomasi, R. & Mischi, G. 2016, 'A predictive analytical model for the elasto-plastic behaviour of a light timber-frame shear-wall', *Construction and Building Materials*, vol. 102, pp. 1113–26.

Ccanchi, E. & Taboada, A. 2018, 'Evaluation of the seismic performance of a dwelling of confined masonry walls', *Proceedings of the 11th International Conference on Structural Analysis of Historical Constructions*, Cusco, Peru.

Chacón, M., de la Llera, J., Hube, M., Marques, J. & Lemnitzer, A. 2017, 'Epistemic uncertainty in the seismic response of RC free-plan buildings', *Engineering Structures*, vol. 141, pp. 687–702.

Chandramohan, R. 2016, *Duration of earthquake ground motion: influence on structural collapse risk and integration in design and assessment practice*, Ph.D. Dissertation, Department of Civil and Environmental Engineering, Stanford University, Stanford, CA.

Chandramohan, R., Baker, J. & Deierlein, G. 2016, 'Quantifying the influence of ground motion duration on structural collapse capacity using spectrally equivalent records', *Earthquake Spectra*, vol. 32, no. 2, pp. 927–50.

Chui, Y., Ni, C. & Jaing, L. 1998, 'Finite-element model for nailed wood joints under reversed cyclic load', *Journal of Structural Engineering*, vol. 124, no. 1, pp. 96–103.

Contreras, V. & Boroschek, R. 2012, 'Strong ground motion attenuation relations for Chilean subduction zone interface earthquakes', *15th World Conference on Earthquake Engineering*, Lisbon, Portugal.

CORMA 2014, *Actualización de estudio evaluación del aporte económico y social del sector forestal en chile y análisis de encadenamientos, año 2014*, Corporación Chilena de la Madera, Santiago, Chile.

Cornell, C. 2005, 'On earthquake record selection for nonlinear dynamic analysis', *Proceedings of the Luis Esteva symposium*, Mexico City, Mexico.

Dean, P. & Shenton, H. 2005, 'Experimental investigation of the effect of vertical load on the capacity of wood shear walls', *Journal of Structural Engineering*, vol. 131, no. 7, pp. 1104–13.

Dechent, P., Giuliano, G.C., Dolan, D., Silva, R., Crempien, J., Matamala, J. & Acuña, G. 2016, 'Development of a simplified design seismic-resistant method for timber multi story buildings', *World Conference on Timber Engineering*, Vienna, Austria.

Dechent, P., Silva, R., Dolan, D., Giuliano, G., Crempien, J. & Matamala, J. 2017, 'Simplified design seismic-resistant method for low-rise light-framed shear wall buildings', *16th World Conference on Earthquake Engineering*, Santiago, Chile.

Dolan, D., Dechent, P. & Giuliano, G. 2008, 'Comparison of Chilean and US seismic design provisions for timber structures', *51st International Convention of Society of Wood Science and Technology*, Concepcion, Chile.

Dolan, J. 1989, *The dynamic responses of timber shear walls*, Ph.D. Dissertation, Faculty of Civil Engineering, University of British Columbia, Vancouver, Canada.

Dolan, J. & Foschi, R. 1991, 'Structural analysis model for static loads on timber shear walls', *Journal of Structural Engineering*, vol. 117, no. 3, pp. 851–61.

Dolan, J. & Madsen, B. 1992, 'Monotonic and cyclic nail connection tests', *Canadian Journal of Civil Engineering*, vol. 19, no. 1, pp. 97–104.

Durham, J., Lam, F. & Prion, G. 2001, 'Seismic resistance of wood shear walls with large OSB panels', *Journal of Structural Engineering*, vol. 127, no. 12, pp. 1460–6.

Eads, L., Miranda, E. & Lignos, D. 2016, 'Spectral shape metrics and structural collapse potential', *Earthquake Engineering and Structural Dynamics*, vol. 45, pp. 1643–59.

Easley, J., Foomani, M. & Dodds, R. 1982, 'Formulas for wood shear walls', *Journal of the Structural Division*, vol. 108, no. 11, pp. 2460–78.

Ellingwood, B., Rosowsky, D., Li, Y. & Kim, J.H. 2004, 'Fragility assessment of light-frame wood construction subjected to wind and earthquake hazards', *Journal of Structural Engineering*, vol. 130, no. 12, pp. 1921–30.

FEMA 2000, *FEMA 356: Prestandard and commentary for the seismic rehabilitation of buildings*, Federal Emergency Management Agency, Washington, D.C.

FEMA 2009, *Quantification of building seismic performance factors*, Federal Emergency Management Agency, Washington, D.C.

Filiatrault, A. 1990, 'Static and dynamic analysis of timber shear walls', *Canadian Journal of Civil Engineering*, vol. 17, no. 4, pp. 643–51.

Follesa, M., Fragiacomo, M., Casagrande, D., Tomasi, R., Piazza, M., Vassallo, D., Canetti, D. & Rossi, S. 2018, 'The new provisions for the seismic design of timber buildings in Europe', *Engineering Structures*, vol. 168, pp. 736–47.

Folz, B. & Filiatrault, A. 2001, 'Cyclic analysis of wood shear walls', *Journal of Structural Engineering*, vol. 127, no. 4, pp. 433–41.

Folz, B. & Filiatrault, A. 2004a, 'Seismic analysis of woodframe structures. I: model formulation', *Journal of Structural Engineering*, vol. 130, no. 9, pp. 1353–60.

Folz, B. & Filiatrault, A. 2004b, 'Seismic analysis of woodframe structures. II: model implementation and verification', *Journal of Structural Engineering*, vol. 130, no. 9, pp. 1361–70.

Foschaar, J., Baker, J. & Deierlein, G. 2012, 'Preliminary assessment of ground motion duration effects on structural collapse', *15th World Conference on Earthquake Engineering*, Lisbon, Portugal.

Foschi, R. 2000, 'Modeling the hysteretic response of mechanical connections for wood structures', *Proceedings of the 6th World Conference on Timber Engineering*, Whistler, Canada.

Goulet, C., Haselton, C., Mitrani-Reiser, J., Beck, J., Deierlein, G., Porter, K. & Stewart, J. 2006, 'Evaluation of the seismic performance of a code-conforming reinforced-concrete frame building - from seismic hazard to collapse safety and economic losses', *Earthquake Engineering and Structural Dynamics*, vol. 36, no. 13, pp. 1973–97.

Guendelman, T. 2002, *Análisis y diseño sísmico de edificios de hormigón armado*, Universidad de la Serena, La Serena, Chile.

Guerrero, A. 2018, *Propuesta de formas espectrales para las normas chilenas de diseño* *sísmico*, Master Dissertation, Department of Structural and Geotechnical Engineering, Pontificia Universidad Católica de Chile, Santiago, Chile.

Guíñez, F., Santa María, H. & Almazán, J.L. 2019, 'Monotonic and cyclic behaviour of wood frame shear walls for mid-height timber buildings', *Engineering Structures*, vol. 189, pp. 100–10, viewed 2 July 2019, <https://www.sciencedirect.com/science/article/pii/S0141029618334631?via%3Dihub>.

Gupta, A. & Kuo, G. 1987, 'Wood-framed shear walls with uplifting', *Journal of Structural Engineering*, vol. 113, no. 2, pp. 241–59.

Gustavsson, L., Pingoud, K. & Sathre, R. 2006, 'Carbon dioxide balance of wood substitution: comparing concrete- and wood-framed buildings', *Mitigation and Adaptation Strategies for Global Change*, vol. 11, no. 3, pp. 667–91.

Gutkowski, R. & Castillo, A. 1988, 'Single- and double-sheathed wood shear wall study', *Journal of Structural Engineering*, vol. 113, no. 2, pp. 241–59.

Harmsen, S. 2001, 'Mean and modal ε in the deaggregation of probabilistic ground motion', *Bulletin of the Seismological Society of America*, vol. 91, no. 6, pp. 1537–52.

Harmsen, S., Frankel, A. & Petersen, M. 2003, *Deaggregation of U.S. seismic hazard sources: The 2002 Update*, U.S. Geological Survey Open-File Report 03-440, Sunrise Valley Drive Reston, VA.

Haselton, C. 2006, *Assessing seismic collapse safety of modern reinforced concrete moment-frame buildings*, Ph.D. Dissertation, Department of Civil and Environmental Engineering, Stanford University, Stanford, CA.

Haselton, C. & Baker, J. 2006, 'Ground motion intensity measures for collapse capacity prediction: choice of optimal spectral period and effect of spectral shape', *Proceedings 8th National Conference on Earthquake Engineering*, San Francisco, CA.

Haselton, C. & Deierlein, G. 2007, *Assessing seismic collapse safety of modern reinforced concrete frame buildings*, Technical Report No. 156, John A. Blume Earthquake Engineering Center, Stanford University, Stanford, CA.

Huang, X. 2013, *Diaphragm stiffness in wood-frame construction*, Master Dissertation, Faculty of Graduate and Postdoctoral Studies, University Of British Columbia, Vancouver, Canada.

Hummel, J., Seim, W. & Otto, S. 2016, 'Steifigkeit und Eigenfrequenzen im mehrgeschossigen Holzbau', *Bautechnik*, vol. 93, no. 11, pp. 781–94.

Ibarra, L. & Krawinkler, H. 2005a, 'Effect of uncertainty in system deterioration parameters on the variance of collapse capacity', *9th International Conference on Structural Safety and Reliability*, Rome, Italy.

Ibarra, L. & Krawinkler, H. 2005b, *Global collapse of frame structures under seismic excitations*, PEER Report 2005/06, and John A. Blume Earthquake Engineering Center Technical Report No.152, Department of Civil Engineering, Stanford University, Stanford, CA.

Iervolino, I., Maddaloni, G. & Cosenza, E. 2008, 'Eurocode 8 compliant real record sets for seismic analysis of structures', *Journal of Earthquake Engineering*, vol. 12, no. 1, pp. 54–90.

INFOR 2016, *Anuario forestal 2015*, Instituto Forestal, Santiago, Chile.

INFOR 2017a, *Anuario forestal 2016*, Instituto Forestal, Santiago, Chile.

INFOR 2017b, *Ensayos de flexión, tracción y compresión a madera aserrada de Pino Radiata*, Instituto Forestal, Concepción, Chile.

INN 2013, *Análisis y diseño de edificios con aislación sísmica*, NCh 2745-2013, Instituto Nacional de Normalización, Santiago, Chile.

INN 2009, *Diseño sísmico de edificios*, NCh 433.Of1996Mod2012, Instituto Nacional de Normalización, Santiago, Chile.

INN 2014, *Madera - Construcciones en Madera – Cálculo*, NCh 1198, Instituto Nacional de Normalización, Santiago, Chile.

INN 2006, *Madera estructural. Determinación de propiedades físicas y mecánicas de la* *madera clasificada por su resistencia. Parte 1: Métodos de ensayo en tamaño estructural. NCh 3028/1-Of 2006*, Instituto Nacional de Normalización, Santiago, Chile.

Itani, R. & Cheung, C. 1984, 'Nonlinear analysis of sheathed wood diaphragms', *Journal of Structural Engineering*, vol. 110, no. 9, pp. 2137–47.

Jara, A. & Benedetti, F. 2017, *Informe No. 14 – Registro de estudio de ensayos de conectores*, University of the Bío Bío, Concepción, Chile.

Jayamon, J., Line, P. & Charney, F. 2015, 'An assessment of uncertainty in the performance evaluation of wood shear wall structures', *Structures Congress*, Portland, Oregon.

Jayamon, J., Line, P. & Charney, F. 2017, 'Seismic performance assessment of wood-frame shear wall structures subjected to ground motion variations', *World Conference on Earthquake Engineering*, Santiago, Chile.

Jayamon, J., Line, P. & Charney, F. 2019, 'Sensitivity of wood-frame shear wall collapse performance to variations in hysteretic model parameters', *Journal of Structural Engineering*, vol. 145, no. 1, pp. 1–12.

Jayamon, J., Line, P. & Charney, F. 2018, 'State-of-the-art review on damping in wood-frame shear wall structures', *Journal of Structural Engineering*, vol. 144, no. 12, pp. 1–13.

Johnston, A., Dean, P. & Shenton, H. 2006, 'Effects of vertical load and hold-down anchors on the cyclic response of wood framed shear walls', *Journal of Structural Engineering*, vol. 132, no. 9, pp. 1426–34.

Judd, J. & Fonseca, F. 2005, 'Analytical model for sheathing-to-framing connections in wood shear walls and diaphragms', *Journal of Structural Engineering*, vol. 131, no. 2, pp. 345–52.

Katsanos, E., Sextos, A. & Manolis, G. 2010, 'Selection of earthquake ground motion records: a state-of-the-art review from a structural engineering perspective', *Soil Dynamics and Earthquake Engineering*, vol. 30, pp. 157–69.

Krawinkler, H., Parisi, F., Ibarra, L., Ayoub, A. & Medina, R. 2001, *Development of a testing protocol for woodframe structures*, CUREE Report W-02, Task 1.3.2, Consortium of

Universities for Research in Earthquake Engineering, Richmond, CA.

Kunnath, S. & Chai, Y. 2004, ‘Cumulative damage-based inelastic cyclic demand spectrum’, *Earthquake Engineering and Structural Dynamics*, vol. 33, no. 4, pp. 499–520.

Langlois, J.D., Gupta, R. & Miller, T.H. 2004, ‘Effects of reference displacement and damage accumulation in wood shear walls’, *Journal of Structural Engineering*, vol. 130, no. 3, pp. 470–9.

Lebeda, D., Gupta, R., Rosowsky, D. & Dolan, D. 2005, ‘Effect of hold-down misplacement on strength and stiffness of wood shear walls’, *Practice Periodical on Structural Design and Construction*, vol. 10, no. 2, pp. 79–87.

Lee, K. & Rosowsky, D. 2006, ‘Fragility analysis of woodframe buildings considering combined snow and earthquake loading’, *Structural Safety*, vol. 28, no. 3, pp. 289–303.

Li, M., Lam, F., Yeh, B., Skaggs, T., Rammer, D. & Wacker, J. 2012, ‘Modeling force transfer around openings in wood-frame shear walls’, *Journal of Structural Engineering*, vol. 138, no. 12, pp. 1419–26.

Liel, B. 2008, *Assessing the collapse risk of California’s existing reinforced concrete frame structure: metrics for seismic safety decisions*, Ph.D. Dissertation, Department of Civil and Environmental Engineering, Stanford University, Stanford, CA.

van de Lindt, J. 2004, ‘Evolution of Wood Shear Wall Testing , Modeling , and Reliability Analysis : Bibliography’, *Practice Periodical on Structural Design and Construction*, vol. 9, no. 1, pp. 44–53.

van de Lindt, J., Bahmani, P., Mochizuki, G., Pryor, S., Gershfeld, M., Tian, J., Symans, M. & Rammer, D. 2016, ‘Experimental seismic behavior of a full-scale four-story soft-story wood-frame building with retrofits. II: shake table test results’, *Journal of Structural Engineering (United States)*, vol. 142, no. 4, pp. 1–14.

van de Lindt, J. & Gupta, R. 2006, ‘Damage and damage prediction for wood shearwalls subjected to simulated earthquake loads’, *Journal of Structural Engineering*, vol. 20, no. 2, pp. 176–84.

van de Lindt, J., Pei, S., Liu, H. & Filiatrault, A. 2010, ‘Three-dimensional seismic response of a full-scale light-frame wood building: numerical study’, *Journal of Structural Engineering*, vol. 136, no. 1, pp. 56–65.

van de Lindt, J., Pei, S., Pang, W. & Shirazi, S. 2012, ‘Collapse testing and analysis of a light-frame wood garage wall’, *Journal of Structural Engineering*, vol. 138, no. 4, pp. 492–501.

van de Lindt, J., Pei, S., Pryor, S., Shimizu, H. & Isoda, H. 2010, ‘Experimental seismic response of a full-scale six-story light-frame wood building’, *Journal of Structural Engineering*, vol. 136, no. 10, pp. 1262–72.

van de Lindt, J., Rosowsky, D., Pang, W. & Pei, S. 2013, ‘Performance-based seismic design of midrise woodframe buildings’, *Journal of Structural Engineering*, vol. 139, no. 8, pp. 1294–302.

Malhotra, P. 2002, ‘Cyclic-demand spectrum’, *Earthquake Engineering and Structural Dynamics*, vol. 31, no. 7, pp. 1441–57.

Mergos, P. & Beyer, K. 2015, ‘Displacement-based seismic design of symmetric single-storey wood-frame buildings with the aid of N2 method’, *Frontiers in Built Environment*, vol. 1, no. 10, pp. 1–11.

Nassani, D.E. 2014, ‘A simple model for calculating the fundamental period of vibration in steel structures’, *APCBEE Procedia*, vol. 9, pp. 339–46.

Orellana, P. 2020, *Cyclic behavior of wood-frame shear walls with axial compressive load and bending moment for mid-rise timber buildings*, Master Dissertation, School of Engineering, Pontifical Catholic University of Chile, Santiago, Chile.

Pang, W. & Hassanzadeh, S. 2012, ‘Corotational model for cyclic analysis of light-frame wood shear walls and diaphragms’, *Journal of Structural Engineering*, vol. 139, no. 8, pp. 1303–17.

Pang, W., Rosowsky, D., Pei, S. & van de Lindt, J. 2007, ‘Evolutionary parameter hysteretic model for wood shear walls’, *Journal of Structural Engineering*, vol. 133, no. 8, pp. 1118–29.

Pang, W., Rosowsky, D., Pei, S. & van de Lindt, J. 2010, 'Simplified direct displacement design of a six-story woodframe building and pretest seismic performance assessment', *Journal of Structural Engineering*, vol. 136, no. 7, pp. 813–25.

PEER 2002, *PEER NGA database*, Pacific Earthquake Engineering Research Center, University of California, Berkeley, CA.

Pei, S. & van de Lindt, J. 2009, 'Coupled shear-bending formulation for seismic analysis of stacked wood shear wall systems', *Earthquake Engineering and Structural Dynamics*, vol. 38, pp. 1631–47.

Pei, S. & van de Lindt, J. 2011, 'Seismic numerical modeling of a six-story light-frame wood building: comparison with experiments', *Journal of Earthquake Engineering*, vol. 15, no. 6, pp. 924–41.

Pei, S. & van de Lindt, J. 2010, *User's manual for SAPWood for Windows. Version 2.0*, Colorado State University, Fort Collins, Colorado.

Pei, S., van de Lindt, J., Pryor, S., Shimizu, H., Isoda, H. & Rammer, D. 2010, *Seismic testing of a full-scale mid-rise building: the NEESWood capstone test*, Technical report MCEER-10-0008, Colorado State University, Fort Collins, CO.

Raghunandan, M. & Liel, A. 2013, 'Effect of ground motion duration on earthquake-induced structural collapse', *Structural Safety*, vol. 41, pp. 119–33.

Raghunandan, M., Liel, A. & Luco, N. 2015, 'Collapse risk of buildings in the Pacific Northwest Region due to subduction earthquakes', *Earthquake Spectra*, vol. 31, no. 4, pp. 2087–115.

Rossi, S., Casagrande, D., Tomasi, R. & Piazza, M. 2016, 'Seismic elastic analysis of light timber-frame multi-storey buildings: Proposal of an iterative approach', *Construction and Building Materials*, vol. 102, pp. 1154–67.

Sadeghi Marzaleh, A., Nerbano, S., Sebastiani Croce, A. & Steiger, R. 2018, 'OSB sheathed light-frame timber shear walls with strong anchorage subjected to vertical load, bending moment, and monotonic lateral load', *Engineering Structures*, vol. 173, pp. 787–99.

Santa María, H., Caicedo, N., Montaño, J. & Almazán, J. 2016, 'Towards timber mid-rise buildings in Chile: structural design challenge and regulation gaps', *Proceedings of the WCTE 2016 World Conference on Timber Engineering*, Vienna, Austria.

Santa María, H., Hube, M., Rivera, F., Yepes-Estrada, C. & Valcárcel, J. 2017, 'Development of national and local exposure models of residential structures in Chile', *Natural Hazards*, vol. 86, pp. 55–79.

Sartori, T. & Tomasi, R. 2013, 'Experimental investigation on sheathing-to-framing connections in wood shear walls', *Engineering Structures*, vol. 56, pp. 2197–205.

Schick, M. & Seim, W. 2019, 'Overstrength values for light frame timber wall elements based on reliability methods', *Engineering Structures*, vol. 185, pp. 230–42.

Schwendner, S., Hummel, J. & Seim, W. 2018, 'Evaluation of the behaviour factor q for light-frame timber buildings - a comparative study', *World Conference on Timber Engineering*, Seoul, South Korea.

Segura, G. 2017, *Determinación del módulo de corte de tableros de fibra orientada a través de ensayo de análisis modal*, Bachelor's Dissertation, Department of Civil and Environmental Engineering, Universidad del BíoBío, Concepción, Chile.

Seible, F., Filiatrault, A. & Uang, C. 1999, 'Workshop on Seismic Testing, Analysis and Design of Woodframe Construction', *Proceedings of the Invitational Workshop on Seismic Testing, Analysis and Design of Woodframe Construction*, Richmond, CA.

Seim, W., Hummel, J. & Vogt, T. 2014, 'Earthquake design of timber structures - Remarks on force-based design procedures for different wall systems', *Engineering Structures*, vol. 76, pp. 124–37.

Seim, W., Kramar, M., Pazlar, T. & Vogt, T. 2016, 'OSB and GFB as sheathing materials for timber-framed shear walls: comparative study of seismic resistance', *Journal of Structural Engineering*, vol. 142, no. 4, p. E4015004.

Shenton, H., Dinehart, D. & Elliott, T. 1998, 'Stiffness and energy degradation of wood frame shear walls', *Canadian Journal of Civil Engineering*, vol. 25, no. 3, pp. 412–23.

Shome, N. & Cornell, C. 1999, *Probabilistic seismic demand analysis of nonlinear structures*, RMS Program, Stanford, CA.

Simpson Strong-Tie 2018, *Seismic and wind anchor tiedown system guide*, Simpson Strong-Tie Company Inc, Canada.

Simpson Strong-Tie 2015, *Wood construction connectors*, Simpson Strong-Tie Company Inc, Pleasanton, CA.

Upton, B., Miner, R., Spinney, M. & Heath, L. 2008, 'The greenhouse gas and energy impacts of using wood instead of alternatives in residential construction in the United States', *Biomass and Bioenergy*, vol. 32, no. 1, pp. 1–10.

Vamvatsikos, D. & Cornell, C. 2002, 'Incremental dynamic analysis', *Earthquake Engineering and Structural Dynamics*, vol. 31, no. 3, pp. 491–514.

Vielma, J. & Cando, M. 2017, 'Evaluación del factor de comportamiento de la Norma Ecuatoriana de la Construcción para estructuras metálicas porticadas', *Revista Internacional de Métodos Numéricos para Cálculo y Diseño en Ingeniería*, vol. 33, no. 3, pp. 271–9.

Wescott, J. 2005, *Horizontal stiffness of wood diaphragms*, Ph.D. Dissertation, Faculty of Civil Engineering, Virginia Polytechnic Institute and State University, Blacksburg, VA.

Westenenk, B., de la Llera, J., Besa, J., Jünemann, R., Moehle, J., Lüders, C., Inaudi, J., Elwood, K. & Hwang, S. 2012, 'Response of reinforced concrete buildings in Concepción during the Maule earthquake', *Earthquake Spectra*, vol. 28, no. 1, pp. 257–80.

White, M. & Dolan, J. 1995, 'Nonlinear shear-wall analysis', *Journal of Structural Engineering*, vol. 121, no. 11, pp. 1629–35.

WHO 2016, *Ambient air pollution: a global assessment of exposure and burden of disease*, World Health Organization, Geneva, Switzerland.

Xu, J. & Dolan, J. 2009, 'Development of a wood-frame shear wall model in ABAQUS', *Journal of Structural Engineering*, vol. 135, no. 8, pp. 977–84.

Yin, Y. & Li, Y. 2010, 'Seismic collapse risk of light-frame wood construction considering aleatoric and epistemic uncertainties', *Structural Safety*, vol. 32, no. 4, pp. 250–61.

Zareian, F. 2006, *Simplified performance-based earthquake engineering*, Ph.D. Dissertation, Department of Civil and Environmental Engineering, Stanford University, Stanford, CA.

APPENDIX A

STATIC AND DYNAMIC RESULTS OF THE ARCHETYPES UNDER ANALYSIS

This appendix presents the full results of static and dynamic analyses carried out on each of the 201 archetypes presented in Section 1.2.4. Each archetype was assigned an ID that contains all its information. For instance, Archetype #1's ID is: 3_1_C_002_5-5_D_II_3_MGP10_HD. This stands for the following:

- *3*: three stories.
- *1*: archetype number of the subset.
- *C*: architectural archetype “C”.
- *002*: maximum allowable drift Δ_{max} equal to 0.002H.
- *5-5*: R factor equal to 5.5.
- *D*: soil class “D”.
- *II*: occupancy category “II”.
- *3*: seismic zone “3”.
- *MGP10*: timber grade.
- *HD*: anchorage system “discrete hold-downs”.

Table A-1 presents the results for each archetype as follows: Ω_x and Ω_y = over-strength factor in each direction, Ω_m = mean over-strength factor, μ_x and μ_y = ductility in each direction, μ_m = mean ductility, CMR = collapse margin ratio, SSF = spectral shape factor, and ACMR = adjusted collapse margin ratio.

Table A-1. Full static and dynamic results of the archetypes under analysis.

#	Archetype ID	Static results				Dynamic results		
		Ω_x	Ω_y	μ_x	μ_y	CMR	SSF	ACMR
1	3_1_C_002_5-5_D_II_3_MGP10_HD	3.20	3.55	5.15	6.20	1.85	1.31	2.90
2	3_2_C_004_6-5_D_II_3_MGP10_HD	2.48	3.21	4.87	5.33	1.21	1.29	1.87
3	3_3_C_002_5-5_C_II_3_MGP10_HD	2.83	3.86	5.17	5.97	1.78	1.30	2.78

4	3_4_C_004_6-5_C_II_3_MGP10_HD	2.87	3.80	4.64	5.16	1.40	1.28	2.15
5	3_5_C_002_5-5_B_II_3_MGP10_HD	3.26	4.11	5.45	6.00	1.78	1.31	2.79
6	3_6_C_004_6-5_B_II_3_MGP10_HD	3.63	4.27	6.32	5.18	1.50	1.31	2.36
7	3_7_C_002_5-5_A_II_3_MGP10_HD	3.51	5.93	5.11	5.15	1.49	1.29	2.31
8	3_8_C_004_6-5_A_II_3_MGP10_HD	4.38	6.65	5.10	5.19	1.54	1.29	2.39
9	3_9_C_002_5-5_D_II_1_MGP10_HD	2.81	4.23	5.73	5.21	1.91	1.14	2.62
10	3_10_C_004_6-5_D_II_1_MGP10_HD	2.71	4.72	4.96	5.15	1.34	1.13	1.82
11	3_11_C_002_5-5_C_II_1_MGP10_HD	3.91	5.13	5.11	5.21	2.09	1.14	2.84
12	3_12_C_004_6-5_C_II_1_MGP10_HD	3.89	6.18	5.12	5.15	1.42	1.14	1.94
13	3_13_C_002_5-5_B_II_1_MGP10_HD	4.89	6.75	5.12	5.16	1.86	1.14	2.53
14	3_14_C_004_6-5_B_II_1_MGP10_HD	6.54	8.81	5.11	5.08	1.88	1.13	2.55
15	3_15_C_002_5-5_A_II_1_MGP10_HD	7.97	11.99	5.11	5.08	3.04	1.13	4.14
16	3_16_C_004_6-5_A_II_1_MGP10_HD	9.53	14.16	5.11	5.08	3.03	1.13	4.12
17	4_1_C_004_6-5_B_II_3_MGP10_HD	2.52	4.15	4.81	4.57	1.21	1.27	1.85
18	4_2_C_002_5-5_A_II_3_MGP10_HD	3.96	5.16	4.49	4.69	1.92	1.29	2.97
19	4_3_C_004_6-5_A_II_3_MGP10_HD	4.17	5.85	4.36	4.72	1.79	1.30	2.80
20	4_4_C_002_5-5_D_II_1_MGP10_HD	2.25	3.91	5.38	5.01	1.80	1.14	2.45
21	4_5_C_004_6-5_D_II_1_MGP10_HD	2.12	3.56	5.35	4.63	1.28	1.15	1.77
22	4_6_C_002_5-5_C_II_1_MGP10_HD	3.25	5.01	4.92	5.68	1.78	1.14	2.43
23	4_7_C_004_6-5_C_II_1_MGP10_HD	3.67	5.14	4.53	4.69	1.21	1.15	1.67
24	4_8_C_002_5-5_B_II_1_MGP10_HD	4.92	6.77	4.52	4.73	1.87	1.16	2.60
25	4_9_C_004_6-5_B_II_1_MGP10_HD	6.08	8.40	4.53	4.66	1.97	1.18	2.78
26	4_10_C_002_5-5_A_II_1_MGP10_HD	7.19	11.12	4.53	4.62	3.15	1.19	4.49
27	4_11_C_004_6-5_A_II_1_MGP10_HD	8.57	13.29	4.55	4.64	3.01	1.19	4.30
28	5_1_C_002_5-5_A_II_3_MGP10_HD	5.04	5.25	3.71	4.49	2.27	1.30	3.54
29	5_2_C_004_6-5_A_II_3_MGP10_HD	3.69	4.94	5.55	4.80	2.04	1.41	3.44
30	5_3_C_004_6-5_C_II_1_MGP10_HD	3.32	4.27	4.68	4.48	1.14	1.23	1.68
31	5_4_C_002_5-5_B_II_1_MGP10_HD	6.03	6.47	3.91	4.69	1.91	1.22	2.80
32	5_5_C_004_6-5_B_II_1_MGP10_HD	5.94	7.33	4.56	4.66	1.90	1.25	2.85
33	5_6_C_002_5-5_A_II_1_MGP10_HD	6.95	9.90	4.15	4.93	2.52	1.24	3.77
34	5_7_C_004_6-5_A_II_1_MGP10_HD	6.46	10.24	4.32	4.65	2.45	1.25	3.67
35	3_1_D_002_5-5_D_II_3_MGP10_HD	3.26	5.77	4.97	3.78	1.87	1.26	2.83
36	3_2_D_004_6-5_D_II_3_MGP10_HD	2.89	3.00	5.75	5.41	1.24	1.30	1.94
37	3_3_D_002_5-5_C_II_3_MGP10_HD	3.08	4.17	5.74	4.79	1.77	1.29	2.74
38	3_4_D_004_6-5_C_II_3_MGP10_HD	2.50	3.05	5.39	5.45	1.34	1.30	2.09
39	3_5_D_002_5-5_B_II_3_MGP10_HD	3.52	5.73	5.78	2.58	1.82	1.26	2.74
40	3_6_D_004_6-5_B_II_3_MGP10_HD	3.19	3.59	5.38	5.51	1.62	1.30	2.52
41	3_7_D_002_5-5_A_II_3_MGP10_HD	4.41	5.17	5.16	5.16	2.26	1.29	3.51
42	3_8_D_004_6-5_A_II_3_MGP10_HD	5.05	5.79	5.12	5.11	2.22	1.30	3.47
43	3_9_D_002_5-5_D_II_1_MGP10_HD	3.42	5.54	5.65	5.32	1.85	1.14	2.53
44	3_10_D_004_6-5_D_II_1_MGP10_HD	3.28	3.84	5.17	5.14	1.68	1.14	2.29
45	3_11_D_002_5-5_C_II_1_MGP10_HD	4.17	5.76	5.32	5.72	2.32	1.14	3.18
46	3_12_D_004_6-5_C_II_1_MGP10_HD	4.30	4.94	5.11	5.15	2.08	1.14	2.83

47	3_13_D_002_5-5_B_II_1_MGP10_HD	5.53	7.36	5.14	6.05	2.47	1.14	3.39
48	3_14_D_004_6-5_B_II_1_MGP10_HD	6.73	7.63	5.12	5.11	2.80	1.15	3.87
49	3_15_D_002_5-5_A_II_1_MGP10_HD	9.21	10.86	5.13	5.13	4.25	1.17	5.96
50	3_16_D_004_6-5_A_II_1_MGP10_HD	10.88	13.01	5.13	5.11	4.29	1.18	6.07
51	4_1_D_004_6-5_B_II_3_MGP10_HD	3.19	3.62	4.61	5.65	1.07	1.29	1.65
52	4_2_D_002_5-5_A_II_3_MGP10_HD	4.79	5.44	5.37	4.52	2.12	1.31	3.32
53	4_3_D_004_6-5_A_II_3_MGP10_HD	4.72	5.10	4.87	4.73	2.21	1.34	3.54
54	4_4_D_002_5-5_D_II_1_MGP10_HD	3.49	4.59	4.74	4.68	1.78	1.13	2.42
55	4_5_D_004_6-5_D_II_1_MGP10_HD	2.64	3.17	4.83	5.20	1.44	1.16	2.01
56	4_6_D_002_5-5_C_II_1_MGP10_HD	4.12	4.92	4.43	4.97	1.62	1.13	2.19
57	4_7_D_004_6-5_C_II_1_MGP10_HD	3.93	4.33	4.61	4.65	1.76	1.18	2.49
58	4_8_D_002_5-5_B_II_1_MGP10_HD	5.50	6.77	4.62	4.37	2.63	1.18	3.73
59	4_9_D_004_6-5_B_II_1_MGP10_HD	6.58	7.38	4.63	4.65	2.91	1.21	4.21
60	4_10_D_002_5-5_A_II_1_MGP10_HD	8.19	10.16	4.63	4.55	4.22	1.21	6.14
61	4_11_D_004_6-5_A_II_1_MGP10_HD	9.68	11.14	4.61	4.65	4.25	1.22	6.22
62	5_1_D_004_6-5_B_II_3_MGP10_HD	2.77	3.08	5.47	5.08	1.31	1.34	2.10
63	5_2_D_002_5-5_A_II_3_MGP10_HD	3.14	6.78	4.82	4.17	1.85	1.27	2.81
64	5_3_D_004_6-5_A_II_3_MGP10_HD	4.09	4.92	5.30	5.20	2.18	1.42	3.70
65	5_4_D_004_6-5_D_II_1_MGP10_HD	1.98	2.63	5.28	5.10	1.27	1.18	1.80
66	5_5_D_004_6-5_C_II_1_MGP10_HD	3.39	3.81	4.76	4.31	1.56	1.27	2.38
67	5_6_D_002_5-5_B_II_1_MGP10_HD	5.31	6.41	4.62	4.04	2.46	1.24	3.65
68	5_7_D_004_6-5_B_II_1_MGP10_HD	5.75	6.39	4.65	4.30	2.63	1.27	3.99
69	5_8_D_002_5-5_A_II_1_MGP10_HD	6.46	9.62	4.19	4.80	3.17	1.27	4.82
70	5_9_D_004_6-5_A_II_1_MGP10_HD	7.63	8.77	4.65	4.30	3.41	1.27	5.19
71	3_1_P_002_5-5_D_II_3_MGP10_HD	3.88	2.91	4.02	6.04	1.90	1.29	2.93
72	3_2_P_004_6-5_D_II_3_MGP10_HD	4.33	3.01	4.45	5.66	1.73	1.29	2.67
73	3_3_P_002_5-5_C_II_3_MGP10_HD	3.07	2.31	4.98	5.87	1.86	1.30	2.91
74	3_4_P_004_6-5_C_II_3_MGP10_HD	2.71	2.63	6.84	5.40	1.58	1.32	2.50
75	3_5_P_002_5-5_B_II_3_MGP10_HD	3.50	2.68	5.27	5.77	1.94	1.30	3.04
76	3_6_P_004_6-5_B_II_3_MGP10_HD	2.78	3.10	6.39	5.63	1.61	1.32	2.54
77	3_7_P_002_5-5_A_II_3_MGP10_HD	4.24	4.04	5.35	5.08	2.41	1.29	3.74
78	3_8_P_004_6-5_A_II_3_MGP10_HD	4.34	4.49	5.07	5.13	2.13	1.29	3.29
79	3_9_P_002_5-5_D_II_1_MGP10_HD	4.54	3.18	3.32	5.49	1.87	1.12	2.52
80	3_10_P_004_6-5_D_II_1_MGP10_HD	5.11	5.77	5.12	5.23	2.90	1.14	3.95
81	3_11_P_002_5-5_C_II_1_MGP10_HD	4.28	3.63	5.11	5.15	2.62	1.14	3.57
82	3_12_P_004_6-5_C_II_1_MGP10_HD	3.97	4.01	5.26	5.10	1.98	1.14	2.70
83	3_13_P_002_5-5_B_II_1_MGP10_HD	5.06	4.85	5.33	5.10	2.75	1.14	3.76
84	3_14_P_004_6-5_B_II_1_MGP10_HD	5.79	5.84	5.05	5.11	2.29	1.14	3.14
85	3_15_P_002_5-5_A_II_1_MGP10_HD	7.56	8.25	5.06	5.12	3.73	1.16	5.19
86	3_16_P_004_6-5_A_II_1_MGP10_HD	8.94	9.75	5.06	5.12	3.73	1.16	5.19
87	4_1_P_002_5-5_A_II_3_MGP10_HD	3.93	3.70	4.90	4.60	2.41	1.33	3.84
88	4_2_P_004_6-5_A_II_3_MGP10_HD	4.40	4.06	4.78	4.63	2.20	1.34	3.55
89	4_3_P_002_5-5_D_II_1_MGP10_HD	3.21	2.63	5.01	5.88	1.98	1.14	2.71

90	4_4_P_004_6-5_D_II_1_MGP10_HD	2.43	2.58	5.54	4.34	1.51	1.16	2.10
91	4_5_P_002_5-5_C_II_1_MGP10_HD	4.53	3.69	5.00	4.91	2.15	1.13	2.92
92	4_6_P_004_6-5_C_II_1_MGP10_HD	3.48	3.55	4.79	4.62	1.72	1.19	2.46
93	4_7_P_002_5-5_B_II_1_MGP10_HD	4.92	4.81	4.54	4.61	2.65	1.20	3.80
94	4_8_P_004_6-5_B_II_1_MGP10_HD	5.55	5.88	4.60	4.62	2.61	1.21	3.77
95	4_9_P_002_5-5_A_II_1_MGP10_HD	6.95	7.37	4.64	4.61	3.67	1.21	5.34
96	4_10_P_004_6-5_A_II_1_MGP10_HD	8.05	8.71	4.60	4.62	3.65	1.21	5.31
97	5_1_P_002_5-5_A_II_3_MGP10_HD	5.55	3.45	2.99	5.08	1.92	1.28	2.96
98	5_2_P_004_6-5_A_II_3_MGP10_HD	3.47	3.81	5.07	4.68	2.39	1.39	4.00
99	5_3_P_004_6-5_C_II_1_MGP10_HD	3.16	3.14	4.73	4.27	1.54	1.27	2.34
100	5_4_P_002_5-5_B_II_1_MGP10_HD	5.81	4.47	4.48	4.28	3.42	1.26	5.18
101	5_5_P_004_6-5_B_II_1_MGP10_HD	5.35	5.28	4.87	4.27	2.43	1.27	3.71
102	5_6_P_002_5-5_A_II_1_MGP10_HD	6.24	6.06	4.50	4.28	3.58	1.26	5.42
103	5_7_P_004_6-5_A_II_1_MGP10_HD	6.50	7.16	4.22	4.26	3.04	1.26	4.59
104	3_1_Q_002_5-5_D_II_3_MGP10_HD	4.72	3.26	3.79	5.24	2.09	1.27	3.18
105	3_2_Q_004_6-5_D_II_3_MGP10_HD	2.84	2.53	6.79	5.85	1.51	1.33	2.41
106	3_3_Q_002_5-5_C_II_3_MGP10_HD	4.29	3.36	5.28	4.88	1.89	1.29	2.92
107	3_4_Q_004_6-5_C_II_3_MGP10_HD	2.76	2.64	5.99	5.42	1.51	1.31	2.37
108	3_5_Q_002_5-5_B_II_3_MGP10_HD	4.54	3.11	5.74	5.67	1.85	1.31	2.90
109	3_6_Q_004_6-5_B_II_3_MGP10_HD	3.44	3.13	5.81	5.45	1.76	1.31	2.76
110	3_7_Q_002_5-5_A_II_3_MGP10_HD	4.38	4.49	5.24	5.22	2.66	1.29	4.13
111	3_8_Q_004_6-5_A_II_3_MGP10_HD	4.73	4.64	5.10	5.12	2.37	1.30	3.70
112	3_9_Q_002_5-5_D_II_1_MGP10_HD	4.12	3.36	4.70	5.41	2.20	1.13	3.00
113	3_10_Q_004_6-5_D_II_1_MGP10_HD	3.19	3.05	5.07	5.12	1.67	1.13	2.28
114	3_11_Q_002_5-5_C_II_1_MGP10_HD	5.43	3.89	4.95	5.29	2.76	1.14	3.76
115	3_12_Q_004_6-5_C_II_1_MGP10_HD	4.33	4.18	5.12	5.13	2.14	1.14	2.93
116	3_13_Q_002_5-5_B_II_1_MGP10_HD	6.02	5.41	5.33	5.20	3.30	1.14	4.53
117	3_14_Q_004_6-5_B_II_1_MGP10_HD	6.45	6.49	5.11	5.13	2.91	1.16	4.05
118	3_15_Q_002_5-5_A_II_1_MGP10_HD	9.17	8.62	5.09	5.09	4.35	1.17	6.12
119	3_16_Q_004_6-5_A_II_1_MGP10_HD	10.68	10.18	5.11	5.13	4.27	1.17	6.00
120	4_1_Q_004_6-5_B_II_3_MGP10_HD	3.89	2.90	3.50	5.20	1.67	1.26	2.53
121	4_2_Q_002_5-5_A_II_3_MGP10_HD	4.30	3.89	4.87	4.65	2.37	1.32	3.77
122	4_3_Q_004_6-5_A_II_3_MGP10_HD	4.48	4.35	4.68	4.73	2.31	1.34	3.73
123	4_4_Q_002_5-5_D_II_1_MGP10_HD	6.08	2.75	3.81	5.97	2.17	1.13	2.95
124	4_5_Q_004_6-5_D_II_1_MGP10_HD	2.79	2.69	4.56	4.80	1.62	1.15	2.23
125	4_6_Q_002_5-5_C_II_1_MGP10_HD	6.10	3.73	7.08	5.04	1.78	1.15	2.45
126	4_7_Q_004_6-5_C_II_1_MGP10_HD	3.82	3.64	4.72	4.61	2.00	1.20	2.87
127	4_8_Q_002_5-5_B_II_1_MGP10_HD	5.74	4.98	4.53	4.63	3.35	1.20	4.83
128	4_9_Q_004_6-5_B_II_1_MGP10_HD	6.41	6.17	4.62	4.62	3.07	1.22	4.49
129	4_10_Q_002_5-5_A_II_1_MGP10_HD	8.28	7.83	4.54	4.60	4.63	1.22	6.79
130	4_11_Q_004_6-5_A_II_1_MGP10_HD	9.23	9.04	4.62	4.62	4.49	1.22	6.59
131	5_1_Q_004_6-5_A_II_3_MGP10_HD	3.83	3.98	4.75	4.68	2.35	1.38	3.90
132	5_2_Q_004_6-5_C_II_1_MGP10_HD	3.48	3.19	4.38	4.27	1.74	1.26	2.63

133	5_3_Q_002_5-5_B_II_1_MGP10_HD	5.95	5.04	4.55	4.77	3.19	1.27	4.88
134	5_4_Q_004_6-5_B_II_1_MGP10_HD	5.67	5.43	4.27	4.28	2.85	1.26	4.31
135	5_5_Q_002_5-5_A_II_1_MGP10_HD	7.41	6.76	4.22	4.26	3.89	1.26	5.87
136	5_6_Q_004_6-5_A_II_1_MGP10_HD	7.41	7.33	4.27	4.27	3.82	1.26	5.77
137	5_1_C_004_6-5_D_II_3_MGP10_ATS	2.80	3.44	4.31	3.52	1.51	1.25	2.26
138	5_2_C_002_5-5_C_II_3_MGP10_ATS	3.04	5.31	4.38	3.36	1.90	1.24	2.84
139	5_3_C_004_6-5_C_II_3_MGP10_ATS	3.88	3.81	4.33	3.59	1.80	1.25	2.70
140	5_4_C_002_5-5_B_II_3_MGP10_ATS	3.75	5.06	4.15	4.42	1.88	1.26	2.84
141	5_5_C_004_6-5_B_II_3_MGP10_ATS	3.54	4.74	3.82	4.21	1.35	1.31	2.13
142	5_6_C_002_5-5_A_II_3_MGP10_ATS	6.99	9.50	4.20	3.23	2.69	1.26	4.05
143	5_7_C_004_6-5_A_II_3_MGP10_ATS	4.72	6.23	3.70	4.35	2.12	1.34	3.42
144	5_8_C_002_5-5_D_II_1_MGP10_ATS	4.68	5.81	3.35	4.43	2.24	1.12	3.00
145	5_9_C_004_6-5_D_II_1_MGP10_ATS	3.25	3.79	3.62	4.20	1.33	1.16	1.86
146	5_10_C_002_5-5_C_II_1_MGP10_ATS	6.02	8.23	4.26	4.11	2.53	1.13	3.43
147	5_11_C_004_6-5_C_II_1_MGP10_ATS	4.31	5.41	4.12	4.25	1.13	1.22	1.65
148	5_12_C_002_5-5_B_II_1_MGP10_ATS	11.78	8.36	3.10	4.32	2.07	1.17	2.91
149	5_13_C_004_6-5_B_II_1_MGP10_ATS	7.42	9.06	4.12	4.25	1.93	1.23	2.84
150	5_14_C_002_5-5_A_II_1_MGP10_ATS	16.63	12.20	4.23	3.18	3.23	1.19	4.64
151	5_15_C_004_6-5_A_II_1_MGP10_ATS	8.34	12.72	3.99	4.29	2.50	1.23	3.68
152	6_1_C_002_7-0_B_II_3_MGP10_ATS	5.92	9.46	4.15	4.42	1.73	1.34	2.79
153	6_2_C_004_7-0_B_II_3_MGP10_ATS	2.84	4.69	3.82	4.21	1.78	1.34	2.85
154	6_3_C_002_7-0_D_II_1_MGP10_ATS	5.19	6.25	3.31	4.43	1.51	1.16	2.10
155	6_4_C_004_7-0_D_II_1_MGP10_ATS	2.91	3.36	3.62	4.20	1.50	1.16	2.09
156	5_1_D_004_6-5_D_II_3_MGP10_ATS	3.50	4.35	4.34	4.39	1.68	1.26	2.54
157	5_2_D_002_5-5_C_II_3_MGP10_ATS	3.83	4.48	4.30	4.58	2.10	1.27	3.19
158	5_3_D_004_6-5_C_II_3_MGP10_ATS	4.63	5.43	4.38	4.47	2.03	1.26	3.09
159	5_4_D_002_5-5_B_II_3_MGP10_ATS	5.03	5.36	4.49	4.64	2.41	1.27	3.67
160	5_5_D_004_6-5_B_II_3_MGP10_ATS	4.10	4.80	3.85	4.01	1.48	1.31	2.32
161	5_6_D_002_5-5_A_II_3_MGP10_ATS	5.76	7.50	3.98	4.34	2.45	1.30	3.82
162	5_7_D_004_6-5_A_II_3_MGP10_ATS	5.54	6.30	4.06	3.90	2.18	1.35	3.53
163	5_8_D_002_5-5_D_II_1_MGP10_ATS	4.93	4.66	4.41	4.27	2.12	1.12	2.86
164	5_9_D_004_6-5_D_II_1_MGP10_ATS	2.99	3.94	4.15	4.11	1.36	1.17	1.91
165	5_10_D_002_5-5_C_II_1_MGP10_ATS	6.43	6.20	3.61	4.29	2.35	1.13	3.19
166	5_11_D_004_6-5_C_II_1_MGP10_ATS	4.46	5.89	4.17	4.43	1.54	1.26	2.32
167	5_12_D_002_5-5_B_II_1_MGP10_ATS	11.80	12.55	2.57	4.19	2.70	1.16	3.76
168	5_13_D_004_6-5_B_II_1_MGP10_ATS	7.58	10.21	4.05	4.15	2.62	1.25	3.94
169	5_14_D_002_5-5_A_II_1_MGP10_ATS	13.41	14.53	4.31	2.79	3.65	1.20	5.27
170	5_15_D_004_6-5_A_II_1_MGP10_ATS	9.76	13.57	4.16	4.44	3.55	1.26	5.37
171	5_1_P_004_6-5_C_II_3_MGP10_ATS	3.83	3.47	4.44	2.82	2.03	1.23	3.00
172	5_2_P_004_6-5_B_II_3_MGP10_ATS	3.81	3.77	4.27	4.23	1.78	1.30	2.77
173	5_3_P_002_5-5_A_II_3_MGP10_ATS	6.18	6.38	4.25	4.32	3.02	1.32	4.77
174	5_4_P_004_6-5_A_II_3_MGP10_ATS	5.32	5.00	4.17	4.16	2.53	1.37	4.14
175	5_5_P_002_5-5_D_II_1_MGP10_ATS	4.01	3.92	4.54	4.35	2.30	1.13	3.13

176	5_6_P_004_6-5_D_II_1_MGP10_ATS	3.54	2.98	4.01	4.07	1.55	1.16	2.17
177	5_7_P_002_5-5_C_II_1_MGP10_ATS	5.77	4.28	4.32	3.83	2.60	1.16	3.60
178	5_8_P_004_6-5_C_II_1_MGP10_ATS	4.10	4.02	4.30	3.78	1.63	1.25	2.45
179	5_9_P_002_5-5_B_II_1_MGP10_ATS	9.98	8.61	4.47	4.71	2.93	1.25	4.40
180	5_10_P_004_6-5_B_II_1_MGP10_ATS	7.30	6.72	4.39	3.79	2.55	1.25	3.83
181	5_11_P_002_5-5_A_II_1_MGP10_ATS	13.37	8.36	4.43	4.14	4.47	1.26	6.75
182	5_12_P_004_6-5_A_II_1_MGP10_ATS	8.38	8.97	4.26	3.78	3.20	1.25	4.80
183	6_1_P_002_7-0_B_II_3_MGP10_ATS	2.94	3.68	4.27	4.23	1.74	1.26	2.64
184	6_2_P_004_7-0_B_II_3_MGP10_ATS	3.88	3.98	4.27	4.23	1.80	1.33	2.87
185	6_3_P_002_7-0_D_II_1_MGP10_ATS	4.35	4.36	4.54	4.35	1.56	1.18	2.21
186	6_4_P_004_7-0_D_II_1_MGP10_ATS	3.18	2.74	4.01	4.07	1.58	1.17	2.21
187	5_1_Q_004_6-5_D_II_3_MGP10_ATS	3.55	3.49	4.43	4.41	1.67	1.26	2.53
188	5_2_Q_002_5-5_C_II_3_MGP10_ATS	3.74	3.73	4.69	4.41	2.13	1.27	3.24
189	5_3_Q_004_6-5_C_II_3_MGP10_ATS	4.48	4.41	4.38	4.31	2.14	1.26	3.24
190	5_4_Q_002_5-5_B_II_3_MGP10_ATS	4.55	4.39	4.62	3.96	2.42	1.26	3.66
191	5_5_Q_004_6-5_B_II_3_MGP10_ATS	6.07	3.78	4.16	3.98	1.74	1.25	2.61
192	5_6_Q_002_5-5_A_II_3_MGP10_ATS	8.43	7.64	4.60	4.11	3.37	1.32	5.34
193	5_7_Q_004_6-5_A_II_3_MGP10_ATS	5.59	5.31	4.29	4.25	2.56	1.37	4.20
194	5_8_Q_002_5-5_D_II_1_MGP10_ATS	5.90	4.28	4.21	4.19	2.72	1.12	3.66
195	5_9_Q_004_6-5_D_II_1_MGP10_ATS	3.71	3.10	4.23	4.16	1.56	1.16	2.17
196	5_10_Q_002_5-5_C_II_1_MGP10_ATS	6.78	4.69	4.31	3.92	2.81	1.14	3.83
197	5_11_Q_004_6-5_C_II_1_MGP10_ATS	5.02	4.13	4.39	4.22	1.91	1.26	2.88
198	5_12_Q_002_5-5_B_II_1_MGP10_ATS	11.99	9.01	4.33	4.34	3.36	1.23	4.98
199	5_13_Q_004_6-5_B_II_1_MGP10_ATS	8.24	6.96	4.35	4.12	3.20	1.26	4.84
200	5_14_Q_002_5-5_A_II_1_MGP10_ATS	17.02	11.56	3.04	4.72	4.36	1.23	6.44
201	5_15_Q_004_6-5_A_II_1_MGP10_ATS	11.93	9.15	4.20	4.16	4.18	1.26	6.30

APPENDIX B

PERFORMANCE GROUPS

This appendix presents a full description of the performance groups developed to bin each of the 201 archetypes of this research. These groups were employed in the evaluation of the two sets seismic performance factors (SPFs), as described in Section 1.3.1.

Table B-1. Description and features of each performance group.

Group #	SPFs	Anchorage system	Seismic zone	Soil class	Fundamental period	Number of archetypes
1	5.5 & 0.002	HD	Zone 1	Soil A	Long	12
2	5.5 & 0.002	HD	Zone 1	Soil B	Long	12
3	5.5 & 0.002	HD	Zone 1	Soil C	Short	2
4	5.5 & 0.002	HD	Zone 1	Soil C	Long	6
5	5.5 & 0.002	HD	Zone 1	Soil D	Short	8
6	5.5 & 0.002	HD	Zone 3	Soil A	Long	11
7	5.5 & 0.002	HD	Zone 3	Soil B	Long	4
8	5.5 & 0.002	HD	Zone 3	Soil C	Short	4
9	5.5 & 0.002	HD	Zone 3	Soil D	Short	4
10	5.5 & 0.002	ATS	Zone 1	Soil A	Long	4
11	5.5 & 0.002	ATS	Zone 1	Soil B	Long	4
12	5.5 & 0.002	ATS	Zone 1	Soil C	Long	4
13	5.5 & 0.002	ATS	Zone 1	Soil D	Short	4
14	5.5 & 0.002	ATS	Zone 3	Soil A	Long	4
15	5.5 & 0.002	ATS	Zone 3	Soil B	Long	3
16	5.5 & 0.002	ATS	Zone 3	Soil C	Short	3
17	6.5 & 0.004	HD	Zone 1	Soil A	Long	12
18	6.5 & 0.004	HD	Zone 1	Soil B	Long	12
19	6.5 & 0.004	HD	Zone 1	Soil C	Long	12
20	6.5 & 0.004	HD	Zone 1	Soil D	Short	9
21	6.5 & 0.004	HD	Zone 3	Soil A	Long	12
22	6.5 & 0.004	HD	Zone 3	Soil B	Long	8
23	6.5 & 0.004	HD	Zone 3	Soil C	Short	4
24	6.5 & 0.004	HD	Zone 3	Soil D	Short	4
25	6.5 & 0.004	ATS	Zone 1	Soil A	Long	4
26	6.5 & 0.004	ATS	Zone 1	Soil B	Long	4
27	6.5 & 0.004	ATS	Zone 1	Soil C	Long	4
28	6.5 & 0.004	ATS	Zone 1	Soil D	Short	8
29	6.5 & 0.004	ATS	Zone 3	Soil A	Long	4
30	6.5 & 0.004	ATS	Zone 3	Soil B	Long	8

31	6.5 & 0.004	ATS	Zone 3	Soil C	Short	3
32	6.5 & 0.004	ATS	Zone 3	Soil C	Long	1
33	6.5 & 0.004	ATS	Zone 3	Soil D	Short	3

APPENDIX C

RESULTS VALIDATION

Appendix C presents the full static and dynamic results of each of the 201 archetypes sorted out by performance groups. Nomenclature in Table C-1 stands for: Ω_m = mean over-strength, μ_m = mean ductility, CMR = collapse margin ratio, SSF = spectral shape factor, ACMR = adjusted collapse margin ratio, $ACMR_{min}$ = minimum collapse margin ratio to guarantee a 20% collapse probability (10% for performance groups).

Table C-1. Static and dynamic results sorted out by performance groups.

Archetype ID	Ω_m	μ_m	CMR	SSF	ACMR	$ACMR_{min}$	Result
Performance group #1							
3_15_C_002_5-5_A_II_1_MGP10	9.98	5.10	3.04	1.13	4.14	1.49	Pass
4_10_C_002_5-5_A_II_1_MGP10	9.16	4.58	3.15	1.19	4.49	1.49	Pass
5_6_C_002_5-5_A_II_1_MGP10	8.42	4.54	2.52	1.24	3.77	1.49	Pass
3_15_D_002_5-5_A_II_1_MGP10	10.03	5.13	4.25	1.17	5.96	1.49	Pass
4_10_D_002_5-5_A_II_1_MGP10	9.17	4.59	4.22	1.21	6.14	1.49	Pass
5_8_D_002_5-5_A_II_1_MGP10	8.04	4.50	3.17	1.27	4.82	1.49	Pass
3_15_P_002_5-5_A_II_1_MGP10	7.90	5.09	3.73	1.16	5.19	1.49	Pass
4_9_P_002_5-5_A_II_1_MGP10	7.16	4.63	3.67	1.21	5.34	1.49	Pass
5_6_P_002_5-5_A_II_1_MGP10	6.15	4.39	3.58	1.26	5.42	1.49	Pass
3_15_Q_002_5-5_A_II_1_MGP10	8.89	5.09	4.35	1.17	6.12	1.49	Pass
4_10_Q_002_5-5_A_II_1_MGP10	8.06	4.57	4.63	1.22	6.79	1.49	Pass
5_5_Q_002_5-5_A_II_1_MGP10	7.09	4.24	3.89	1.26	5.87	1.49	Pass
Mean	8.34	4.70	3.68	1.21	5.34	1.84	Pass
Performance group #2							
3_13_C_002_5-5_B_II_1_MGP10	5.82	5.14	1.86	1.14	2.53	1.49	Pass
4_8_C_002_5-5_B_II_1_MGP10	5.84	4.62	1.87	1.16	2.60	1.49	Pass
5_4_C_002_5-5_B_II_1_MGP10	6.25	4.30	1.91	1.22	2.80	1.49	Pass
3_13_D_002_5-5_B_II_1_MGP10	6.45	5.59	2.47	1.14	3.39	1.49	Pass
4_8_D_002_5-5_B_II_1_MGP10	6.13	4.49	2.63	1.18	3.73	1.49	Pass

5_6_D_002_5-5_B_II_1_MGP10	5.86	4.33	2.46	1.24	3.65	1.49	Pass
3_13_P_002_5-5_B_II_1_MGP10	4.96	5.22	2.75	1.14	3.76	1.49	Pass
4_7_P_002_5-5_B_II_1_MGP10	4.87	4.57	2.65	1.20	3.80	1.49	Pass
5_4_P_002_5-5_B_II_1_MGP10	5.14	4.38	3.42	1.26	5.18	1.49	Pass
3_13_Q_002_5-5_B_II_1_MGP10	5.72	5.27	3.30	1.14	4.53	1.49	Pass
4_8_Q_002_5-5_B_II_1_MGP10	5.36	4.58	3.35	1.20	4.83	1.49	Pass
5_3_Q_002_5-5_B_II_1_MGP10	5.50	4.66	3.19	1.27	4.88	1.49	Pass
Mean	5.66	4.76	2.66	1.19	3.81	1.84	Pass
Performance group #3							
3_11_P_002_5-5_C_II_1_MGP10	3.96	5.13	2.62	1.14	3.57	1.49	Pass
3_11_Q_002_5-5_C_II_1_MGP10	4.66	5.12	2.76	1.14	3.76	1.49	Pass
Mean	4.31	5.13	2.69	1.14	3.66	1.84	Pass
Performance group #4							
3_11_C_002_5-5_C_II_1_MGP10	4.52	5.16	2.09	1.14	2.84	1.49	Pass
4_6_C_002_5-5_C_II_1_MGP10	4.13	5.30	1.78	1.14	2.43	1.49	Pass
3_11_D_002_5-5_C_II_1_MGP10	4.97	5.52	2.32	1.14	3.18	1.49	Pass
4_6_D_002_5-5_C_II_1_MGP10	4.52	4.70	1.62	1.13	2.19	1.49	Pass
4_5_P_002_5-5_C_II_1_MGP10	4.11	4.96	2.15	1.13	2.92	1.49	Pass
4_6_Q_002_5-5_C_II_1_MGP10	4.91	6.06	1.78	1.15	2.45	1.49	Pass
Mean	4.53	5.28	1.95	1.14	2.67	1.84	Pass
Performance group #5							
3_9_C_002_5-5_D_II_1_MGP10	3.52	5.47	1.91	1.14	2.62	1.49	Pass
4_4_C_002_5-5_D_II_1_MGP10	3.08	5.19	1.80	1.14	2.45	1.49	Pass
3_9_D_002_5-5_D_II_1_MGP10	4.48	5.48	1.85	1.14	2.53	1.49	Pass
4_4_D_002_5-5_D_II_1_MGP10	4.04	4.71	1.78	1.13	2.42	1.49	Pass
3_9_P_002_5-5_D_II_1_MGP10	3.86	4.40	1.87	1.12	2.52	1.49	Pass
4_3_P_002_5-5_D_II_1_MGP10	2.92	5.44	1.98	1.14	2.71	1.49	Pass
3_9_Q_002_5-5_D_II_1_MGP10	3.74	5.05	2.20	1.13	3.00	1.49	Pass
4_4_Q_002_5-5_D_II_1_MGP10	4.41	4.89	2.17	1.13	2.95	1.49	Pass
Mean	3.76	5.08	1.95	1.13	2.65	1.84	Pass
Performance group #6							
3_7_C_002_5-5_A_II_3_MGP10	4.72	5.13	1.49	1.29	2.31	1.49	Pass
4_2_C_002_5-5_A_II_3_MGP10	4.56	4.59	1.92	1.29	2.97	1.49	Pass

5_1_C_002_5-5_A_II_3_MGP10	5.14	4.10	2.27	1.30	3.54	1.49	Pass
3_7_D_002_5-5_A_II_3_MGP10	4.79	5.16	2.26	1.29	3.51	1.49	Pass
4_2_D_002_5-5_A_II_3_MGP10	5.12	4.94	2.12	1.31	3.32	1.49	Pass
5_2_D_002_5-5_A_II_3_MGP10	4.96	4.50	1.85	1.27	2.81	1.49	Pass
3_7_P_002_5-5_A_II_3_MGP10	4.14	5.22	2.41	1.29	3.74	1.49	Pass
4_1_P_002_5-5_A_II_3_MGP10	3.81	4.75	2.41	1.33	3.84	1.49	Pass
5_1_P_002_5-5_A_II_3_MGP10	4.50	4.03	1.92	1.28	2.96	1.49	Pass
3_7_Q_002_5-5_A_II_3_MGP10	4.43	5.23	2.66	1.29	4.13	1.49	Pass
4_2_Q_002_5-5_A_II_3_MGP10	4.10	4.76	2.37	1.32	3.77	1.49	Pass
Mean	4.57	4.76	2.15	1.30	3.35	1.84	Pass
Performance group #7							
3_5_C_002_5-5_B_II_3_MGP10	3.68	5.72	1.78	1.31	2.79	1.49	Pass
3_5_D_002_5-5_B_II_3_MGP10	4.62	4.18	1.82	1.26	2.74	1.49	Pass
3_5_P_002_5-5_B_II_3_MGP10	3.09	5.52	1.94	1.30	3.04	1.49	Pass
3_5_Q_002_5-5_B_II_3_MGP10	3.83	5.71	1.85	1.31	2.90	1.49	Pass
Mean	3.81	5.28	1.85	1.29	2.87	1.84	Pass
Performance group #8							
3_3_C_002_5-5_C_II_3_MGP10	3.35	5.57	1.78	1.30	2.78	1.49	Pass
3_3_D_002_5-5_C_II_3_MGP10	3.62	5.27	1.77	1.29	2.74	1.49	Pass
3_3_P_002_5-5_C_II_3_MGP10	2.69	5.42	1.86	1.30	2.91	1.49	Pass
3_3_Q_002_5-5_C_II_3_MGP10	3.83	5.08	1.89	1.29	2.92	1.49	Pass
Mean	3.37	5.33	1.83	1.30	2.84	1.84	Pass
Performance group #9							
3_1_C_002_5-5_D_II_3_MGP10	3.37	5.67	1.85	1.31	2.90	1.49	Pass
3_1_D_002_5-5_D_II_3_MGP10	4.51	4.38	1.87	1.26	2.83	1.49	Pass
3_1_P_002_5-5_D_II_3_MGP10	3.39	5.03	1.90	1.29	2.93	1.49	Pass
3_1_Q_002_5-5_D_II_3_MGP10	3.99	4.51	2.09	1.27	3.18	1.49	Pass
Mean	3.82	4.90	1.93	1.28	2.96	1.84	Pass
Performance group #10							
5_14_C_002_5-5_A_II_1_MGP10_ATS	14.42	3.70	3.23	1.19	4.64	1.49	Pass
5_14_D_002_5-5_A_II_1_MGP10_ATS	13.97	3.55	3.65	1.20	5.27	1.49	Pass
5_11_P_002_5-5_A_II_1_MGP10_ATS	10.86	4.29	4.47	1.26	6.75	1.49	Pass
5_14_Q_002_5-5_A_II_1_MGP10_ATS	14.29	3.88	4.36	1.23	6.44	1.49	Pass

Mean	13.39	3.86	3.94	1.22	5.77	1.84	Pass
Performance group #11							
5_12_C_002_5-5_B_II_1_MGP10_ATS	10.07	3.71	2.07	1.17	2.91	1.49	Pass
5_12_D_002_5-5_B_II_1_MGP10_ATS	12.18	3.38	2.70	1.16	3.76	1.49	Pass
5_9_P_002_5-5_B_II_1_MGP10_ATS	9.30	4.59	2.93	1.25	4.40	1.49	Pass
5_12_Q_002_5-5_B_II_1_MGP10_ATS	10.50	4.34	3.36	1.23	4.98	1.49	Pass
Mean	10.51	4.00	2.78	1.20	4.01	1.84	Pass
Performance group #12							
5_10_C_002_5-5_C_II_1_MGP10_ATS	7.12	4.18	2.53	1.13	3.43	1.49	Pass
5_10_D_002_5-5_C_II_1_MGP10_ATS	6.31	3.95	2.35	1.13	3.19	1.49	Pass
5_7_P_002_5-5_C_II_1_MGP10_ATS	5.03	4.08	2.60	1.16	3.60	1.49	Pass
5_10_Q_002_5-5_C_II_1_MGP10_ATS	5.74	4.11	2.81	1.14	3.83	1.49	Pass
Mean	6.05	4.08	2.57	1.14	3.51	1.84	Pass
Performance group #13							
5_8_C_002_5-5_D_II_1_MGP10_ATS	5.25	3.89	2.24	1.12	3.00	1.49	Pass
5_8_D_002_5-5_D_II_1_MGP10_ATS	4.80	4.34	2.12	1.12	2.86	1.49	Pass
5_5_P_002_5-5_D_II_1_MGP10_ATS	3.97	4.45	2.30	1.13	3.13	1.49	Pass
5_8_Q_002_5-5_D_II_1_MGP10_ATS	5.09	4.20	2.72	1.12	3.66	1.49	Pass
Mean	4.77	4.22	2.34	1.12	3.16	1.84	Pass
Performance group #14							
5_6_C_002_5-5_A_II_3_MGP10_ATS	8.24	3.72	2.69	1.26	4.05	1.49	Pass
5_6_D_002_5-5_A_II_3_MGP10_ATS	6.63	4.16	2.45	1.30	3.82	1.49	Pass
5_3_P_002_5-5_A_II_3_MGP10_ATS	6.28	4.28	3.02	1.32	4.77	1.49	Pass
5_6_Q_002_5-5_A_II_3_MGP10_ATS	8.03	4.35	3.37	1.32	5.34	1.49	Pass
Mean	7.30	4.13	2.89	1.30	4.50	1.84	Pass
Performance group #15							
5_4_C_002_5-5_B_II_3_MGP10_ATS	4.41	4.29	1.88	1.26	2.84	1.49	Pass
5_4_D_002_5-5_B_II_3_MGP10_ATS	5.19	4.57	2.41	1.27	3.67	1.49	Pass
5_4_Q_002_5-5_B_II_3_MGP10_ATS	4.47	4.29	2.42	1.26	3.66	1.49	Pass
Mean	4.69	4.38	2.24	1.26	3.39	1.84	Pass
Performance group #16							
5_2_C_002_5-5_C_II_3_MGP10_ATS	4.18	3.87	1.90	1.24	2.84	1.49	Pass

5_2_D_002_5-5_C_II_3_MGP10_ATS	4.16	4.44	2.10	1.27	3.19	1.49	Pass
5_2_Q_002_5-5_C_II_3_MGP10_ATS	3.73	4.55	2.13	1.27	3.24	1.49	Pass
Mean	4.02	4.29	2.05	1.26	3.09	1.84	Pass
Performance group #17							
3_16_C_004_6-5_A_II_1_MGP10	11.85	5.10	3.03	1.13	4.12	1.49	Pass
4_11_C_004_6-5_A_II_1_MGP10	10.93	4.59	3.01	1.19	4.30	1.49	Pass
5_7_C_004_6-5_A_II_1_MGP10	8.35	4.49	2.45	1.25	3.67	1.49	Pass
3_16_D_004_6-5_A_II_1_MGP10	11.95	5.12	4.29	1.18	6.07	1.49	Pass
4_11_D_004_6-5_A_II_1_MGP10	10.41	4.63	4.25	1.22	6.22	1.49	Pass
5_9_D_004_6-5_A_II_1_MGP10	8.20	4.48	3.41	1.27	5.19	1.49	Pass
3_16_P_004_6-5_A_II_1_MGP10	9.34	5.09	3.73	1.16	5.19	1.49	Pass
4_10_P_004_6-5_A_II_1_MGP10	8.38	4.61	3.65	1.21	5.31	1.49	Pass
5_7_P_004_6-5_A_II_1_MGP10	6.83	4.24	3.04	1.26	4.59	1.49	Pass
3_16_Q_004_6-5_A_II_1_MGP10	10.43	5.12	4.27	1.17	6.00	1.49	Pass
4_11_Q_004_6-5_A_II_1_MGP10	9.14	4.62	4.49	1.22	6.59	1.49	Pass
5_6_Q_004_6-5_A_II_1_MGP10	7.37	4.27	3.82	1.26	5.77	1.49	Pass
Mean	9.43	4.70	3.62	1.21	5.25	1.84	Pass
Performance group #18							
3_14_C_004_6-5_B_II_1_MGP10	7.67	5.10	1.88	1.13	2.55	1.49	Pass
4_9_C_004_6-5_B_II_1_MGP10	7.24	4.60	1.97	1.18	2.78	1.49	Pass
5_5_C_004_6-5_B_II_1_MGP10	6.63	4.61	1.90	1.25	2.85	1.49	Pass
3_14_D_004_6-5_B_II_1_MGP10	7.18	5.12	2.80	1.15	3.87	1.49	Pass
4_9_D_004_6-5_B_II_1_MGP10	6.98	4.64	2.91	1.21	4.21	1.49	Pass
5_7_D_004_6-5_B_II_1_MGP10	6.07	4.48	2.63	1.27	3.99	1.49	Pass
3_14_P_004_6-5_B_II_1_MGP10	5.82	5.08	2.29	1.14	3.14	1.49	Pass
4_8_P_004_6-5_B_II_1_MGP10	5.72	4.61	2.61	1.21	3.77	1.49	Pass
5_5_P_004_6-5_B_II_1_MGP10	5.31	4.57	2.43	1.27	3.71	1.49	Pass
3_14_Q_004_6-5_B_II_1_MGP10	6.47	5.12	2.91	1.16	4.05	1.49	Pass
4_9_Q_004_6-5_B_II_1_MGP10	6.29	4.62	3.07	1.22	4.49	1.49	Pass
5_4_Q_004_6-5_B_II_1_MGP10	5.55	4.27	2.85	1.26	4.31	1.49	Pass
Mean	6.41	4.73	2.52	1.20	3.64	1.84	Pass
Performance group #19							
3_12_C_004_6-5_C_II_1_MGP10	5.04	5.13	1.42	1.14	1.94	1.49	Pass

4_7_C_004_6-5_C_II_1_MGP10	4.41	4.61	1.21	1.15	1.67	1.49	Pass
5_3_C_004_6-5_C_II_1_MGP10	3.79	4.58	1.14	1.23	1.68	1.49	Pass
3_12_D_004_6-5_C_II_1_MGP10	4.62	5.13	2.08	1.14	2.83	1.49	Pass
4_7_D_004_6-5_C_II_1_MGP10	4.13	4.63	1.76	1.18	2.49	1.49	Pass
5_5_D_004_6-5_C_II_1_MGP10	3.60	4.53	1.56	1.27	2.38	1.49	Pass
3_12_P_004_6-5_C_II_1_MGP10	3.99	5.18	1.98	1.14	2.70	1.49	Pass
4_6_P_004_6-5_C_II_1_MGP10	3.51	4.71	1.72	1.19	2.46	1.49	Pass
5_3_P_004_6-5_C_II_1_MGP10	3.15	4.50	1.54	1.27	2.34	1.49	Pass
3_12_Q_004_6-5_C_II_1_MGP10	4.25	5.12	2.14	1.14	2.93	1.49	Pass
4_7_Q_004_6-5_C_II_1_MGP10	3.73	4.67	2.00	1.20	2.87	1.49	Pass
5_2_Q_004_6-5_C_II_1_MGP10	3.33	4.33	1.74	1.26	2.63	1.49	Pass
Mean	3.96	4.76	1.69	1.19	2.41	1.84	Pass
Performance group #20							
3_10_C_004_6-5_D_II_1_MGP10	3.71	5.06	1.34	1.13	1.82	1.49	Pass
4_5_C_004_6-5_D_II_1_MGP10	2.84	4.99	1.28	1.15	1.77	1.49	Pass
3_10_D_004_6-5_D_II_1_MGP10	3.56	5.15	1.68	1.14	2.29	1.49	Pass
4_5_D_004_6-5_D_II_1_MGP10	2.91	5.01	1.44	1.16	2.01	1.49	Pass
5_4_D_004_6-5_D_II_1_MGP10	2.30	5.19	1.27	1.18	1.80	1.49	Pass
3_10_P_004_6-5_D_II_1_MGP10	5.44	5.17	2.90	1.14	3.95	1.49	Pass
4_4_P_004_6-5_D_II_1_MGP10	2.50	4.94	1.51	1.16	2.10	1.49	Pass
3_10_Q_004_6-5_D_II_1_MGP10	3.12	5.09	1.67	1.13	2.28	1.49	Pass
4_5_Q_004_6-5_D_II_1_MGP10	2.74	4.68	1.62	1.15	2.23	1.49	Pass
Mean	3.24	5.03	1.63	1.15	2.25	1.84	Pass
Performance group #21							
3_8_C_004_6-5_A_II_3_MGP10	5.51	5.14	1.54	1.29	2.39	1.49	Pass
4_3_C_004_6-5_A_II_3_MGP10	5.01	4.54	1.79	1.30	2.80	1.49	Pass
5_2_C_004_6-5_A_II_3_MGP10	4.31	5.18	2.04	1.41	3.44	1.49	Pass
3_8_D_004_6-5_A_II_3_MGP10	5.42	5.12	2.22	1.30	3.47	1.49	Pass
4_3_D_004_6-5_A_II_3_MGP10	4.91	4.80	2.21	1.34	3.54	1.49	Pass
5_3_D_004_6-5_A_II_3_MGP10	4.51	5.25	2.18	1.42	3.70	1.49	Pass
3_8_P_004_6-5_A_II_3_MGP10	4.41	5.10	2.13	1.29	3.29	1.49	Pass
4_2_P_004_6-5_A_II_3_MGP10	4.23	4.70	2.20	1.34	3.55	1.49	Pass
5_2_P_004_6-5_A_II_3_MGP10	3.64	4.88	2.39	1.39	4.00	1.49	Pass
3_8_Q_004_6-5_A_II_3_MGP10	4.68	5.11	2.37	1.30	3.70	1.49	Pass

4_3_Q_004_6-5_A_II_3_MGP10	4.41	4.71	2.31	1.34	3.73	1.49	Pass
5_1_Q_004_6-5_A_II_3_MGP10	3.91	4.72	2.35	1.38	3.90	1.49	Pass
Mean	4.58	4.94	2.15	1.34	3.46	1.84	Pass
Performance group #22							
3_6_C_004_6-5_B_II_3_MGP10	3.95	5.75	1.50	1.31	2.36	1.49	Pass
4_1_C_004_6-5_B_II_3_MGP10	3.34	4.69	1.21	1.27	1.85	1.49	Pass
3_6_D_004_6-5_B_II_3_MGP10	3.39	5.44	1.62	1.30	2.52	1.49	Pass
4_1_D_004_6-5_B_II_3_MGP10	3.41	5.13	1.07	1.29	1.65	1.49	Pass
5_1_D_004_6-5_B_II_3_MGP10	2.93	5.27	1.31	1.34	2.10	1.49	Pass
3_6_P_004_6-5_B_II_3_MGP10	2.94	6.01	1.61	1.32	2.54	1.49	Pass
3_6_Q_004_6-5_B_II_3_MGP10	3.29	5.63	1.76	1.31	2.76	1.49	Pass
4_1_Q_004_6-5_B_II_3_MGP10	3.40	4.35	1.67	1.26	2.53	1.49	Pass
Mean	3.33	5.28	1.47	1.30	2.29	1.84	Pass
Performance group #23							
3_4_C_004_6-5_C_II_3_MGP10	3.34	4.90	1.40	1.28	2.15	1.49	Pass
3_4_D_004_6-5_C_II_3_MGP10	2.77	5.42	1.34	1.30	2.09	1.49	Pass
3_4_P_004_6-5_C_II_3_MGP10	2.67	6.12	1.58	1.32	2.50	1.49	Pass
3_4_Q_004_6-5_C_II_3_MGP10	2.70	5.71	1.51	1.31	2.37	1.49	Pass
Mean	2.87	5.54	1.46	1.30	2.28	1.84	Pass
Performance group #24							
3_2_C_004_6-5_D_II_3_MGP10	2.84	5.10	1.21	1.29	1.87	1.49	Pass
3_2_D_004_6-5_D_II_3_MGP10	2.94	5.58	1.24	1.30	1.94	1.49	Pass
3_2_P_004_6-5_D_II_3_MGP10	3.67	5.05	1.73	1.29	2.67	1.49	Pass
3_2_Q_004_6-5_D_II_3_MGP10	2.68	6.32	1.51	1.33	2.41	1.49	Pass
Mean	3.03	5.51	1.42	1.30	2.22	1.84	Pass
Performance group #25							
5_15_C_004_6-5_A_II_1_MGP10_ATS	10.53	4.14	2.50	1.23	3.68	1.49	Pass
5_15_D_004_6-5_A_II_1_MGP10_ATS	11.67	4.30	3.55	1.26	5.37	1.49	Pass
5_12_P_004_6-5_A_II_1_MGP10_ATS	8.67	4.02	3.20	1.25	4.80	1.49	Pass
5_15_Q_004_6-5_A_II_1_MGP10_ATS	10.54	4.18	4.18	1.26	6.30	1.49	Pass
Mean	10.35	4.16	3.36	1.25	5.04	1.84	Pass
Performance group #26							

5_13_C_004_6-5_B_II_1_MGP10_ATS	8.24	4.19	1.93	1.23	2.84	1.49	Pass
5_13_D_004_6-5_B_II_1_MGP10_ATS	8.89	4.10	2.62	1.25	3.94	1.49	Pass
5_10_P_004_6-5_B_II_1_MGP10_ATS	7.01	4.09	2.55	1.25	3.83	1.49	Pass
5_13_Q_004_6-5_B_II_1_MGP10_ATS	7.60	4.24	3.20	1.26	4.84	1.49	Pass
Mean	7.94	4.15	2.58	1.25	3.86	1.84	Pass
Performance group #27							
5_11_C_004_6-5_C_II_1_MGP10_ATS	4.86	4.19	1.13	1.22	1.65	1.49	Pass
5_11_D_004_6-5_C_II_1_MGP10_ATS	5.17	4.30	1.54	1.26	2.32	1.49	Pass
5_8_P_004_6-5_C_II_1_MGP10_ATS	4.06	4.04	1.63	1.25	2.45	1.49	Pass
5_11_Q_004_6-5_C_II_1_MGP10_ATS	4.58	4.31	1.91	1.26	2.88	1.49	Pass
Mean	4.67	4.21	1.55	1.25	2.33	1.84	Pass
Performance group #28							
5_9_C_004_6-5_D_II_1_MGP10_ATS	3.52	3.91	1.33	1.16	1.86	1.49	Pass
6_3_C_002_7-0_D_II_1_MGP10_ATS	5.72	3.87	1.51	1.16	2.10	1.49	Pass
6_4_C_004_7-0_D_II_1_MGP10_ATS	3.13	3.91	1.50	1.16	2.09	1.49	Pass
5_9_D_004_6-5_D_II_1_MGP10_ATS	3.47	4.13	1.36	1.17	1.91	1.49	Pass
5_6_P_004_6-5_D_II_1_MGP10_ATS	3.26	4.04	1.55	1.16	2.17	1.49	Pass
6_3_P_002_7-0_D_II_1_MGP10_ATS	4.35	4.45	1.56	1.18	2.21	1.49	Pass
6_4_P_004_7-0_D_II_1_MGP10_ATS	2.96	4.04	1.58	1.17	2.21	1.49	Pass
5_9_Q_004_6-5_D_II_1_MGP10_ATS	3.40	4.19	1.56	1.16	2.17	1.49	Pass
Mean	3.73	4.07	1.49	1.16	2.09	1.84	Pass
Performance group #29							
5_7_C_004_6-5_A_II_3_MGP10_ATS	5.48	4.02	2.12	1.34	3.42	1.49	Pass
5_7_D_004_6-5_A_II_3_MGP10_ATS	5.92	3.98	2.18	1.35	3.53	1.49	Pass
5_4_P_004_6-5_A_II_3_MGP10_ATS	5.16	4.17	2.53	1.37	4.14	1.49	Pass
5_7_Q_004_6-5_A_II_3_MGP10_ATS	5.45	4.27	2.56	1.37	4.20	1.49	Pass
Mean	5.50	4.11	2.35	1.36	3.82	1.84	Pass
Performance group #30							
5_5_C_004_6-5_B_II_3_MGP10_ATS	4.14	4.01	1.35	1.31	2.13	1.49	Pass
6_1_C_002_7-0_B_II_3_MGP10_ATS	7.69	4.29	1.73	1.34	2.79	1.49	Pass
6_2_C_004_7-0_B_II_3_MGP10_ATS	3.76	4.01	1.78	1.34	2.85	1.49	Pass
5_5_D_004_6-5_B_II_3_MGP10_ATS	4.45	3.93	1.48	1.31	2.32	1.49	Pass
5_2_P_004_6-5_B_II_3_MGP10_ATS	3.79	4.25	1.78	1.30	2.77	1.49	Pass

6_1_P_002_7-0_B_II_3_MGP10_ATS	3.31	4.25	1.74	1.26	2.64	1.49	Pass
6_2_P_004_7-0_B_II_3_MGP10_ATS	3.93	4.25	1.80	1.33	2.87	1.49	Pass
5_5_Q_004_6-5_B_II_3_MGP10_ATS	4.93	4.07	1.74	1.25	2.61	1.49	Pass
Mean	4.50	4.13	1.68	1.30	2.62	1.84	Pass
Performance group #31							
5_3_D_004_6-5_C_II_3_MGP10_ATS	5.03	4.43	2.03	1.26	3.09	1.49	Pass
5_1_P_004_6-5_C_II_3_MGP10_ATS	3.65	3.63	2.03	1.23	3.00	1.49	Pass
5_3_Q_004_6-5_C_II_3_MGP10_ATS	4.45	4.35	2.14	1.26	3.24	1.49	Pass
Mean	4.37	4.14	2.07	1.25	3.11	1.84	Pass
Performance group #32							
5_3_C_004_6-5_C_II_3_MGP10_ATS	3.84	3.96	1.80	1.25	2.70	1.49	Pass
Mean	3.84	3.96	1.80	1.25	2.70	1.84	Pass
Performance group #33							
5_1_C_004_6-5_D_II_3_MGP10_ATS	3.12	3.91	1.51	1.25	2.26	1.49	Pass
5_1_D_004_6-5_D_II_3_MGP10_ATS	3.92	4.37	1.68	1.26	2.54	1.49	Pass
5_1_Q_004_6-5_D_II_3_MGP10_ATS	3.52	4.42	1.67	1.26	2.53	1.49	Pass
Mean	3.52	4.23	1.62	1.26	2.44	1.84	Pass

APPENDIX D

FRAGILITY FUNCTIONS

Appendix D presents the fragility functions for each of the 201 archetypes analyzed in this research. As defined by the FEMA 356 standard (FEMA 2000), three performance levels were included: immediate occupancy IO, life safety LS, and collapse prevention CP. Each performance level is associated to an interstory drift level: 1%, 2%, and 3%, respectively. The fragility functions presented below assume a lognormal distribution of the probability of exceedance (Baker 2015), with a mean ln θ and standard deviation β computed employing the following equations:

$$\ln\theta = \frac{1}{n}\sum_{i=1}^{n} \ln IM_i \qquad \text{Eq. D-1}$$

$$\beta = \sqrt{\frac{1}{n\text{-}1}\sum_{i=1}^{n}\left(\ln\left(\frac{IM_i}{\theta}\right)\right)^2} \qquad \text{Eq. D-2}$$

Table D-1 lists the mean and standard deviation values of the fragility functions for each of the archetypes described in Section 1.2.4. Subsequently, the fragility functions are plotted for each performance level. Further information about the calculation of fragility function can be found in the technical note provided by Baker (Baker 2015).

Table D-1. Mean and standard deviation values (three performance levels) for each archetype.

#	Archetype ID	IO		LS		CP	
		ln θ	**β**	**ln θ**	**β**	**ln θ**	**β**
1	3_1_C_002_5-5_D_II_3_MGP10_HD	0.043	0.358	0.610	0.425	0.911	0.456
2	3_2_C_004_6-5_D_II_3_MGP10_HD	-0.256	0.335	0.316	0.367	0.617	0.403
3	3_3_C_002_5-5_C_II_3_MGP10_HD	-0.062	0.359	0.485	0.412	0.790	0.449
4	3_4_C_004_6-5_C_II_3_MGP10_HD	-0.305	0.311	0.270	0.354	0.590	0.398
5	3_5_C_002_5-5_B_II_3_MGP10_HD	-0.096	0.344	0.445	0.372	0.742	0.420
6	3_6_C_004_6-5_B_II_3_MGP10_HD	-0.396	0.255	0.148	0.362	0.460	0.396

7	3_7_C_002_5-5_A_II_3_MGP10_HD	-0.901	0.255	-0.320	0.302	-0.009	0.303
8	3_8_C_004_6-5_A_II_3_MGP10_HD	-0.951	0.215	-0.376	0.277	-0.083	0.294
9	3_9_C_002_5-5_D_II_1_MGP10_HD	-0.487	0.285	0.080	0.361	0.409	0.409
10	3_10_C_004_6-5_D_II_1_MGP10_HD	-0.764	0.239	-0.199	0.291	0.099	0.341
11	3_11_C_002_5-5_C_II_1_MGP10_HD	-0.587	0.245	-0.033	0.306	0.291	0.340
12	3_12_C_004_6-5_C_II_1_MGP10_HD	-0.972	0.207	-0.394	0.272	-0.092	0.284
13	3_13_C_002_5-5_B_II_1_MGP10_HD	-0.953	0.218	-0.369	0.298	-0.083	0.293
14	3_14_C_004_6-5_B_II_1_MGP10_HD	-1.056	0.236	-0.472	0.237	-0.166	0.274
15	3_15_C_002_5-5_A_II_1_MGP10_HD	-1.031	0.206	-0.464	0.228	-0.158	0.270
16	3_16_C_004_6-5_A_II_1_MGP10_HD	-1.048	0.219	-0.468	0.236	-0.165	0.283
17	4_1_C_004_6-5_B_II_3_MGP10_HD	-0.783	0.260	-0.222	0.307	0.078	0.317
18	4_2_C_002_5-5_A_II_3_MGP10_HD	-0.916	0.228	-0.331	0.274	-0.014	0.300
19	4_3_C_004_6-5_A_II_3_MGP10_HD	-1.030	0.265	-0.445	0.304	-0.135	0.333
20	4_4_C_002_5-5_D_II_1_MGP10_HD	-0.453	0.282	0.100	0.377	0.388	0.383
21	4_5_C_004_6-5_D_II_1_MGP10_HD	-0.785	0.262	-0.224	0.297	0.086	0.304
22	4_6_C_002_5-5_C_II_1_MGP10_HD	-0.799	0.218	-0.216	0.271	0.093	0.289
23	4_7_C_004_6-5_C_II_1_MGP10_HD	-1.263	0.302	-0.709	0.317	-0.405	0.353
24	4_8_C_002_5-5_B_II_1_MGP10_HD	-1.214	0.284	-0.664	0.322	-0.368	0.353
25	4_9_C_004_6-5_B_II_1_MGP10_HD	-1.262	0.299	-0.705	0.315	-0.402	0.346
26	4_10_C_002_5-5_A_II_1_MGP10_HD	-1.249	0.302	-0.686	0.330	-0.382	0.349
27	4_11_C_004_6-5_A_II_1_MGP10_HD	-1.319	0.299	-0.742	0.316	-0.439	0.346
28	5_1_C_002_5-5_A_II_3_MGP10_HD	-0.823	0.252	-0.250	0.257	0.049	0.282
29	5_2_C_004_6-5_A_II_3_MGP10_HD	-1.092	0.307	-0.544	0.320	-0.227	0.361
30	5_3_C_004_6-5_C_II_1_MGP10_HD	-1.627	0.345	-1.016	0.318	-0.709	0.356
31	5_4_C_002_5-5_B_II_1_MGP10_HD	-1.506	0.329	-0.934	0.298	-0.630	0.319
32	5_5_C_004_6-5_B_II_1_MGP10_HD	-1.672	0.332	-1.053	0.305	-0.736	0.351
33	5_6_C_002_5-5_A_II_1_MGP10_HD	-1.710	0.344	-1.097	0.297	-0.767	0.335
34	5_7_C_004_6-5_A_II_1_MGP10_HD	-1.748	0.359	-1.134	0.334	-0.826	0.372
35	3_1_D_002_5-5_D_II_3_MGP10_HD	0.075	0.301	0.615	0.390	0.895	0.447
36	3_2_D_004_6-5_D_II_3_MGP10_HD	-0.187	0.313	0.316	0.353	0.622	0.394
37	3_3_D_002_5-5_C_II_3_MGP10_HD	-0.003	0.302	0.506	0.378	0.796	0.424
38	3_4_D_004_6-5_C_II_3_MGP10_HD	-0.294	0.263	0.246	0.377	0.534	0.442
39	3_5_D_002_5-5_B_II_3_MGP10_HD	-0.001	0.302	0.503	0.391	0.783	0.397
40	3_6_D_004_6-5_B_II_3_MGP10_HD	-0.325	0.263	0.220	0.373	0.543	0.454
41	3_7_D_002_5-5_A_II_3_MGP10_HD	-0.606	0.212	-0.046	0.286	0.276	0.357
42	3_8_D_004_6-5_A_II_3_MGP10_HD	-0.719	0.228	-0.163	0.267	0.152	0.327
43	3_9_D_002_5-5_D_II_1_MGP10_HD	-0.489	0.244	0.082	0.324	0.390	0.373
44	3_10_D_004_6-5_D_II_1_MGP10_HD	-0.571	0.236	-0.007	0.322	0.311	0.398
45	3_11_D_002_5-5_C_II_1_MGP10_HD	-0.538	0.252	0.016	0.317	0.369	0.380

46	3_12_D_004_6-5_C_II_1_MGP10_HD	-0.651	0.238	-0.099	0.301	0.226	0.362
47	3_13_D_002_5-5_B_II_1_MGP10_HD	-0.711	0.222	-0.162	0.270	0.138	0.318
48	3_14_D_004_6-5_B_II_1_MGP10_HD	-0.758	0.234	-0.202	0.278	0.113	0.314
49	3_15_D_002_5-5_A_II_1_MGP10_HD	-0.832	0.221	-0.280	0.245	0.038	0.297
50	3_16_D_004_6-5_A_II_1_MGP10_HD	-0.831	0.224	-0.285	0.239	0.016	0.284
51	4_1_D_004_6-5_B_II_3_MGP10_HD	-0.785	0.222	-0.224	0.259	0.108	0.274
52	4_2_D_002_5-5_A_II_3_MGP10_HD	-0.812	0.191	-0.234	0.240	0.094	0.255
53	4_3_D_004_6-5_A_II_3_MGP10_HD	-0.884	0.211	-0.301	0.243	0.014	0.268
54	4_4_D_002_5-5_D_II_1_MGP10_HD	-0.467	0.229	0.061	0.282	0.390	0.329
55	4_5_D_004_6-5_D_II_1_MGP10_HD	-0.693	0.235	-0.115	0.266	0.201	0.298
56	4_6_D_002_5-5_C_II_1_MGP10_HD	-0.875	0.209	-0.331	0.258	-0.009	0.276
57	4_7_D_004_6-5_C_II_1_MGP10_HD	-0.973	0.257	-0.413	0.270	-0.103	0.308
58	4_8_D_002_5-5_B_II_1_MGP10_HD	-1.016	0.265	-0.427	0.283	-0.133	0.324
59	4_9_D_004_6-5_B_II_1_MGP10_HD	-1.031	0.278	-0.438	0.284	-0.132	0.315
60	4_10_D_002_5-5_A_II_1_MGP10_HD	-1.058	0.295	-0.472	0.285	-0.155	0.315
61	4_11_D_004_6-5_A_II_1_MGP10_HD	-1.049	0.297	-0.466	0.287	-0.164	0.320
62	5_1_D_004_6-5_B_II_3_MGP10_HD	-0.953	0.330	-0.382	0.354	-0.076	0.367
63	5_2_D_002_5-5_A_II_3_MGP10_HD	-0.767	0.271	-0.214	0.292	0.067	0.325
64	5_3_D_004_6-5_A_II_3_MGP10_HD	-1.061	0.312	-0.493	0.327	-0.176	0.364
65	5_4_D_004_6-5_D_II_1_MGP10_HD	-0.766	0.274	-0.220	0.285	0.062	0.310
66	5_5_D_004_6-5_C_II_1_MGP10_HD	-1.444	0.384	-0.861	0.367	-0.548	0.373
67	5_6_D_002_5-5_B_II_1_MGP10_HD	-1.400	0.347	-0.803	0.345	-0.472	0.360
68	5_7_D_004_6-5_B_II_1_MGP10_HD	-1.434	0.383	-0.861	0.366	-0.543	0.369
69	5_8_D_002_5-5_A_II_1_MGP10_HD	-1.503	0.350	-0.904	0.336	-0.602	0.355
70	5_9_D_004_6-5_A_II_1_MGP10_HD	-1.499	0.354	-0.915	0.342	-0.599	0.372
71	3_1_P_002_5-5_D_II_3_MGP10_HD	0.073	0.354	0.652	0.445	0.916	0.473
72	3_2_P_004_6-5_D_II_3_MGP10_HD	0.064	0.297	0.610	0.349	0.918	0.388
73	3_3_P_002_5-5_C_II_3_MGP10_HD	-0.035	0.376	0.526	0.454	0.811	0.505
74	3_4_P_004_6-5_C_II_3_MGP10_HD	-0.138	0.307	0.391	0.396	0.684	0.451
75	3_5_P_002_5-5_B_II_3_MGP10_HD	-0.049	0.337	0.495	0.385	0.806	0.441
76	3_6_P_004_6-5_B_II_3_MGP10_HD	-0.238	0.309	0.269	0.401	0.548	0.458
77	3_7_P_002_5-5_A_II_3_MGP10_HD	-0.628	0.230	-0.066	0.290	0.264	0.346
78	3_8_P_004_6-5_A_II_3_MGP10_HD	-0.749	0.260	-0.198	0.337	0.129	0.367
79	3_9_P_002_5-5_D_II_1_MGP10_HD	-0.396	0.223	0.109	0.276	0.419	0.344
80	3_10_P_004_6-5_D_II_1_MGP10_HD	-0.203	0.382	0.347	0.444	0.650	0.477
81	3_11_P_002_5-5_C_II_1_MGP10_HD	-0.416	0.270	0.139	0.351	0.462	0.401
82	3_12_P_004_6-5_C_II_1_MGP10_HD	-0.719	0.263	-0.167	0.315	0.173	0.359
83	3_13_P_002_5-5_B_II_1_MGP10_HD	-0.733	0.224	-0.175	0.282	0.157	0.325
84	3_14_P_004_6-5_B_II_1_MGP10_HD	-0.918	0.235	-0.347	0.296	-0.041	0.313

85	3_15_P_002_5-5_A_II_1_MGP10_HD	-0.930	0.220	-0.367	0.278	-0.058	0.290
86	3_16_P_004_6-5_A_II_1_MGP10_HD	-0.930	0.220	-0.367	0.278	-0.058	0.290
87	4_1_P_002_5-5_A_II_3_MGP10_HD	-0.817	0.219	-0.225	0.231	0.115	0.279
88	4_2_P_004_6-5_A_II_3_MGP10_HD	-0.936	0.222	-0.344	0.270	-0.030	0.295
89	4_3_P_002_5-5_D_II_1_MGP10_HD	-0.429	0.278	0.161	0.333	0.488	0.371
90	4_4_P_004_6-5_D_II_1_MGP10_HD	-0.631	0.281	-0.054	0.313	0.241	0.330
91	4_5_P_002_5-5_C_II_1_MGP10_HD	-0.554	0.237	-0.053	0.251	0.273	0.285
92	4_6_P_004_6-5_C_II_1_MGP10_HD	-1.038	0.263	-0.453	0.309	-0.153	0.330
93	4_7_P_002_5-5_B_II_1_MGP10_HD	-1.088	0.329	-0.513	0.345	-0.208	0.382
94	4_8_P_004_6-5_B_II_1_MGP10_HD	-1.111	0.314	-0.548	0.346	-0.255	0.378
95	4_9_P_002_5-5_A_II_1_MGP10_HD	-1.162	0.295	-0.596	0.344	-0.299	0.363
96	4_10_P_004_6-5_A_II_1_MGP10_HD	-1.177	0.307	-0.606	0.337	-0.306	0.367
97	5_1_P_002_5-5_A_II_3_MGP10_HD	-0.882	0.269	-0.363	0.267	-0.055	0.263
98	5_2_P_004_6-5_A_II_3_MGP10_HD	-0.948	0.337	-0.391	0.353	-0.081	0.381
99	5_3_P_004_6-5_C_II_1_MGP10_HD	-1.496	0.393	-0.885	0.386	-0.582	0.400
100	5_4_P_002_5-5_B_II_1_MGP10_HD	-1.252	0.346	-0.634	0.340	-0.290	0.359
101	5_5_P_004_6-5_B_II_1_MGP10_HD	-1.556	0.385	-0.940	0.358	-0.639	0.383
102	5_6_P_002_5-5_A_II_1_MGP10_HD	-1.458	0.354	-0.875	0.335	-0.549	0.348
103	5_7_P_004_6-5_A_II_1_MGP10_HD	-1.618	0.373	-1.016	0.337	-0.717	0.373
104	3_1_Q_002_5-5_D_II_3_MGP10_HD	0.209	0.271	0.765	0.361	1.029	0.413
105	3_2_Q_004_6-5_D_II_3_MGP10_HD	-0.018	0.307	0.495	0.380	0.771	0.448
106	3_3_Q_002_5-5_C_II_3_MGP10_HD	0.067	0.279	0.609	0.354	0.879	0.384
107	3_4_Q_004_6-5_C_II_3_MGP10_HD	-0.156	0.309	0.348	0.385	0.640	0.460
108	3_5_Q_002_5-5_B_II_3_MGP10_HD	0.036	0.264	0.525	0.326	0.814	0.351
109	3_6_Q_004_6-5_B_II_3_MGP10_HD	-0.206	0.275	0.335	0.370	0.639	0.424
110	3_7_Q_002_5-5_A_II_3_MGP10_HD	-0.530	0.252	0.030	0.320	0.358	0.383
111	3_8_Q_004_6-5_A_II_3_MGP10_HD	-0.646	0.254	-0.105	0.326	0.205	0.363
112	3_9_Q_002_5-5_D_II_1_MGP10_HD	-0.261	0.199	0.295	0.288	0.591	0.360
113	3_10_Q_004_6-5_D_II_1_MGP10_HD	-0.565	0.269	-0.006	0.344	0.304	0.414
114	3_11_Q_002_5-5_C_II_1_MGP10_HD	-0.346	0.222	0.230	0.288	0.538	0.348
115	3_12_Q_004_6-5_C_II_1_MGP10_HD	-0.633	0.247	-0.086	0.307	0.220	0.376
116	3_13_Q_002_5-5_B_II_1_MGP10_HD	-0.573	0.236	-0.009	0.276	0.322	0.318
117	3_14_Q_004_6-5_B_II_1_MGP10_HD	-0.700	0.232	-0.186	0.262	0.109	0.319
118	3_15_Q_002_5-5_A_II_1_MGP10_HD	-0.814	0.220	-0.272	0.265	0.053	0.299
119	3_16_Q_004_6-5_A_II_1_MGP10_HD	-0.827	0.220	-0.287	0.257	0.034	0.293
120	4_1_Q_004_6-5_B_II_3_MGP10_HD	-0.307	0.213	0.228	0.250	0.542	0.306
121	4_2_Q_002_5-5_A_II_3_MGP10_HD	-0.783	0.200	-0.226	0.235	0.120	0.267
122	4_3_Q_004_6-5_A_II_3_MGP10_HD	-0.880	0.232	-0.285	0.254	0.028	0.274
123	4_4_Q_002_5-5_D_II_1_MGP10_HD	-0.210	0.229	0.297	0.217	0.571	0.244

124	4_5_Q_004_6-5_D_II_1_MGP10_HD	-0.595	0.259	-0.009	0.310	0.314	0.318
125	4_6_Q_002_5-5_C_II_1_MGP10_HD	-0.567	0.255	-0.140	0.246	0.155	0.250
126	4_7_Q_004_6-5_C_II_1_MGP10_HD	-0.905	0.228	-0.310	0.258	-0.012	0.296
127	4_8_Q_002_5-5_B_II_1_MGP10_HD	-0.873	0.240	-0.281	0.273	0.029	0.282
128	4_9_Q_004_6-5_B_II_1_MGP10_HD	-1.013	0.262	-0.410	0.310	-0.127	0.336
129	4_10_Q_002_5-5_A_II_1_MGP10_HD	-0.986	0.259	-0.402	0.298	-0.093	0.331
130	4_11_Q_004_6-5_A_II_1_MGP10_HD	-1.011	0.287	-0.417	0.314	-0.127	0.329
131	5_1_Q_004_6-5_A_II_3_MGP10_HD	-0.946	0.344	-0.402	0.358	-0.102	0.395
132	5_2_Q_004_6-5_C_II_1_MGP10_HD	-1.389	0.370	-0.808	0.362	-0.487	0.379
133	5_3_Q_002_5-5_B_II_1_MGP10_HD	-1.248	0.317	-0.673	0.324	-0.363	0.358
134	5_4_Q_004_6-5_B_II_1_MGP10_HD	-1.433	0.401	-0.838	0.396	-0.525	0.389
135	5_5_Q_002_5-5_A_II_1_MGP10_HD	-1.371	0.356	-0.793	0.342	-0.473	0.353
136	5_6_Q_004_6-5_A_II_1_MGP10_HD	-1.429	0.381	-0.838	0.377	-0.531	0.385
137	5_1_C_004_6-5_D_II_3_MGP10_ATS	-0.082	0.384	0.514	0.452	0.863	0.482
138	5_2_C_002_5-5_C_II_3_MGP10_ATS	-0.060	0.402	0.503	0.464	0.858	0.499
139	5_3_C_004_6-5_C_II_3_MGP10_ATS	-0.190	0.320	0.412	0.387	0.770	0.416
140	5_4_C_002_5-5_B_II_3_MGP10_ATS	-0.292	0.333	0.304	0.372	0.659	0.420
141	5_5_C_004_6-5_B_II_3_MGP10_ATS	-1.100	0.329	-0.486	0.333	-0.139	0.357
142	5_6_C_002_5-5_A_II_3_MGP10_ATS	-0.666	0.239	-0.027	0.273	0.323	0.281
143	5_7_C_004_6-5_A_II_3_MGP10_ATS	-1.127	0.332	-0.511	0.353	-0.180	0.361
144	5_8_C_002_5-5_D_II_1_MGP10_ATS	-0.364	0.248	0.262	0.276	0.641	0.300
145	5_9_C_004_6-5_D_II_1_MGP10_ATS	-0.846	0.239	-0.229	0.257	0.104	0.286
146	5_10_C_002_5-5_C_II_1_MGP10_ATS	-0.591	0.231	0.049	0.252	0.412	0.278
147	5_11_C_004_6-5_C_II_1_MGP10_ATS	-1.650	0.320	-1.021	0.302	-0.693	0.328
148	5_12_C_002_5-5_B_II_1_MGP10_ATS	-1.318	0.368	-0.742	0.325	-0.421	0.299
149	5_13_C_004_6-5_B_II_1_MGP10_ATS	-1.651	0.321	-1.011	0.310	-0.676	0.330
150	5_14_C_002_5-5_A_II_1_MGP10_ATS	-1.341	0.354	-0.770	0.311	-0.440	0.285
151	5_15_C_004_6-5_A_II_1_MGP10_ATS	-1.711	0.362	-1.081	0.339	-0.762	0.346
152	6_1_C_002_7-0_B_II_3_MGP10_ATS	-0.917	0.281	-0.286	0.296	0.059	0.326
153	6_2_C_004_7-0_B_II_3_MGP10_ATS	-0.931	0.293	-0.299	0.310	0.044	0.312
154	6_3_C_002_7-0_D_II_1_MGP10_ATS	-0.744	0.260	-0.116	0.296	0.234	0.293
155	6_4_C_004_7-0_D_II_1_MGP10_ATS	-0.746	0.272	-0.116	0.289	0.231	0.287
156	5_1_D_004_6-5_D_II_3_MGP10_ATS	0.030	0.324	0.612	0.383	0.955	0.436
157	5_2_D_002_5-5_C_II_3_MGP10_ATS	0.021	0.328	0.635	0.417	0.973	0.464
158	5_3_D_004_6-5_C_II_3_MGP10_ATS	0.008	0.298	0.599	0.376	0.927	0.434
159	5_4_D_002_5-5_B_II_3_MGP10_ATS	0.031	0.305	0.611	0.394	0.950	0.420
160	5_5_D_004_6-5_B_II_3_MGP10_ATS	-0.987	0.341	-0.372	0.333	-0.036	0.335
161	5_6_D_002_5-5_A_II_3_MGP10_ATS	-0.832	0.272	-0.196	0.302	0.132	0.322
162	5_7_D_004_6-5_A_II_3_MGP10_ATS	-1.114	0.337	-0.507	0.318	-0.167	0.347

163	5_8_D_002_5-5_D_II_1_MGP10_ATS	-0.347	0.247	0.250	0.284	0.593	0.288
164	5_9_D_004_6-5_D_II_1_MGP10_ATS	-0.842	0.274	-0.213	0.302	0.127	0.309
165	5_10_D_002_5-5_C_II_1_MGP10_ATS	-0.630	0.214	-0.024	0.225	0.319	0.248
166	5_11_D_004_6-5_C_II_1_MGP10_ATS	-1.441	0.328	-0.835	0.339	-0.520	0.335
167	5_12_D_002_5-5_B_II_1_MGP10_ATS	-1.065	0.371	-0.476	0.320	-0.156	0.297
168	5_13_D_004_6-5_B_II_1_MGP10_ATS	-1.459	0.330	-0.850	0.336	-0.519	0.342
169	5_14_D_002_5-5_A_II_1_MGP10_ATS	-1.272	0.295	-0.701	0.294	-0.372	0.317
170	5_15_D_004_6-5_A_II_1_MGP10_ATS	-1.453	0.329	-0.842	0.333	-0.515	0.328
171	5_1_P_004_6-5_C_II_3_MGP10_ATS	-0.078	0.379	0.533	0.453	0.887	0.487
172	5_2_P_004_6-5_B_II_3_MGP10_ATS	-0.698	0.250	-0.064	0.270	0.274	0.288
173	5_3_P_002_5-5_A_II_3_MGP10_ATS	-0.664	0.262	-0.025	0.275	0.311	0.297
174	5_4_P_004_6-5_A_II_3_MGP10_ATS	-1.016	0.352	-0.397	0.346	-0.046	0.363
175	5_5_P_002_5-5_D_II_1_MGP10_ATS	-0.370	0.318	0.290	0.340	0.647	0.369
176	5_6_P_004_6-5_D_II_1_MGP10_ATS	-0.709	0.270	-0.078	0.299	0.260	0.315
177	5_7_P_002_5-5_C_II_1_MGP10_ATS	-0.654	0.253	-0.002	0.282	0.338	0.294
178	5_8_P_004_6-5_C_II_1_MGP10_ATS	-1.492	0.349	-0.848	0.360	-0.511	0.368
179	5_9_P_002_5-5_B_II_1_MGP10_ATS	-1.192	0.341	-0.607	0.331	-0.290	0.305
180	5_10_P_004_6-5_B_II_1_MGP10_ATS	-1.544	0.329	-0.914	0.319	-0.573	0.351
181	5_11_P_002_5-5_A_II_1_MGP10_ATS	-1.240	0.349	-0.637	0.339	-0.289	0.354
182	5_12_P_004_6-5_A_II_1_MGP10_ATS	-1.603	0.337	-0.970	0.323	-0.637	0.360
183	6_1_P_002_7-0_B_II_3_MGP10_ATS	-0.684	0.279	-0.005	0.286	0.388	0.299
184	6_2_P_004_7-0_B_II_3_MGP10_ATS	-0.858	0.317	-0.220	0.326	0.135	0.353
185	6_3_P_002_7-0_D_II_1_MGP10_ATS	-0.751	0.268	-0.107	0.285	0.260	0.305
186	6_4_P_004_7-0_D_II_1_MGP10_ATS	-0.779	0.270	-0.096	0.291	0.268	0.297
187	5_1_Q_004_6-5_D_II_3_MGP10_ATS	0.028	0.376	0.622	0.418	0.945	0.469
188	5_2_Q_002_5-5_C_II_3_MGP10_ATS	0.041	0.352	0.639	0.414	0.982	0.465
189	5_3_Q_004_6-5_C_II_3_MGP10_ATS	0.027	0.360	0.608	0.421	0.964	0.475
190	5_4_Q_002_5-5_B_II_3_MGP10_ATS	-0.003	0.316	0.587	0.364	0.928	0.410
191	5_5_Q_004_6-5_B_II_3_MGP10_ATS	-0.454	0.302	0.156	0.271	0.534	0.255
192	5_6_Q_002_5-5_A_II_3_MGP10_ATS	-0.570	0.211	0.082	0.218	0.436	0.242
193	5_7_Q_004_6-5_A_II_3_MGP10_ATS	-0.976	0.335	-0.365	0.345	-0.021	0.349
194	5_8_Q_002_5-5_D_II_1_MGP10_ATS	-0.126	0.248	0.483	0.301	0.824	0.314
195	5_9_Q_004_6-5_D_II_1_MGP10_ATS	-0.696	0.245	-0.063	0.258	0.273	0.283
196	5_10_Q_002_5-5_C_II_1_MGP10_ATS	-0.460	0.206	0.155	0.215	0.498	0.247
197	5_11_Q_004_6-5_C_II_1_MGP10_ATS	-1.345	0.333	-0.723	0.335	-0.388	0.340
198	5_12_Q_002_5-5_B_II_1_MGP10_ATS	-1.058	0.339	-0.446	0.325	-0.123	0.314
199	5_13_Q_004_6-5_B_II_1_MGP10_ATS	-1.345	0.327	-0.736	0.337	-0.396	0.359
200	5_14_Q_002_5-5_A_II_1_MGP10_ATS	-1.168	0.359	-0.574	0.325	-0.240	0.298
201	5_15_Q_004_6-5_A_II_1_MGP10_ATS	-1.362	0.343	-0.750	0.348	-0.402	0.353

Archetype #1: 3_1_C_002_5-5_D_II_3_MGP10_HD

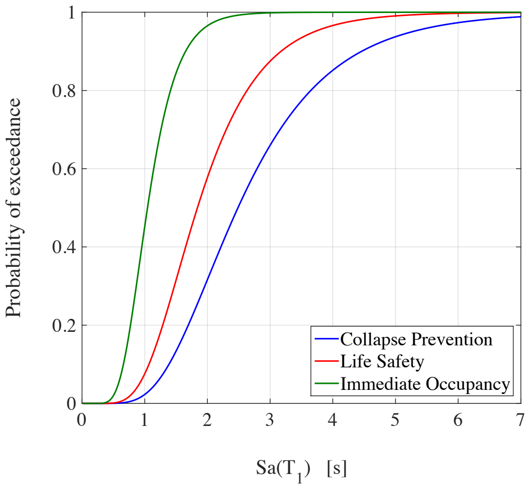

Archetype #2: 3_2_C_004_6-5_D_II_3_MGP10_HD

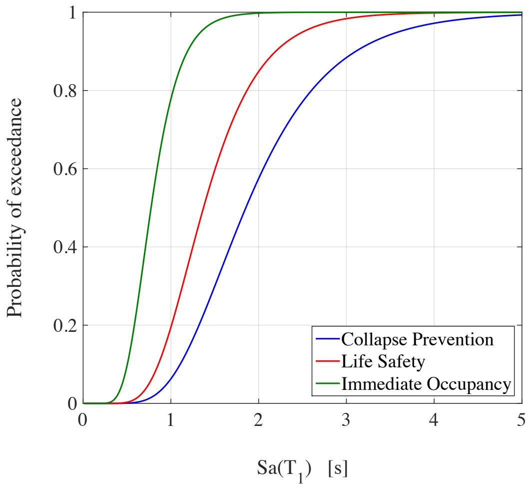

Archetype #3: 3_3_C_002_5-5_C_II_3_MGP10_HD

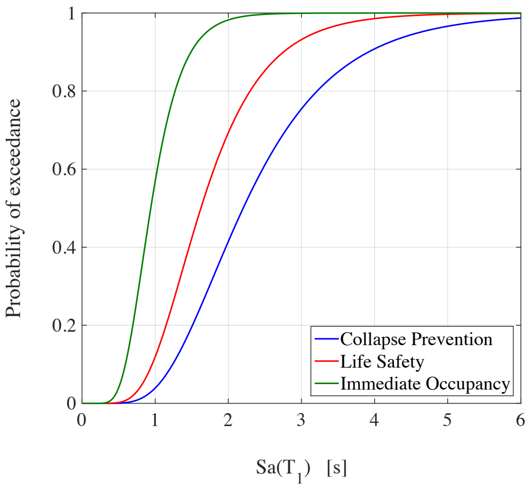

Archetype #4: 3_4_C_004_6-5_C_II_3_MGP10_HD

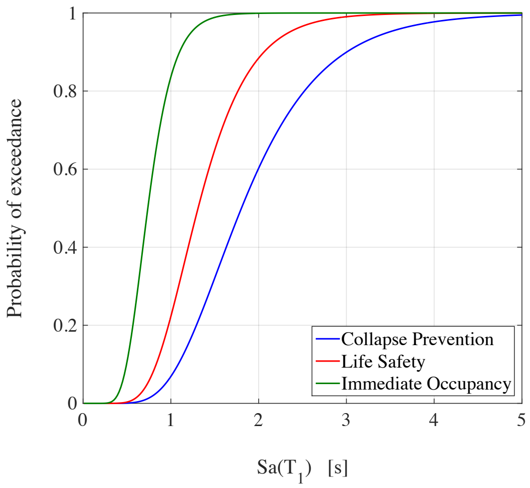

Archetype #5: 3_5_C_002_5-5_B_II_3_MGP10_HD

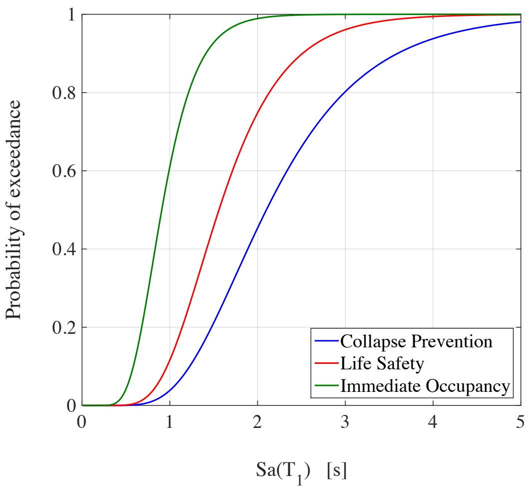

Archetype #6: 3_6_C_004_6-5_B_II_3_MGP10_HD

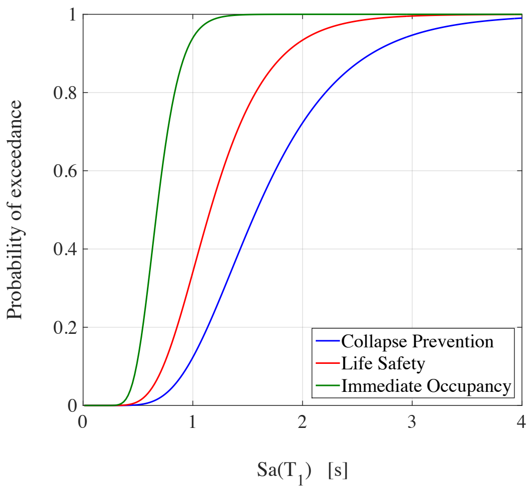

Archetype #7: 3_7_C_002_5-5_A_II_3_MGP10_HD

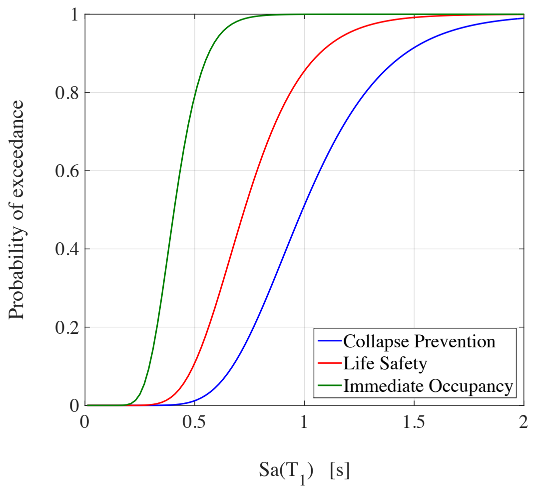

Archetype #8: 3_8_C_004_6-5_A_II_3_MGP10_HD

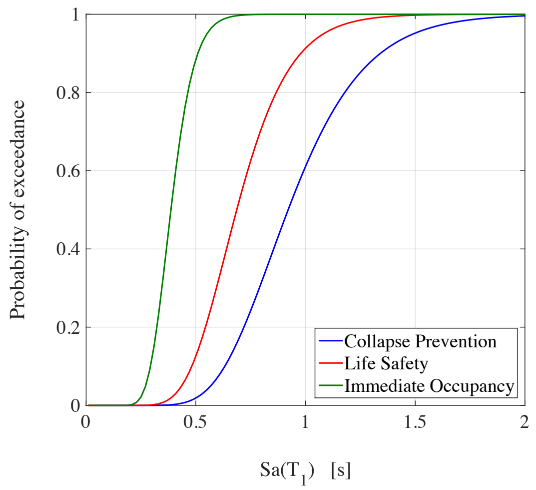

Archetype #9: 3_9_C_002_5-5_D_II_1_MGP10_HD

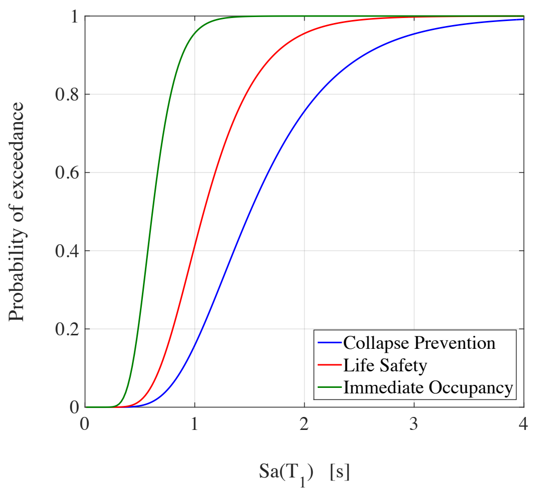

Archetype #10: 3_10_C_004_6-5_D_II_1_MGP10_HD

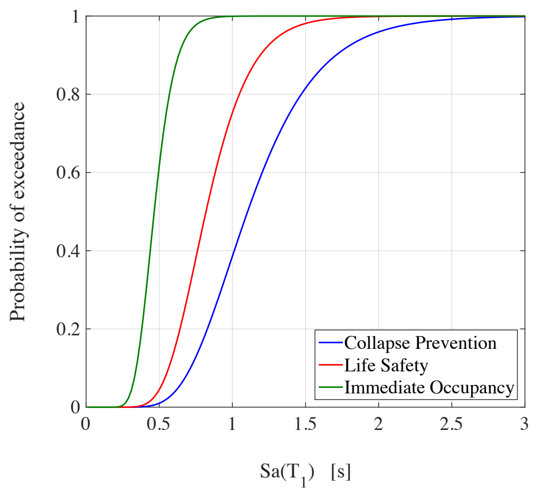

Archetype #11: 3_11_C_002_5-5_C_II_1_MGP10_HD

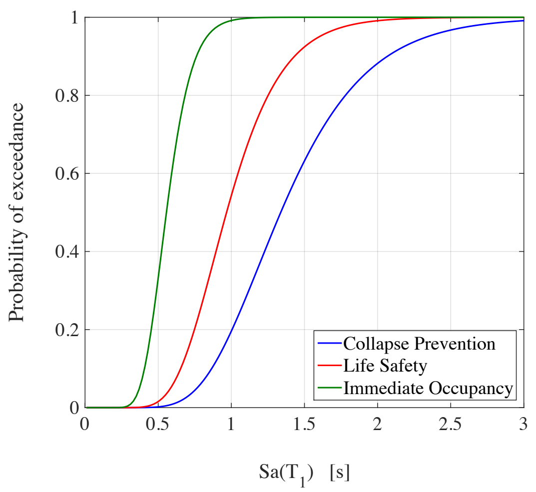

Archetype #12: 3_12_C_004_6-5_C_II_1_MGP10_HD

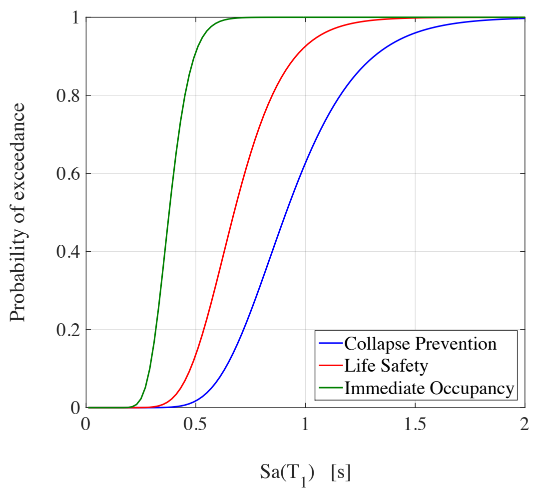

Archetype #13: 3_13_C_002_5-5_B_II_1_MGP10_HD

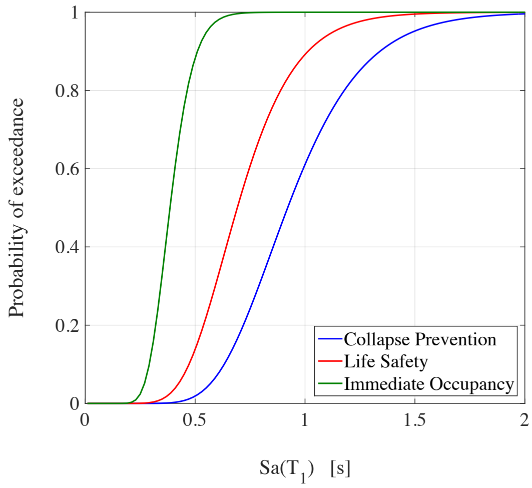

Archetype #14: 3_14_C_004_6-5_B_II_1_MGP10_HD

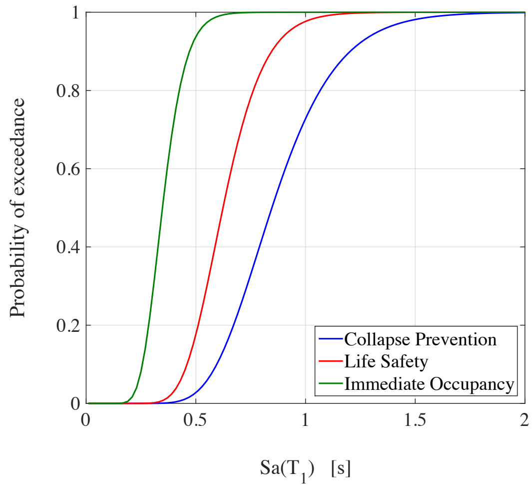

Archetype #15: 3_15_C_002_5-5_A_II_1_MGP10_HD

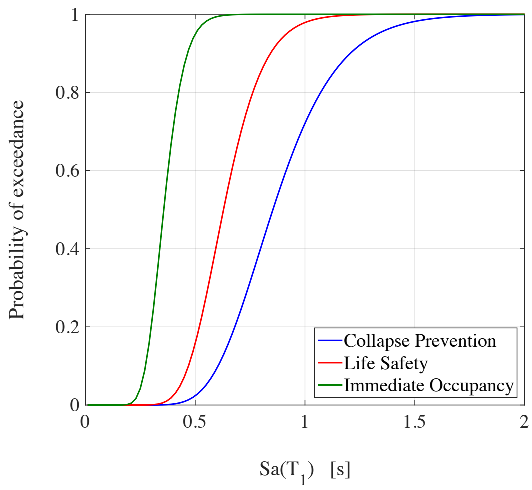

Archetype #16: 3_16_C_004_6-5_A_II_1_MGP10_HD

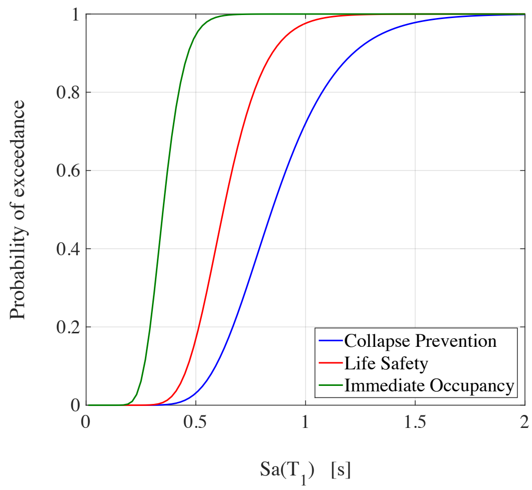

Archetype #17: 4_1_C_004_6-5_B_II_3_MGP10_HD

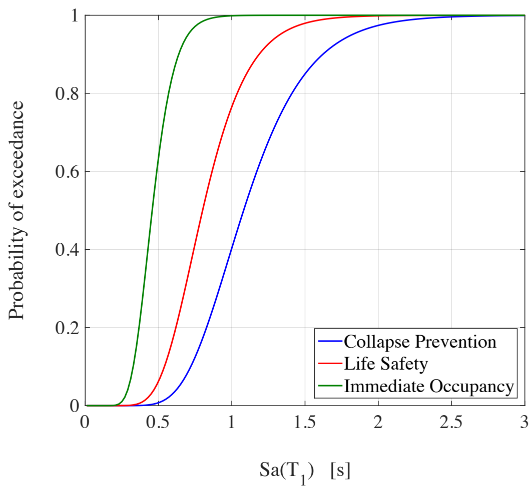

Archetype #18: 4_2_C_002_5-5_A_II_3_MGP10_HD

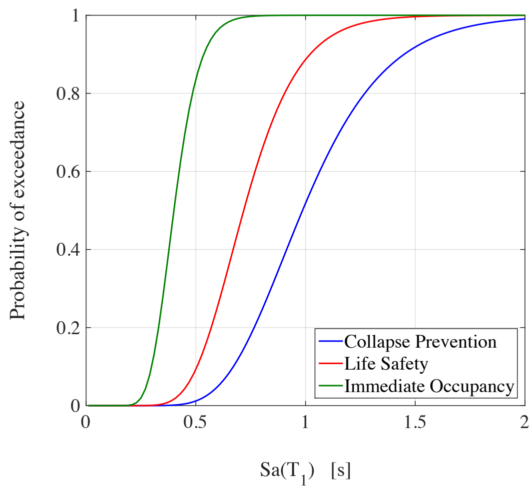

Archetype #19: 4_3_C_004_6-5_A_II_3_MGP10_HD

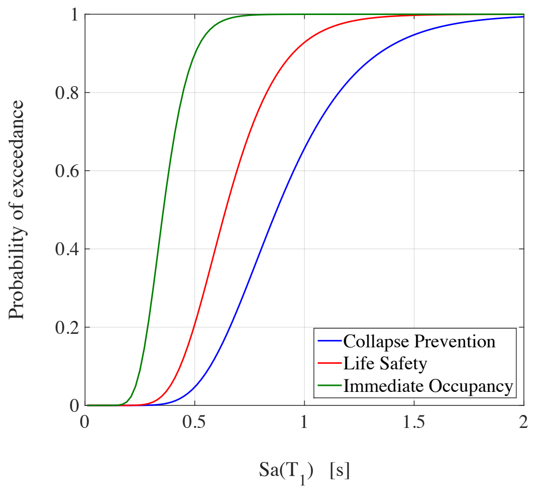

Archetype #20: 4_4_C_002_5-5_D_II_1_MGP10_HD

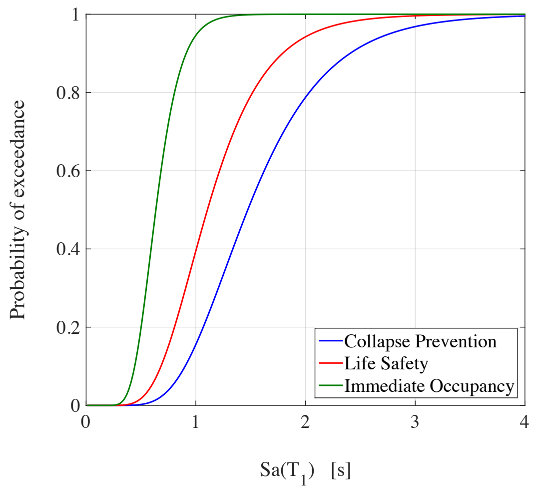

Archetype #21: 4_5_C_004_6-5_D_II_1_MGP10_HD

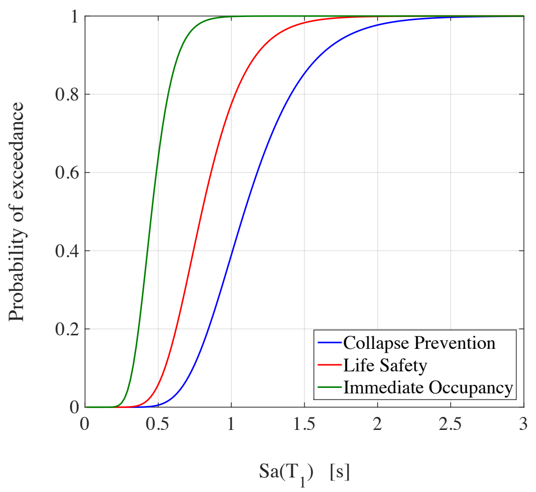

Archetype #22: 4_6_C_002_5-5_C_II_1_MGP10_HD

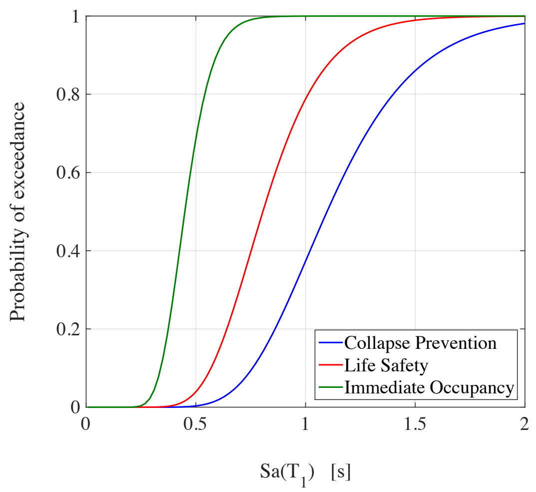

Archetype #23: 4_7_C_004_6-5_C_II_1_MGP10_HD

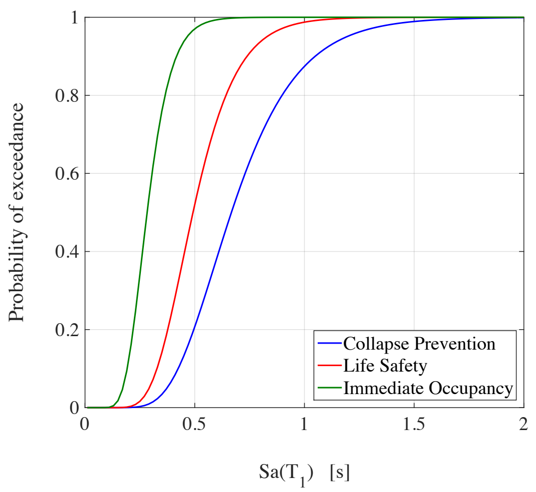

Archetype #24: 4_8_C_002_5-5_B_II_1_MGP10_HD

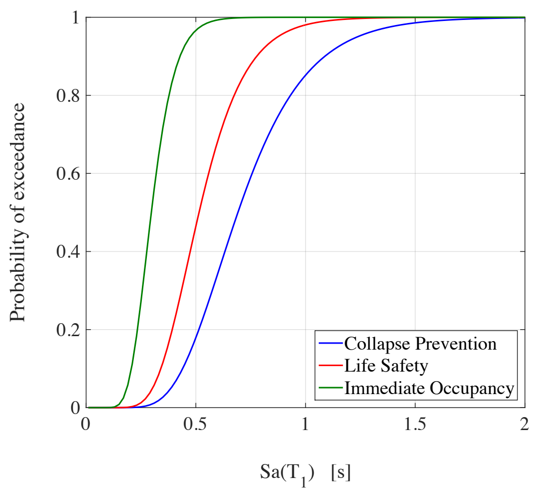

Archetype #25: 4_9_C_004_6-5_B_II_1_MGP10_HD

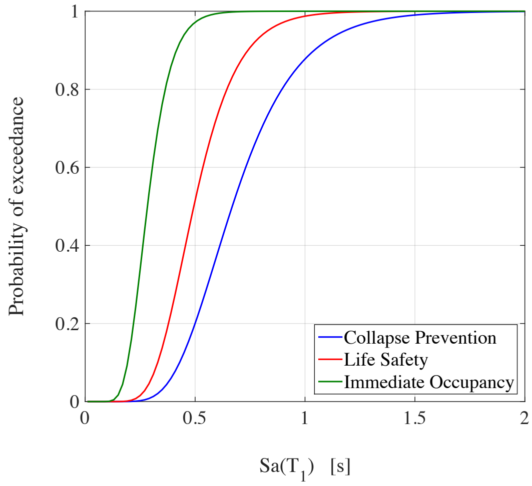

Archetype #26: 4_10_C_002_5-5_A_II_1_MGP10_HD

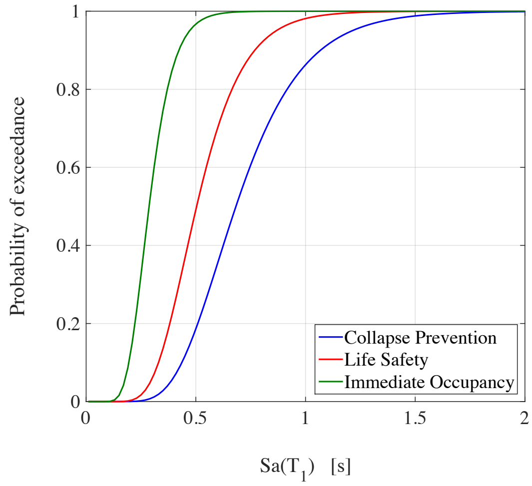

Archetype #27: 4_11_C_004_6-5_A_II_1_MGP10_HD

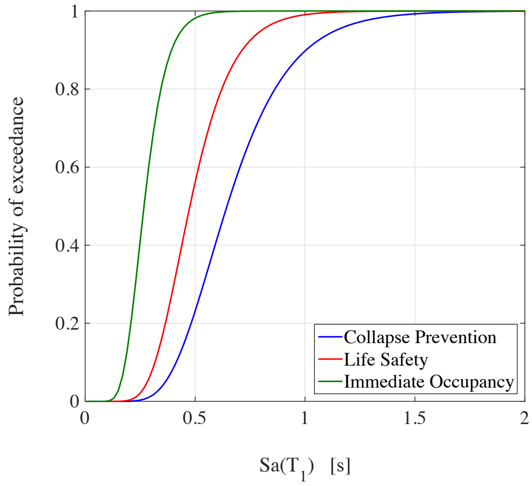

Archetype #28: 5_1_C_002_5-5_A_II_3_MGP10_HD

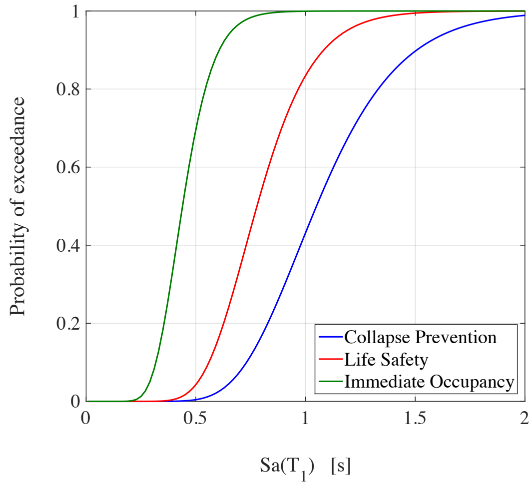

Archetype #29: 5_2_C_004_6-5_A_II_3_MGP10_HD

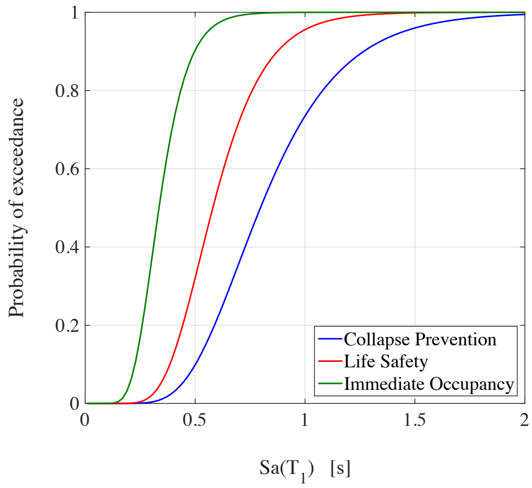

Archetype #30: 5_3_C_004_6-5_C_II_1_MGP10_HD

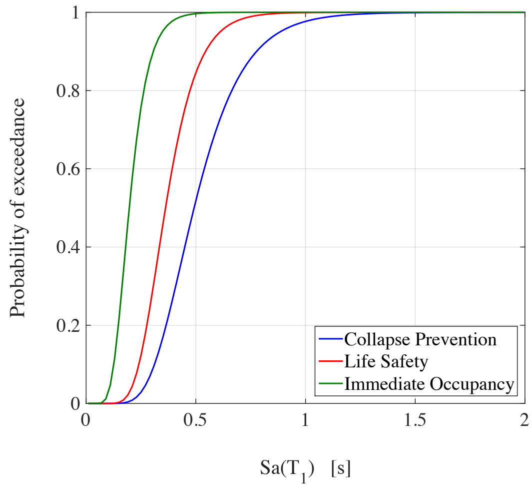

Archetype #31: 5_4_C_002_5-5_B_II_1_MGP10_HD

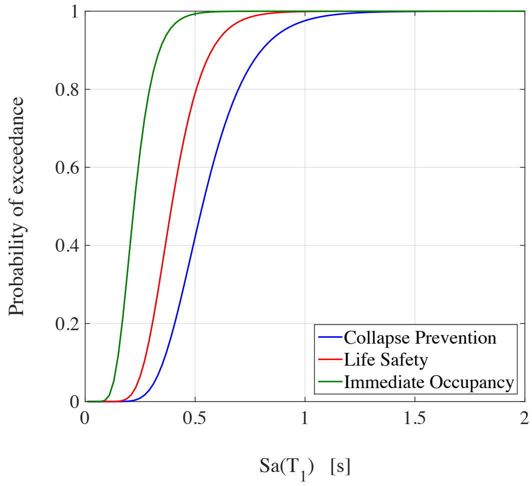

Archetype #32: 5_5_C_004_6-5_B_II_1_MGP10_HD

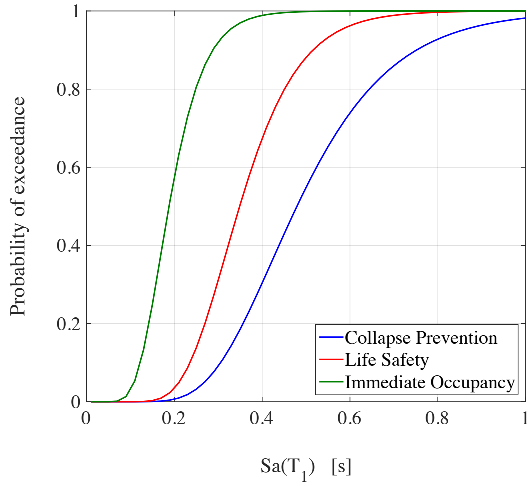

Archetype #33: 5_6_C_002_5-5_A_II_1_MGP10_HD

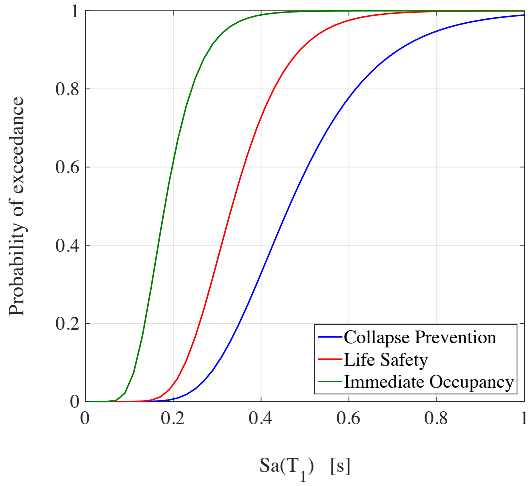

Archetype #34: 5_7_C_004_6-5_A_II_1_MGP10_HD

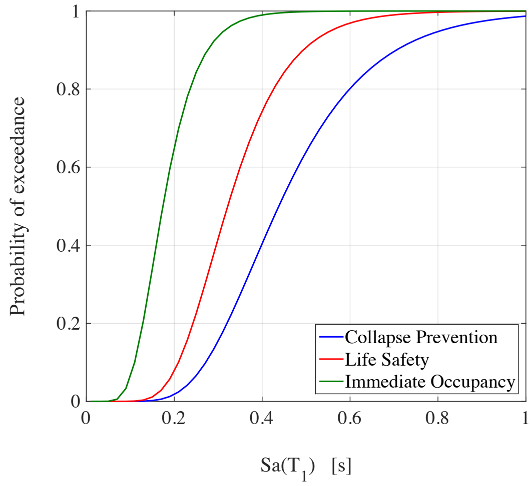

Archetype #35: 3_1_D_002_5-5_D_II_3_MGP10_HD

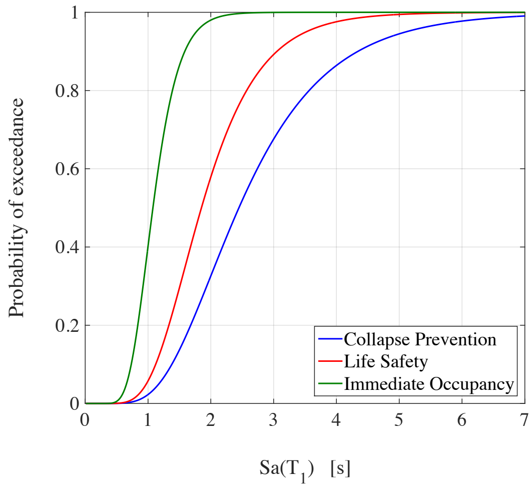

Archetype #36: 3_2_D_004_6-5_D_II_3_MGP10_HD

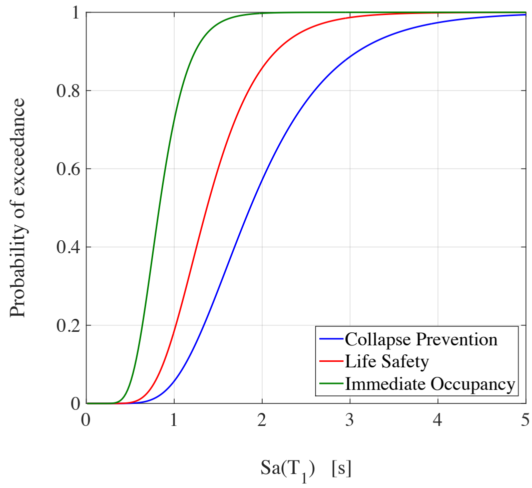

Archetype #37: 3_3_D_002_5-5_C_II_3_MGP10_HD

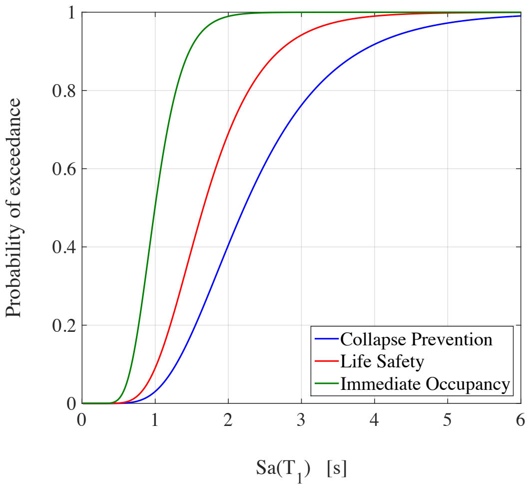

Archetype #38: 3_4_D_004_6-5_C_II_3_MGP10_HD

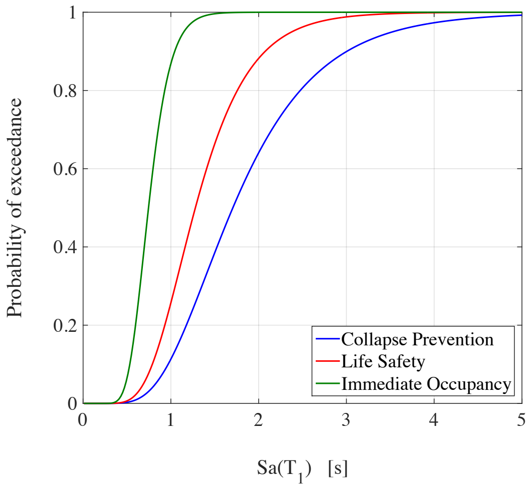

Archetype #39: 3_5_D_002_5-5_B_II_3_MGP10_HD

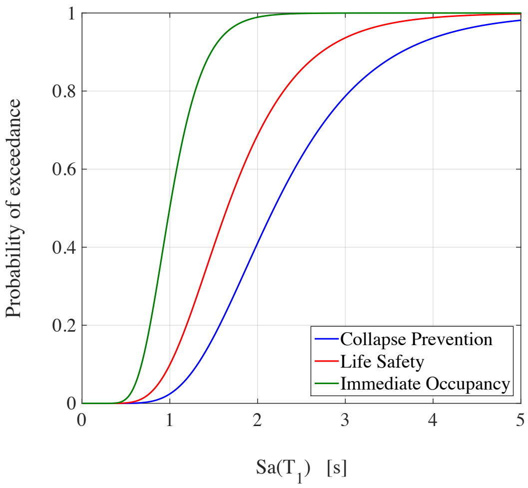

Archetype #40: 3_6_D_004_6-5_B_II_3_MGP10_HD

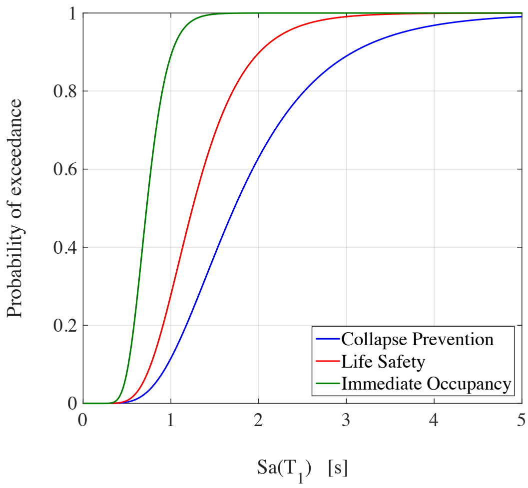

Archetype #41: 3_7_D_002_5-5_A_II_3_MGP10_HD

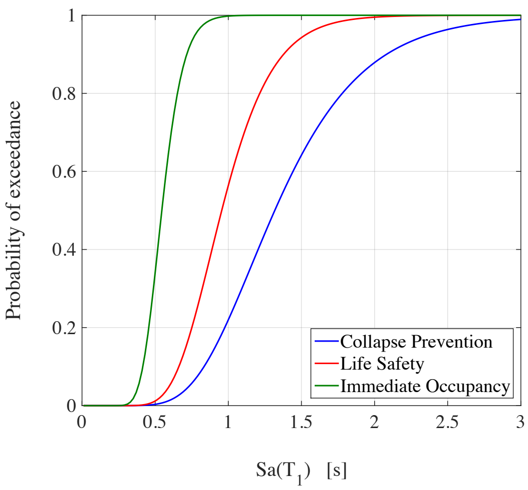

Archetype #42: 3_8_D_004_6-5_A_II_3_MGP10_HD

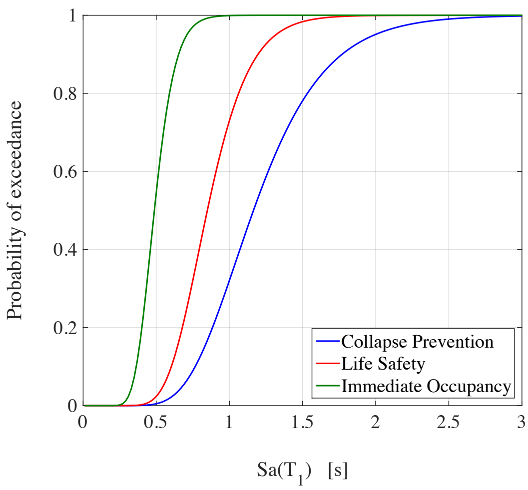

Archetype #43: 3_9_D_002_5-5_D_II_1_MGP10_HD

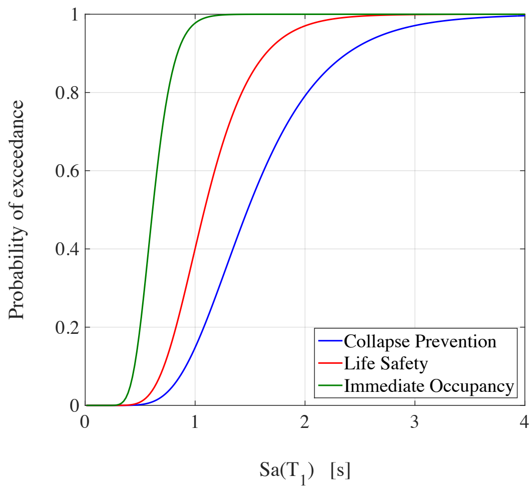

Archetype #44: 3_10_D_004_6-5_D_II_1_MGP10_HD

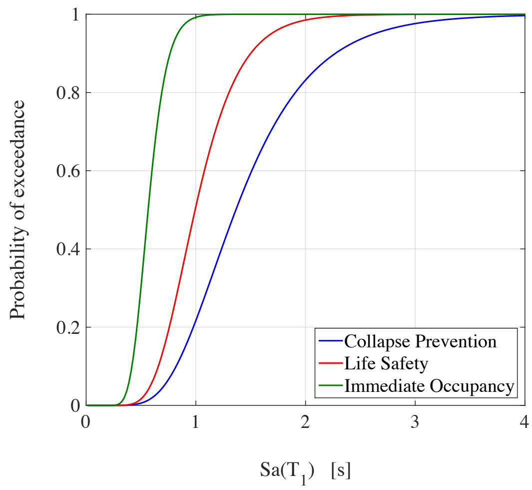

Archetype #45: 3_11_D_002_5-5_C_II_1_MGP10_HD

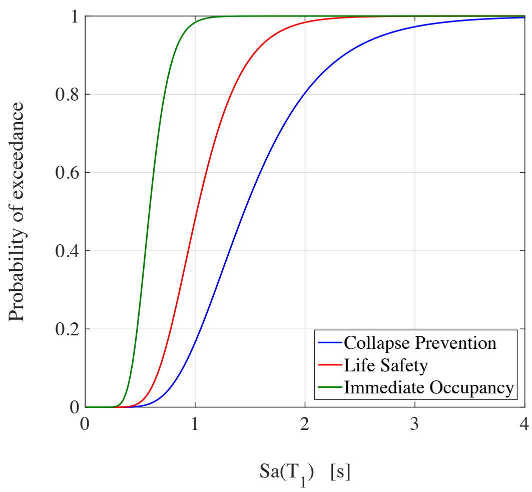

Archetype #46: 3_12_D_004_6-5_C_II_1_MGP10_HD

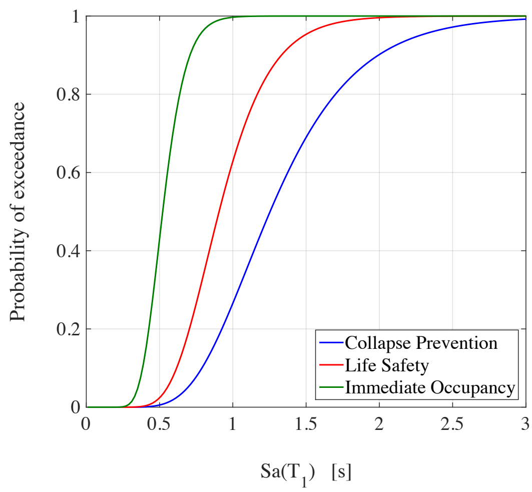

Archetype #47: 3_13_D_002_5-5_B_II_1_MGP10_HD

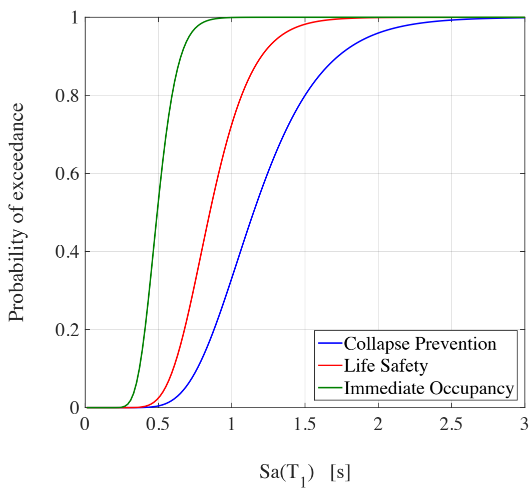

Archetype #48: 3_14_D_004_6-5_B_II_1_MGP10_HD

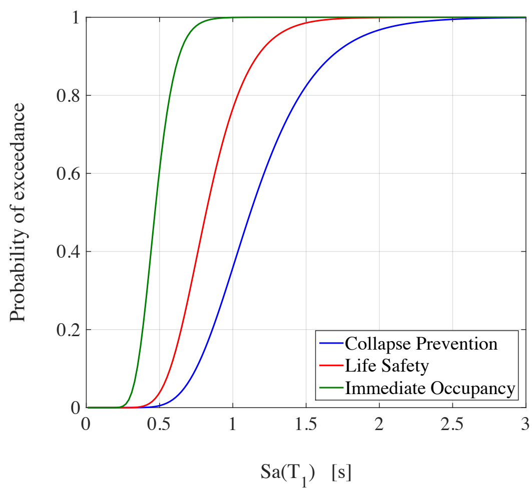

Archetype #49: 3_15_D_002_5-5_A_II_1_MGP10_HD

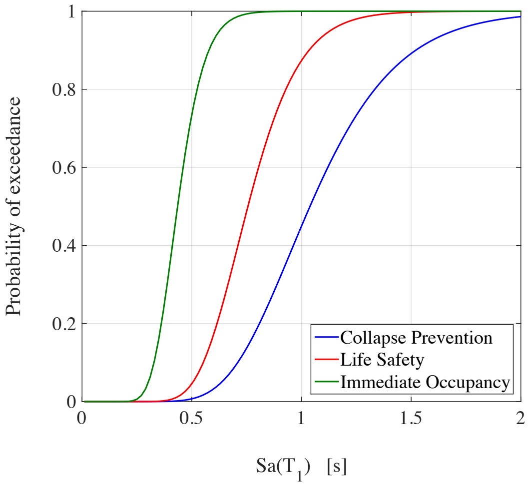

Archetype #50: 3_16_D_004_6-5_A_II_1_MGP10_HD

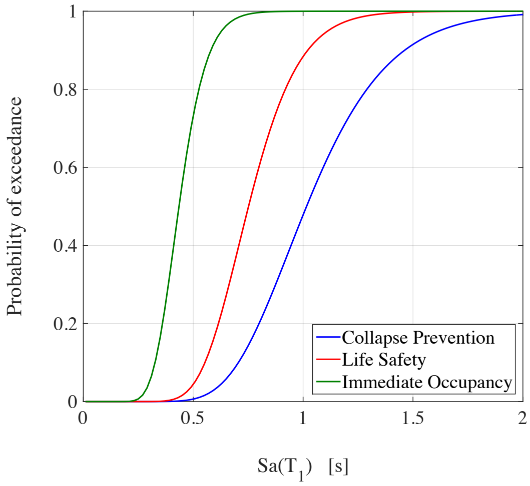

Archetype #51: 4_1_D_004_6-5_B_II_3_MGP10_HD

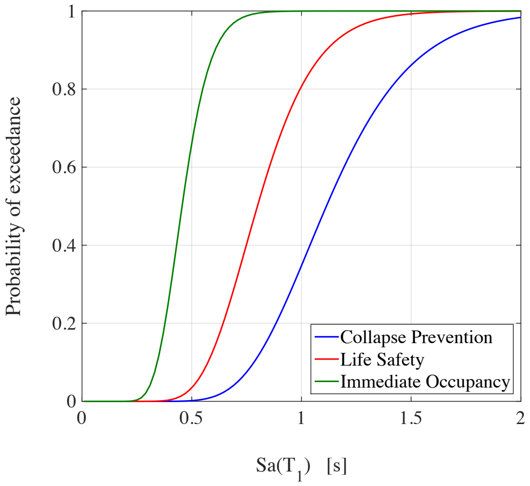

Archetype #52: 4_2_D_002_5-5_A_II_3_MGP10_HD

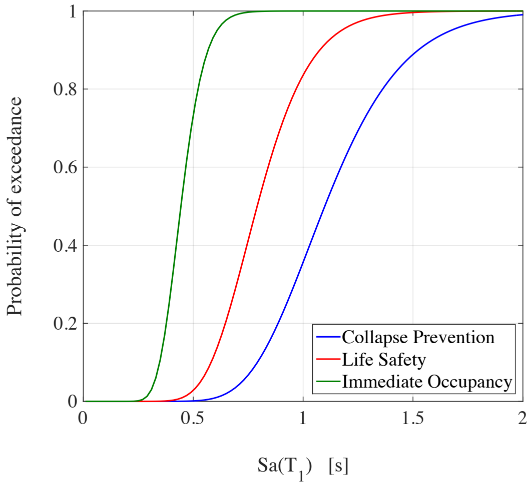

Archetype #53: 4_3_D_004_6-5_A_II_3_MGP10_HD

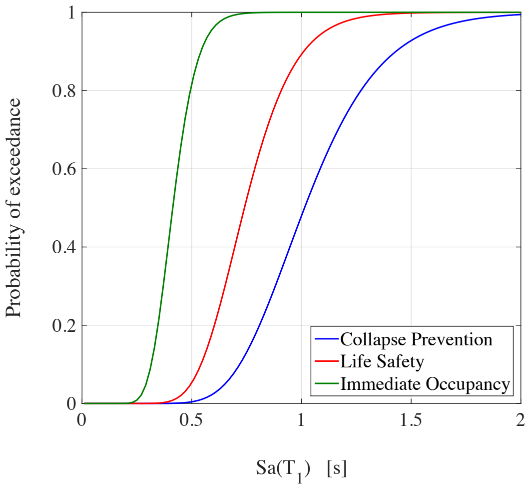

Archetype #54: 4_4_D_002_5-5_D_II_1_MGP10_HD

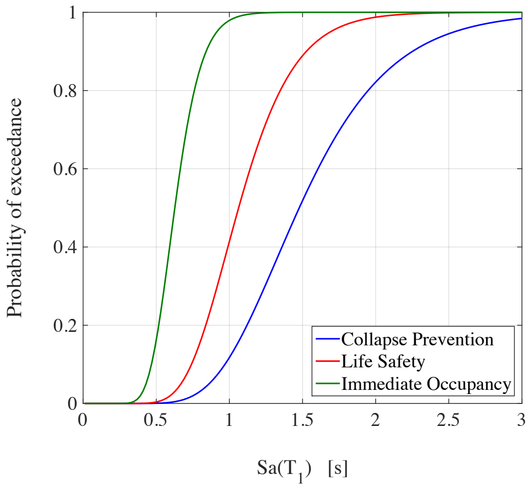

Archetype #55: 4_5_D_004_6-5_D_II_1_MGP10_HD

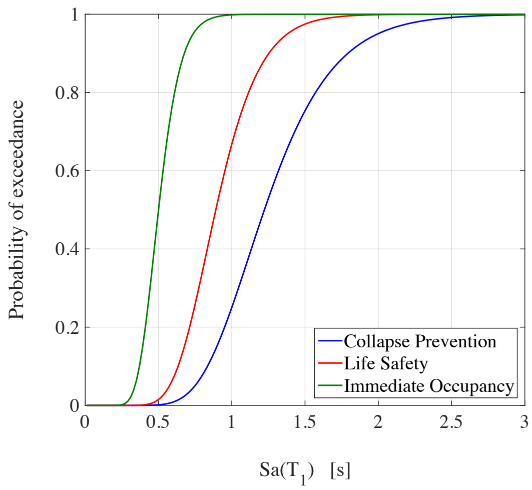

Archetype #56: 4_6_D_002_5-5_C_II_1_MGP10_HD

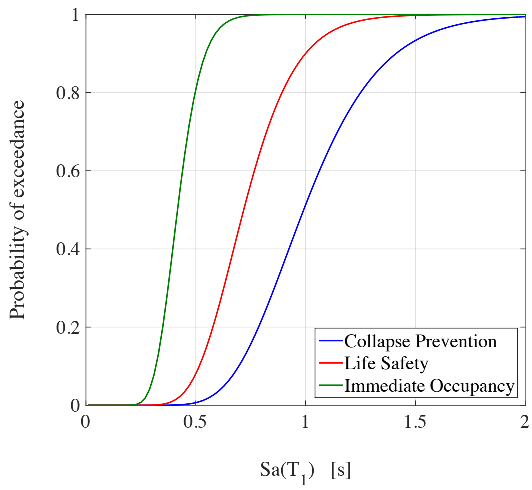

Archetype #57: 4_7_D_004_6-5_C_II_1_MGP10_HD

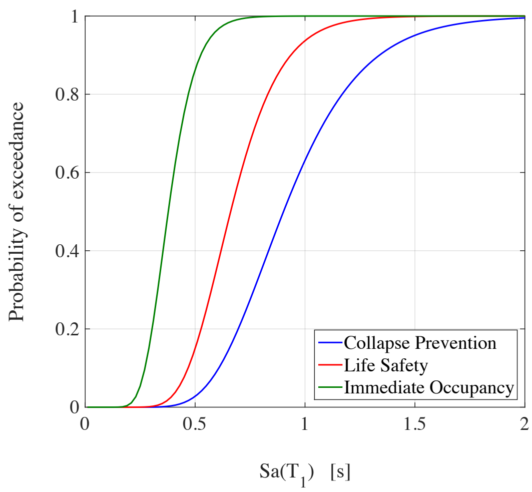

Archetype #58: 4_8_D_002_5-5_B_II_1_MGP10_HD

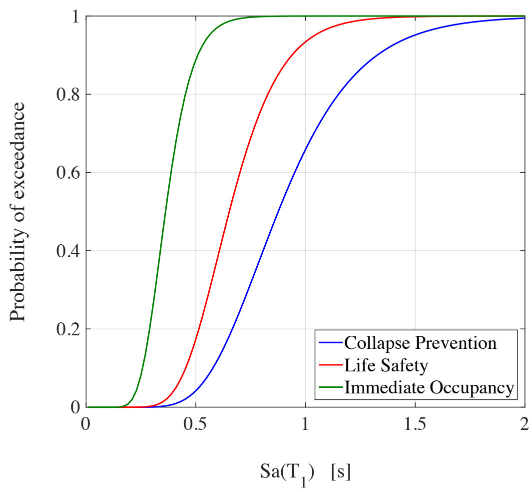

Archetype #59: 4_9_D_004_6-5_B_II_1_MGP10_HD

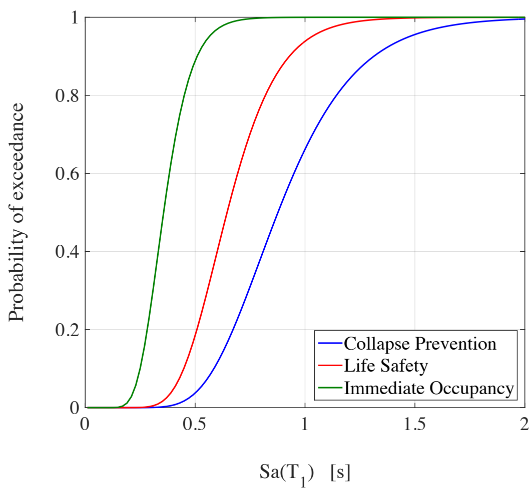

Archetype #60: 4_10_D_002_5-5_A_II_1_MGP10_HD

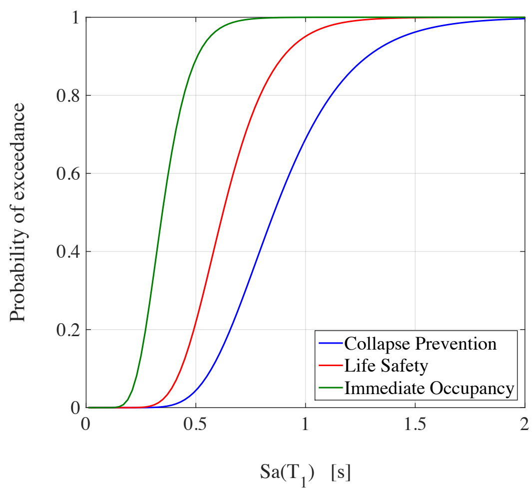

Archetype #61: 4_11_D_004_6-5_A_II_1_MGP10_HD

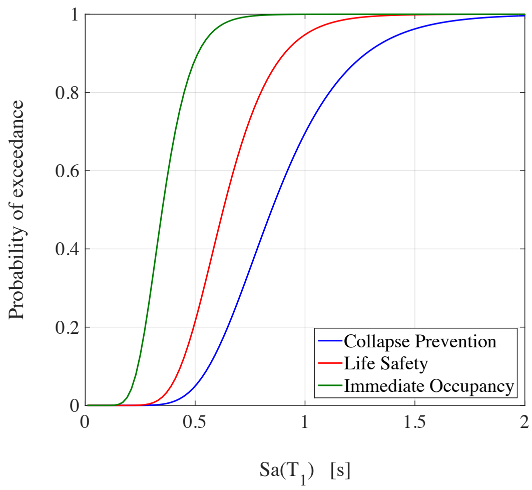

Archetype #62: 5_1_D_004_6-5_B_II_3_MGP10_HD

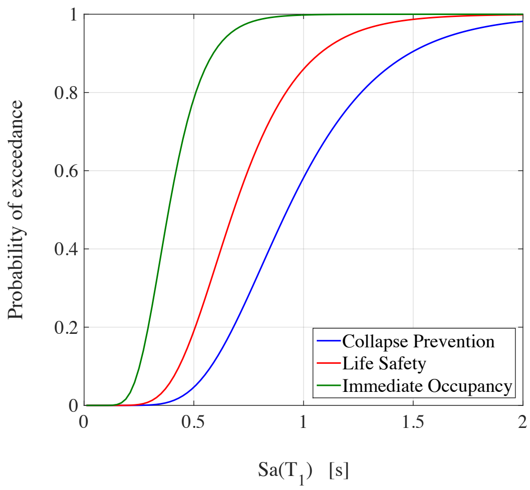

Archetype #63: 5_2_D_002_5-5_A_II_3_MGP10_HD

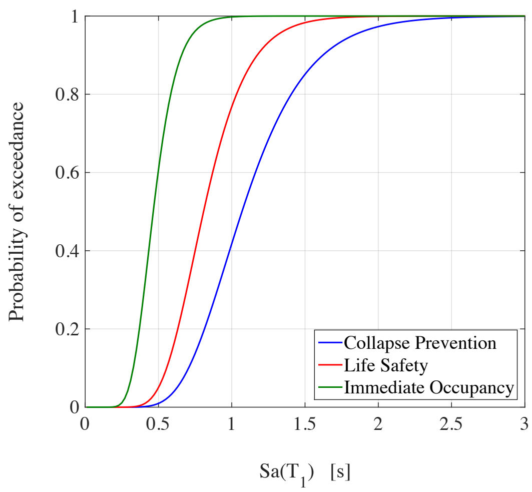

Archetype #64: 5_3_D_004_6-5_A_II_3_MGP10_HD

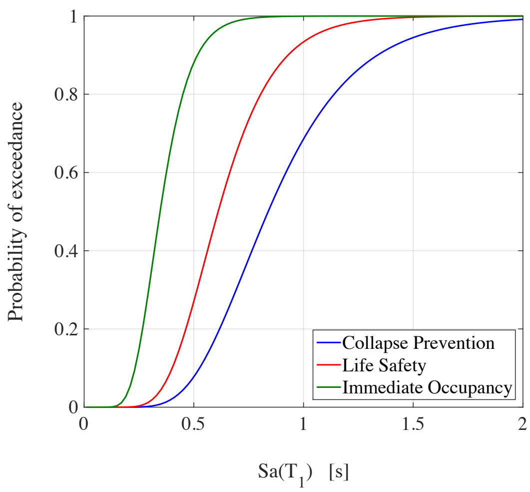

Archetype #65: 5_4_D_004_6-5_D_II_1_MGP10_HD

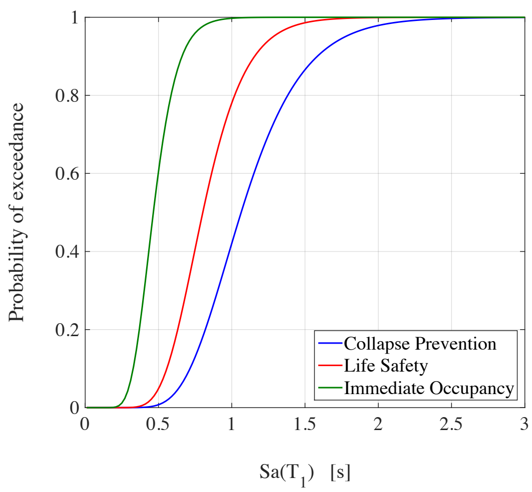

Archetype #66: 5_5_D_004_6-5_C_II_1_MGP10_HD

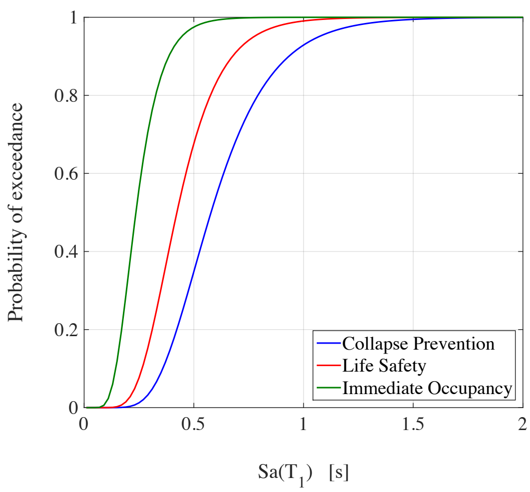

Archetype #67: 5_6_D_002_5-5_B_II_1_MGP10_HD

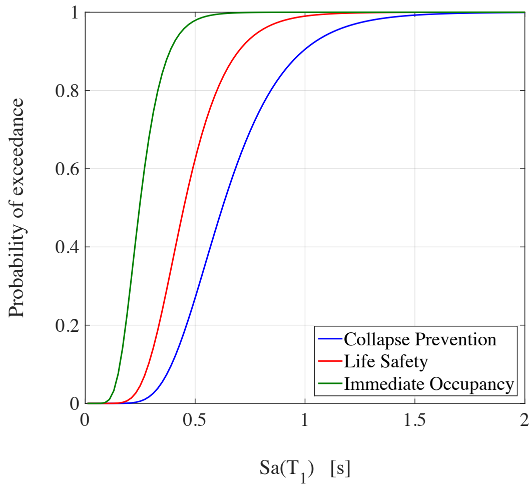

Archetype #68: 5_7_D_004_6-5_B_II_1_MGP10_HD

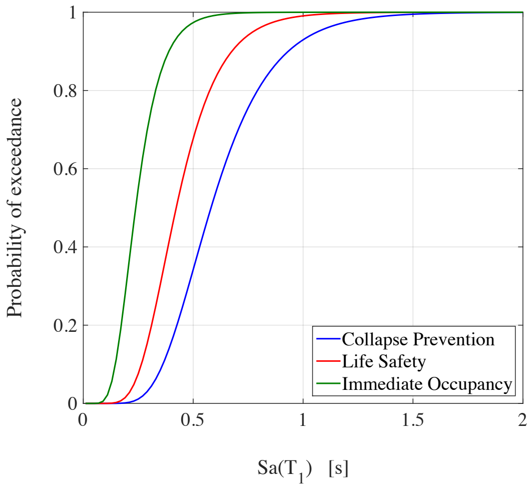

Archetype #69: 5_8_D_002_5-5_A_II_1_MGP10_HD

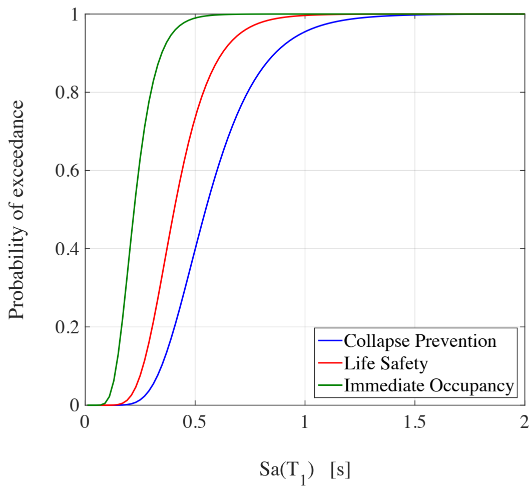

Archetype #70: 5_9_D_004_6-5_A_II_1_MGP10_HD

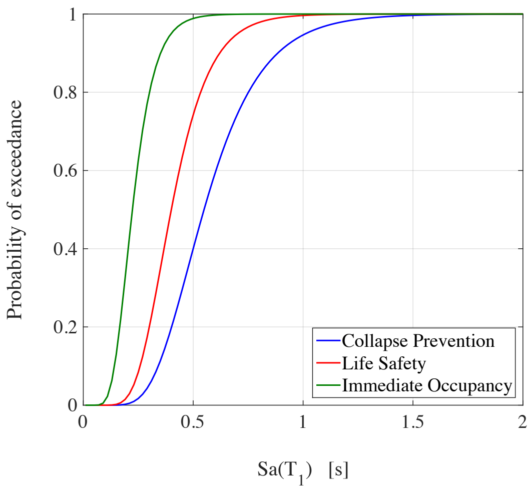

Archetype #71: 3_1_P_002_5-5_D_II_3_MGP10_HD

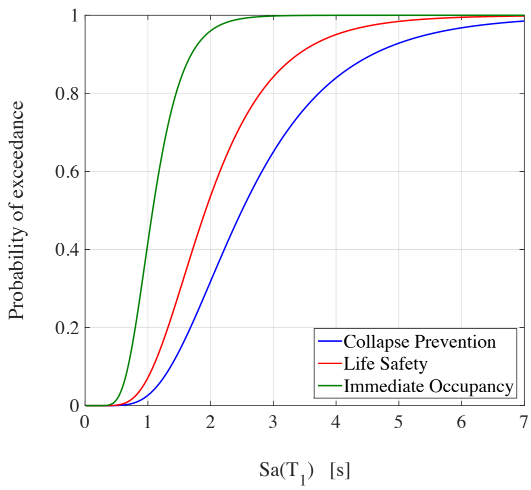

Archetype #72: 3_2_P_004_6-5_D_II_3_MGP10_HD

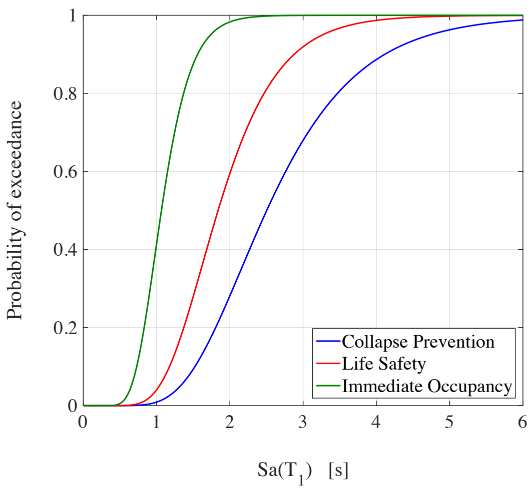

Archetype #73: 3_3_P_002_5-5_C_II_3_MGP10_HD

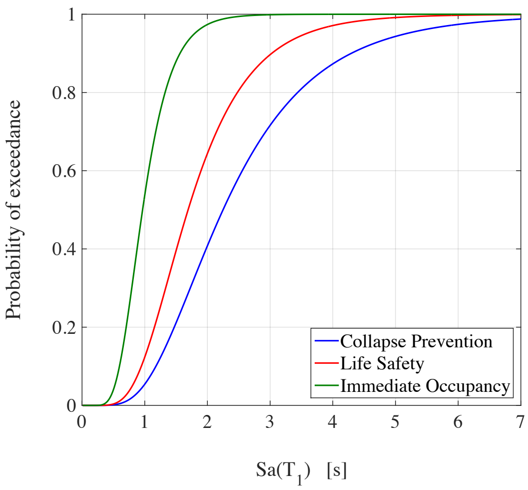

Archetype #74: 3_4_P_004_6-5_C_II_3_MGP10_HD

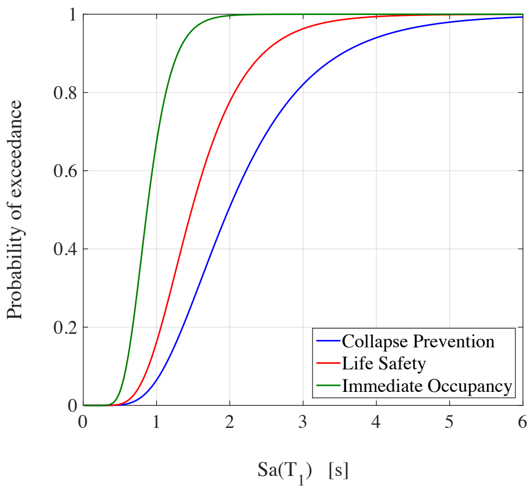

Archetype #75: 3_5_P_002_5-5_B_II_3_MGP10_HD

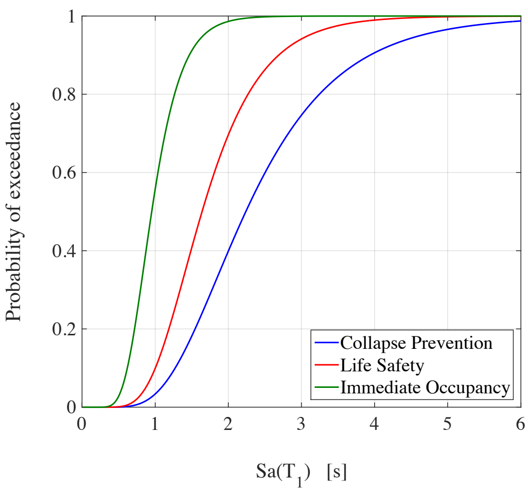

Archetype #76: 3_6_P_004_6-5_B_II_3_MGP10_HD

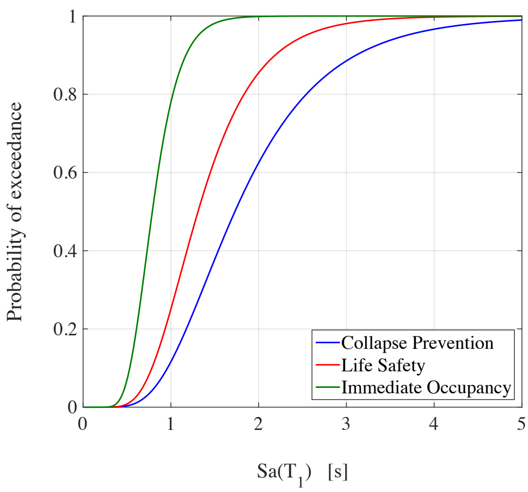

Archetype #77: 3_7_P_002_5-5_A_II_3_MGP10_HD

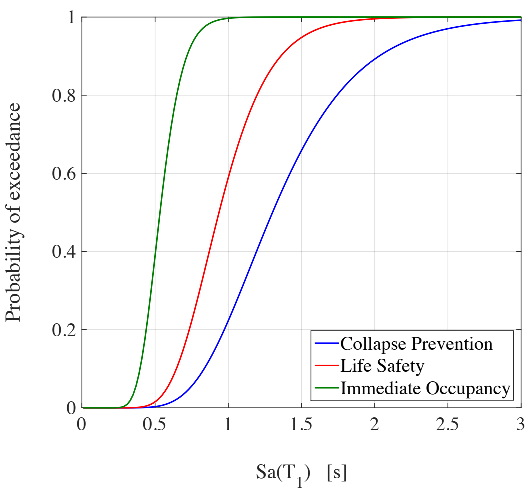

Archetype #78: 3_8_P_004_6-5_A_II_3_MGP10_HD

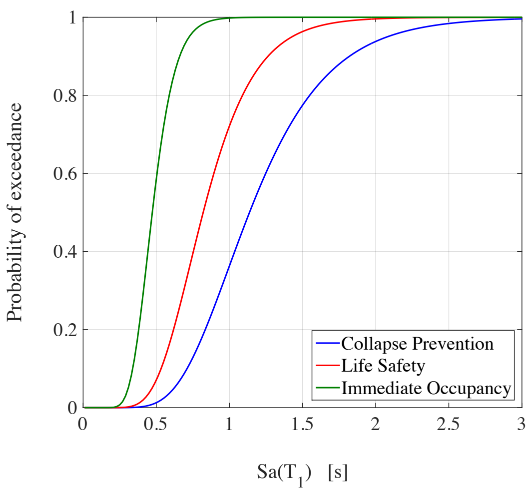

Archetype #79: 3_9_P_002_5-5_D_II_1_MGP10_HD

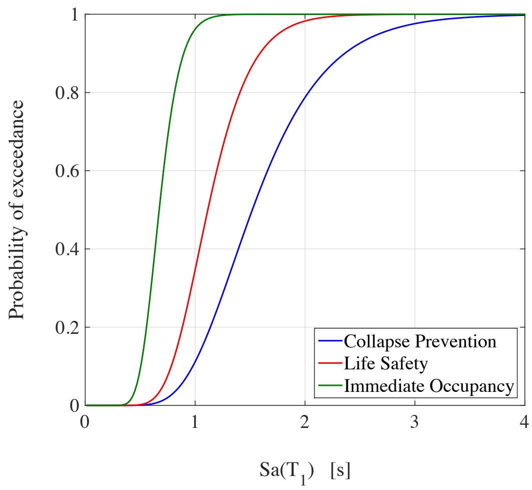

Archetype #80: 3_10_P_004_6-5_D_II_1_MGP10_HD

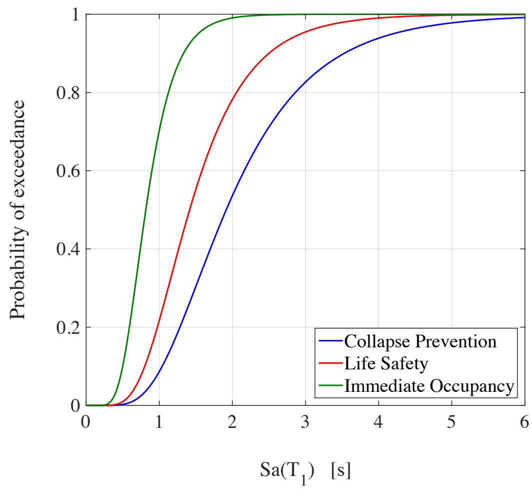

Archetype #81: 3_11_P_002_5-5_C_II_1_MGP10_HD

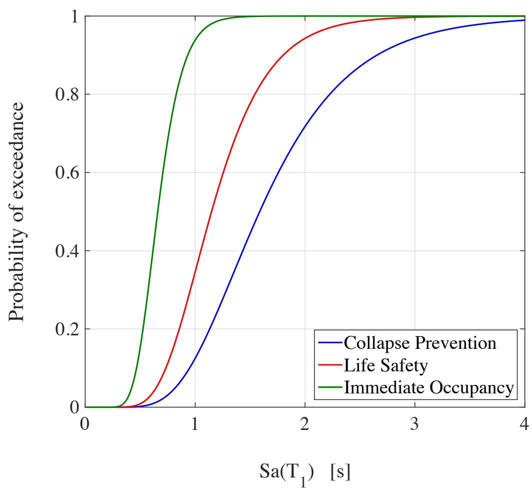

Archetype #82: 3_12_P_004_6-5_C_II_1_MGP10_HD

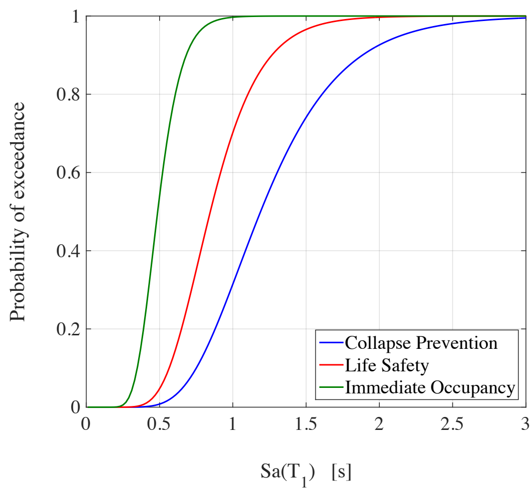

Archetype #83: 3_13_P_002_5-5_B_II_1_MGP10_HD

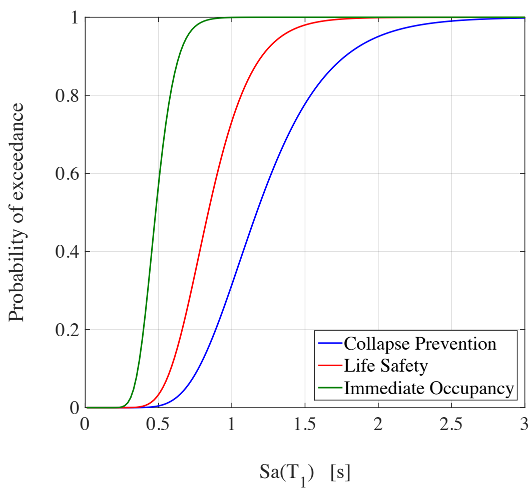

Archetype #84: 3_14_P_004_6-5_B_II_1_MGP10_HD

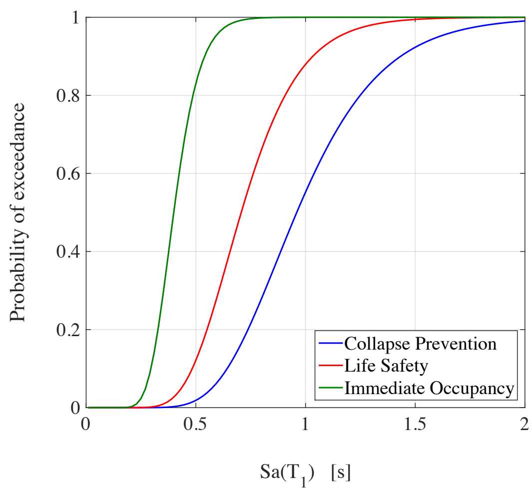

Archetype #85: 3_15_P_002_5-5_A_II_1_MGP10_HD

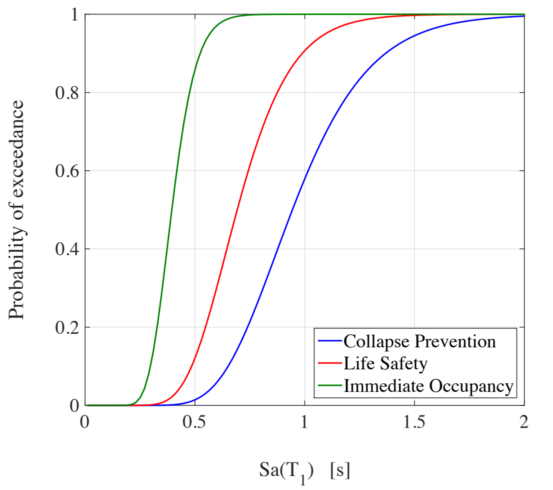

Archetype #86: 3_16_P_004_6-5_A_II_1_MGP10_HD

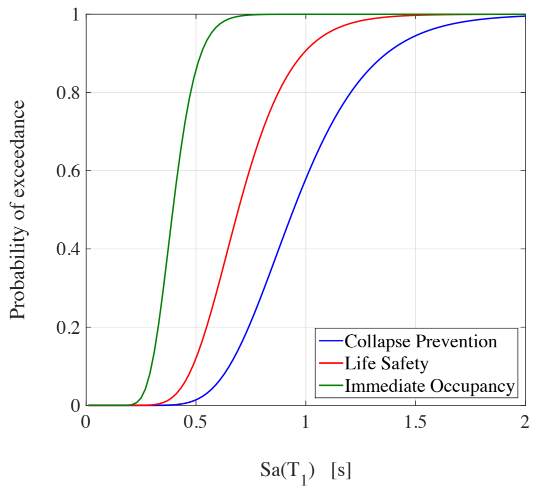

Archetype #87: 4_1_P_002_5-5_A_II_3_MGP10_HD

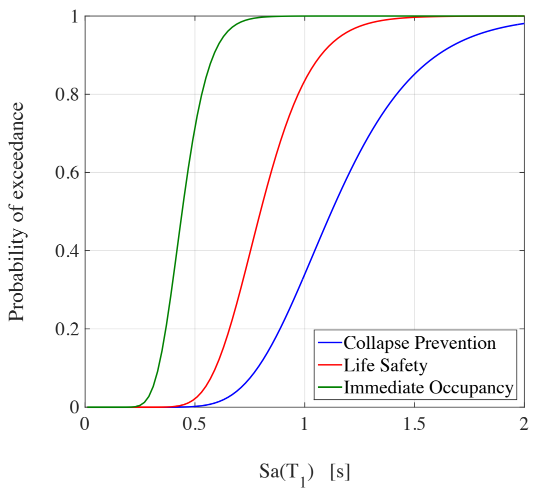

Archetype #88: 4_2_P_004_6-5_A_II_3_MGP10_HD

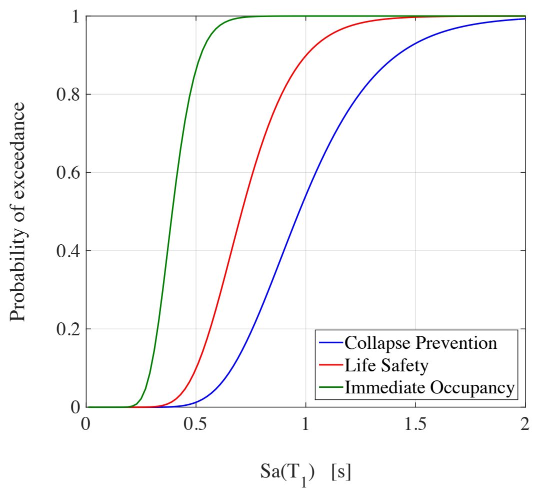

Archetype #89: 4_3_P_002_5-5_D_II_1_MGP10_HD

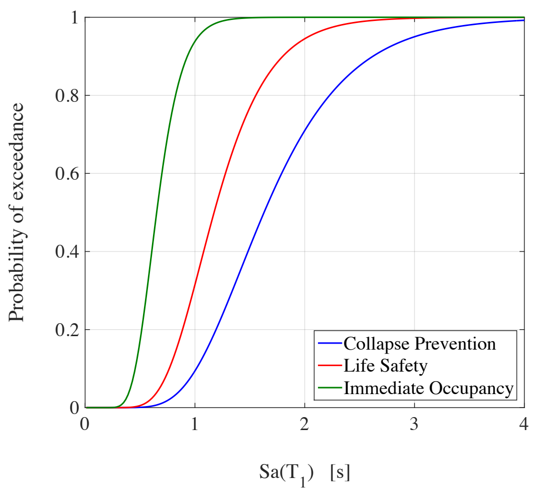

Archetype #90: 4_4_P_004_6-5_D_II_1_MGP10_HD

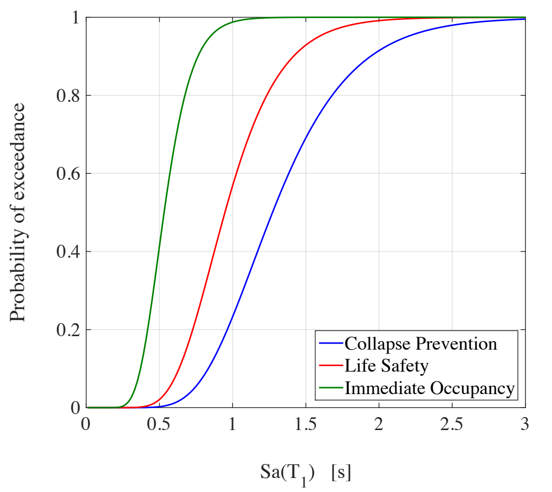

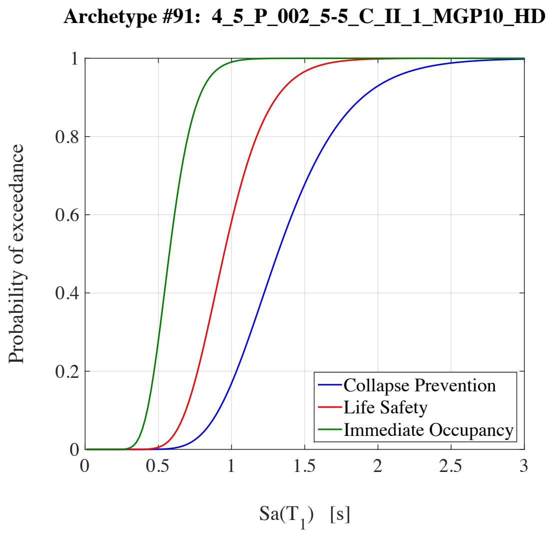
Archetype #91: 4_5_P_002_5-5_C_II_1_MGP10_HD
Probability of exceedance
Sa(T1) [s]
Collapse Prevention
Life Safety
Immediate Occupancy

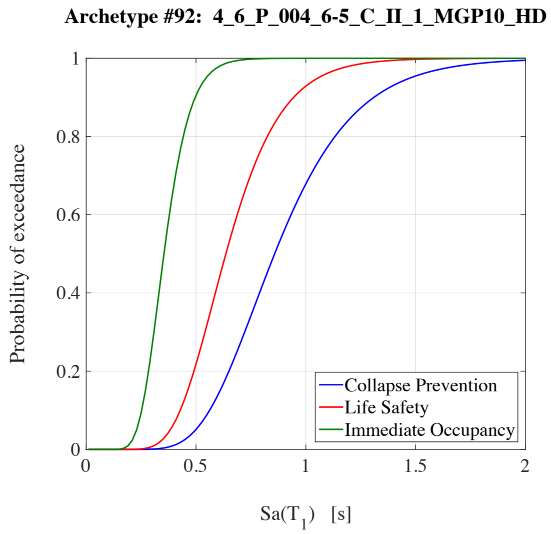
Archetype #92: 4_6_P_004_6-5_C_II_1_MGP10_HD
Probability of exceedance
Sa(T1) [s]
Collapse Prevention
Life Safety
Immediate Occupancy

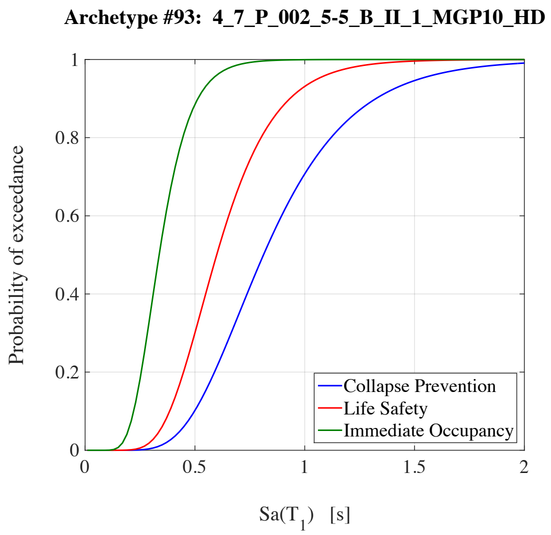
Archetype #93: 4_7_P_002_5-5_B_II_1_MGP10_HD
Probability of exceedance
Sa(T1) [s]
Collapse Prevention
Life Safety
Immediate Occupancy

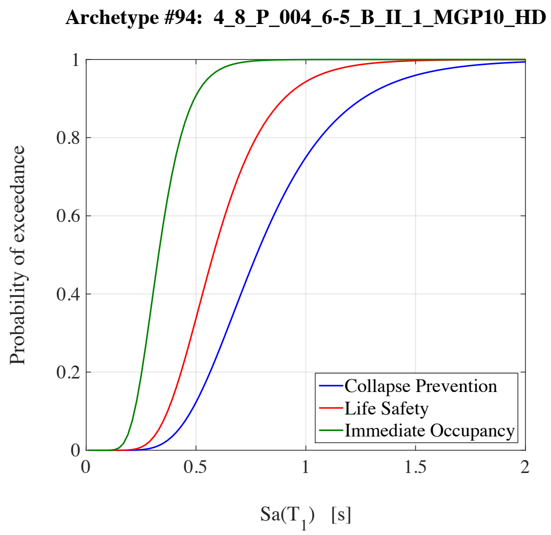
Archetype #94: 4_8_P_004_6-5_B_II_1_MGP10_HD
Probability of exceedance
Sa(T1) [s]
Collapse Prevention
Life Safety
Immediate Occupancy

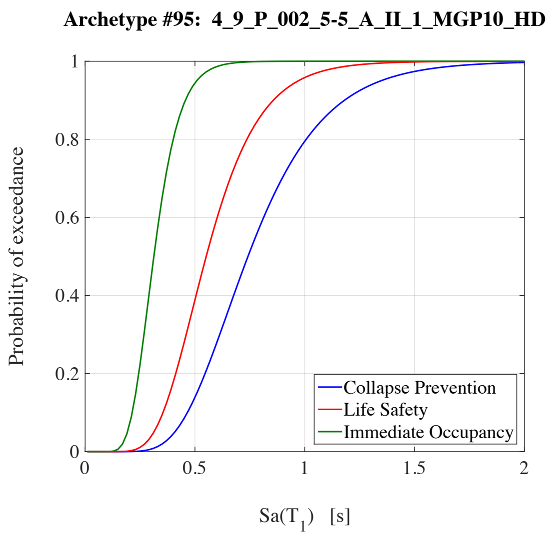
Archetype #95: 4_9_P_002_5-5_A_II_1_MGP10_HD
Probability of exceedance
Sa(T1) [s]
Collapse Prevention
Life Safety
Immediate Occupancy

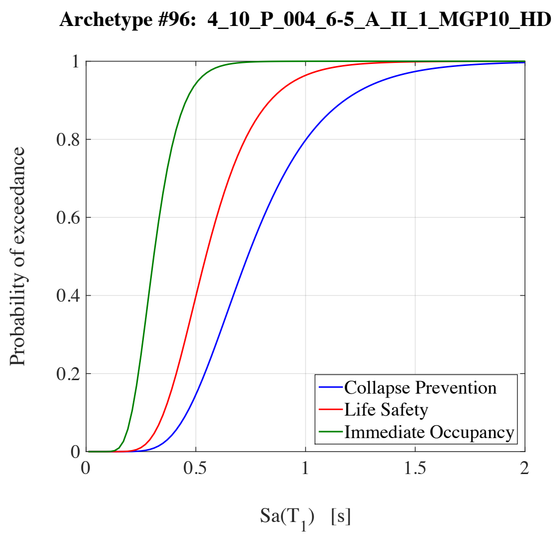
Archetype #96: 4_10_P_004_6-5_A_II_1_MGP10_HD
Probability of exceedance
Sa(T1) [s]
Collapse Prevention
Life Safety
Immediate Occupancy

Archetype #97: 5_1_P_002_5-5_A_II_3_MGP10_HD

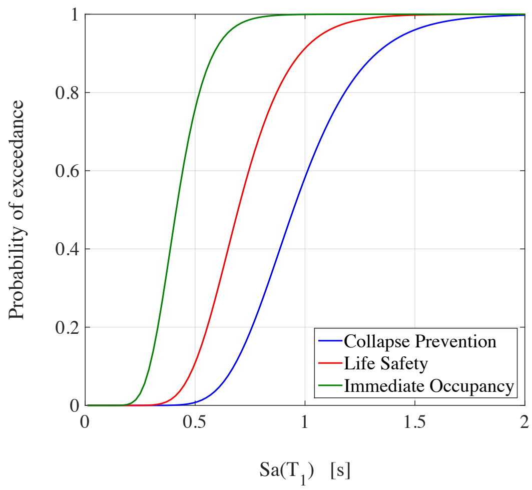

Archetype #98: 5_2_P_004_6-5_A_II_3_MGP10_HD

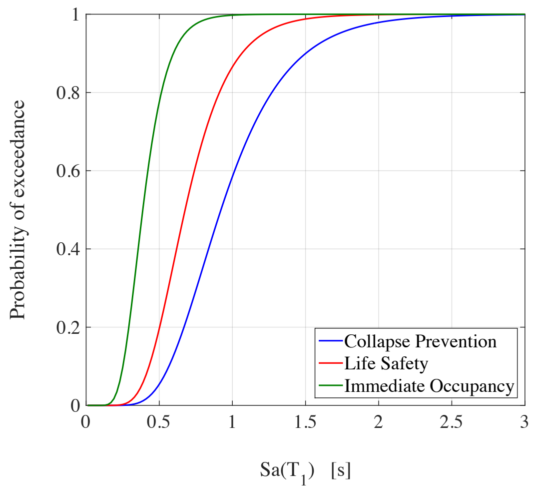

Archetype #99: 5_3_P_004_6-5_C_II_1_MGP10_HD

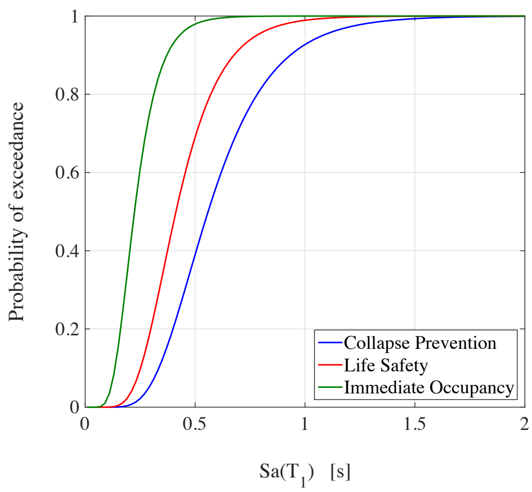

Archetype #100: 5_4_P_002_5-5_B_II_1_MGP10_HD

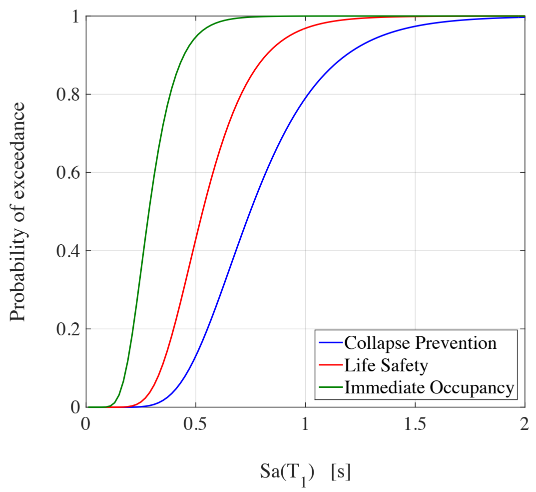

Archetype #101: 5_5_P_004_6-5_B_II_1_MGP10_HD

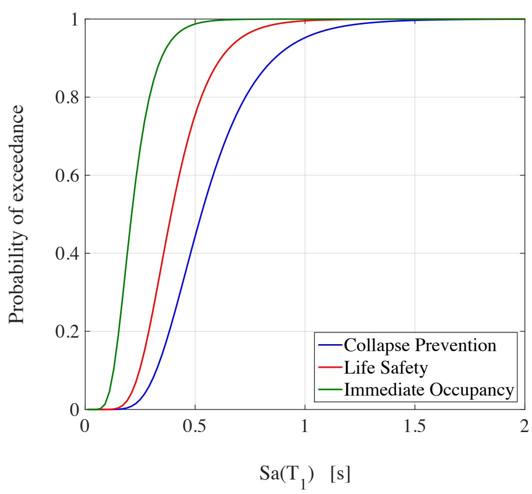

Archetype #102: 5_6_P_002_5-5_A_II_1_MGP10_HD

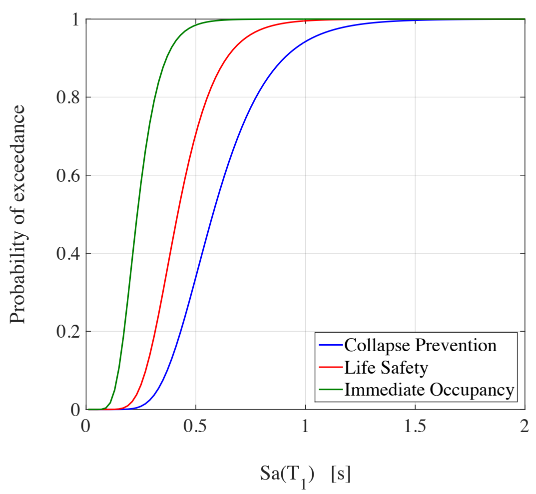

Archetype #103: 5_7_P_004_6-5_A_II_1_MGP10_HD

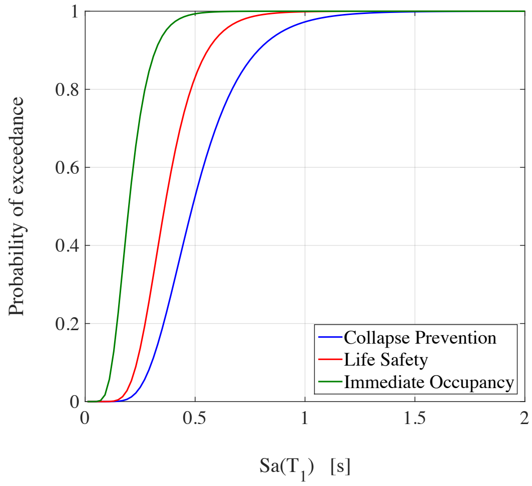

Archetype #104: 3_1_Q_002_5-5_D_II_3_MGP10_HD

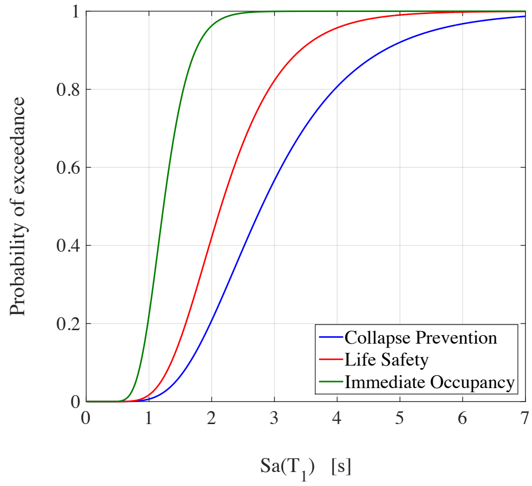

Archetype #105: 3_2_Q_004_6-5_D_II_3_MGP10_HD

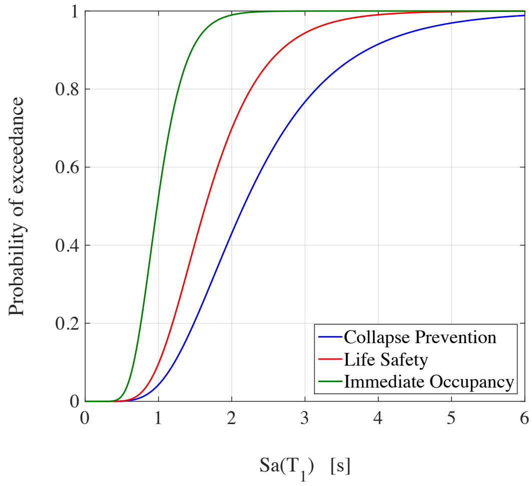

Archetype #106: 3_3_Q_002_5-5_C_II_3_MGP10_HD

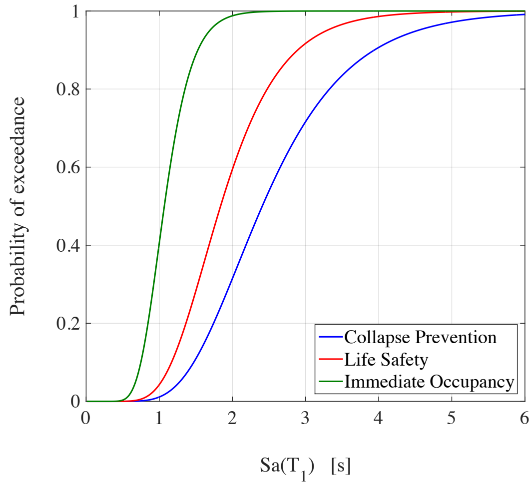

Archetype #107: 3_4_Q_004_6-5_C_II_3_MGP10_HD

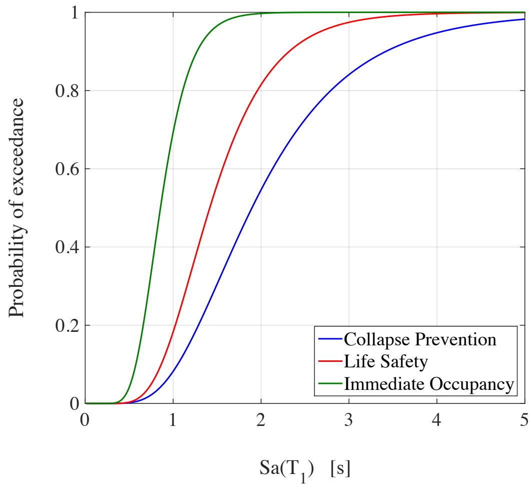

Archetype #108: 3_5_Q_002_5-5_B_II_3_MGP10_HD

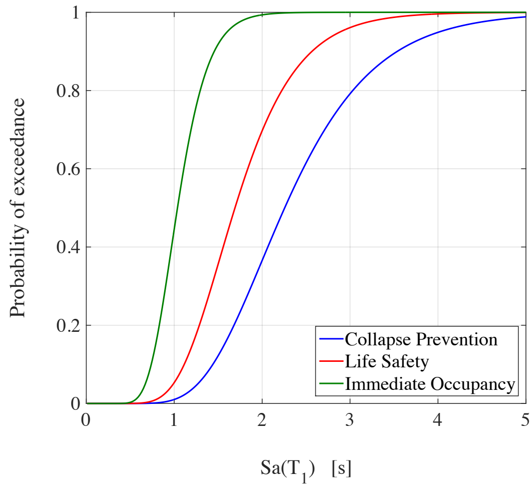

Archetype #109: 3_6_Q_004_6-5_B_II_3_MGP10_HD

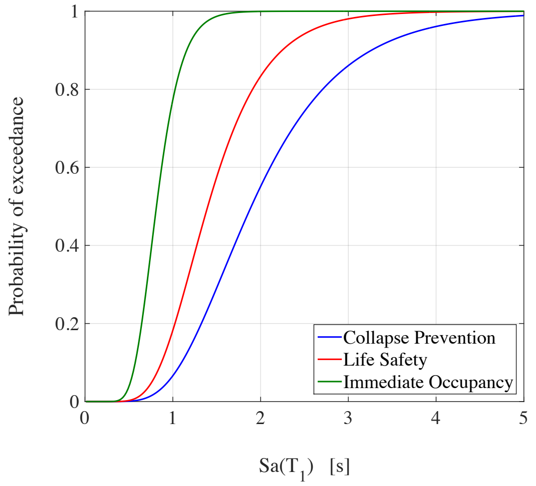

Archetype #110: 3_7_Q_002_5-5_A_II_3_MGP10_HD

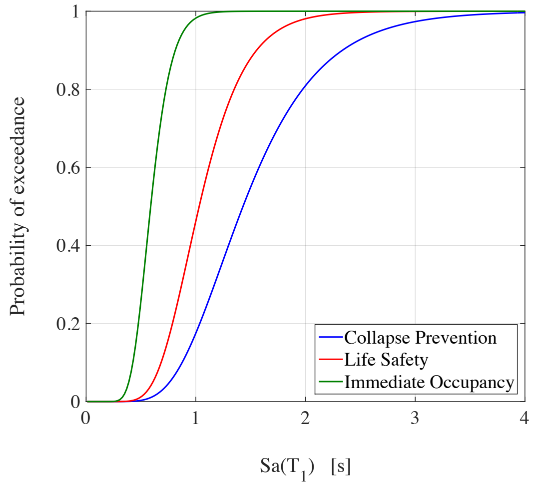

Archetype #111: 3_8_Q_004_6-5_A_II_3_MGP10_HD

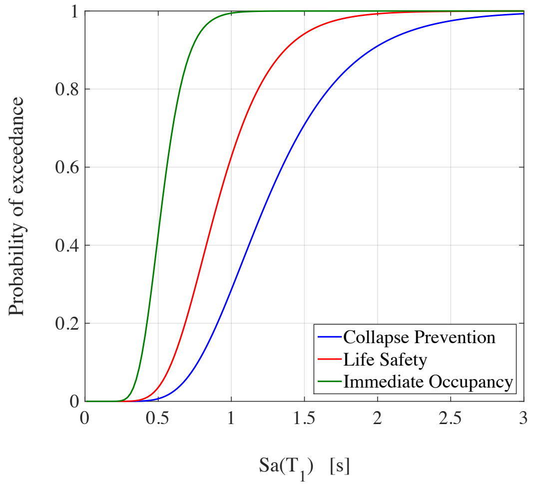

Archetype #112: 3_9_Q_002_5-5_D_II_1_MGP10_HD

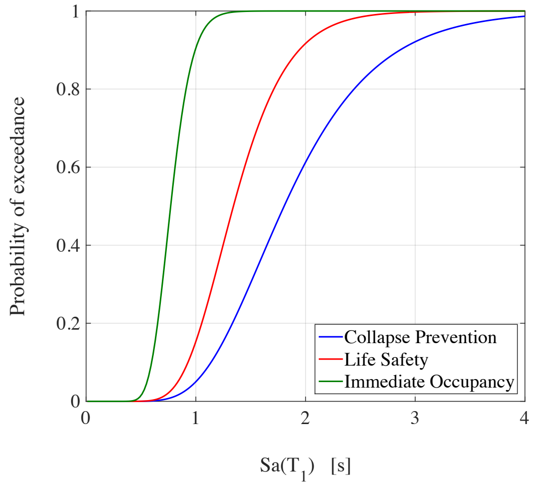

Archetype #113: 3_10_Q_004_6-5_D_II_1_MGP10_HD

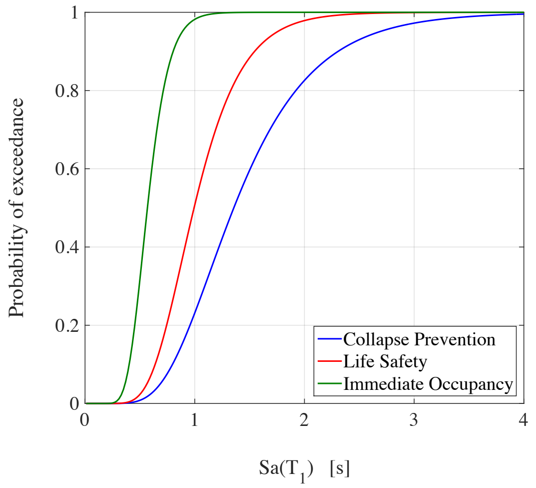

Archetype #114: 3_11_Q_002_5-5_C_II_1_MGP10_HD

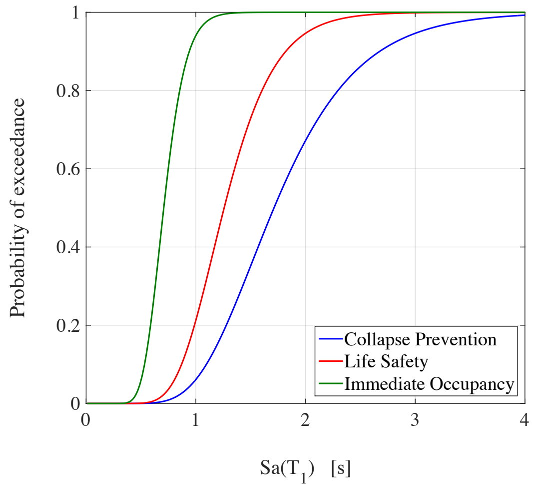

Archetype #115: 3_12_Q_004_6-5_C_II_1_MGP10_HD

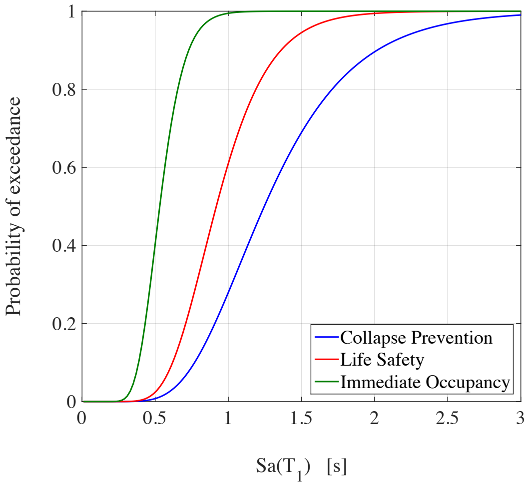

Archetype #116: 3_13_Q_002_5-5_B_II_1_MGP10_HD

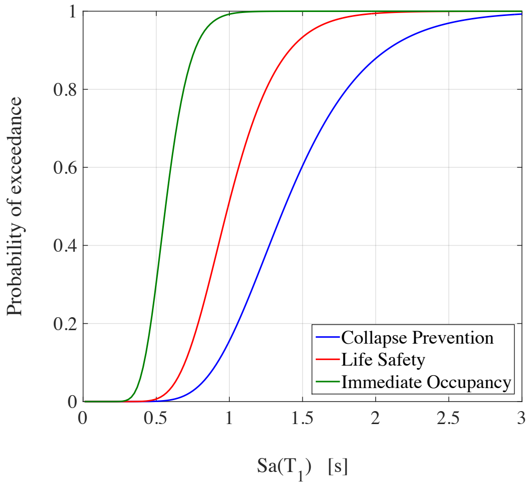

Archetype #117: 3_14_Q_004_6-5_B_II_1_MGP10_HD

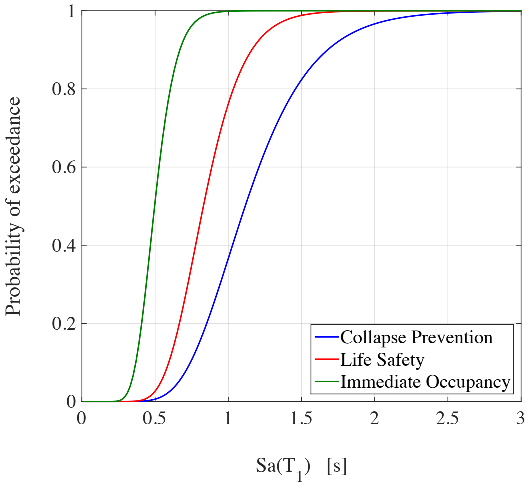

Archetype #118: 3_15_Q_002_5-5_A_II_1_MGP10_HD

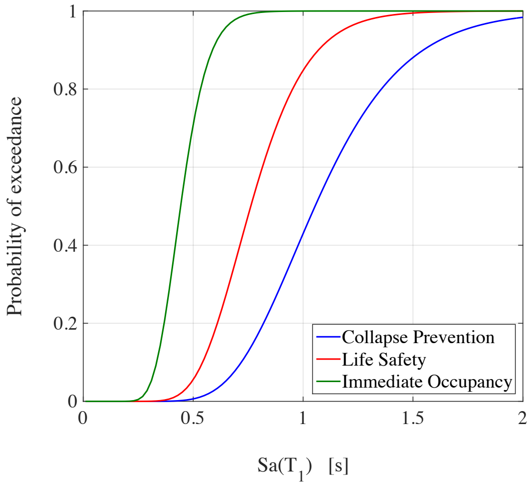

Archetype #119: 3_16_Q_004_6-5_A_II_1_MGP10_HD

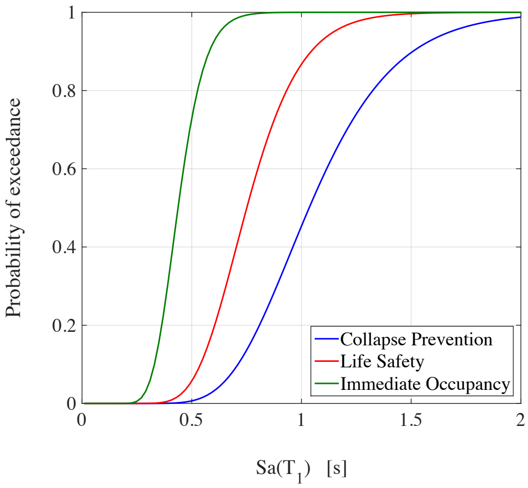

Archetype #120: 4_1_Q_004_6-5_B_II_3_MGP10_HD

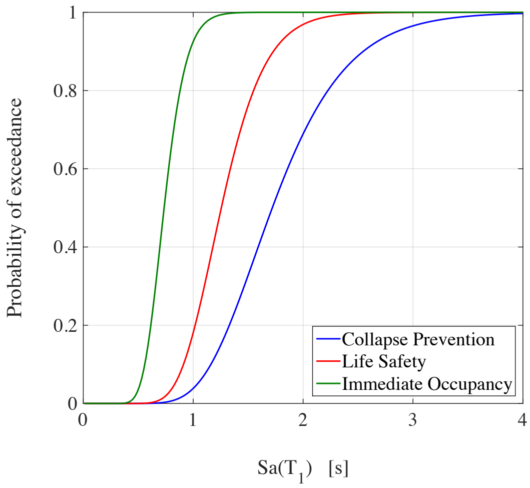

Archetype #121: 4_2_Q_002_5-5_A_II_3_MGP10_HD

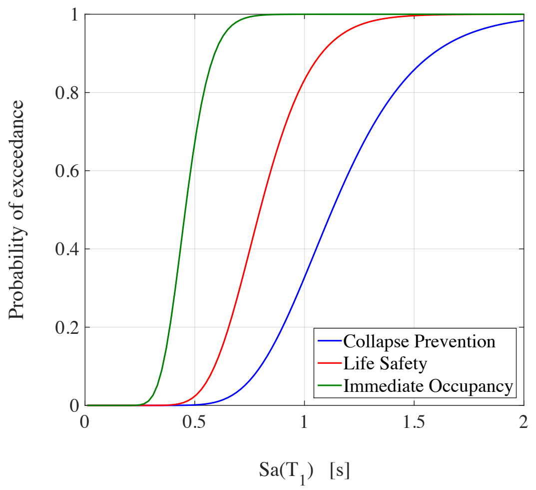

Archetype #122: 4_3_Q_004_6-5_A_II_3_MGP10_HD

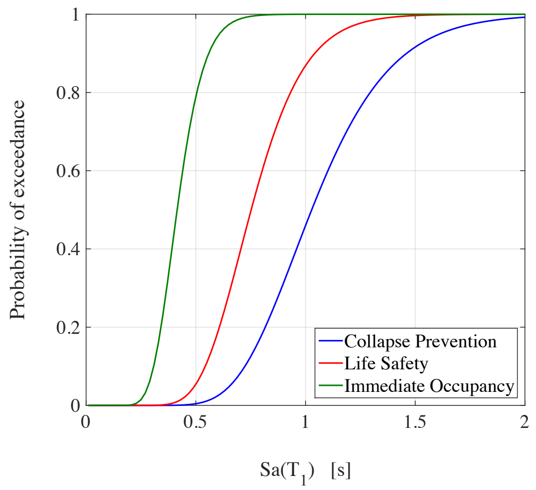

Archetype #123: 4_4_Q_002_5-5_D_II_1_MGP10_HD

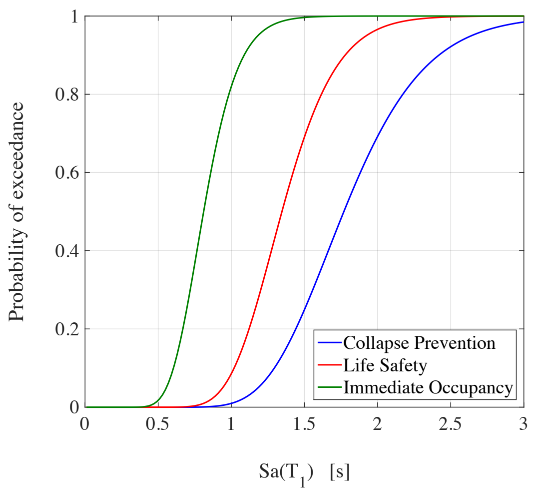

Archetype #124: 4_5_Q_004_6-5_D_II_1_MGP10_HD

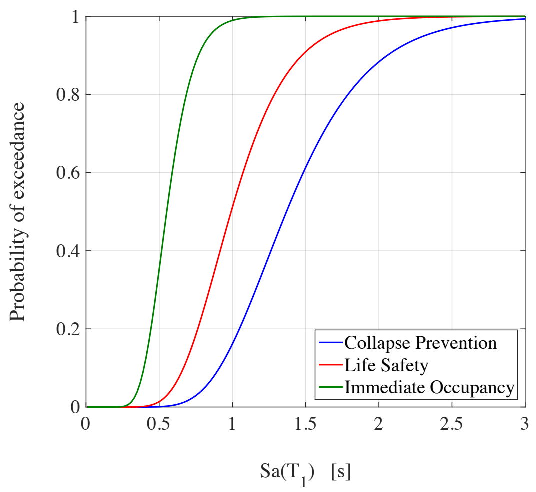

Archetype #125: 4_6_Q_002_5-5_C_II_1_MGP10_HD

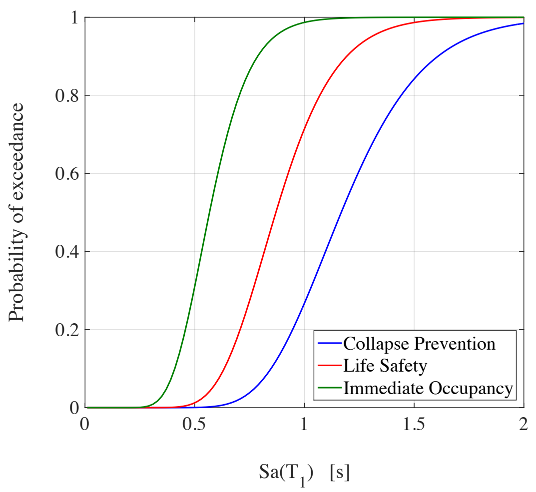

Archetype #126: 4_7_Q_004_6-5_C_II_1_MGP10_HD

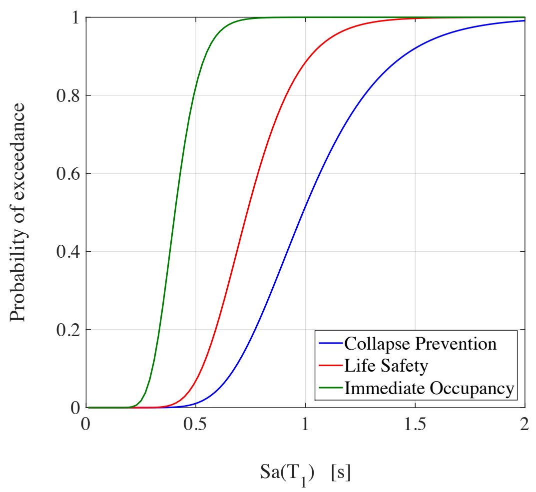

Archetype #127: 4_8_Q_002_5-5_B_II_1_MGP10_HD

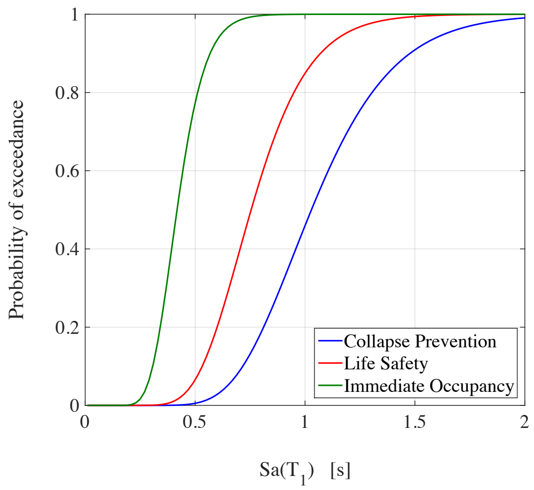

Archetype #128: 4_9_Q_004_6-5_B_II_1_MGP10_HD

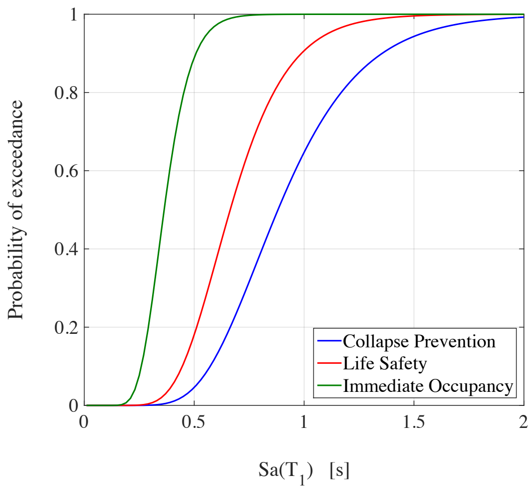

Archetype #129: 4_10_Q_002_5-5_A_II_1_MGP10_HD

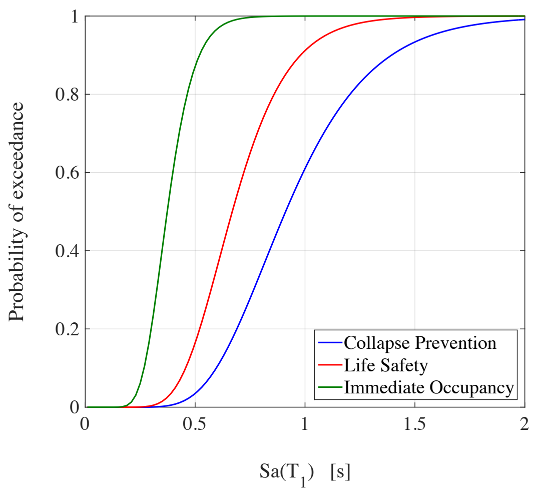

Archetype #130: 4_11_Q_004_6-5_A_II_1_MGP10_HD

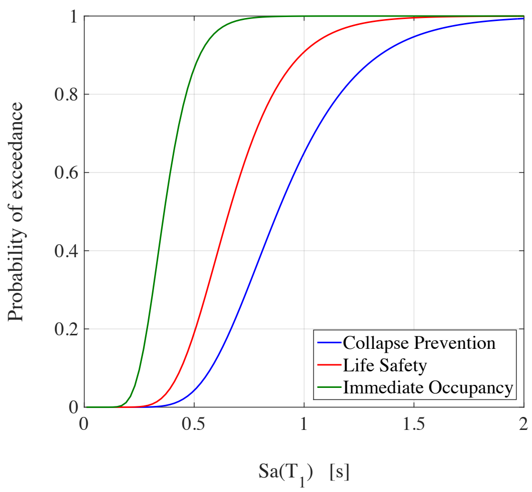

Archetype #131: 5_1_Q_004_6-5_A_II_3_MGP10_HD

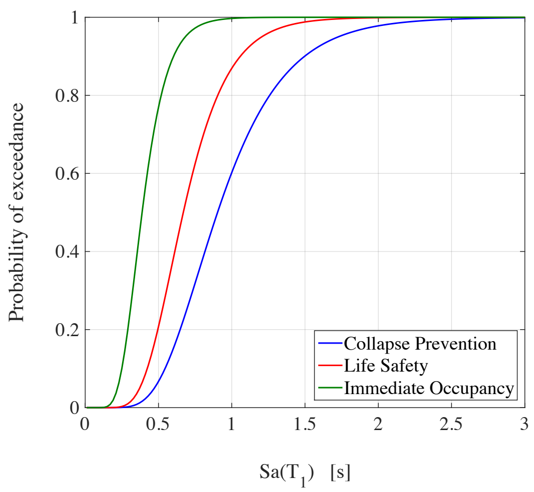

Archetype #132: 5_2_Q_004_6-5_C_II_1_MGP10_HD

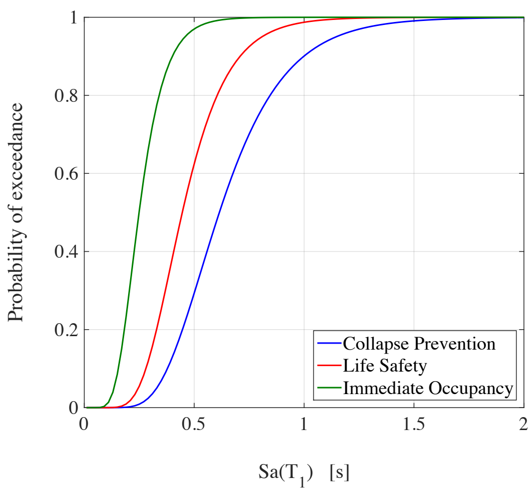

Archetype #133: 5_3_Q_002_5-5_B_II_1_MGP10_HD

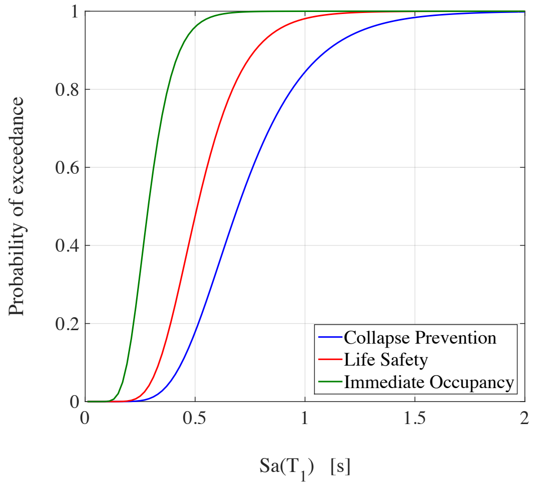

Archetype #134: 5_4_Q_004_6-5_B_II_1_MGP10_HD

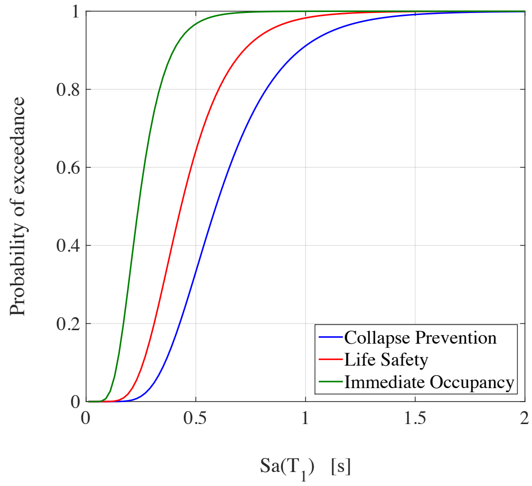

Archetype #135: 5_5_Q_002_5-5_A_II_1_MGP10_HD

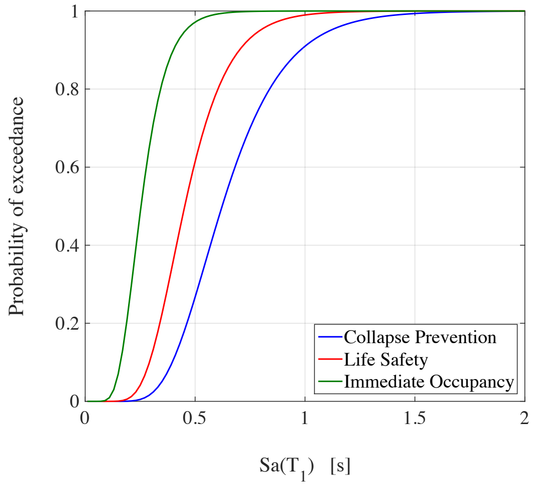

Archetype #136: 5_6_Q_004_6-5_A_II_1_MGP10_HD

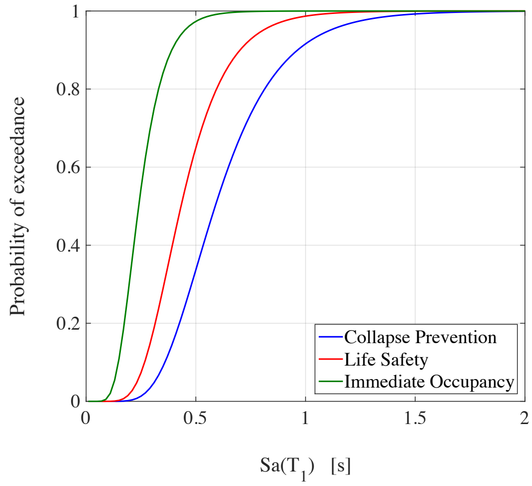

Archetype #137: 5_1_C_004_6-5_D_II_3_MGP10_ATS

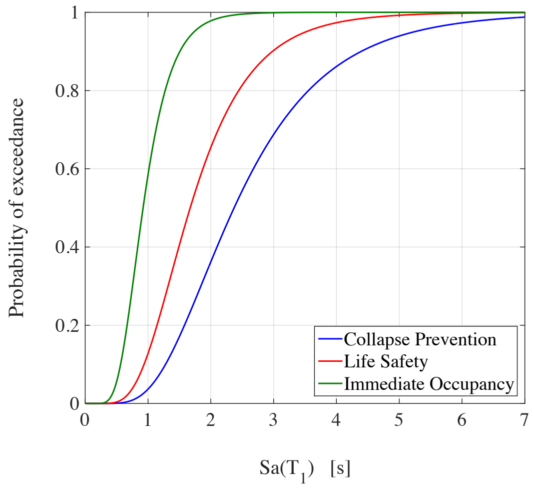

Archetype #138: 5_2_C_002_5-5_C_II_3_MGP10_ATS

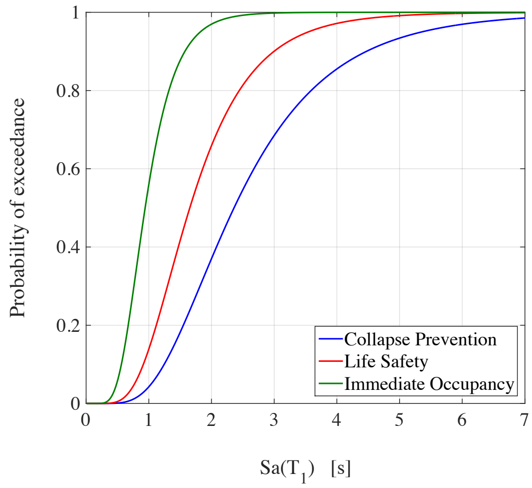

Archetype #139: 5_3_C_004_6-5_C_II_3_MGP10_ATS

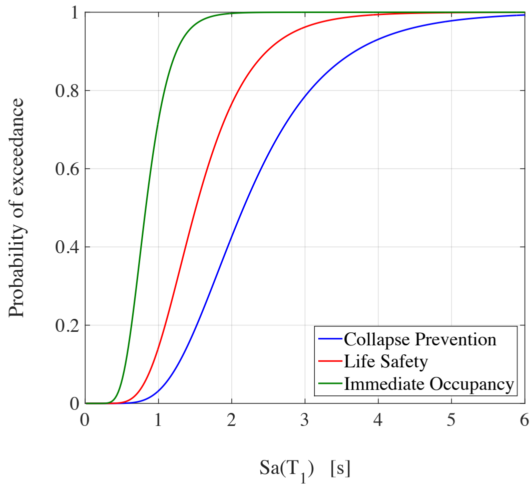

Archetype #140: 5_4_C_002_5-5_B_II_3_MGP10_ATS

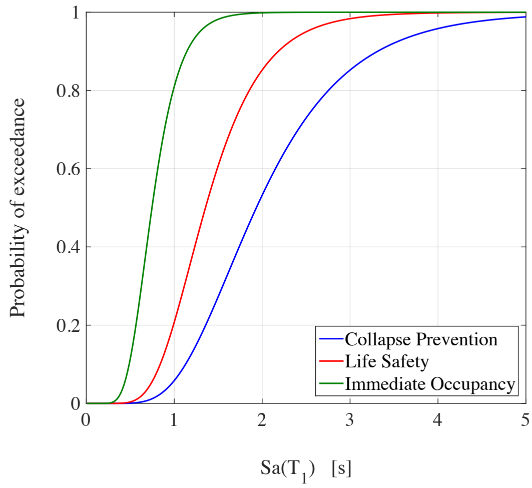

Archetype #141: 5_5_C_004_6-5_B_II_3_MGP10_ATS

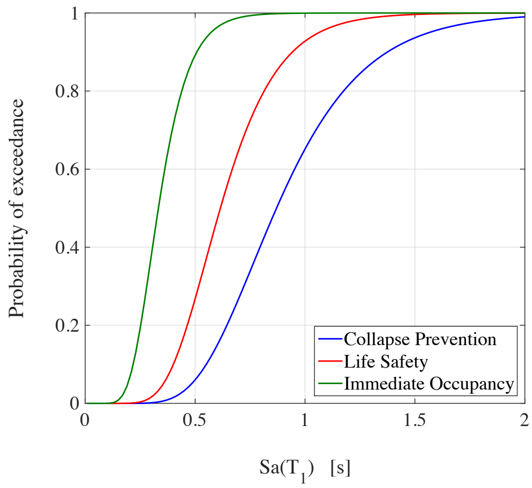

Archetype #142: 5_6_C_002_5-5_A_II_3_MGP10_ATS

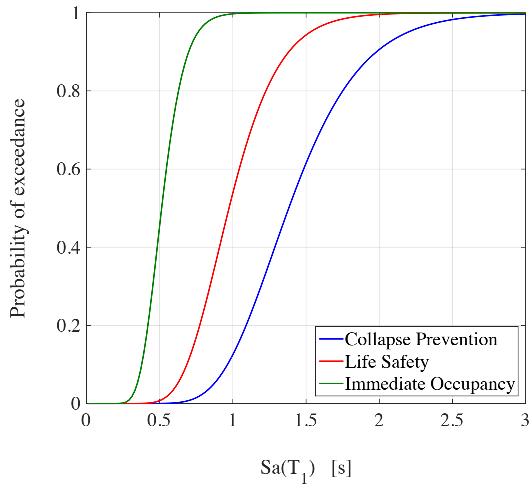

Archetype #143: 5_7_C_004_6-5_A_II_3_MGP10_ATS

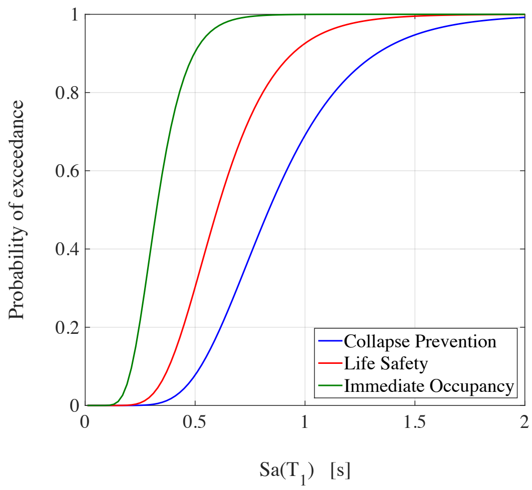

Archetype #144: 5_8_C_002_5-5_D_II_1_MGP10_ATS

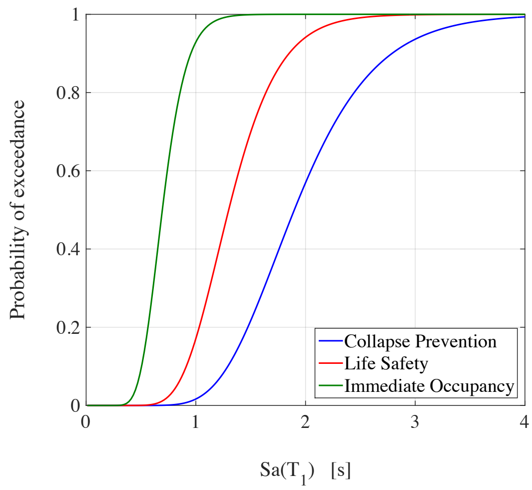

Archetype #145: 5_9_C_004_6-5_D_II_1_MGP10_ATS

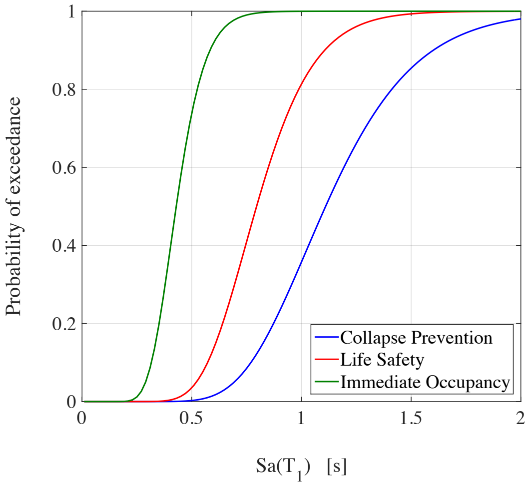

Archetype #146: 5_10_C_002_5-5_C_II_1_MGP10_ATS

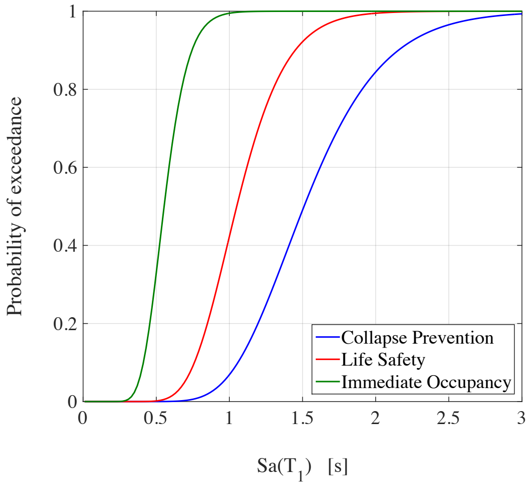

Archetype #147: 5_11_C_004_6-5_C_II_1_MGP10_ATS

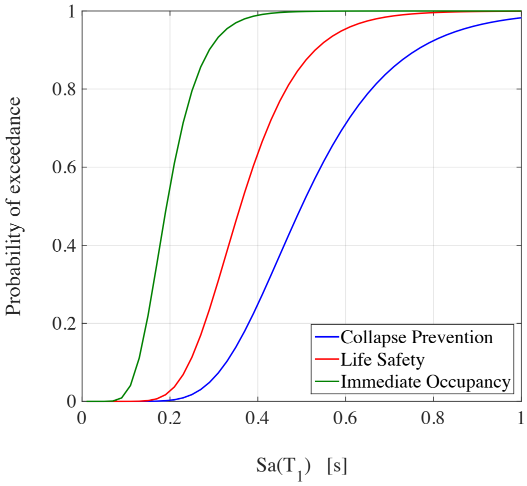

Archetype #148: 5_12_C_002_5-5_B_II_1_MGP10_ATS

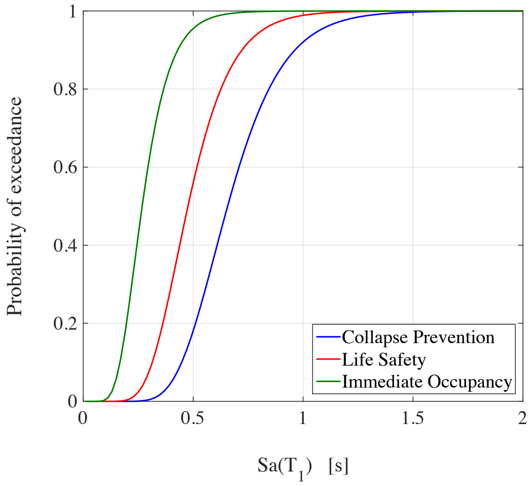

Archetype #149: 5_13_C_004_6-5_B_II_1_MGP10_ATS

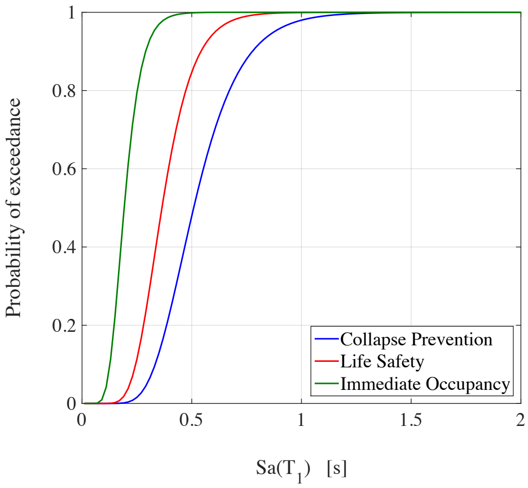

Archetype #150: 5_14_C_002_5-5_A_II_1_MGP10_ATS

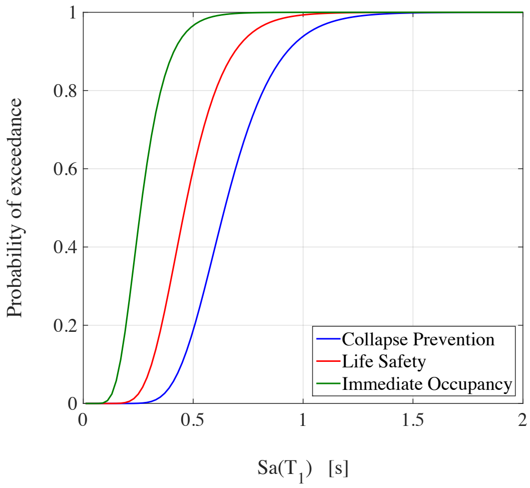

Archetype #151: 5_15_C_004_6-5_A_II_1_MGP10_ATS

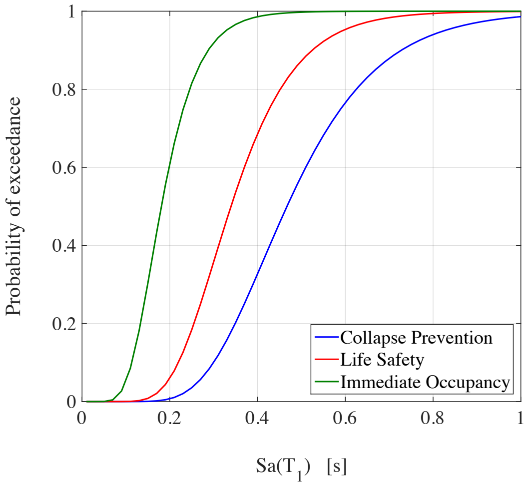

Archetype #152: 6_1_C_002_7-0_B_II_3_MGP10_ATS

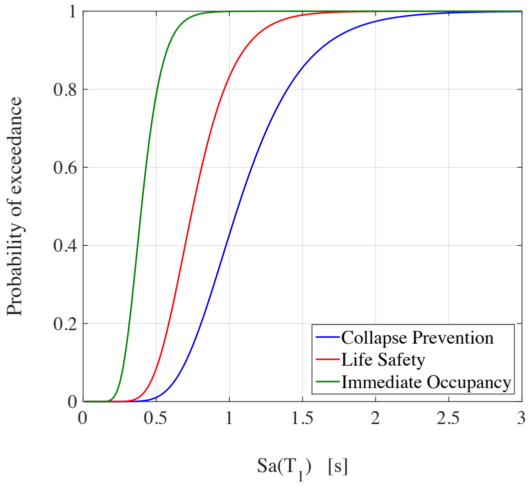

Archetype #153: 6_2_C_004_7-0_B_II_3_MGP10_ATS

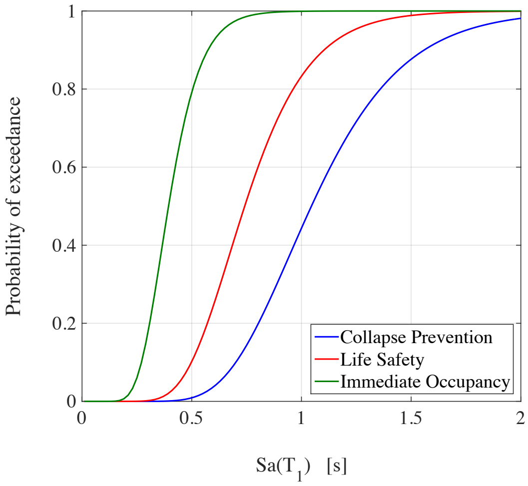

Archetype #154: 6_3_C_002_7-0_D_II_1_MGP10_ATS

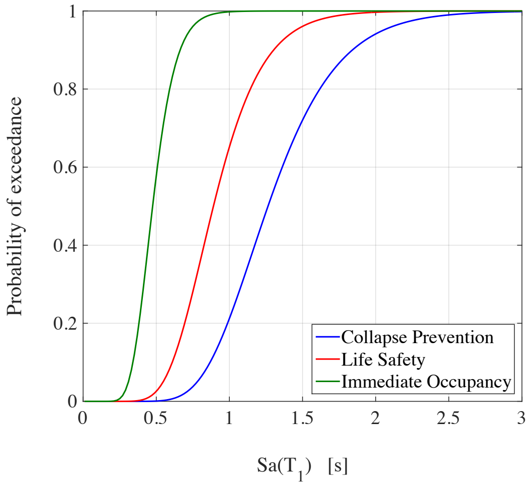

Archetype #155: 6_4_C_004_7-0_D_II_1_MGP10_ATS

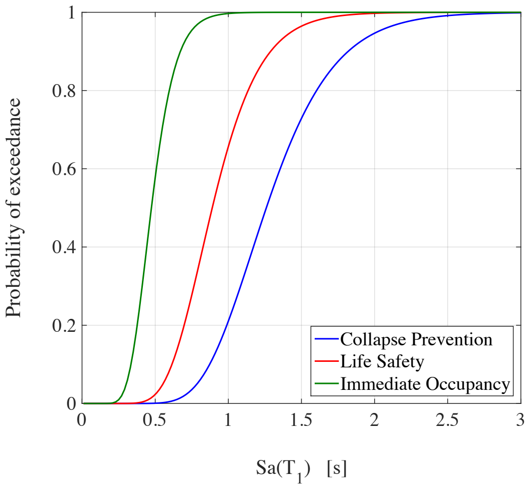

Archetype #156: 5_1_D_004_6-5_D_II_3_MGP10_ATS

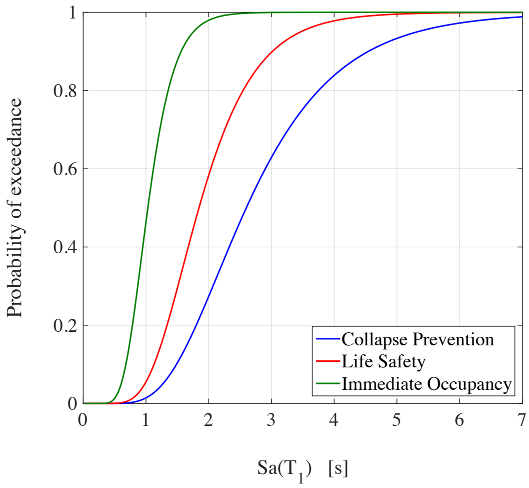

Archetype #157: 5_2_D_002_5-5_C_II_3_MGP10_ATS

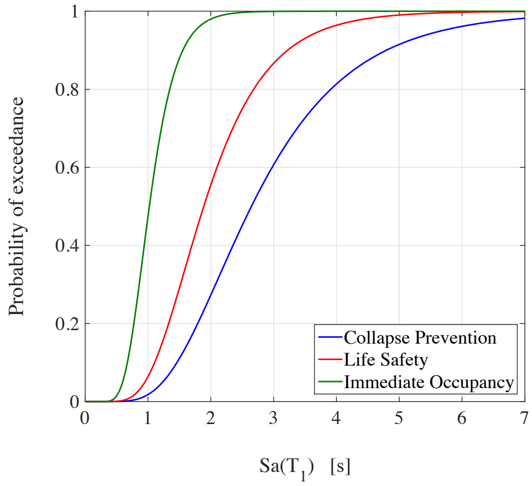

Archetype #158: 5_3_D_004_6-5_C_II_3_MGP10_ATS

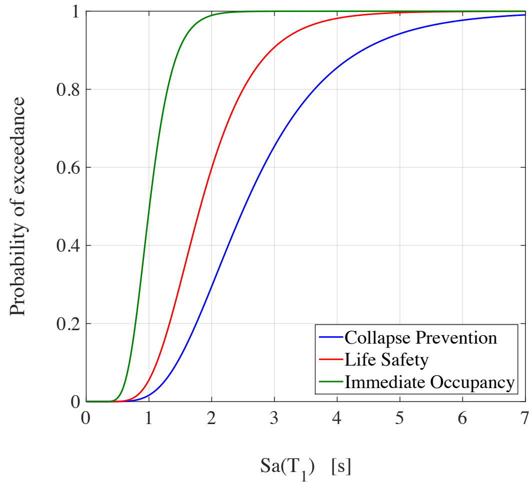

Archetype #159: 5_4_D_002_5-5_B_II_3_MGP10_ATS

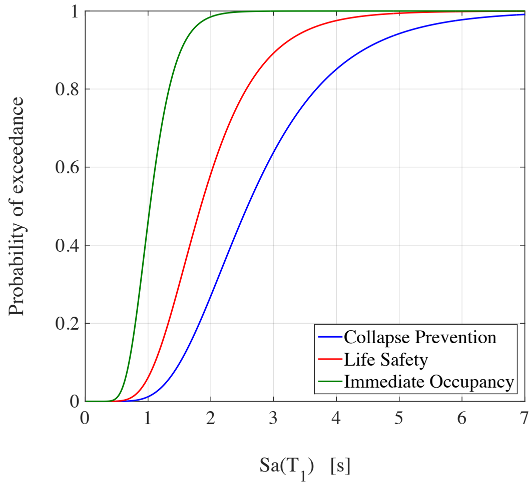

Archetype #160: 5_5_D_004_6-5_B_II_3_MGP10_ATS

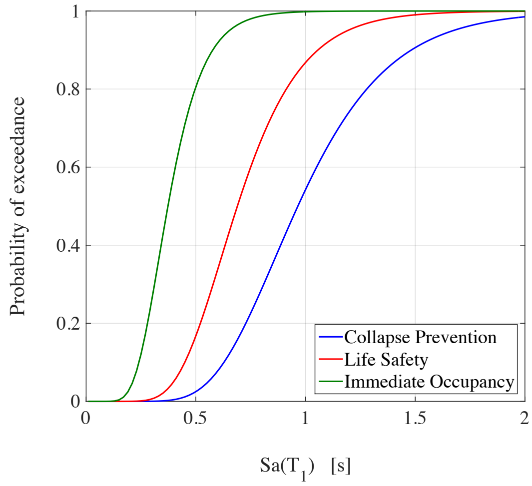

Archetype #161: 5_6_D_002_5-5_A_II_3_MGP10_ATS

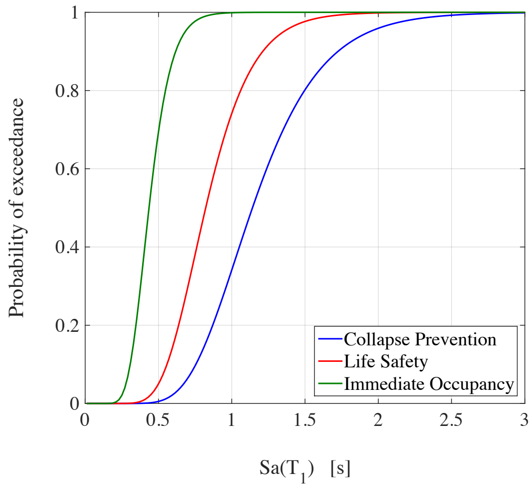

Archetype #162: 5_7_D_004_6-5_A_II_3_MGP10_ATS

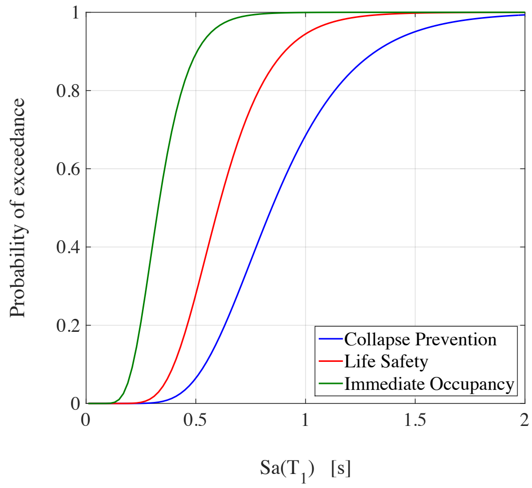

Archetype #163: 5_8_D_002_5-5_D_II_1_MGP10_ATS

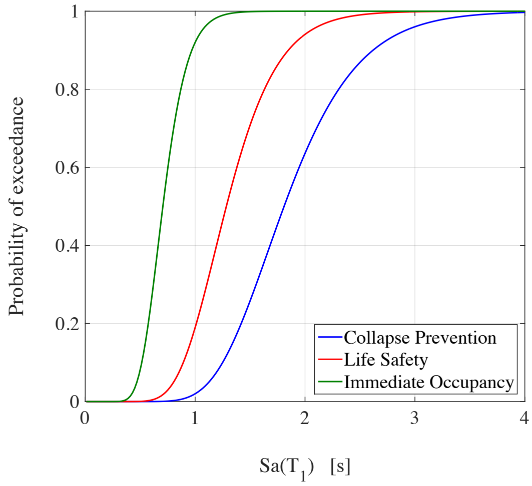

Archetype #164: 5_9_D_004_6-5_D_II_1_MGP10_ATS

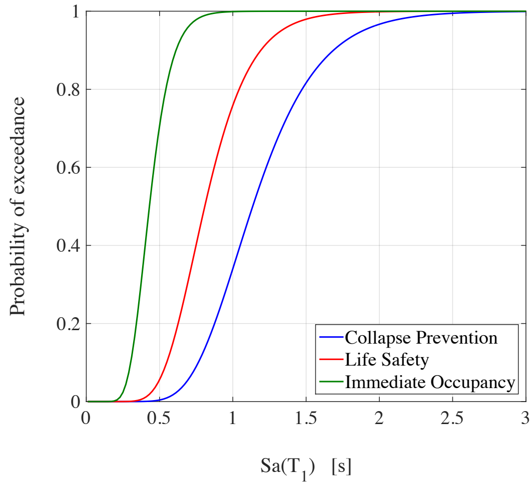

Archetype #165: 5_10_D_002_5-5_C_II_1_MGP10_ATS

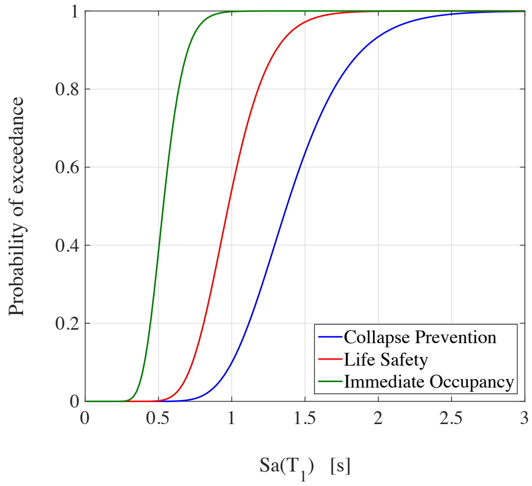

Archetype #166: 5_11_D_004_6-5_C_II_1_MGP10_ATS

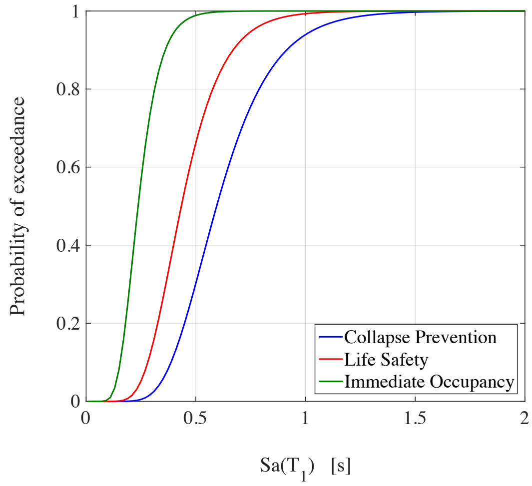

Archetype #167: 5_12_D_002_5-5_B_II_1_MGP10_ATS

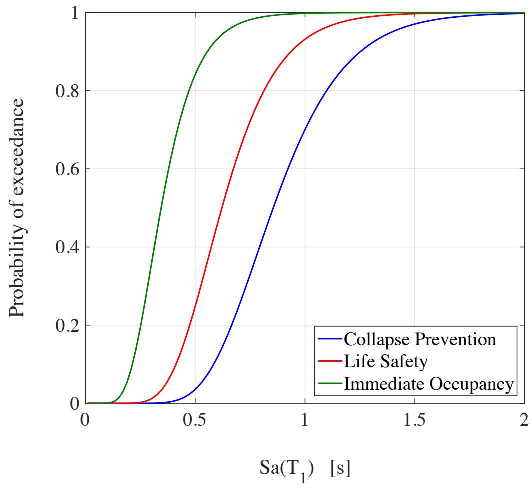

Archetype #168: 5_13_D_004_6-5_B_II_1_MGP10_ATS

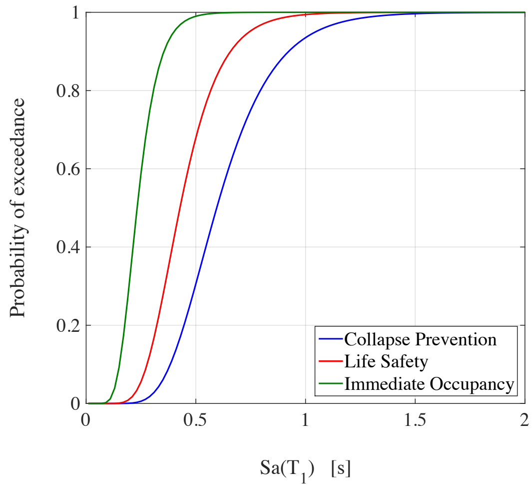

Archetype #169: 5_14_D_002_5-5_A_II_1_MGP10_ATS

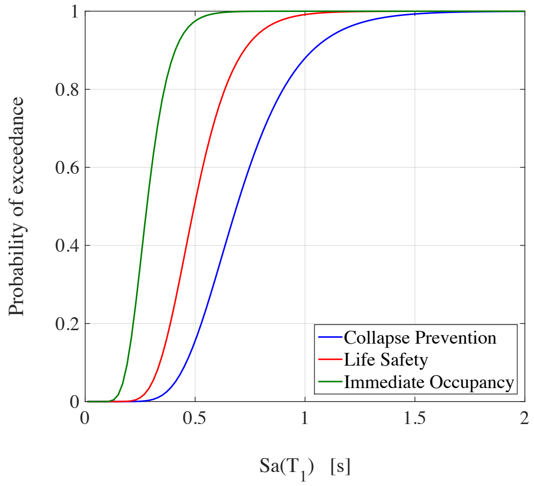

Archetype #170: 5_15_D_004_6-5_A_II_1_MGP10_ATS

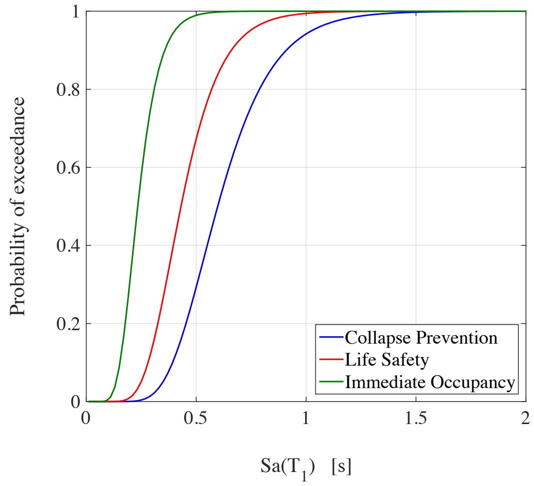

Archetype #171: 5_1_P_004_6-5_C_II_3_MGP10_ATS

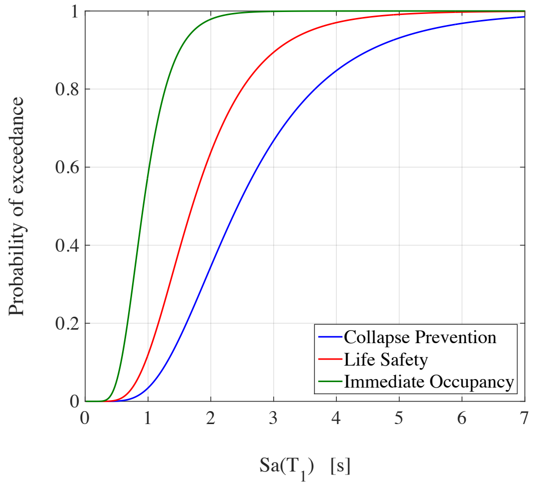

Archetype #172: 5_2_P_004_6-5_B_II_3_MGP10_ATS

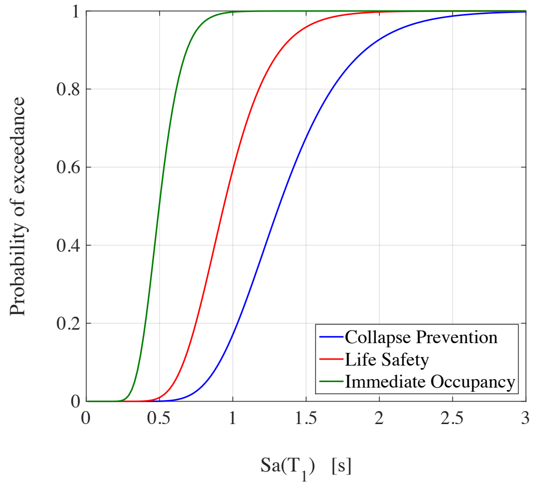

Archetype #173: 5_3_P_002_5-5_A_II_3_MGP10_ATS

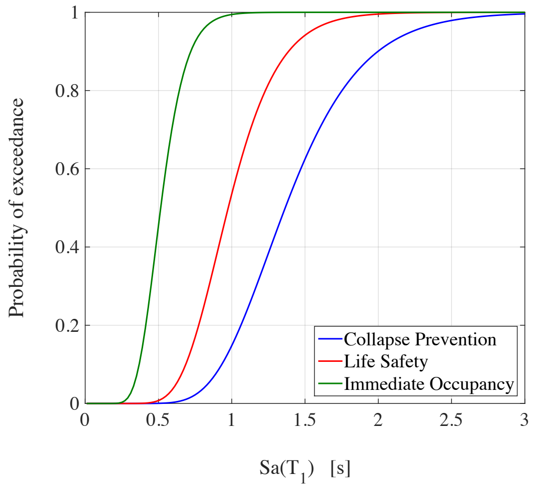

Archetype #174: 5_4_P_004_6-5_A_II_3_MGP10_ATS

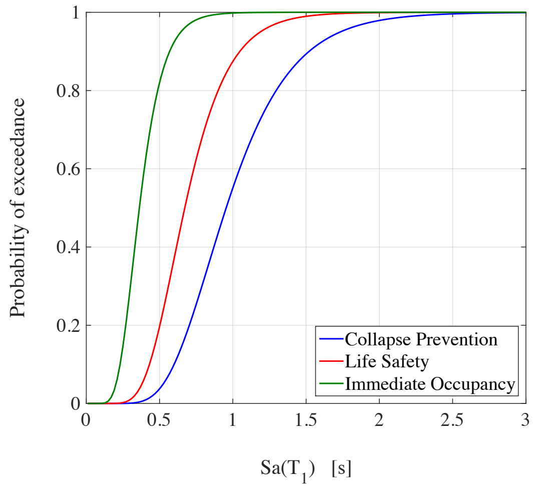

Archetype #175: 5_5_P_002_5-5_D_II_1_MGP10_ATS

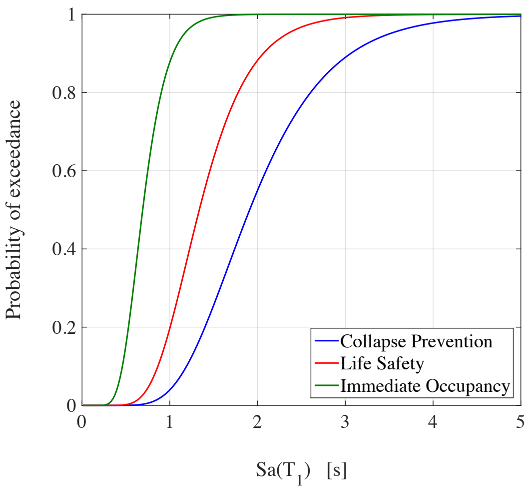

Archetype #176: 5_6_P_004_6-5_D_II_1_MGP10_ATS

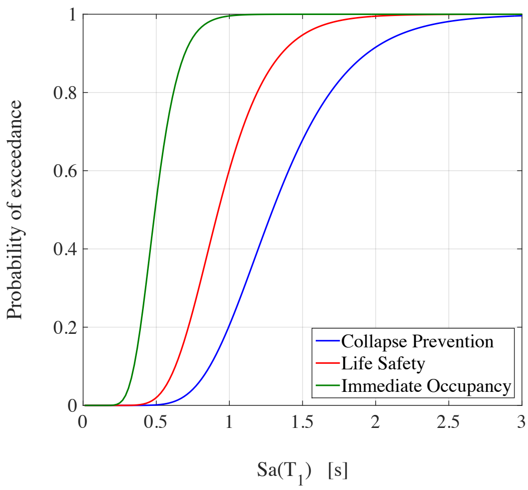

Archetype #177: 5_7_P_002_5-5_C_II_1_MGP10_ATS

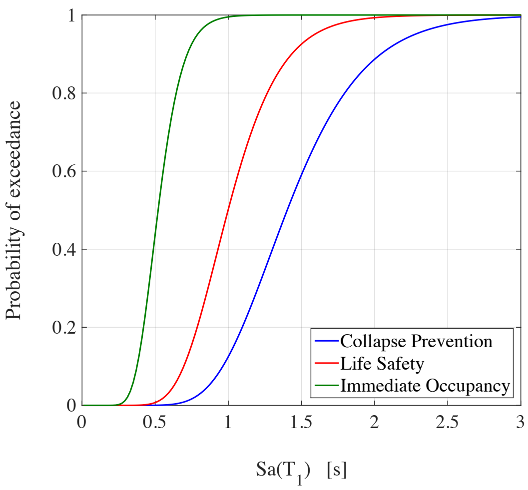

Archetype #178: 5_8_P_004_6-5_C_II_1_MGP10_ATS

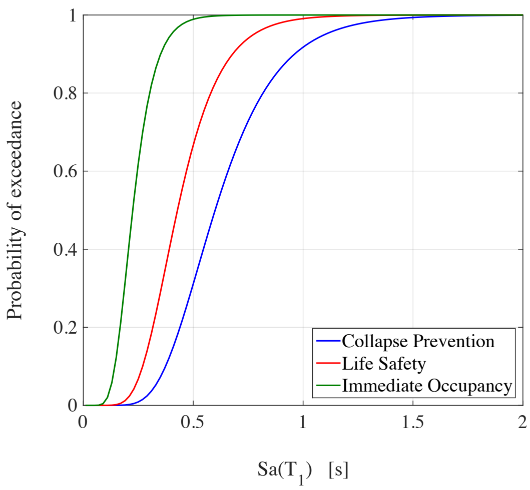

Archetype #179: 5_9_P_002_5-5_B_II_1_MGP10_ATS

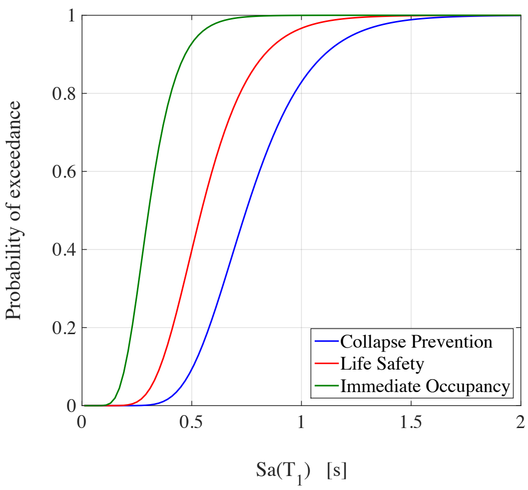

Archetype #180: 5_10_P_004_6-5_B_II_1_MGP10_ATS

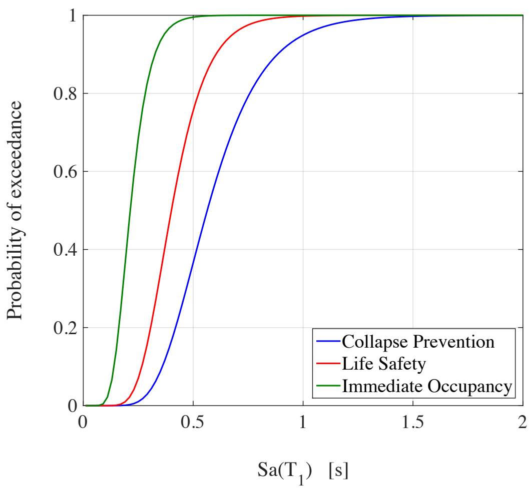

Archetype #181: 5_11_P_002_5-5_A_II_1_MGP10_ATS

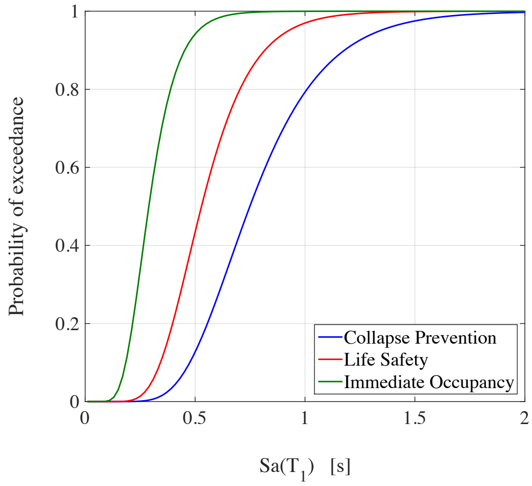

Archetype #182: 5_12_P_004_6-5_A_II_1_MGP10_ATS

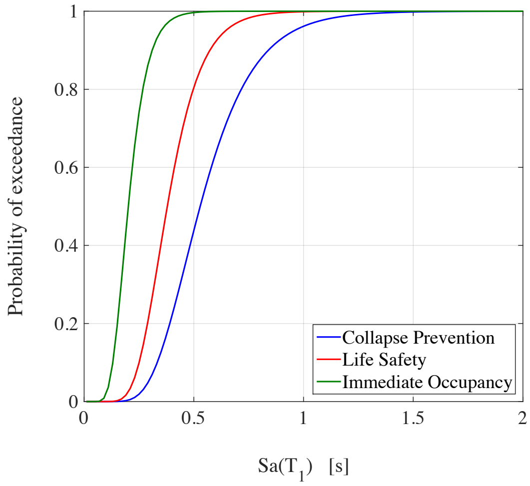

Archetype #183: 6_1_P_002_7-0_B_II_3_MGP10_ATS

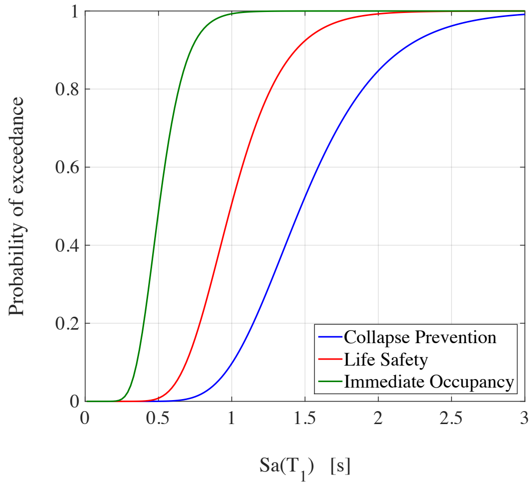

Archetype #184: 6_2_P_004_7-0_B_II_3_MGP10_ATS

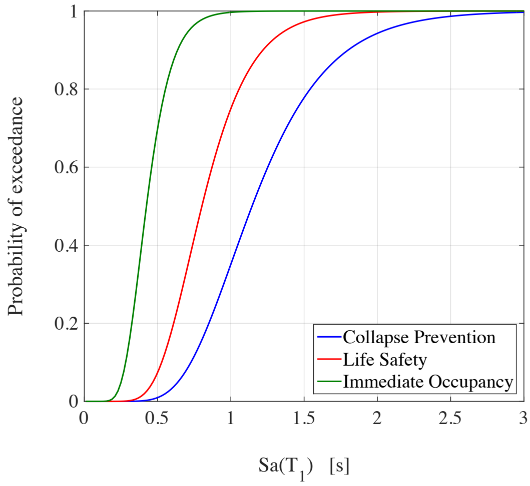

Archetype #185: 6_3_P_002_7-0_D_II_1_MGP10_ATS

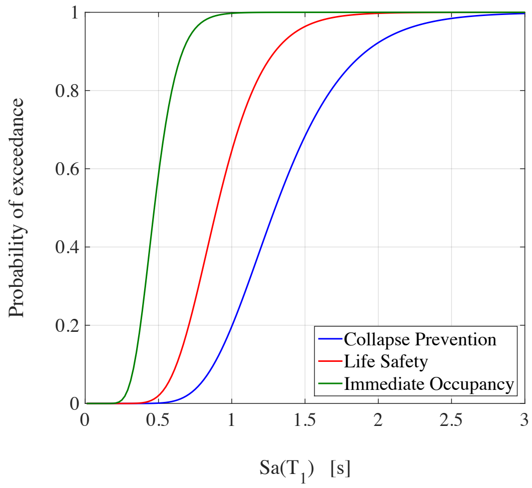

Archetype #186: 6_4_P_004_7-0_D_II_1_MGP10_ATS

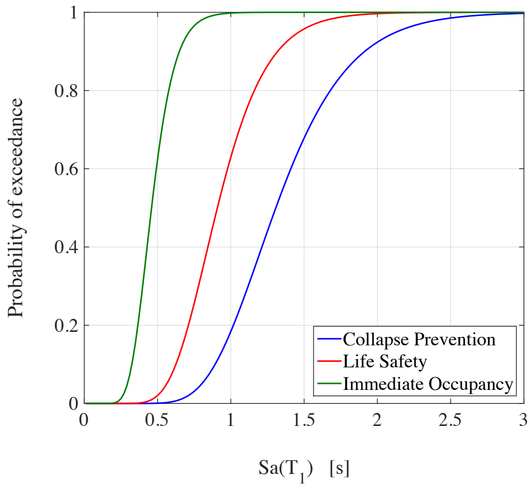

Archetype #187: 5_1_Q_004_6-5_D_II_3_MGP10_ATS

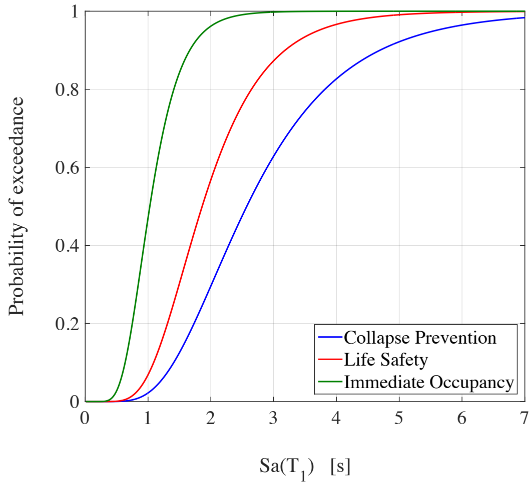

Archetype #188: 5_2_Q_002_5-5_C_II_3_MGP10_ATS

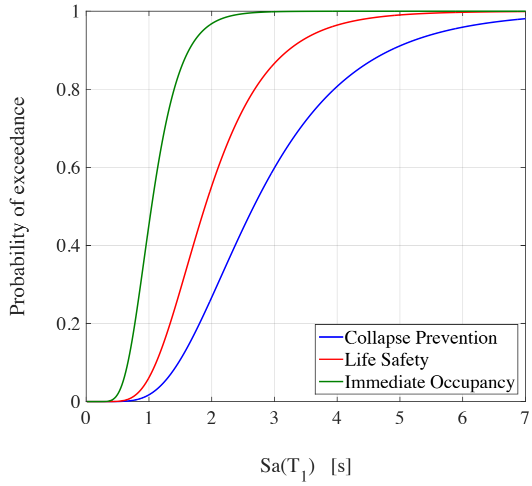

Archetype #189: 5_3_Q_004_6-5_C_II_3_MGP10_ATS

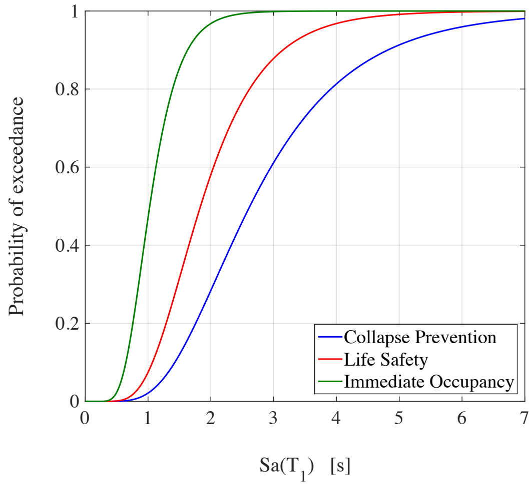

Archetype #190: 5_4_Q_002_5-5_B_II_3_MGP10_ATS

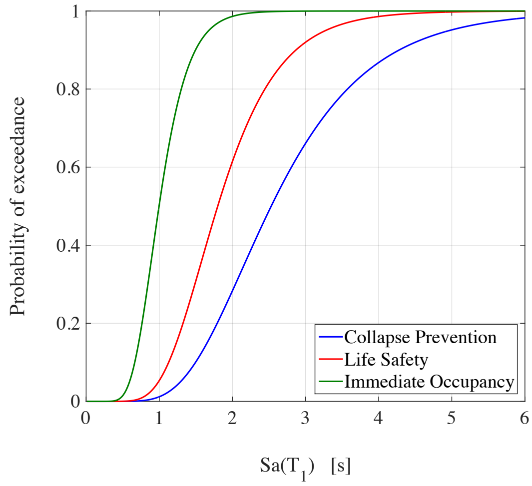

Archetype #191: 5_5_Q_004_6-5_B_II_3_MGP10_ATS

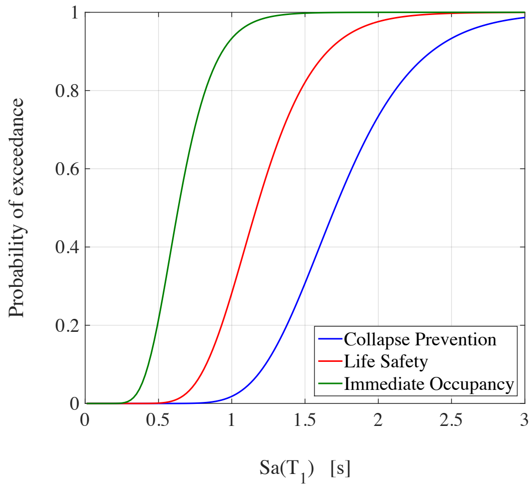

Archetype #192: 5_6_Q_002_5-5_A_II_3_MGP10_ATS

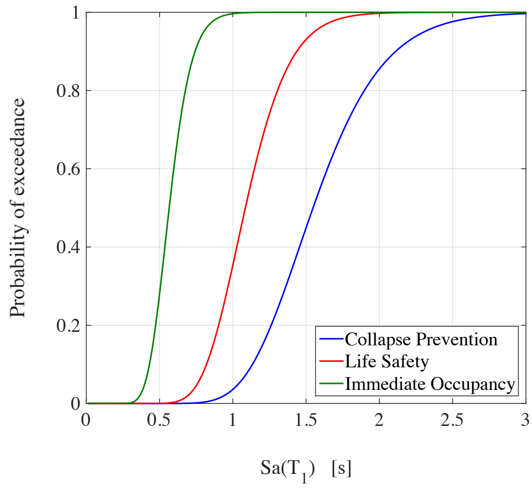

Archetype #193: 5_7_Q_004_6-5_A_II_3_MGP10_ATS

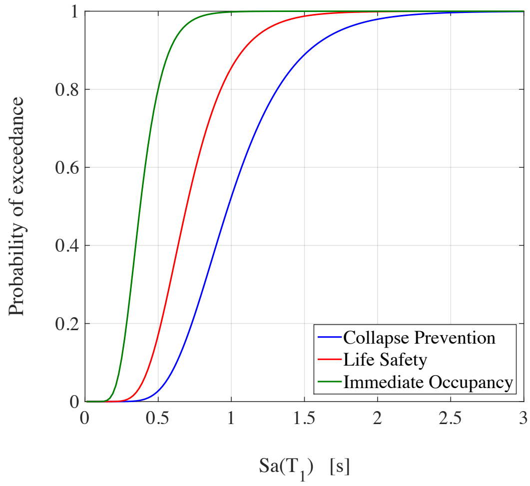

Archetype #194: 5_8_Q_002_5-5_D_II_1_MGP10_ATS

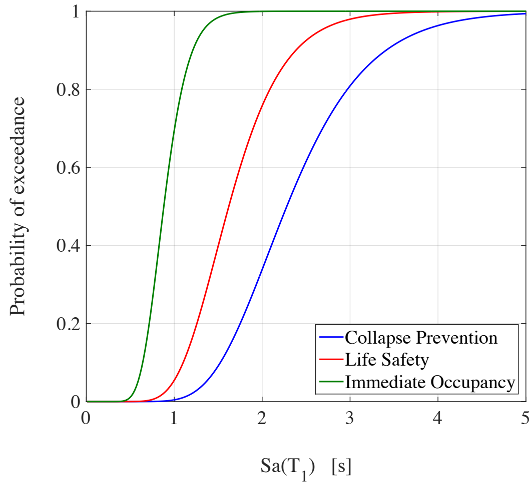

Archetype #195: 5_9_Q_004_6-5_D_II_1_MGP10_ATS

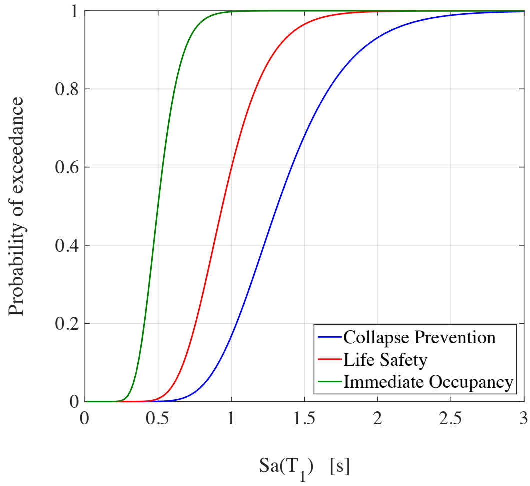

Archetype #196: 5_10_Q_002_5-5_C_II_1_MGP10_ATS

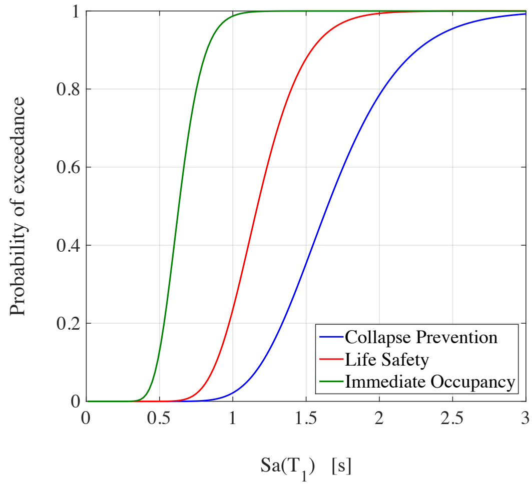

Archetype #197: 5_11_Q_004_6-5_C_II_1_MGP10_ATS

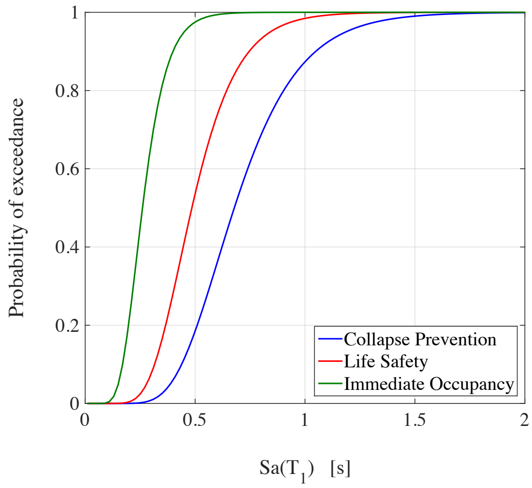

Archetype #198: 5_12_Q_002_5-5_B_II_1_MGP10_ATS

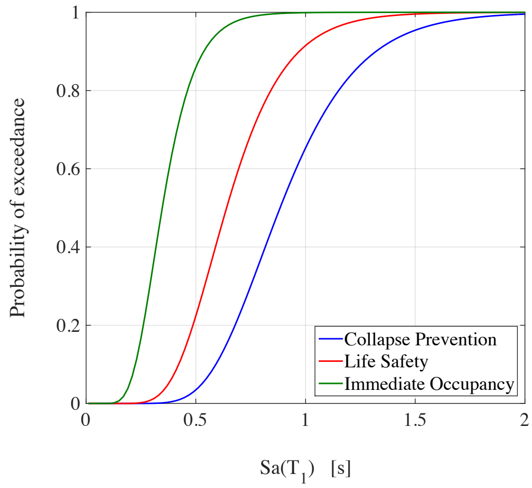

Archetype #199: 5_13_Q_004_6-5_B_II_1_MGP10_ATS

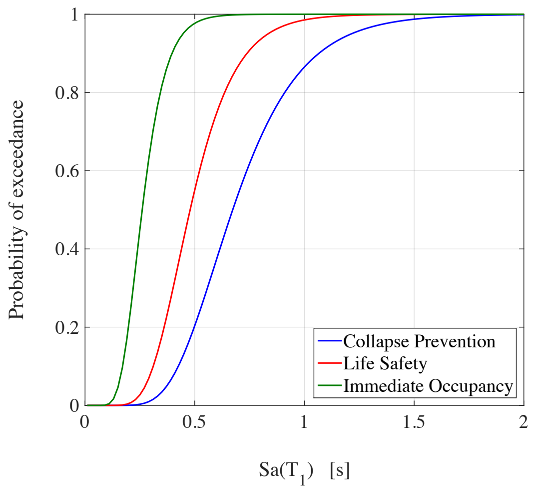

Archetype #200: 5_14_Q_002_5-5_A_II_1_MGP10_ATS

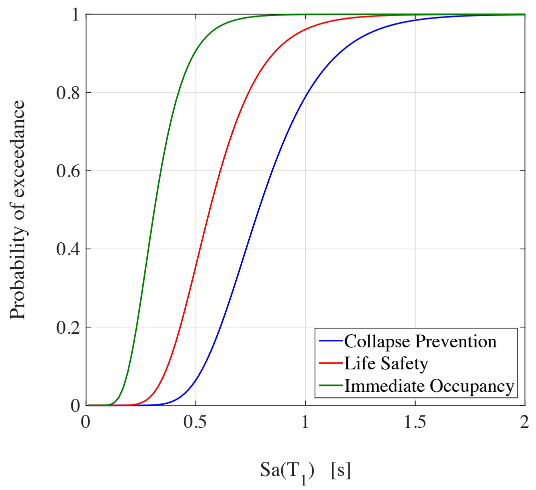

Archetype #201: 5_15_Q_004_6-5_A_II_1_MGP10_ATS